

Dissertation
submitted to the
Combined Faculties for the Natural Sciences and for Mathematics
of the Ruperto-Carola University of Heidelberg, Germany
for the degree of
Doctor of Natural Sciences

put forward by
Dipl. Phys. Pascal Bohleber
Born in Stuttgart
Oral examination: 18.11.2011

**Ground-penetrating radar assisted ice core
research: The challenge of Alpine glaciers and
dielectric ice properties**

Referees: PD Dr. Olaf Eisen
Prof. Dr. Kurt Roth

Abstract

Ice cores from Alpine drilling sites may provide long-term climate records. They are more complicated to interpret than their polar counterparts, however. The present thesis investigates the assistance for Alpine ice core research via ground-penetrating radar (GPR). First, the potential for reconstructing atmospheric signals is assessed for stable water isotope records based on a multi-core array at Colle Gnifetti (Monte Rosa, 4450 m asl). Here, a common atmospheric signal is revealed by time series analysis though adequate knowledge of the age-depth distribution is still needed for proper interpretation. Mapping isochronous GPR-reflections allows to consistently link the ice core chronologies up to 80 years before present. This is extended up to 120 years and over the whole drilling area by simple 2.5-dimensional flow modelling. Interpreting GPR-reflections in terms of physical ice core properties crucially relies on the complex dielectric permittivity. Aimed at investigating this material property specifically at radio-frequencies, previously constrained by sparse data only, a coaxial transmission line is adapted for glacier ice. Measurements of pure, artificial and natural ice samples between 1 MHz and 1.5 GHz at -20°C reveal for the permittivity of isotropic ice a real part of 3.16 ± 0.03 . The only signs of dispersion are found below 10 MHz, potentially associated with the high frequency tail of the Debye-dispersion.

Zusammenfassung

Auch aus Eiskernen alpiner Bohrplätze lassen sich klimarelevante Zeitreihen gewinnen. Im Vergleich zu polaren Eiskernstudien ist deren Interpretation jedoch wesentlich komplexer. Die vorliegende Arbeit untersucht, inwieweit Eisradarmessungen geeignet sind, alpine Eiskernstudien zu unterstützen. Hierzu werden zunächst Messreihen stabiler Wasserisotope aus vier Eiskernen des Gletschers Colle Gnifetti (Monte Rosa, 4450 m ü. NN) mittels Zeitreihenanalysen auf ein gemeinsames, atmosphärisches Signal hin untersucht. Hieraus ergibt sich, dass zur adäquaten Interpretation dieses Signals die Kenntnis der Alters-Tiefenverteilung des Probennahmegebietes unerlässlich ist. Das Verfolgen von isochronen Radarreflexionen erlaubt es, die Eiskerndatierungen über die letzten 80 Jahre konsistent miteinander zu verbinden und mittels einfacher, 2, 5 dimensionaler Fließmodellierung auf die letzten 120 Jahre sowie den gesamten Bohrplatz zu erweitern. Die Interpretation von Radarreflexionen als physikalische Eigenschaften von Eiskernen wird erst mittels der komplexen dielektrischen Permittivität möglich. Um diese Materialeigenschaft auch im Bereich von Radarfrequenzen zu untersuchen, in dem sie gegenwärtig nur unzureichend bekannt ist, wurde ein Aufbau zur Permittivitätsmessung mittels eines koaxialen Wellenleiters für Gletschereis angepasst. Messungen von künstlichen und natürlichen Eisproben zwischen 1 MHz und 1,5 GHz bei -20°C ergaben einen Realteil der Permittivität von 3.16 ± 0.03 . Dispersion wurde nur bei Frequenzen unterhalb 10 MHz beobachtet, was möglicherweise auf den hochfrequenten Teil der Debye-Relaxation in Eis zurückzuführen ist.

Contents

1	Introduction	1
2	The set of problems of water isotope records from alpine ice cores	5
2.1	Introductory remarks	5
2.2	Glaciological settings at Colle Gnifetti	6
2.3	The Colle Gnifetti water isotope time series	12
2.3.1	Raw data	12
2.3.2	Common signal investigation	12
2.3.3	Common signal extraction	18
2.4	Assessment of atmospheric signal within common ice core signal	21
2.5	Implications, needs and perspective	26
3	Age-depth distribution mapping of an Alpine drilling site	29
3.1	Introductory remarks	29
3.2	GPR measurements and data processing	30
3.3	Inter-core dating coherency evaluation	35
3.3.1	Lateral age-interpolation by internal reflection horizons	35
3.3.2	Pairwise inter-core dating comparison	38
3.3.3	Overall inter-core dating coherency	40
3.4	Mapping the internal age distribution at the CG drilling area	43
3.4.1	Considering ice dynamics for modelling alpine glacier flow	44
3.4.2	Adaptions of the ice slab for a flow model of an alpine glacier	47
3.4.3	The ice flow model	49
3.4.4	Input generation from GPR and ice core data	51
3.4.5	Results	52
3.5	Identification of catchment area and upstream-effects	55
3.6	Summary and critical assessment	57
3.7	Internal GPR–reflections investigated with borehole radar and physical ice core properties	60
3.7.1	Borehole radar	61
3.7.2	Physical properties in KCI versus internal reflections in GPR	70
3.7.3	Critical assessment and future perspective	73

4	The Permittivity of Ice in the MHz-range	75
4.1	Introductory remarks	75
4.2	A brief introduction to the permittivity of ice	76
4.2.1	Considerations from electromagnetic theory and ice physics	76
4.2.2	General ice characteristics up to GHz-frequencies	79
4.2.3	Implications for the interaction of ice with electromagnetic radiation	80
4.2.4	Permittivity measurements on ice in and around the MHz-range	82
4.3	Coaxial Transmission Line Cell Measurements	85
4.3.1	The Setup	85
4.3.2	Calibration and measurement	86
4.3.3	Setup refinements	87
4.3.4	The forward model	89
4.4	Permittivity computation from S-parameters	92
4.4.1	Overview	92
4.4.2	Validation of the Debye-model optimisation	94
4.5	Performance assessment of the coaxial cell setup	99
4.5.1	Reproducibility of S-parameter measurements	99
4.5.2	Uncertainty in permittivity estimation	99
4.5.3	Validation with reference materials	100
4.5.4	Critical assessment and future perspective	101
4.6	Permittivity of artificial ice	104
4.6.1	Sample preparation and characteristics	104
4.6.2	Permittivity of pure artificial ice	105
4.6.3	Influence of acidity and temperature	109
4.6.4	Discussion: The permittivity of artificial ice in the MHz-range	112
4.7	Permittivity of natural ice	116
4.7.1	Sample preparation and characteristics	117
4.7.2	Permittivity of natural firn and ice	118
4.7.3	Discussion: Permittivity of natural firn and ice	119
4.8	Future perspective	120
Lists		141
	List of figures	141
	List of tables	143
	List of acronyms and abbreviations	143
Appendices		145
Acknowledgements		183

1 Introduction

Preface

The present thesis comprises a dyadic outline with two only loosely connected parts. The first part is a field study on ground-penetrating radar (GPR) assisted ice core research at an Alpine drilling site. The special set of problems associated with small scale mountain drilling sites is illustrated via water isotope records, preceding the investigation on mapping three dimensional age distribution by means of GPR supplementing ice core chronologies. The second part is dedicated to a laboratory study focused on measurements of the dielectric ice properties at radio frequencies. Although concerned with dielectric material properties, this topic is closely related to the use of GPR on glaciers and ice sheets, and hence addressed from the perspective of glaciological applications, rather than materials science. Since introductory remarks are given at the beginning of each self-contained part, the following serves as a general overview on the background of the present work.

A detailed assessment of the current anthropogenic impact on climate requires precise knowledge of natural climate variability. Any reconstruction of pre-industrial climate conditions must rely on natural proxy archives, such as tree rings, sea sediments, and glacier ice. Polar ice sheets store information on climate variability over several glacial–interglacial cycles by means of stratigraphic archiving of precipitation, which can be retrieved by drilling ice cores [Petit *et al.*, 1999]. Thereby, not only past temperature changes can be reconstructed from the isotopic composition of water molecules [Dansgaard, 1964], but also the concentration of atmospheric trace substances within enclosed air bubbles [Lüthi *et al.*, 2008]. This unique combination of information in a common archive has made polar ice cores a large success, and an indispensable tool in paleoclimate research. The adequate interpretation of ice cores as stratified paleoclimate archives requires a profound understanding for the past and present state of the ice sheet affecting its internal layering. In this context, ground-penetrating radar (GPR) provides a powerful remote sensing method to investigate the geometry and internal structure of glaciers and ice sheets, making GPR nowadays a standard tool in glaciology [Bogorodsky *et al.*, 1985; Dowdeswell and Evans, 2004]. This especially concerns the application of GPR with respect to numerical ice sheet modeling and the synchronisation of ice

cores by means of internal reflection horizons (IRH) indicating englacial isochrones. From GPR-assisted ice core research in Greenland and Antarctica, knowledge of the past climate variability has been obtained over up to 800.000 years before present (BP) [Andersen *et al.*, 2004; Lambert *et al.*, 2008; Lüthi *et al.*, 2008].

As a matter of fact, findings from polar ice cores are less representative for mid- or low-latitudes. Here, glaciers and ice caps of high mountain ranges may provide complementary information in reducing this latitudinal gap. Required to adequately preserve stratigraphic integrity undisturbed by melting, suitable drilling sites are confined to high summit regions of the mountain range. In the European Alps¹, ice core studies have been performed at Col Du Dome, Mont Blanc [Vincent *et al.*, 1997; Preunkert *et al.*, 2000], Fiescherhorn, Bernese Alps [Schwerzmann *et al.*, 2006] as well as at Colle Gnifetti and Colle del Lys in the Monte Rosa region [Oeschger *et al.*, 1977; Schotterer *et al.*, 1978; Haeberli and Funk, 1991; Hoelzle *et al.*, 2011]. Among these sites, Colle Gnifetti (CG) stands out as the only site where net snow accumulation is low enough to, in spite of the limited glacier depth, provide for records exceeding the instrumental period at a reasonable time resolution, i.e. over the last millennium and possibly beyond. However, as pointed out by Wagenbach [1992], the low net accumulation caused by wind erosion features a pronounced spatio-temporal variability, thereby introducing substantial depositional noise to the respective ice core records. In presence of such depositional noise, an external atmospheric influence is expected to be identifiable as a common imprint on ice core records from multiple drilling sites on the same glacier. Hence, the multi-core array established at Colle Gnifetti by the Institute for Environmental Physics (IUP), University Heidelberg, provides the opportunity for a dedicated common signal investigation in the records of four ice cores drilled to bedrock.

In contrast to the strong signals of anthropogenic aerosol increase [Preunkert *et al.*, 2001], depositional noise especially challenges the comparatively weak water isotope trends [Wagenbach, 1989]. The identification of a respective common signal is additionally hampered by considerable uncertainty in the individual ice core chronologies. Consequently, no immediately useful long-term temperature signal could be reconstructed from the CG water isotope records so far. Focused on the depth range where dating errors are presumably only a minor obstacle, the present work aims at assessing to what extent the CG water isotope records reflect past atmospheric temperature changes. In contrast to polar ice cores, dating even shallow parts of an alpine glacier is a challenge due to its complex flow and accumulation irregular in space and time [Haeberli *et al.*, 1988]. Here, remedy may be found in ground-penetrating radar (GPR): Eisen *et al.* [2003a] connected CG ice core drilling sites on one flow line with a GPR-profile and showed that it is possible to cross-link age-depth relations by tracing internal reflection horizons (IRH), associated with englacial isochrone layers. However, as IRHs were found to be confined to roughly the upper 50% only, the GPR-based isochrone map-

¹if not stated otherwise, “Alpine” refers to the European Alps, whereas “alpine” will be used to generally refer to high mountain ranges.

ping was restricted to shallow depths and approximately the last 70 years BP. With an additional ice core drilled on a separate flow line and the desire to obtain a coherent dating scenario for larger depths and ages, this problem now becomes essentially three dimensional. In the present work it is approached by combining GPR and ice core data with a simple ice-flow model. Using IRHs in GPR-profiles and linking the respective drilling sites should allow for an inter-core dating comparison, eventually resulting in a coherent dating scenario. In contrast to the earlier finite-difference flow modelling attempts at Colle Gnifetti by Wagner [1996] and Lüthi [2000], the simple flow model employed here has to be designed for reproducing only the relative age-information inherent in GPR-IRHs and thus to be able to predict isochrone layers at larger depths and on arbitrary flow lines. In doing so, the approach should eventually allow for: (i) overcoming the vertical depth-limitation of a dating comparison by GPR-IRHs only, thus facilitating the assessment of the inter-core dating coherence at older ages; (ii) a lateral interpolation of the ice core based age information leading to a three-dimensional map of the age-distribution within the ice core drilling area at Colle Gnifetti; and (iii) to calculate back trajectories starting at a drilling site in order to narrow down the respective borehole catchment areas.

Internal reflection horizons (IRH) play a crucial role in the application of GPR to glaciers and ice sheets. Reflections of the electromagnetic wave occur at distinct spatial changes of the dielectric ice properties. Detailed knowledge of the physical origin of these changes is mandatory for an adequate interpretation of the respective IRH, especially regarding its isochrone character, and allows for spatial extrapolation of ice property independently of ice cores. The spatial extrapolation is of special relevance within studies at polar ice sheets, regarding their comparatively large scales. From polar studies, IRHs are known to coincide with variations in density, acidity [Robin *et al.*, 1969] and changes in crystal orientation fabric [Fujita and Mae, 1994; Eisen *et al.*, 2007]. Strong density variations are confined to the upper firn layers, whereas stress-induced changes in crystal orientation fabric associated with internal deformation processes have been observed in the lowermost parts [Azuma *et al.*, 2000; Weikusat *et al.*, 2009]. The majority of IRHs in polar areas is acidity-based, which presumably stem from volcanic acidity layers and are thus regarded as isochrones [Millar, 1981; Siegert, 1999; Hempel *et al.*, 2000]. An approach identifying the physical origin of an IRH requires forward modeling of radargrams based on the extensive data provided by ice cores [Miners *et al.*, 2002; Eisen *et al.*, 2003b, 2006]. In this context, knowledge of the complex relative dielectric permittivity of ice is crucial, as it is the essential material parameter connecting physical properties with the propagation characteristics of the electromagnetic wave. Dielectric profiling (DEP) is a routinely deployed measurement technique to infer the permittivity of an ice core at typically a few 100 kHz [Moore and Paren, 1987; Moore *et al.*, 1989; Moore, 1993; Wilhelms, 2000]. As GPR generally operates in the MHz-range, these data need to be scaled accordingly. For this purpose, precise knowledge of the frequency dependence of the ice permittivity is required. This knowledge may be

provided by means of laboratory measurements covering kHz- and MHz-frequencies. Existing high accuracy permittivity measurements are based on capacitive techniques in the kHz-range (e.g., in addition to DEP: Gough [1972]; Matsuoka *et al.* [1996]) and resonator methods at GHz-frequencies [Matsuoka *et al.*, 1997a,b]. In the MHz-range, however, only sparse data on the permittivity of pure ice exist so far [Johari, 1976; Johari and Charette, 1975]. Between 100 MHz and the GHz-range, present knowledge relies on the data by Westphal reported in Evans [1965], however lacking any details concerning measurement technique and uncertainties. Hence, the present state of knowledge on the permittivity of pure ice in the MHz-range appears unsatisfactory with respect to the precise data at adjacent frequency ranges. An adequate measurement technique is called for in order to (i) obtain precise data on the permittivity of pure ice at MHz-frequencies. Thereby a reliable scaling of DEP-measurements would be possible; and (ii) to perform measurements at radio frequencies directly on natural ice samples (e.g. ice cores), and with respect to variations in density, acidity and crystal orientation fabric. Within this context, two-port coaxial transmission line cells in combination with a vector network analyzer have been used to determine the frequency dependent complex permittivity of soil materials in the MHz-range [Shang *et al.*, 1999; Gorriti and Slob, 2005a; Wagner *et al.*, 2011]. In 2005, a similar coaxial transmission line cell developed by Oswald [2000] was established at the Institute for Environmental Physics (IUP) for measurements of soil samples [Oswald *et al.*, 2006].

The second part of the present work is thus aimed at measuring the permittivity of ice in the MHz-range by means of the coaxial cell transmission line technique. To do so, the IUP's coaxial cell setup has to be adapted for ice measurements. Measurements of artificial as well as natural ice samples are attempted as to investigate the permittivity of ice in the MHz-range, mainly focusing on the real part and its frequency dependence. Additional attention is paid to the influence of variable density and acidity content of the samples, as well as regarding systematic differences between artificial and natural ice. Thereby, results should open the door for a more comprehensive picture of the dielectric permittivity of ice, which is of broad interest for glaciological applications of GPR.

2 The set of problems of water isotope records from alpine ice cores

2.1 Introductory remarks

In ice core studies performed at mountain drilling sites, the straightforward interpretation of ice core records as past atmospheric signals strongly suffers from depositional noise. In the European Alps, Colle Gnifetti (CG) uniquely offers conditions suitable for ice core records exceeding the instrumental period (i.e. ca. the last 250 years) at a reasonable time resolution. At the same time, due to pronounced spatio-temporal variability in net accumulation combined with a complex flow regime, CG distinctly features the outstanding challenges met at mountain drilling sites pointed out by Wagenbach [1992]. As a consequence, Colle Gnifetti provides for long-term ice core studies only if the pronounced set of problems associated with depositional noise effects is sufficiently understood.

As a selected example of how depositional noise masks the archiving of an atmospheric signal in Alpine ice cores, the present study considers the water isotope records from CG ice cores for the following reasons:

- A dense network of long-term instrumental temperature as well as precipitation data is available for comparison with ice core water isotope records [Auer *et al.*, 2007; Böhm *et al.*, 2010; Chimani *et al.*, 2011].
- While the strong signals of anthropogenic aerosol increase are only little affected (e.g. Preunkert *et al.* [2001]), the relatively weak long-term trends in water isotopes may be buried in depositional noise [Wagenbach, 1989].
- A distinct atmospheric signal is expected on top of the noise as the recent temperature increase over the last century should be reflected in the ice core water isotope records.

The present study is limited on an evaluation of the depositional noise influence from a glaciological perspective. Consequently, the basic issue regarding what fraction of the water isotope variability is directly associated with air temperature changes is not addressed here [Rozanski *et al.*, 1992; Fricke and O'Neil, 1999; Hoffmann *et al.*, 2006]. Based on the central hypothesis that, in contrast to the local influence of depositional noise, an atmospheric signal should reflect in a common signal, the water isotope time

series from the four deep CG ice cores are considered. Thus, the main task is to assess if, and on what time scale (or frequency threshold, respectively) a signal common to all records can be identified. To this end, the present chapter gives a brief overview on the relevant glaciological settings at Colle Gnifetti before focusing on the intercomparison of water isotope time series by means of dedicated time series analysis. Based on the outcome of the common signal investigation, a single record representative for the common isotope variability is to be compiled. Limited on assessing as to what extent the common isotope record may reflect a common atmospheric cause, an adequate instrumental temperature data set is synthesized for comparison. The main emphasis of the discussion is placed on the implications from this exemplary study regarding the effects of depositional noise influence for Colle Gnifetti and potentially, other mountain drilling sites.

2.2 Glaciological settings at Colle Gnifetti

Colle Gnifetti forms a small firn saddle at around 4500 m above sea level (asl) with a maximal glacier thickness of around 140 m near the saddle point and a maximal horizontal extent of 400 m (Figure 2.1). Glaciological features of Colle Gnifetti are thoroughly described in the literature, e.g. see: Haeberli *et al.* [1988]; Lüthi [2000]; Eisen *et al.* [2003a] for geometry and glacier flow, Haeberli and Funk [1991] for the temperature distribution and Alean *et al.* [1983] with respect to the surface accumulation pattern. Thus, in the following, only a brief overview is presented, mainly relevant in the context of water isotope records.

Geodetic observations suggest that the saddle geometry is near steady state [Lüthi, 2000] and remained almost unchanged over the last century [Wagner, 1996]. Although a recent systematic increase in englacial temperatures has been observed [Hoelzle *et al.*, 2011], the glacier is cold throughout and frozen to bedrock, with an englacial 20 m temperature level close to -14°C [Haeberli and Funk, 1991]. Therefore, the percolation of meltwater is restricted to the uppermost firn layers. The frozen-to-bedrock basal ice entails a zero horizontal velocity and concentrates shear deformation near bedrock. In the upper parts, vertical strain (which is of $O(\approx \dot{b}/H)$ with surface accumulation \dot{b} and ice thickness H) is much larger (by about a factor of 30) as compared to the respective sections in an ice-sheet, thus going along with rapid annual layer thinning. For these reasons, the lowermost sections of the glacier are expected to comprise a large amount of annual layers. Maximum age constraints were obtained from radiocarbon analysis by Jenk *et al.* [2009] and May [2009] indicating a tentative maximum age of ≈ 10 ka.

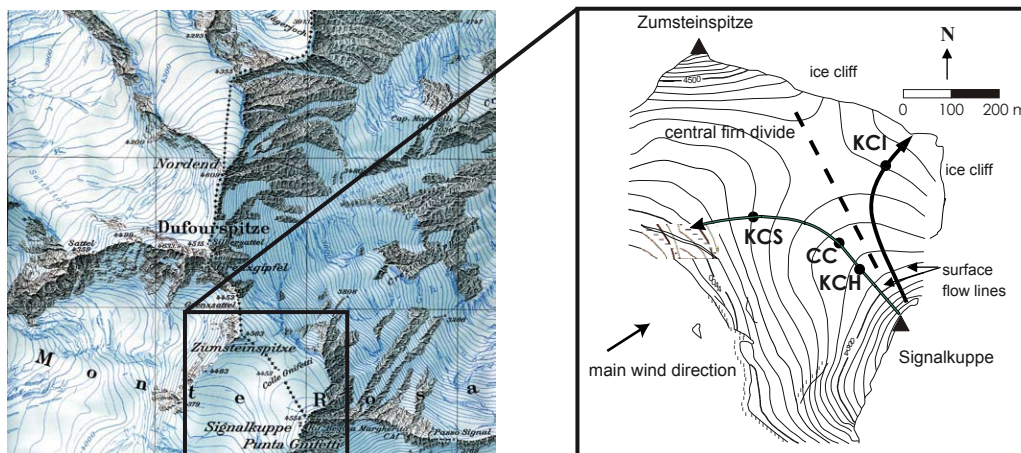


Figure 2.1: The Colle Gnifetti location and ice core array. Left: The Colle Gnifetti saddle located between Zumsteinspitze and Signalkuppe in the Monte Rosa massif, Swiss-Italian Alps (©2011 swisstopo). Right: The ice core array. Four deep ice cores were drilled featuring the same catchment area in the north-facing flank of Colle Gnifetti. Approximate flow lines are indicated by black arrows, the surface topography by contour lines at 20 m altitude spacing. The dashed line indicates the approximate location of the central firn divide.

Ice core array and chronologies

The IUP ice core array at Colle Gnifetti comprises four deep cores drilled within the CG north-facing flank (see Figure 2.1 for the drilling site locations and Table 2.1 for characteristic core parameter²). The ice cores KCH, CC and KCS were drilled roughly along a common flow line upwind the central firn divide. Specifically dedicated to the long-term time scale (i.e. the last millennium), the KCI ice core was drilled down-wind of the central firn divide within an “island of minimum accumulation” identified by ground-penetrating radar [Böhlert, 2005].

The age-depth distribution of Colle Gnifetti (and other small scale mountain glaciers) becomes strongly non-linear already after 100 years or so. A direct transfer of dating techniques applied within the upper parts of polar ice cores (such as simple down-core counting of annual layers over large depths) is not possible. Therefore, a combination of different dating methods has to be used. The Colle Gnifetti ice core datings are based on the counting of remnant seasonal cycles in impurities combined with absolute time horizons such the 1963 tritium peak, large Saharan dust deposits (1977, 1947, and 1901 AD) and the volcanic Katmai eruption of 1912 AD. Except for KCI, annual layer counting was performed in profiles of ionic impurities, especially relying on ammonium as it

²Note that depths reported in water equivalent units (m w.e.) commonly used to account for the compaction of snow and firn. The length in w.e. denotes the thickness of a respective layer when compressed to the density of water.

Table 2.1: Characteristic parameters of the Colle Gnifetti ice cores. Note the exceptional low surface accumulation of KCI. Core depth marked with (*) indicate that a small amount of basal ice before bedrock may not have been recovered in the respective ice core drilling. Firn-ice transition was set to the approximate depth range, where the local mean density values exceeds 0.83 g/cm^3 .

Ice core	CC	KCH	KCS	KCI
Year of drilling	1982	1995	1995	2005
Total depth [m]	64	60*	100	62*
Total depth [m w.e.]	50	45*	79	48*
Mean surface accumulation [m w.e./year]	0.22	0.23	0.51	0.14
Relative depth of 1900 AD	33%	44%	47%	24%
Firn-ice transition depth [m]	31	28	43	27
Firn-ice transition age [before drilling]	104	105	63	220

provides the largest summer/winter contrast [Preunkert, 1994]. In the low accumulation KCI core identification of annual cycles was mainly based on combining continuous flow analyses of mineral dust and electrical meltwater conductivity at cm depth resolution backed-up with density profiles at sub-cm resolution [Bohleber, 2008]. Within the last 120 years the maximal dating uncertainty was estimated to be less than 3-5 years (see Schäfer [1995] for CC, Armbruster [2000] for KCH and KCS, and Bohleber [2008] for KCI). By integrating a vertical velocity function from theoretical ice flow considerations (see section 3.4.1 in chapter 3), the age-depth relation from annual layer counting was extrapolated as a best guess beyond depths where annual layers can no more be resolved.

Water isotope records

Measurements of stable water isotope (^{18}O and ^2H (=Deuterium, D)) concentrations by mass spectrometry are performed relative to a standard (Here: the Vienna Standard Mean Ocean Water (VSMOW)), thus conventionally reported using the δ -notation:

$$\delta^{18}\text{O} = \frac{R_{\text{sample}} - R_{\text{standard}}}{R_{\text{standard}}} \cdot 1000 \text{ [‰]} \quad (2.1)$$

with the relation $R = \frac{[H_2^{18}O]}{[H_2^{16}O]}$ and $R = \frac{[HDO]}{[H_2O]}$ in case of δD respectively. Overall accuracies for $\delta^{18}\text{O}$ and δD analyses by mass spectrometry in the IUP laboratory are typically 0.05 and 0.7 ‰ for $\delta^{18}\text{O}$ and δD , respectively [Keck, 2001]. The measurement uncertainty is negligible compared to the natural occurring variability. In the following, the $\delta^{18}\text{O}$ datasets will be considered.

The correlation between the ambient temperature and the concentration of the stable water isotopes in precipitation provides the very foundation of a quantitative reconstruction of the past temperature in ice core analysis. Meteoric water is observed to be

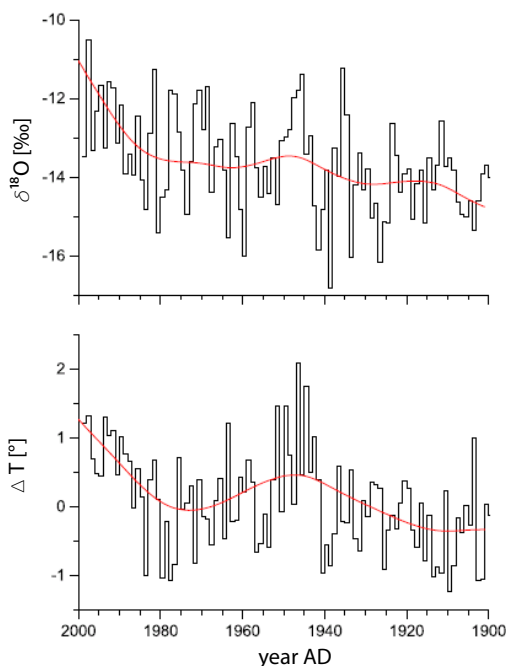


Figure 2.2: Centennial trends in Colle Gnifetti isotope records compared to instrumental temperature by Keck [2001]. Upper graph: Stacked isotope records from KCH, CC and KCS resampled to formal annual resolution. Lower graph: Instrumental temperatures. Red: Overall 20th century trends indicated by robust cubic spline smoothing. Note how the distinct recent warming signal reflects in a comparatively weak long-term isotope trend only.

increasingly depleted in heavy isotopes with distance from the ocean water source, increasing altitude and latitude. The decreasing temperature relative to the tropical source region appears as the predominant factor for these effects [Dansgaard, 1964]. Strong temporal temperature effects comprise the seasonal variation in isotopic composition of precipitation especially at continental and polar regions. Assuming for simplicity a spatially constant subtropical source region with an almost stable temperature-regime, this variation can be assigned to the seasonal variation in cloud condensation temperatures (easily being in the order of 20°C at polar or alpine glaciers).

A central parameter for quantitative temperature reconstruction is the so-called sensitivity of the isotope thermometer with respect to the ambient temperature, represented by the $\Delta\delta^{18}\text{O}/\Delta T$ -relation. Adopting a simple Rayleigh model (e.g. see Mook [2006]) for precipitation transported to the Greenland ice-sheet, Dansgaard [1964] predicted an $\delta^{18}\text{O}$ -temperature relationship of $\approx 0.69[\text{‰}/\text{°C}]$ which has been verified in respective ice core studies (e.g. see the review of Jouzel *et al.* [1997]). Due to the shortcomings in climatic interpretation of isotope records at CG this $\Delta\delta^{18}\text{O}/\Delta T$ -relation cannot be used. Instead, an empirical $\Delta\delta^{18}\text{O}/\Delta T$ -relation has to be derived based on a comparison with instrumental temperature.

Using the stacked isotope records from KCH, CC and KCS for a comparison with instrumental temperature, Keck [2001] found a distinct covariation within the last century confined to the very long-term trends³ (Figure 2.2). With the latest core KCI featuring the lowest accumulation and hence the strongest summer bias, the present chapter aims

³Note that, if not stated otherwise, “trend” refers to data smoothed by filtering according to the respective time scale, e.g. decadal, centennial trends.

to assess, if and on what time scale the influence of a potential atmospheric signal can be identified in all four ice cores.

Net snow deposition characteristics and associated noise

The exceptional low net accumulation at Colle Gnifetti is caused by strong winds frequently blowing fresh snow across the steep ice cliff at its eastern side. Evidently, the CG drilling site does not constitute a closed system regarding precipitation. The strong winds move the dry and least consolidated winter snow more easily than the more quickly metamorphosing summer snow which is often additionally protected by melt layers. Due to the extensive wind erosion, only a small percentage ($\approx 10\%$) of the total annual precipitation is preserved and in extreme cases even the complete loss of annual layers may occur. Net snow deposition at CG must therefore be regarded as seasonally unevenly distributed, with a strong bias towards the growing season [Wagenbach, 1989]. Moreover, annual net accumulation on the saddle features a distinct spatial variability, ranging from 0.15 m water equivalent (w.e.) in the north-east-facing flank up to about 1.2 m w.e. at the south-facing slope, where the higher abundance of surface ice layers and ice crusts significantly reduces the snow erosion rate [Alean *et al.*, 1983].

As a consequence of the pronounced spatio-temporal variability in net accumulation at Colle Gnifetti, the archiving of atmospheric signals in the ice core records is hampered by depositional noise on top of systematic depositional effects: Regarding the temporal variability, the typical summer bias in net accumulation is increasing with decreasing accumulation, which is clearly seen in the respective mean water isotope level. An individual annual $\delta^{18}\text{O}$ value depends on the fraction of winter precipitation lost and thus on the individual annual sampling period (Figure 2.3). This depositional noise contributes strongly to the temporal isotope variability showing e.g. for $\delta^{18}\text{O}$, a seasonal range of around 15‰ (roughly corresponding to seasonal temperature range of 20°C) while recent temperature related $\delta^{18}\text{O}$ trends should not be larger than some ‰ (see Figure 2.2). Consequently, the relatively weak long-term trends in $\delta^{18}\text{O}$ signals are especially challenged by the influence of varying seasonal fraction in net snow deposition [Wagenbach, 1989]. In addition, temporal trends in $\delta^{18}\text{O}$ are superimposed by systematic spatial variations in net accumulation upstream of the respective drilling site, the so-called “upstream effect” [Keck, 2001; Wagenbach, 2001].

From ice core studies on ice caps in the Canadian Arctic, Fisher *et al.* [1983, 1985] and Fisher and Koerner [1994] thoroughly studied the effect of wind scouring on water isotope records and showed that the resulting depositional noise has to be taken into account even in case of these km-scale ice bodies. Moreover, depositional noise on short term (e.g. annual) time scales is also observed hampering the detection of a common signal among ice cores from polar ice sheets [Fischer *et al.*, 1998; Crüger *et al.*, 2004; Andersen *et al.*, 2006]. The studies by Fisher *et al.* [1985] and Andersen *et al.* [2006] developed theoretical noise models and estimated signal-to-noise variance ratios in or-

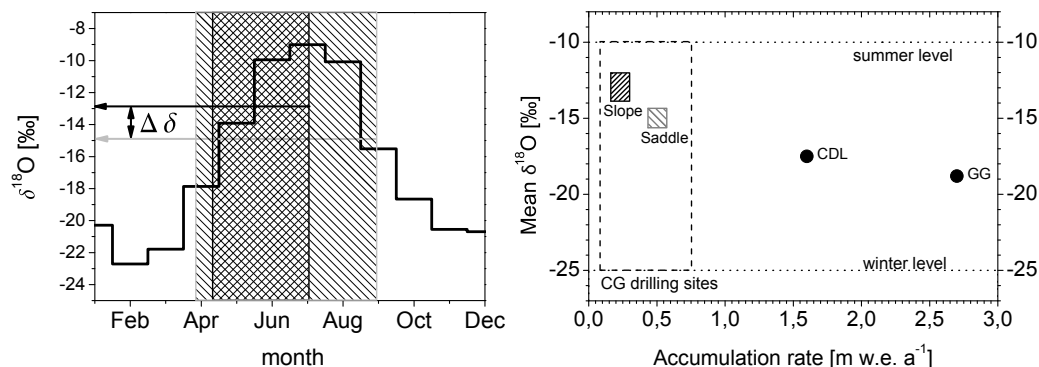


Figure 2.3: Snow sampling influence on $\delta^{18}\text{O}$ mean values. Left: Illustrational scheme of the typical seasonality of $\delta^{18}\text{O}$ in precipitation at CG. The black and grey rectangles represent potential sampling periods of two different drilling sites (or two sampling periods at the same site) producing a difference in $\delta^{18}\text{O}$ -values that is not directly linked to temperature. Right: Mean $\delta^{18}\text{O}$ levels plotted against mean snow accumulation for ice records from different drilling sites within the Monte Rosa region. Rectangles in the Colle Gnifetti area comprise various shallow and deep cores from the north flank and near saddle point, respectively. CDL and GG denote cores drilled at Colle del Lys (B.Stenni, pers. communication) and Grenzgletscher [Eichler *et al.*, 2000] at a saddle and valley site, respectively. The CDL and GG values were transformed to the Colle Gnifetti altitude using a $\delta^{18}\text{O}$ -altitude gradient of 2‰/1km. Winter and summer core levels broadly indicate the overall range of the raw data set.

der to quantify the influence of stratigraphic noise. By these means and for the case of precisely dated, annually resolved $\delta^{18}\text{O}$ records, half of the variance is expected to be noise [Fisher *et al.*, 1985] with noise levels increasing further in the presence of wind scouring [Fisher and Koerner, 1994]. Based on the comparatively well dated ice cores from polar ice caps, the signal-noise separation procedure of Fisher *et al.* [1983, 1985] presupposes precisely aligned time series, or at least, aligned segments of time series. Alternatively, four $\delta^{18}\text{O}$ records from the Agassiz ice cap were compared on a single time scale tuned to match volcanic eruptions [Fisher and Koerner, 1994].

In contrast, the relative uncertainty between the age-depth relations of the Colle Gnifetti ice cores has not been assessed so far. Their individual dating errors in the order of 3-5 years within the last 120 years may seriously bias the study of noise effects. Moreover, the development of similar noise models is not straightforward in view of the extreme temporal variability in net accumulation. Consequently, an immediate transfer of the methods by Fisher and co-authors to CG is hampered, although their results give an expectation on the minimal noise influence to be expected in the CG $\delta^{18}\text{O}$ time series, which are presented in the following section.

2.3 The Colle Gnifetti water isotope time series

2.3.1 Raw data

The stable water isotope records were obtained by continuous sub-sampling at depth resolution typically ranging between 5 and 10 cm (for the past 120 years) and up to 1.5 cm for the lowermost layers. Figure 2.4 presents the entire raw $\delta^{18}\text{O}$ profiles of the four ice cores on a water equivalent (w.e.) depth scale. Note the outstanding diffusional smoothing experienced by the KCI core already in the top 15 m w.e. Due to the relatively high firn temperature but low annual accumulation isotope smoothing at CG is much faster than at polar sites. Re-sampling most of the KCI record even at 1.5 cm depth resolution did not significantly restore the high frequency isotope variability seen in the other (higher accumulation) cores [Bohleber, 2008]. Noting this as a persistent, natural sampling effect, the original coarse KCI resolution was therefore used. On their individual depth scales, the only apparent common feature in the four records comprises $\delta^{18}\text{O}$ -values being well below the respective 20th century level within the last few meters before bedrock. Due to the proximity to bedrock, an investigation on whether this shift is a product of glaciological processes or an indication of ice remnant from the last ice-age and hence representing an atmospheric signal is difficult and still topic of ongoing discussion (for details see Keck [2001]; Wagenbach [2001]).

2.3.2 Common signal investigation

Evidently, a sound intercomparison of the $\delta^{18}\text{O}$ -records can only be performed by accounting for their different glaciological properties converting the depth into a time scale. In the present work, the common signal investigation on the time series was focused on the last 120 years. This restriction ensures lowest dating uncertainty, relatively weak upstream effects and an almost negligible influence of annual layer thinning on the raw data statistics.

Basic characteristics of the CG $\delta^{18}\text{O}$ time series

According to the ice core chronologies (and numerous snow pit studies) the individual values in the raw $\delta^{18}\text{O}$ time series may represent from monthly up to 3 year mean values (the overall maximum time step found at 1880 AD in KCI). To account for the different annual layer stratigraphies the raw $\delta^{18}\text{O}$ time series were transformed to a common resolution of nominal annual means, shown in Figure 2.5. Visual inspection of the “annual” $\delta^{18}\text{O}$ time series already reveals: (i) a high inter-annual variability with almost no inter-core correspondence, (ii) distinct, but only weakly coherent, multi-annual changes, (iii) different degrees of diffusional smoothing and, nevertheless, (iv) an overall increasing trend (from 1880 AD to present) common to all records; (v) influenced by

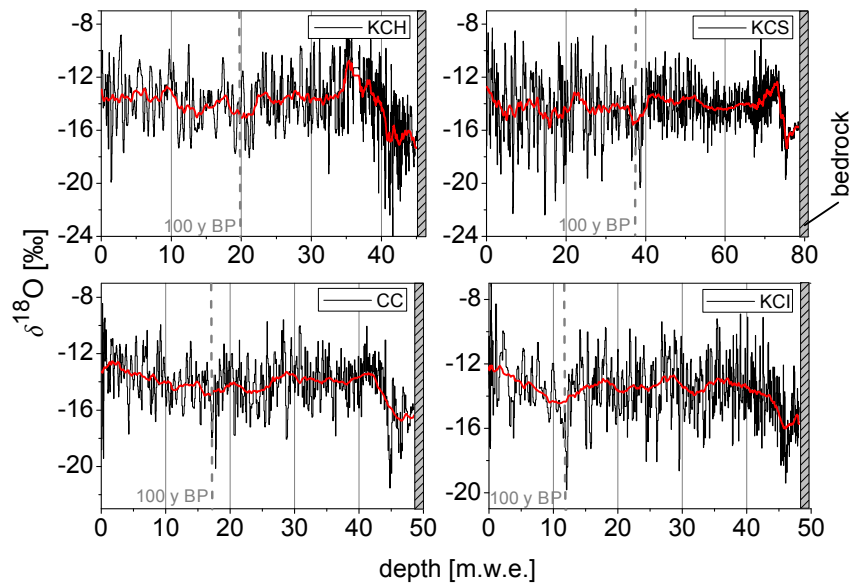


Figure 2.4: Colle Gnifetti ice core raw isotope records. Note the common decrease in mean isotope level shortly above bedrock. For better visual perception only, a 50 point moving average was applied (red). Indicated as a dashed grey vertical line: 100 a BP horizon.

site specific accumulation rates the absolute mean values within this time period range between -14.4‰ (KCS) up to -13.3‰ (KCI) while KCH and CC show similar levels of about -13.9‰ and -13.8‰ , respectively. Being steadily damped with depth, the high frequency (annual to sub-annual) $\delta^{18}\text{O}$ oscillations constitute an individual, instantaneous component of each time series. Hence, the high frequency components unlikely reflect a common external atmospheric signal and are rather associated with site specific depositional regimes. In this context, dedicated time series analysis is called for as to constrain the frequency range on which a common external forcing of the $\delta^{18}\text{O}$ variability may be present within the ice core array.

In order to obtain an adequate benchmark for testing various tools for time series analysis, four artificial $\delta^{18}\text{O}$ time series were considered. These artificial time series were synthesized as to closely reflect the special properties of the CG $\delta^{18}\text{O}$ time series. To this end, all four time series featured a common signal comprising the following components, as to reflect the effects (ii) and (iv) addressed above:

- two harmonic oscillations of 10 and 40 year period, respectively
- a weak long-term, non-linear (quadratic) trend increasing over the last 110 years.

The following individual traits derived from the actual time series were added to this common signal:

- the individual mean $\delta^{18}\text{O}$ (see component (v))

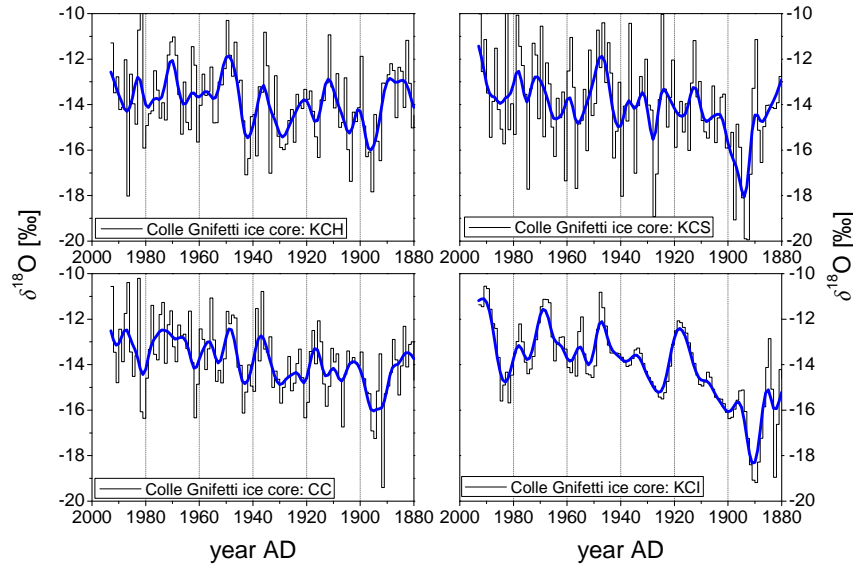


Figure 2.5: Colle Gnifetti isotope time series over the last 120 years displayed as nominal annual means with decadal trends highlighted by Gaussian smoothing (in blue). Note the relatively small effect of this low pass filter on the low accumulation KCI record extensively smoothed already by isotope diffusion. Also note that ice core time series are generally displayed here with age increasing from left to right, corresponding to the top of the ice core records being on the left hand side.

- a seasonal variability of large amplitude, however damped by an exponential decay of characteristic time scale (see components (i) and (iii))
- a white noise component of individual amplitude (see components (i) and (iii))

In order to simulate the instationary averaging (as a result of the non-linear age-depth relations) the artificial time series were subsampled according to an analytical age-depth relation (assuming constant vertical strain \dot{b}/H , with values for surface accumulation \dot{b} and ice thickness H from Table 2.1). In doing so, the high-frequency signal components were averaged out increasingly with depth and individually for each time series as representing one ice core of the array. In the following, the thus obtained four time series are referred to as the “artificial $\delta^{18}\text{O}$ time series”. They shown in the appendix A.1, along with more details regarding their construction.

Methods for common signal investigation

The presence of a common signal can be assessed by means of an adequate measure for the cross-correlation between the respective time series. Such an investigation can be performed in the time- as well as in the frequency domain. However, any attempt at

adequately quantifying the correlation between two of the $\delta^{18}\text{O}$ time series must take into account their special properties due to: (i) the uneven spacing of the raw time series due to the non-linear age-depth relation and (ii) the inherent serial correlation due to isotope diffusion and the averaging as a result of (i). Due to property (i), interpolation was necessary to some extent to obtain to formal annual common resolution. However, it is known that interpolation of unevenly spaced time series may significantly bias statistical results (e.g. in a cross-spectral analysis) since interpolated data points can not be considered independent [Schulz and Stategger, 1997]. Various methods have been developed for the (cross-)spectral analysis of unevenly spaced data [Scargle, 1989; Schulz and Stategger, 1997; Baisch and Bokelmann, 1999; Schulz and Mudelsee, 2002]. However, the application to the CG $\delta^{18}\text{O}$ time series is not straightforward due to the comparatively short length of the time series with respect to the considerable persistence-times (i.e. property (ii), especially relevant for the KCI core). In the present work, a combined approach between time- and frequency-domain based methods was deployed to investigate the correlation among the four $\delta^{18}\text{O}$ time series. Due to the above mentioned challenges associated with properties (i) and (ii), special care was taken when attempting a quantitative interpretation of the results. Moreover, all of the methods deployed in detail have been tested against the artificial time series first, as to obtain an initial performance estimate. While not all of the time series analyses can be reported in full detail here, a brief report on their central findings will be given in the following, with an exemplary more detailed focus on the “binned correlation” investigation.

In a first step, univariate spectral analyses were applied. In order to account for possible interpolation artefacts, the windowed Fourier spectrum of each of the equidistant annual time series was supplemented by the Lomb-Scargle periodogram of the original datasets (both methods implemented in the software Autosignal [SeaSolve, 2003]) as well as the spectral analysis algorithm based on an autoregressive model by Schulz and Mudelsee [2002] (see appendix A.2 for the exemplary Lomb-Scargle periodogram). The spectral analyses consistently show that the KCI spectrum contains no significant components with periods lower than 7-10 years. For KCH, CC and KCS multi-annual changes in the range of 3-5 years contribute to the isotope variability but periods shorter than 5-10 years are not common among them.

Focusing on the time domain for a cross-correlation analysis, Pearson’s correlation coefficient R was estimated by adapting the “binned correlation” approach outlined in Mudelsee [2010] specifically for deployment with the ice core time series. In spite of the serial correlation of the data, the binned correlation allows to calculate a correlation measure with respect to different time scales including confidence intervals based on a bootstrap technique (A detailed description of the technique is given in Mudelsee [2003, 2010], and the respective algorithm is presented in the appendix D). The essential steps involve:

- Dissecting each time series in identical discrete time windows of pre-defined length (i.e. “binning” the time series).

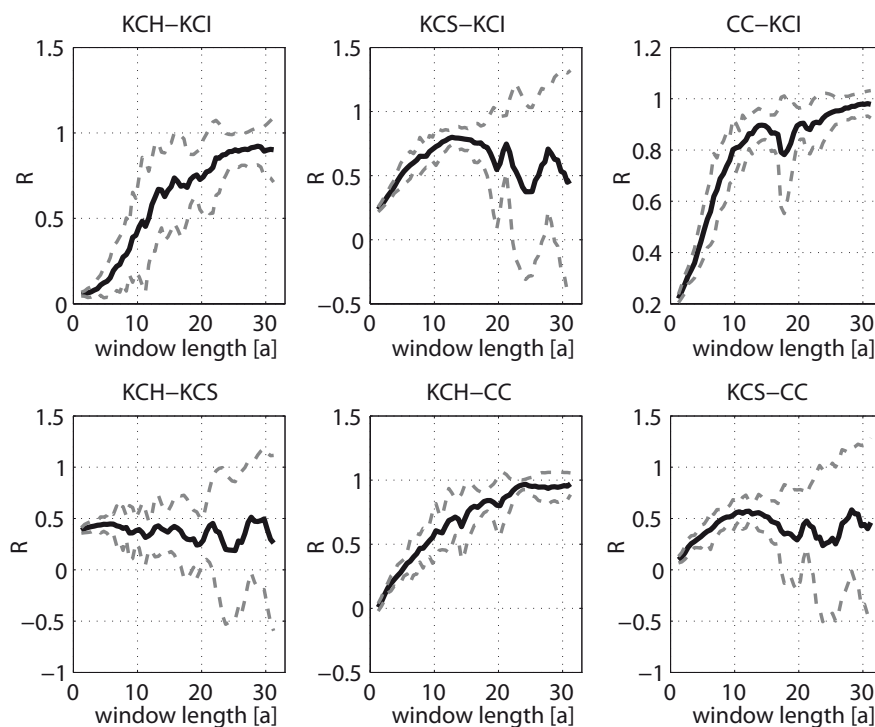


Figure 2.6: Binned correlation coefficient R of each two of the CG $\delta^{18}\text{O}$ time series (1981-1880 AD), plotted as a function of binning window length (black curve). The grey dashed curves indicate the 90 % confidence intervals obtained from multiple runs with varying starting point of the binning.

- Computing the mean of all data points within the respective windows. Associating the mean with the midpoint of the respective time window results in subsampled time series on an equal time scale.
- Calculating the correlation coefficient R between the mean values calculated in the previous step.

Evidently, the computed value for R may depend not only on the length of the binning window but also on the respective starting point of the binning in the time series. The influence of these parameters is taken into account by randomly varying their values in a large number of runs and using the 90 % percentile of the distribution in values of R as uncertainty estimates.

Results from comparing the four $\delta^{18}\text{O}$ time series by this approach for the longest possible period with all four contributing time series (1981-1880 AD) are shown in Figure 2.6. As expected from the visual comparison in Figure 2.5, correlation is low for short time scales and window lengths, respectively. Not least due to the increasing trend present in all time series, R increases with increasing window length. Obviously, for binning windows in the order of the time series length, R is based on very few data points resulting in large uncertainties. Consequently, binning windows were only in-

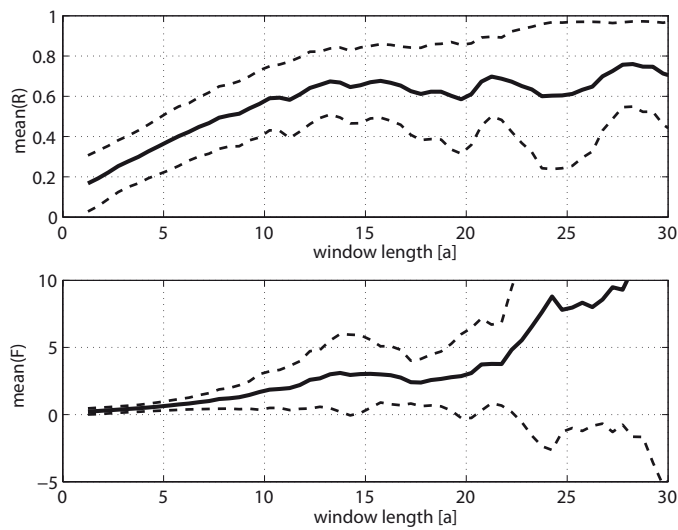


Figure 2.7: The mean of all binned correlation coefficients from CG $\delta^{18}\text{O}$ time series (1981-1880 AD) shown in Figure 2.6, plotted as a function of binning window length (top graph, black curve). Also shown: Signal-to-noise variance ratio F , which must only be interpreted qualitatively due to the dating uncertainties (see text). Grey dashed curves: 90 % confidence intervals (see text).

creased up to 30 years or 1/3 of the time series length. As pointed out by Mudelsee [2010] an adequate window length may be selected according to the persistence times of the time series, which means window of ≈ 10 a for pair including KCI and ≈ 5 a, otherwise (persistence times were calculated according to section 7.5.1. in Mudelsee [2010]). In the present investigation, R was calculated with a variable binning window, as the (qualitative) dependency of R on the respective time scale was of additional interest. Note that R -values calculated including KCS seem to level or even slightly decrease at larger binning windows. This might be due to the comparatively large amount of high frequency variability in KCS (with a substantial amount on the sub-annual scale) masking the weak increasing trend. Additionally, R calculated for pairs including KCS was found to be somewhat sensitive to the start and end point of the time series under consideration.

As an overall result from this investigation the mean value of R (i.e. the mean of the data shown in Figure 2.6) is shown as a function of binning window length in Figure 2.7. For tentative comparison only, the signal-to-noise variance ratio F used by Fisher *et al.* [1985] is also shown. Based on the hypothesis that in contrast to individual noise, the signal is part of both time series, F is defined as: $F = R/(1 - R)$ (note that this approach assumes perfectly aligned time series). For the CG $\delta^{18}\text{O}$ time series, the mean of R seems to level around 0.6 beyond window length of 10-12 years, indicating a persistent covariation among the time series above the decadal time scale. In this interval, F is ≈ 3 , which is at the upper end of the range of 1-3 found at polar drilling sites on the annual time scale, as reported by Fisher *et al.* [1985].

The persistent correlation in long-term signal components (for periods roughly above the decadal scale) was consistently found using cross-correlation analysis in the frequency domain, i.e. by coherence analysis following Usoskin *et al.* [2009] (shown in

the appendix A.2).

Aimed at eliminating the non-coherent high-frequency components from the four $\delta^{18}\text{O}$ time series, different techniques were used for low pass filtering in the frequency space, i.e. Singular Spectrum Analysis (SSA), Gaussian-shaped moving windows as well as Loess filtering [SeaSolve, 2003], all giving virtually the same results. To keep the data reduction transparent, Gaussian smoothing (including appropriate prevention of boundary effects) was selected as the standard low pass filter (with results always cross-checked versus the alternative methods). Moreover, the Gaussian procedure was preferred since it basically prescribes “natural smoothing” by isotope diffusion (e.g. see Johnsen *et al.* [2000]).

In conclusion, various time series analyses consistently suggest that common $\delta^{18}\text{O}$ variability within the core array is restricted to periods larger than 10 years, thus limiting also any association with an atmospheric signal. The broad correspondence of this decadal threshold with the variability seen in the a priori smoothed, raw KCI isotope record appears somewhat fortuitous, but is consistent with visual inspection of the accordingly filtered time series presented in Figure 2.5.

2.3.3 Common signal extraction

In view of the common long-term variability of all four CG $\delta^{18}\text{O}$ time series, an adequate method of data reduction is called for to extract a single, representative $\delta^{18}\text{O}$ record with an amplified signal-to-noise ratio. In a next step, the thus compiled single representative record is to be deployed to assess as to what extent this common ice core signal is actually connected to an atmospheric input.

Stacking individual time series for noise reduction is frequently used with polar ice core studies (e.g. see Fisher and Koerner [1988]; Fischer *et al.* [1998]; Andersen *et al.* [2006]). Generally following this conventional strategy and stacking the individual records to obtain a single representative record, different methods were used for common record compilation, which were intercompared focusing on the above-decadal long-term trends:

The simple stack: The average of the four $\delta^{18}\text{O}$ time series $x_i(t)$ at annual resolution:

$$x_s(t) = \frac{1}{n} \sum_{i=1}^n x_i(t) \text{ with } n = 4.$$

The 3a stack: In order to avoid interpolation, the four time series were subsampled to the lowest common resolution (3 years at 1880 AD in KCI) prior to stacking. Due to its coarse resolution, the 3a stack was mainly used for investigating long-term (i.e. centennial) trends and for cross-checking the simple stack.

The σ -stack: As suggested by Fisher *et al.* [1985], all time series $x_i(t)$ are considered as deviation from their mean (\bar{x}_i) and scaled by their standard deviation (σ_i) prior to stacking: $x_{\sigma s}(t) = \frac{1}{n} \sum_{i=1}^n \frac{x_i(t) - \bar{x}_i}{\sigma_i}$.

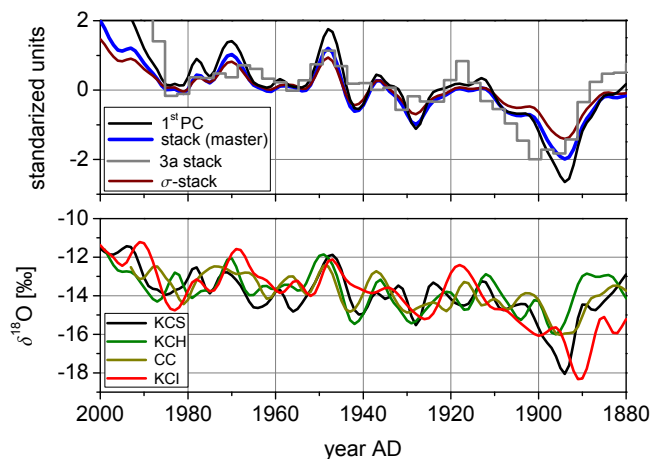


Figure 2.8: Decadal common record compilation of CG $\delta^{18}\text{O}$ time series. Top graph: Decadal trends of various stacking methods (discussed in the text) and the first principal component. All shown as standardized units (see text). Bottom graph: Decadal trends of the four $\delta^{18}\text{O}$ time series shown for visual comparison with the single representative records in the top plot.

The 1st Principal Component: Principal Component Analysis was applied to the four $\delta^{18}\text{O}$ time series at annual resolution (PCA-Algorithm pers. communication from C. Mattula, ZAMG, Vienna). This resulted in the first principal component (PC) (representing the highest common variability, e.g. see Pearson [1901]) with close to equal relative contributions from the individual time series, hence not much different from the simple stack.

The decadal trends of all of the above methods are shown in Figure 2.8 in standardized units (i.e. in deviation to the mean of the entire time period and normalized to unit standard deviation). All methods show virtually identical decadal trends, with only somewhat larger amplitudes in the 1st PC and a slightly more robust σ -stack. The correspondence among the methods is even larger for longer term trends. Exclusion of a single core would only lead to slight alterations in the stack, mostly during periods where the individual decadal changes do not completely align (e.g. 1920–1910, see Figure 2.8). However, there are no substantial indications that a certain $\delta^{18}\text{O}$ record might be flawed, e.g. exceptionally disturbed by depositional noise.

As a result from this analysis, the simple stack (in the following: “the stack”) was chosen as the $\delta^{18}\text{O}$ master record, since it is regarded as being most intuitive. Nonetheless, all findings were checked versus the alternatives, 1st PC and σ -stack.

Uncertainty estimate

Assessing the significance of the smoothed stack variability (which is the eventual signal of interest) needs to consider the instationary strength of the inter-core association. This feature includes periods of clear alignment in the cores decadal trends (i.e. 1970-1930

AD, see Figure 2.8) as well as less coherent phases (i.e. 1930-1910 AD). In estimating the potential disturbance of the smoothed stack by noise introduced by the incoherent high frequency components of the cores a specifically adapted bootstrap approach was developed (for details on the bootstrap-technique, see e.g. Efron [1979]; Mudelsee [2010]). Approaching a dedicated uncertainty estimate was based on the following steps (a description of the respective algorithm is given in the appendix D):

1. According to the specified (e.g. decadal) time scale, Gaussian smoothing is applied to the stack. The resulting trend is in this context regarded as the “signal”.
2. The signal is subtracted from all four individual time series, yielding four time series of “residuals”, regarded as the “noise”⁴.
3. Calculating four new “supplementary” time series by a year-by-year recombination of the signal (1.) with noise (2.), residuals are randomly drawn from all four residual-datasets and added to the signal.
4. A new stack is calculated from four supplementary time series and smoothed according to 1.
5. After performing steps 2.-4. a large number of times (e.g. $n=1000$), the 90% percentile environment is used as a uncertainty estimate for the smoothed stack curve from 1.

The uncertainty bands shown in Figure 2.11 (see section 2.4 below) represent the most likely (at a 90% level) alteration of the decadal stack due to the incoherent high frequency noise. The bootstrap error estimation is confined to the period where all cores contribute to the stack.

Note that while the deployment of the simple stack may appear as a somewhat simple tool, it suffices to capture the common variability, as it is already distinctly expressed among the cores above the decadal scale. The decadal trends obtained by Gaussian smoothing (see Figure 2.5 and 2.8) typically represent roughly 50% of the original time series. This value was calculated as R^2 between trend and original time series in formal annual resolution, however only regarded as a qualitative indication. Here, KCI is an exception due to its large natural smoothing resulting in $R^2 \approx 0.9$. For the stack and the 1st PC, the decadal trends typically represent already roughly 70% of the variability of the unfiltered time series at formal annual resolution.

The use of more sophisticated methods, such as adjusting dedicated noise models relies on precisely linked chronologies, dated on an annual time scale. Andersen *et al.* [2006] compared an optimized noise model with the simple, σ -stack and the 1st PC of accumulation time series of five Greenland ice cores and found largely similar results (although

⁴to check to which extent regarding the residuals as noise was justified, their respective lag-1 autocorrelation was inspected (for pure white noise, this value should be zero [von Storch and Zwiers, 2002]). The lag-1 autocorrelation of the residuals was found basically near zero for the decadal smoothing and longer trends, except for KCI (as expected from its pronounced isotope smoothing introducing high serial correlation).

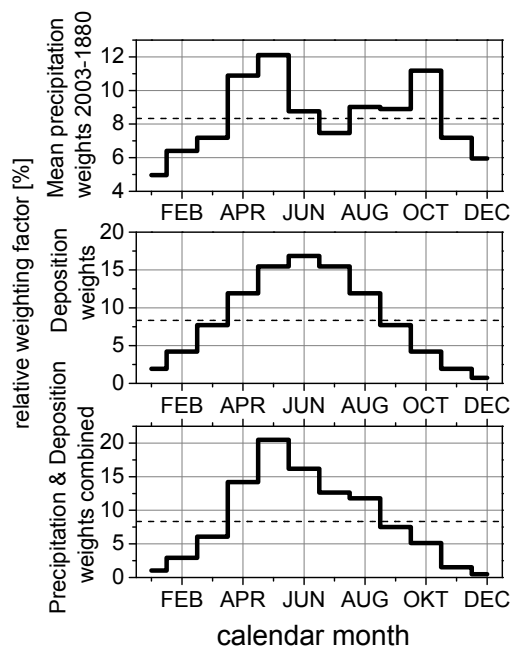


Figure 2.9: Weighting functions for precipitation (top), deposition (middle), combined (bottom) and for reference: The equal monthly weight of 1/12 assigned by a “conventional” annual average (dashed line). Note that precipitation weighting is actually performed on a monthly basis for each year, shown are mean weights (2003-1880). The combined weighting (bottom graph) represents the standardized sum of the upper two weightings.

the noise model yielded the best signal-to-noise ratio). In this context, it seems justified to further deploy the stack together with the bootstrap uncertainty estimate as a master record representing the common $\delta^{18}\text{O}$ variability. Based on this common signal the question remains as to which extent the inter-core agreement is associated with an external atmospheric influence.

2.4 Assessment of atmospheric signal within common ice core signal

As outlined in section 2.2, the Colle Gnifetti ice cores reflect only a very small part of the annual snow precipitation including a distinct bias towards the summer months. Accordingly, a detailed comparison to the common $\delta^{18}\text{O}$ record has to rely on subsampling an instrumental temperature time series representative to the high altitude of the site with respect to the seasonal net snow deposition. However, no long-term temperature recordings and particularly, no reliable information on the past seasonal snow deposition exist for CG. Therefore, a supplementary approach was deployed within the present study, comprising two main steps:

(i) The site relevant temperature time series was based on the (monthly resolved) high alpine subset of the instrumental HISTALP network [Auer *et al.*, 2007]. Additional modification for the high altitude was applied by means of a monthly local lapse rate obtained from the high-resolution temperature data sets for the Monte Rosa region provided by Hiebl *et al.* [2009]. In the following, this data set will be referred to as T_{inst} .

(ii) Sub-sampling T_{inst} was based on the assumption that the preservation of fresh snow deposits can be related to the probability product of local precipitation and insolation-driven snow consolidation, respectively. To obtain the ice core representative temperature series (denoted as T_{mod}), T_{inst} was serially weighted by monthly values of an inferred local precipitation rate p_i as well as by an estimate of the mean seasonality in the (insolation controlled) likelihood for fresh snow preservation d_i ,

$$T_{\text{mod}} = \sum_i \frac{d_i p_i}{\sum_i d_i p_i} T_{\text{inst},i}, \quad (2.2)$$

where $i = 1, \dots, 12$ denotes the respective month of the year. The weighting in equation (2.2) is performed for each year resulting in an annually resolved time series. Time dependent precipitation weights p_i were obtained from the gridded precipitation time series by Efthymiadis *et al.* [2006] for the nearest grid-point in SW-direction. In this context, the assumption was made that the total monthly precipitation amount goes along with the frequency of precipitation events, and thus with the probability for a potential snow input to the glacier archive. Lacking adequate data as a matter of principle, the mean depositional bias was parametrized: The respective weighting factors d_i were estimated by assuming a Gaussian-shaped distribution modelling solar insolation, hence centred at June. The width of the Gaussian function was adjusted to eventually obtain the observed overall $\delta^{18}\text{O}$ ice core mean from the seasonal cycle of $\delta^{18}\text{O}$ in the precipitation. Note that the factors d_i were assumed stationary in time. An illustration on the mean weights is given in Figure 2.9. As the weighting procedure results in the envisaged overrepresentation of the summer month (Figure 2.9, bottom graph), the obtained time series reflects on average a growing-season temperature. A comparison with the simple annual average of T_{inst} showed that while centennial trends are less affected, the modifications according to (2.2) have the potential to alter the decadal trends of T_{inst} (consider the decadal difference around 1900 AD of the trends shown in Figure 2.10) and thus must not be disregarded a-priori for a detailed comparison with ice core isotope records.

Intercomparison of master records

The ice core relevant modified temperature T_{mod} is presented in Figure 2.11 together with its decadal trend and in comparison to the ice core $\delta^{18}\text{O}$ master record. Throughout the period of 1880 - 2003 AD, already a substantial agreement between the two master records is present, interrupted by three approximately decade-long events of anti-correlation (around 1970, 1925 and 1890 AD, named “A”, “B” and “C” respectively). All three instances are coherently observed in the decadal trends of the individual ice cores (reconsider Figure 2.8). Additionally, A, B, C were investigated for significance using the SiZer-algorithm developed by Chaudhuri and Marron [1999] in order to eliminate the possibility of being smoothing artefacts. Interestingly, both vari-

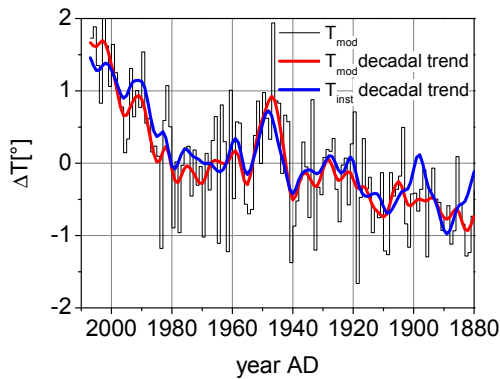


Figure 2.10: Comparison of decadal trends in instrumental temperature data. Shown are annual values of the ice core representative T_{mod} (black) together with its decadal trend (red), both as deviations from the mean of 2003-1880 AD. Decadal trend in blue were calculated from simple annual averages (cf. dashed lines in Figure 2.9) of the instrumental temperature modified for the high altitude of the site only.

ants of mismatch occur: Isotope trend above instrumental data (A) and vice versa (B, C). Potential deficits associated with the crude prediction of precipitation and seasonal net snow accumulation in synthesizing T_{mod} may contribute to the decadal mismatch. The present approach suffers from being uniformly deployed for drilling positions differing in insolation aspect and wind action as well as being stationary and thus independent of inter-annual or long-term changes. However, with respect to the pronounced mismatch seen in Figure 2.11, these deficits do not suffice as an explanation, since the modifications yield only infrequent and minor alterations, as seen in Figure 2.10. Accordingly, the following discussion of the mismatch periods is focused on additional explanations from the glaciological view point. The aim is to illustrate challenges in basically relating the decadal $\delta^{18}\text{O}$ signals to atmospheric temperature variability. To do so, the main argument for ΔT vs. $\Delta\delta^{18}\text{O}$ decadal anti-correlation relies on the depositional regime being not independent from meteorological conditions:

- A:** In case of cold summer periods accompanied by weak solar insolation, the annual net snow accumulation would be exceptionally low. Apart from an enhanced possibility of missing entire annual layers eroded by wind, the fraction of nevertheless actually deposited precipitation would be governed by the occurrence of warm anomalies. Hence, the respective layers would correspond to a few warmest periods only which may not necessarily be representative for the summer half year conditions.
- B:** In contrast, relatively warm conditions with high solar insolation (or less wind action, i.e. the opponent of insolation in snow preservation) may increase the sampling period or even lead to a substantial deposition of winter snow. In this context, it is important to note that a single melt layer may protect a substantial amount of snow underneath, comparatively large with respect to the small mean accumulation rates. Consequently, a large negative $\delta^{18}\text{O}$ anomaly would be observed, obviously lacking a respective counterpart in a time series of summer temperature only.

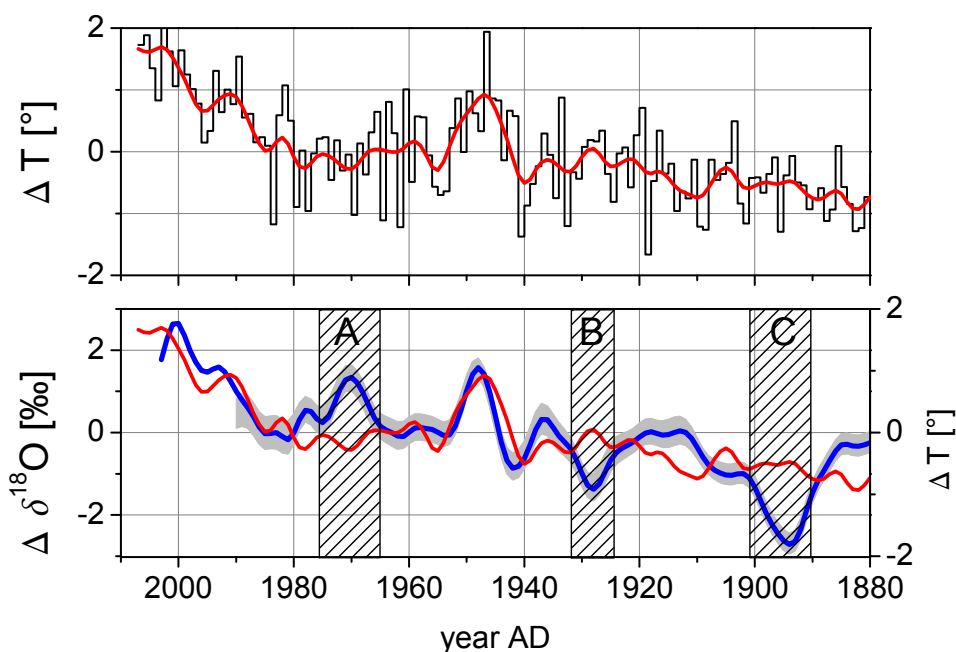


Figure 2.11: Intercomparison of decadal trends of the modified instrumental temperature (top graph, decadal trends in red) and the ice core $\delta^{18}\text{O}$ common record (bottom graph). Data are shown as deviations from the mean value of the entire period (2003-1880 AD). Additionally in the bottom graph: Bootstrap uncertainty estimation for the decadal trends in the $\delta^{18}\text{O}$ common record shown as grey bands; Decadal trend in modified instrumental temperature (red line) from the top graph for better visual comparison (separate temperature axis on the right). The distinct phases of decadal anti-correlation marked with A,B,C are discussed in the text.

C: Likewise as for (B), the late 18th century negative $\delta^{18}\text{O}$ excursion additionally stands out in amplitude, which would clearly require persistent archiving of winter time temperature over a substantial time period. The amplitude of this dip (C) is more pronounced for the ice cores drilled at a saddle location (KCI, KCS) compared to the ice cores positioned on the slope (KCH, CC). As the investigated slope positions are generally more shaded, saddle drilling sites are expected to be more affected by insolation. However, as the respective time period around 1900 AD already corresponds to substantial relative depth in KCS and KCI (reconsider Table 2.1), the actual source region is expected to lie considerably upstream of the drilling site. In this context, knowledge of an approximate relation between core depth and upstream location would be desirable.

In short, a number of qualitative arguments may explain the observed mismatch periods on the decadal scale. Regarding longer term (e.g. centennial) trends, however, the

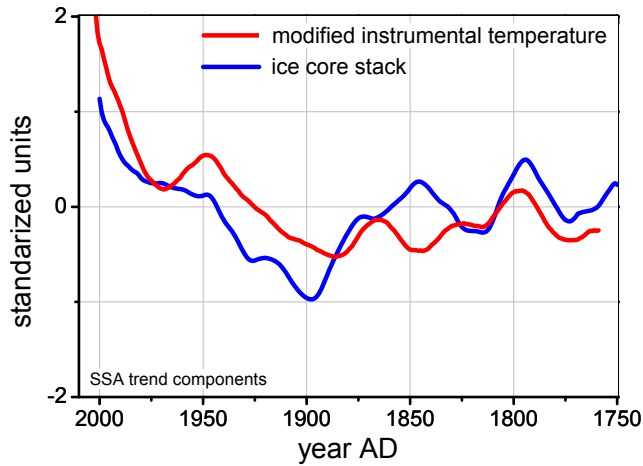


Figure 2.12: Centennial trends reconstructed by Singular Spectrum Analysis (SSA) with window length of about 1/5 of the total time series length. An “outlier corrected” version of the stack master record was used, with reduced influence of the prominent 1890 AD negative excursion (see text). Shown are standardized units with respect to the entire time period.

effects of A, B, C are not expected to be of systematic influence on this time scale. Consequently, this would give rise to an even more distinct covariation between $\delta^{18}\text{O}$ and T_{mod} trends. In order to compare centennial trends of $\delta^{18}\text{O}$ and T_{mod} , it is reasonable to tentatively increase the time period under consideration up to the full instrumental period (back to 1760 AD). As the pronounced decadal dip of C (now roughly in the center of the considered time interval) was also found to substantially influence the centennial trends, an alternative “outlier corrected” version of our stack ignoring all contributions of the constituent cores $\delta^{18}\text{O}$ values below a threshold of -16.5‰ . This threshold is set more or less at the 95% quantile of the distribution of the $\delta^{18}\text{O}$ values, except for the high accumulation KCS where extremely low $\delta^{18}\text{O}$ values are more frequent. Thereby, almost solely the very negative values around 1890 AD in the two saddle cores KCS and KCI are cut. This procedure seems somewhat justified when keeping in mind that C is likely not directly linked to summer temperature. In order to extract the very long-term characteristics of both time series, Singular Spectrum Analysis (SSA) was employed with window length of about 1/5 of the total time series length. A Monte-Carlo significance test against adapted red noise (by Allen and Smith [1996] and Elsässer *et al.* [2011]) shows temperature trends to be significant at a 90% level, isotope trends at 80%. The resulting trends are shown in Figure 2.12.

On the centennial time scale, the recent increase ($\approx 1890\text{ AD} - \text{present}$) becomes the dominant feature throughout the last 100 years BP consistently in both master records, only disturbed by the effect of the decadal anti-correlation (A). Note that A somewhat marks a transition between two regimes within this time period: The strength of the T trend increases for the most recent period from 1980 AD to present. This feature is also exhibited by the isotope trend. While noting that another mismatch between $\delta^{18}\text{O}$ and T_{mod} trends occurs around 1850 AD, a detailed discussion of the time period prior to

1880 AD is beyond the scope of the present study. In principle, an adequate discussion would involve addressing the following main points, including the instrumental data background:

- The lack of a strong multi-decadal trend in the T_{mod} record from 1890 to 1760 AD. Within this time interval T_{mod} is characterized by multi-decadal oscillations around a stationary mean. Since the decadal variability is not invariably shared between $\delta^{18}\text{O}$ and T, this leaves no pronounced signal to be compared to the $\delta^{18}\text{O}$ trends within this time period.
- The lack of substantial long-term T trend before 1890 AD goes back to the corrections applied to the instrumental data to account for systematic warm biases during the “early instrumental period” (EI) period, where instrumental data may be associated with systematic uncertainties [Böhm *et al.*, 2010].
- And not least the increase in formal dating uncertainty, up to between 5 years (KCS) and around 12 years (KCI), 18 years (CC) and unknown for KCH.

2.5 Implications, needs and perspective

As a central result of the present study, a common signal could be identified among the $\delta^{18}\text{O}$ time series from the CG ice cores, however confined to changes longer than the decadal time scale. For shorter periods, depositional noise influence is dominant, which does not come as a surprise with respect to the high spatio-temporal variability in net accumulation at CG. Regarding net accumulation variability on the decadal scale, the comparison with the modified instrumental data set T_{mod} indicated that systematic depositional effects bound to local meteorological conditions may have to be taken into account. A precise assessment of the decadal $\Delta\delta$ vs. ΔT covariation and the anti-correlation-phases would need to consider a variety of meteorological parameters, such as insolation and wind action, hence a rather complicated modelling with uncertain entry data. At the present stage one has to consider the centennial time scale for a persistent $\Delta\delta$ vs. ΔT covariation, however additionally requiring a pronounced atmospheric signal. As it was demonstrated, these requirements are met during the last century at CG, and tentatively, a somewhat weaker correspondence in centennial trends was also found for the entire instrumental period, although an equally distinct ΔT -trend is lacking prior to 1890 AD. However, the comparatively weak long-term (e.g. centennial) trends may be biased by the systematic inflow of ice from source regions with different net accumulation, and thus different mean $\delta^{18}\text{O}$ level (the so-called “upstream-effect”). For the flow line of KCI, upstream-effects have not been examined so far. In an exemplary study for the flow line of KCH, CC and KCS, Keck [2001] investigated the upstream-effect on the $\delta^{18}\text{O}$ time series of KCS and found that its influence on long-term trends may not be disregarded for at least for the last 100 years. Any quantitative

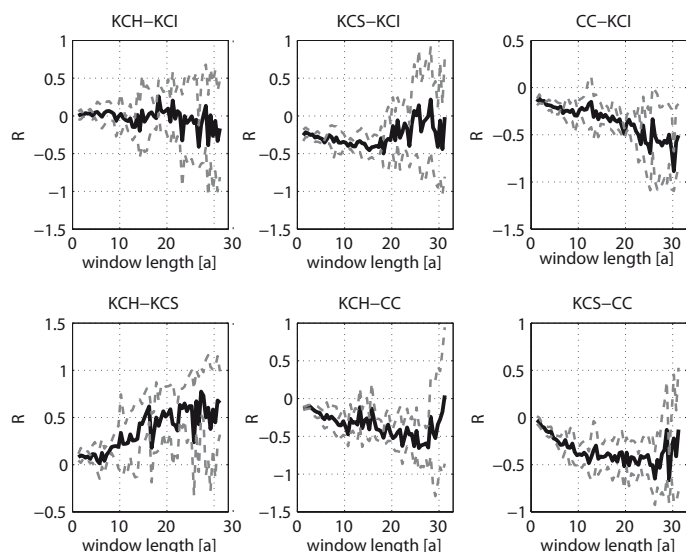


Figure 2.13: Binned correlation coefficient R of each two of the CG $\delta^{18}\text{O}$ time series (1880-1760 AD), plotted as a function of binning window length (black curve). The grey dashed curves indicate the 90 % confidence intervals obtained from multiple runs with varying starting points of the binning.

interpretation of $\delta^{18}\text{O}$ trends thus requires an investigation of upstream-effects. Such an investigation must rely on knowledge of the flow patterns along the flow line and take into account the upstream-variability of mean net accumulation. The use of a flow model is essential for this purpose. Moreover, in the context of a quantitative interpretation of long-term $\delta^{18}\text{O}$ signals as past temperature variability, the need for a calibration of this ice core “isotope thermometer” arises, as outlined in section 2.2. An adequate in-depth discussion of this topic is beyond the scope of the present study, however, a brief report on preliminary findings is included here.

It is important to note that the precise value for the sensitivity factor ($\Delta\delta^{18}\text{O}/\Delta T$) was observed to depend on the method of calculation. The following approach was deployed here: The two master records for $\delta^{18}\text{O}$ and T_{mod} were smoothed according to (i) the decadal time scale (Gaussian smoothing, Figure 2.11) and (ii) the centennial time scale (SSA, Figure 2.12). The recent period (2003-1900 AD) with persistent covariation was used as the “calibration period”. As both ($\delta^{18}\text{O}$ and T_{mod}) records carry uncertainty, orthogonal regression [Jackson and Dunlevy, 1988] was used to calculate $\Delta\delta^{18}\text{O}/\Delta T$. Values between $1.7\text{‰}/\text{°C}$ (decadal smoothing) and $1\text{‰}/\text{°C}$ (centennial scale) were obtained. Both values are substantially larger than the conventional value of $\approx 0.6 - 0.7\text{‰}/\text{°C}$ known from polar ice core studies (e.g. Johnsen *et al.* [1989]) but agree with previous findings by Keck [2001]. Although enhanced values for the sensitivity have also been observed at instrumental Alpine stations when calculated from long-term trends instead of seasonal values [Rozanski *et al.*, 1992], the large values of $\Delta\delta^{18}\text{O}/\Delta T$ obtained at CG are not understood yet. Nevertheless, the upstream-effect may be excluded as a driver for the enhanced sensitivity since it would bias this quantity too low (pers. communication D. Wagenbach).

Regarding ice core studies at other mountain drilling sites, the present investigation illustrates how the drilling of multiple ice cores plays a crucial role in obtaining infor-

mation on past atmospheric variability, especially in case of complex small scale alpine glaciers such as Colle Gnifetti. The comparison of time series from multiple ice cores is a basic requirement in order to separate depositional noise from (atmospheric) signal. A sound common signal investigation calls for accurate chronologies, which are however challenged at comparatively small relative depths and recent ages. In this context, it would be desirable to cross-link the individual chronologies in order to reduce relative dating offsets.

For the example of CG, although very long-term (e.g. centennial) trends remain more or less coherent, a further investigation regarding a persistence of the common decadal $\delta^{18}\text{O}$ signal beyond 1880 AD is hampered by increasing, and largely unknown dating uncertainties when going back in time. This issue becomes especially apparent when applying the “binned correlation” investigation to the ice core $\delta^{18}\text{O}$ time series for the time period 1880-1760 AD. As shown in Figure 2.13, the correlation is much less pronounced in this time interval, especially for small binning windows. Moreover, on the multi-decadal scale, even distinct anti-correlation occurs, which is a result of substantial relative dating offsets combined with a decadal $\delta^{18}\text{O}$ variability.

Evidently, an adequate common signal investigation is substantially flawed by relative dating offsets and would greatly benefit from a single, coherent dating scenario obtained from cross-linking the individual chronologies. From Polar ice core studies, it is well known that such an age-depth link between different drilling sites may be provided by unique absolute time markers, mostly volcanic eruptions such as Laki, 1783 AD [Clausen and Hammer, 1988; Langway *et al.*, 1988; Vinther *et al.*, 2006]. For the CG ice cores, however, the attribution of a volcanic signal in the cores' impurity profile to a certain eruption suffers from large ambiguities due to the combination of the considerable dating uncertainty with a large abundance of equally outstanding impurity events (e.g. see the attempt made by Keck [2001]). Nowadays, glaciological research supplies additional tools for spatial extrapolation of age information—the following chapter presents a novel approach combining ice cores, GPR and flow modelling.

3 Age-depth distribution mapping of an Alpine drilling site

3.1 Introductory remarks

As demonstrated in the previous chapter, the common signal analysis among time series from an alpine glacier calls for cross-linking the individual ice core dating and to assess the coherence of their age-depth relations. Looking once again at polar studies, a standard tool for ice core linking is provided by ground-penetrating radar (GPR), nowadays routinely applied to investigate the geometry and internal structure of ice sheets. Apart from near bedrock regions, the paradigm holds that internal reflection horizons (IRH) are made up by isochrones [Robin *et al.*, 1969; Gudmandsen, 1975; Millar, 1981; Bogorodsky *et al.*, 1985]. IRHs have been successfully used for large-scale mapping of age-depth information and the synchronisation of ice core chronologies [Jacobel and Welch, 2005; Fahnestock *et al.*, 2001]. At Alpine glaciers, GPR is typically applied to determine ice thickness and to map bedrock topography for flow modeling [Binder *et al.*, 2009; Vincent *et al.*, 1997]. Only few studies combined GPR with ice core data for investigating the internal structure of an alpine glacier so far [Pälli *et al.*, 2002]. At Colle Gnifetti, earlier GPR studies were also mainly performed in combination with attempts in flow modelling [Haeberli *et al.*, 1988; Wagner, 1996; Lüthi, 2000; Lüthi and Funk, 2000]. Böhlert [2005] used GPR to map ice thickness and accumulation rates in search of a drilling site featuring exceptional low accumulation (the later KCI core).

The most important basis for the present work is the study by Eisen *et al.* [2003a], who combined ice core data with GPR-profiles at CG and successfully intercompared age-depth relations and impurity signals among the three deep ice cores on one flow line (KCH, CC and KCS). For this purpose, isochrone IRHs were traced along the flow line intersecting the three ice core drilling sites. Clear IRHs were found within the upper 30-50 m only, roughly corresponding to the firn zone and hence, GPR-based isochrone mapping on this flow line was restricted to shallow depths. With the latest ice core, KCI, drilled in 2005 on a separate flow line, an extended area of ice core drilling sites at CG is defined (see Figure 2.1 in chapter 2). The present chapter essentially provides an extension of the approach by Eisen *et al.* [2003a] to the flow line of KCI and strongly increasing the spatial coverage of GPR profiles.

In recent polar studies, a combination of GPR measurements with flow models was employed to investigate englacial isochrone layers with respect to spatial accumulation patterns, as well as regarding the influence of flow effects [Leysinger-Vieli *et al.*, 2004, 2007, 2011]. In a somewhat similar approach, an additional goal of the present study is to overcome the spatial limitation of the GPR-based extrapolation of age information at CG- both in vertical and lateral direction. To this end, ice core and GPR data are supplemented by a simple flow model. In contrast to earlier finite-difference flow modelling attempts at Colle Gnifetti [Wagner, 1996; Lüthi, 2000] this approach is not directed at computing age-depth relations independent of ice cores. Here, ice core and GPR data are used as constraints for the flow model to reproduce the relative age-information inherent to GPR isochrones. Using the modeled isochrone layers at greater depth and on additional flow lines, this approach is aimed at: (i) Assessing the inter-core dating coherence at older ages where no GPR signals are available. (ii) Interpolating the ice core based age information as to approximate the three-dimensional age-distribution, and (iii) constraining the borehole catchment areas for studying upstream effects. In this context, the still open question previously discussed by Eisen *et al.* [2003a] arises as to what extent physical ice properties are related to distinct IRHs and especially to the lack thereof below certain depths at CG. In an attempt to contribute to this investigation, data from the new ice core KCI are compared with local GPR-signals. This includes a pilot study in borehole radar at CG deployed at the still open KCI borehole.

3.2 GPR measurements and data processing

Note that a basic discussion regarding the interaction of electromagnetic radiation with ice is given in chapter 4, section 4.2.3.

Principles of GPR measurements

Ground-penetrating radar can be operated on spaceborne, airborne or ground platforms, i.e. in case of a glacier, on sleds. A basic GPR setup comprises a transmitter (Tx) emitting an electromagnetic signal which travels to a receiver (Rx) along different ray paths, where it is recorded as a function of its travel-time (Figure 3.1). Transmitter and receiver can use a single antenna (monostatic) or two separate (bistatic) antennae. The emitted signal either consists of a short pulse with a certain main frequency or be of changing frequency such as in frequency-modulated continuous-wave radar (FMCW). As there exist a large variety of different GPR-setups, the following overview is only concerned with basic considerations relevant for this work.

Reflections of the GPR signal occur at significant changes in dielectric material properties. If these changes occur within a distance small compared to the wavelength of

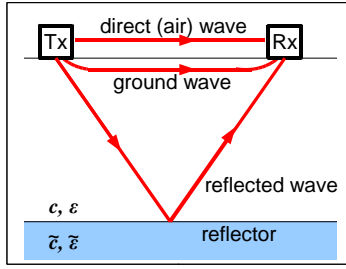


Figure 3.1: Principle of GPR measurement: the transmitter (Tx) emits an electromagnetic signal travelling to the receiver (Rx) via different ray paths: the air wave, ground wave and reflected waves. Refracted ray paths are omitted. Figure from Konrad [2011].

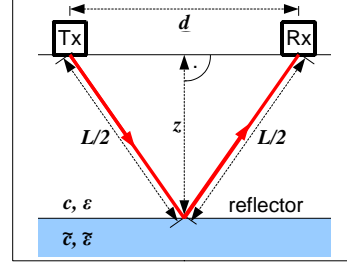


Figure 3.2: Geometric consideration to derive reflector depth; Total travel distance of the reflected signal: $L = c t_{\text{TWT}}$ (“TWT”: two way travel time). Figure from Konrad [2011].

the incoming signal, they can be resolved as a distinct signal in the record. As outlined in the introduction, reflections in a glacier go back to variations in density, acidity and crystal orientation fabrics, as well as to the ice-bedrock interface (For more details refer to section 4.2.3 in chapter 4).

Considering the simple geometry of Figure 3.2, with a surface-parallel, plane interface between two media of different dielectric permittivities, the depth z of the respective reflector z is:

$$z = \frac{1}{2} \sqrt{(c t_{\text{TWT}})^2 - d^2}$$

with a constant propagation speed c above the reflector and an antenna separation d . If $z \gg d$ (which is justified regarding orders of magnitude: $O(z) = 10$ m vs. $O(d) = 10$ cm), d can be neglected and thus:

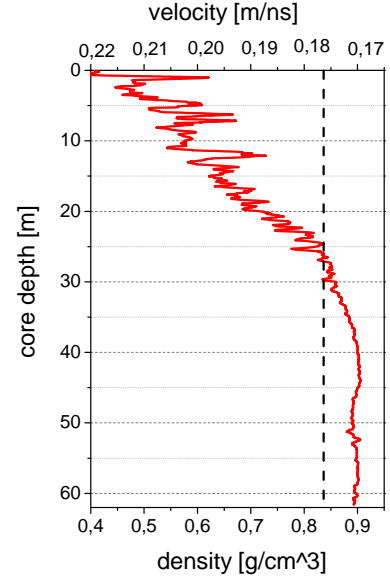
$$z = \frac{1}{2} c t_{\text{TWT}} .$$

If the propagation speed varies vertically above the reflector, one can only obtain an implicit relation for $z(t_{\text{TWT}})$ by integrating

$$t_{\text{TWT}}(z) = 2 \int_0^z \frac{1}{c(\tilde{z})} d\tilde{z} . \quad (3.1)$$

Note that a vertically variable velocity distribution is inherent to the density variations within the firm part of a glacier (Figure 3.3). The dielectric properties of firm regarded as a mixture of air and ice change with depth due to the fraction of ice increasing by densification and occasional melt layers. Parameterizing the volume fraction of ice with density, the propagation speed in firm can be treated theoretically as well as empirically

Figure 3.3: Density profile of the Colle Gnifetti KCI ice core; the high-resolution profile has been slightly smoothed to aid visual perception. Note the firn-ice transition (dashed line) at 0.83 g/cm^3 or roughly 25–30 m absolute core depth. Below, distinct variations disappear, as density becomes almost constant at $\approx 0.89 \text{ g/cm}^3$. Also shown: Additional axis with velocity values calculated from equation (3.2). Density data from the database of IUP Heidelberg.



(for more details, see section 4.2.3). In this context, the empirical relation by Kovacs *et al.* [1995] is well established and thus widely used in glaciological applications:

$$c(z) = c_0 \left(1 + 0.845 \frac{\text{cm}^3}{\text{g}} \cdot \rho(z) \right)^{-1} \quad (3.2)$$

where c_0 is the speed of light in vacuum and ρ the firn-density.

Data acquisition and processing

Apart from our borehole radar pilot study (section 3.7.1), all GPR measurements used in the present work were performed as so-called “common offset” (CO) profiles: Transmitter and receiver are separated at a fixed distance while they are moved together along the surface. This technique maps the spatial extension of an IRH as the point of reflection moves along the reflector (Figure 3.1).

CO profiles were obtained using a monopulse bistatic radar system, RAMAC GPR from Malå Geoscience, Sweden. The shielded 250 MHz antennae are permanently mounted in a skid box at a distance of 36 cm. The sled was pulled along profiles marked by stakes for which GPS coordinates were co-registered (see Figure 3.4). The transmitter was triggered by an odometer behind the sled at nominal intervals of 0.5 m. Trace length was set to $1.5 \mu\text{s}$ with 2048 samples per trace. For each trace 8 samples were stacked as to increase the signal-to-noise ratio. Post-recording processing was performed using the software FOCUS (version 5.4) from Paradigm Geophysical and following a standard processing routine for seismic and GPR measurements in CO setup [Yilmaz, 2001; Navarro and Eisen, 2009], including:



Figure 3.4: GPR common offset measurements at Colle Gnifetti. Transmitter and receiver are mounted on a sled pulled by hand. The transmitter is triggered by a distance wheel behind the sled. Picture from O.Eisen.

Static correction and filtering: Traces are aligned to have the first break of the air wave at $t_{\text{TWT}} = 0$. A trapezoidal bandpass filter around 250 MHz is used for noise suppression.

Gain: In order to account for spherical divergence, amplitudes A are corrected as: $A_{\text{corr}}(t_{\text{TWT}}) \propto A(t_{\text{TWT}})t_{\text{TWT}}^n$. Best results were obtained with a value of $n = 1.2$, reamplifying reflections from deep layers. The detectability of internal reflections, and especially the bedrock reflection is further improved by Automatic Gain Control: Each trace is divided into several time windows. In each window amplitudes are normalized by the respective mean value. This prevents strong reflections to completely dominate the radargram.

Migration: All received signals are allocated to the horizontal position of Rx, although the signal does not necessarily stem from a reflector directly below the antenna. For a punctual diffractor at horizontal location x the distance $l(x)$ between antenna and reflector is $l(x) = \sqrt{z^2 + x^2}$, and thus: $t_{\text{TWT}}(x) = \frac{2}{c} \sqrt{z^2 + x^2}$. Consequently, punctual diffractors appear as hyperbolae in the radargram (Figure 3.5), with their aperture angles determined by the propagation velocity. The so-called “migration” considers a vertical velocity profile in order to allocate the recorded hyperbola to the corresponding position of the punctual diffractor.

Here, two-dimensional migration was used, assuming the diffractors to be located in the vertical plane along the profile. Using the vertical velocity profile based on the KCI density data (Figure 3.3) and equation (3.2), the diffraction hyperbolae successfully vanished in all profiles. An exemplary comparison between raw and processed data is shown in Figure B.1 in appendix B.1.

The use of a two-dimensional migration cannot fully account for three-dimensional reflection patterns arising for complex IRH or bedrock topography. As illustrated in Figure 3.6, if the nearest reflections are not necessarily located directly below Rx, this lead to an underestimation of reflector depth. In this context, the lack of a three-dimensional

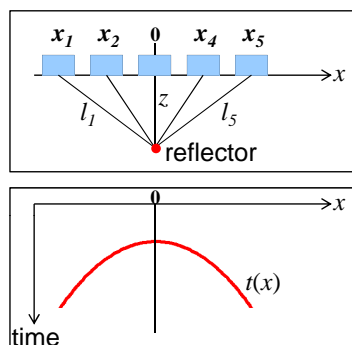


Figure 3.5: Reflection-hyperbolae in a CO-radargram. Top graph: Distance from reflector to the antenna moving along the surface. Bottom graph: resulting hyperbola in the radargram. Figure from Konrad [2011].

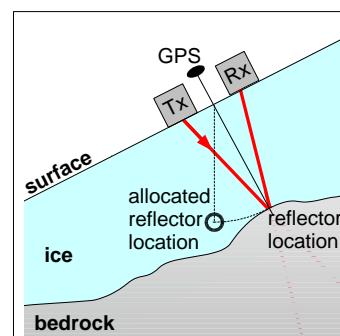


Figure 3.6: Shortcoming in GPR-reflector position allocation. Assuming the reflector to be directly beneath Rx leads to a systematic underestimation of an inclined bedrock. Figure from Konrad [2011].

migration introduces a systematic uncertainty, especially concerning the bedrock reflection. Comparing 3D-migrated alpine GPR profiles to the unmigrated and 2D-migrated data sets, Moran *et al.* [2000] reported an error of 36 % for unmigrated and 15 % for 2D-migrated data relative to the 3D-migrated profile. However, three-dimensional migration would require extensive additional measurements and is beyond the scope of this work.

General characteristics of a radargram from Colle Gnifetti

In order to introduce the general characteristics of a CG radargram, a representative example linking the drilling sites of KCI with KCS is shown in Figure 3.7. Three different regimes can be broadly identified and have been numbered (1)–(3). These features are present in all GPR CO-profiles from Colle Gnifetti. Corresponding to the upper parts of the glacier, distinct IRHs (blue lines) are detectable in regime (1). Below, there appears a large depth interval with no coherent reflections (regime 2) until a somewhat more spread-out reflection indicates bedrock (red line, 3). As indicated by the respective density profiles of the two ice cores, regime (1) approximately coincides with the firn zone. Note that clear IRHs remain present at KCI down to ≈ 20 m. The disappearance of clear IRHs seems to go along with the firn-ice transition. This result suggests that density anomalies such as melt layers are one of the main reasons for IRHs at CG.

In the preceding study, Eisen *et al.* [2003a] concluded that by comparison with ice core data alone, an unambiguous identification of the cause of an IRH is not possible. Nevertheless, since a warm temperature anomaly or a dust-fall induced albedo change are likely to produce extended melt layers at CG, it seems plausible that density-related IRHs may map the englacial isochrone structure. Note that, as pointed out by Eisen

et al. [2003a], the decrease in annual layer thickness, which is also observed horizontally e.g. due to a decrease in surface accumulation upstream from KCS to KCH, may change the characteristics of the IRHs. As annual layers become too small, individual phases may not indicate an isochronous surface anymore. In this case, only a bulk of phases can be regarded as an approximately isochronous layer of distinct physical properties. For a more detailed discussion on possible origins of IRHs at Colle Gnifetti see section 3.7 below. It is important to note that under steady-state condition (which seems reasonable for CG as outlined in chapter 2), the age-depth distribution relative to the surface mapped by a certain isochrone IRH is time-independent [Paterson, 1981]. This also applies to the ice cores, as their datings may be regarded as time-independent age-distributions in respect to the surface for this location, although the cores have been drilled in different years. Thus, when using an ice core chronology to assign specific dates to a certain IRH, they should be given as “years before present” (a BP), with “present” relating to the actual surface (age = 0). This also means that for two profiles recorded at different dates, the physical origin of two IRHs, corresponding to the same age before present are generally different.

3.3 Inter-core dating coherency evaluation

3.3.1 Lateral age-interpolation by internal reflection horizons

The transmitted radar pulse consists of about five half-cycles. Subsequently, phase shifts, distortions and multiple reflections can occur during propagation. In the processed radargram, a single IRH appears as several phases. With an appropriate scaling, a prominent phase of the reflection is traced by eye. The according points in TWT-trace space are saved to an output file. Tracing IRHs is always performed in the direction leading from higher to lower temporal resolution (i.e. higher to lower annual layer thickness) in the radargram, thus avoiding ambiguities due to splitting phases.

Due to roughness, the reflection from the ice-bedrock interface does not appear as a coherent continuous phase but rather as increased backscatter. It is detected by reducing gain until the much weaker signals above the bedrock reflection disappear, leaving its uppermost reflection as a traceable boundary. This procedure yields the results shown in Figure 3.7, where traced IRHs are shown in blue and the picked bedrock reflection in red.

To convert the TWT coordinate of a specific IRH into absolute depth, the velocity profiles based on density data and equation (3.2) of the respective ice core are used at the drilling sites. In between the drilling sites, the density distribution and ice thickness are unknown and need to be interpolated. Two different interpolation methods were deployed based on absolute and relative depth coordinates, respectively (see appendix B.1.1) giving almost identical values for the TWT-depth conversion. With an accord-

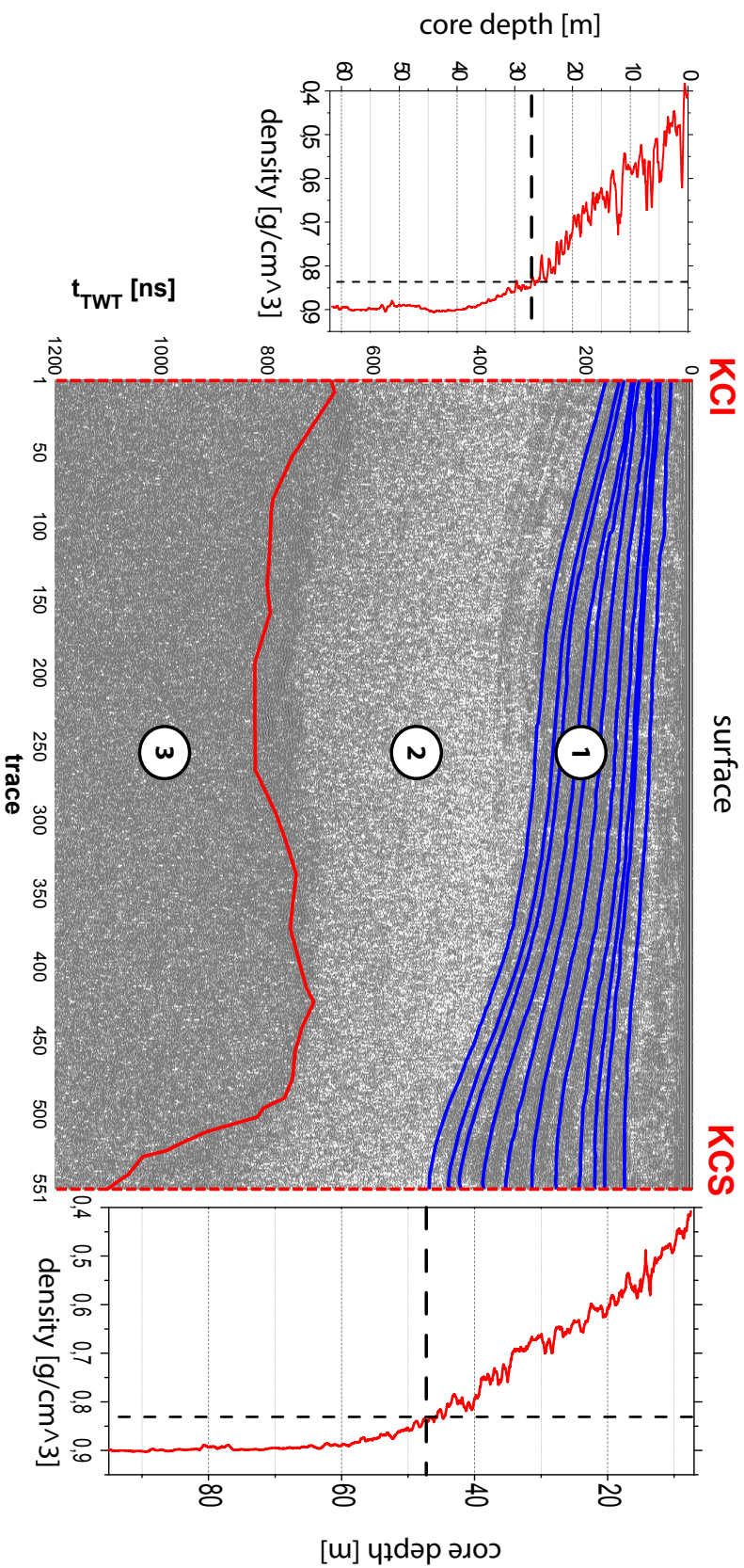


Figure 3.7: Exemplary GPR profile linking the drilling site of KCI with KCS, shown together with the density profiles of the two cores. Dashed lines in the density profiles indicate the firm-ice transition. As in Figure 3.3, density profiles have been slightly smoothed. Note the three different regimes labeled with (1)–(3), discussed in the text. Traced IRHs are shown in blue, the picked bedrock reflection in red. The bedrock reflection shows not as a distinct phase but as increased backscatter. It was detected after reducing gain by picking the most distinct reflection. Additional care in bedrock detection must be taken for profiles parallel to isohypses, as discussed in the text.

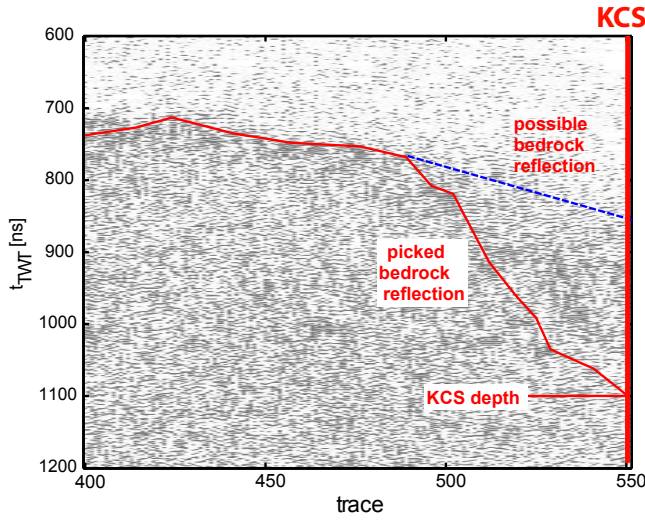


Figure 3.8: Illustration of the ambiguity in bedrock reflection identification. Shown here is the bedrock reflection at KCS on the bottom-right corner of the KCI-KCS GPR profile of Figure 3.7. Bedrock detection solely by reducing gain would result in picking the blue line as bedrock. An alternative is shown in red, which is in better agreement with the KCS core depth of ≈ 100 m and was thus used. Figure modified from Konrad [2011].

ing velocity profile the depth of any internal reflector z^{IRH} at each trace can be calculated from the according TWT $t_{\text{TWT}}^{\text{IRH}}$ by performing the integration in equation (3.1) until $t_{\text{TWT}} = t_{\text{TWT}}^{\text{IRH}}$ and thus $z^{\text{IRH}} = z$. Ice thickness and IRH depth were also converted into water equivalent units according to equation (3.16) (see section 3.4.2 below). In a last step, the depth of each IRH at a drilling site is then converted into age before present according to the age-depth relation of the respective ice core. As outlined above, under the isochrone assumption the two ages assigned by two ideal ice core datings should be identical. However, this is generally not the case. For an adequate assessment of the age difference regarding potential dating errors, an uncertainty estimate for the method used here has to be known.

Uncertainty estimate

Following Pälli *et al.* [2002] and Müller *et al.* [2010], two main sources of uncertainties are considered, with a detailed treatment of the uncertainty estimation in appendix B.1.2. (i) Uncertainty in depth of the IRH Δz^{IRH} results from the vertical resolution of the GPR wavelet as well as potential errors in manually tracing phases in the radargram. This leads to an age uncertainty ΔT^{IRH} according to the depth-dependent slope of the ice core age–depth relation:

$$\Delta T^{\text{IRH}} = \left. \frac{\partial T}{\partial z} \right|_{z=z^{\text{IRH}}} \Delta z^{\text{IRH}}$$

(ii) Uncertainties related to errors in obtaining the ice cores age–depth relations. For the depth range featuring IRHs, or roughly the last 100 a BP, Schäfer [1995], Armbruster [2000] and Bohleber [2008] all report a dating uncertainty of $\Delta T^{\text{DAT}} \approx \pm 3a$ for the Colle Gnifetti ice cores (cf. Table 2.1 in section 2.2).

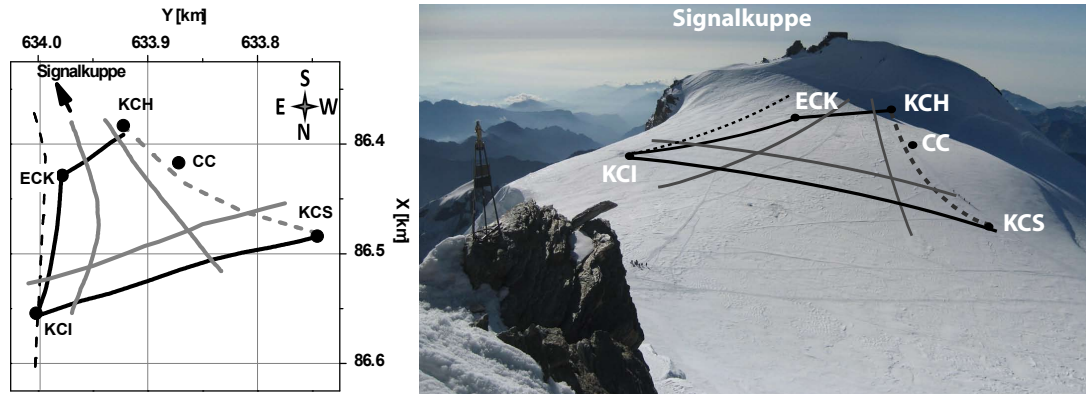


Figure 3.9: Colle Gnifetti GPR profiles linking ice core locations. Left: Profiles with coordinates in Swiss grid. Arrow indicates the summit of Signalkuppe shown in the photograph on the right side. Black lines: Profiles from field campaign in August 2008 linking the KCI borehole to the former KCS and KCH drilling sites. Shown as a black dashed line: Profile along the alleged KCI flow line not used for the inter-core dating comparison. Grey lines: New profiles from field campaign in August 2010 dedicated to the spatial extrapolation of the coherent age information. Grey dashed line: Older profile from Eisen *et al.* [2003a] linking KCS with CC and KCH. Note that “ECK” does not denote an ice core drilling site, but a particular point where the GPR-profile KCI-KCH approximately changes from flow line-parallel to isohypse-parallel. For better illustration of the CG drilling site, the approximate profiles are marked in the photograph shown on the right.

The overall age uncertainty of the IRH age assignment thus amounts to:

$$\Delta T = \sqrt{(\Delta T^{\text{IRH}})^2 + (\Delta T^{\text{DAT}})^2}$$

and typically ranges around ± 4 a. The processing steps travel time-depth conversion, uncertainty estimation and IRH age estimation are performed by means of a MATLAB[®] routine, see appendix (D).

As discussed above the reflection from the inclined bedrock might not stem from the ice-bedrock boundary directly underneath the antenna (cf. Figure 3.6). This entails a potential underestimation and complicates the detection of the bedrock signal in addition to its blurred reflection. Due to the directional radiation characteristic of the transmitter this effect is most influential for profiles measured roughly perpendicular to the bedrock gradient, i.e. parallel to isohypses. If necessary, distinct reflections beneath the first bedrock signal were picked on these profiles (Figure 3.8).

3.3.2 Pairwise inter-core dating comparison

The inter-core dating coherency is evaluated in two steps: First, the technique is validated by reassessing the KCH-KCS comparison. Then, the KCI chronology is compared

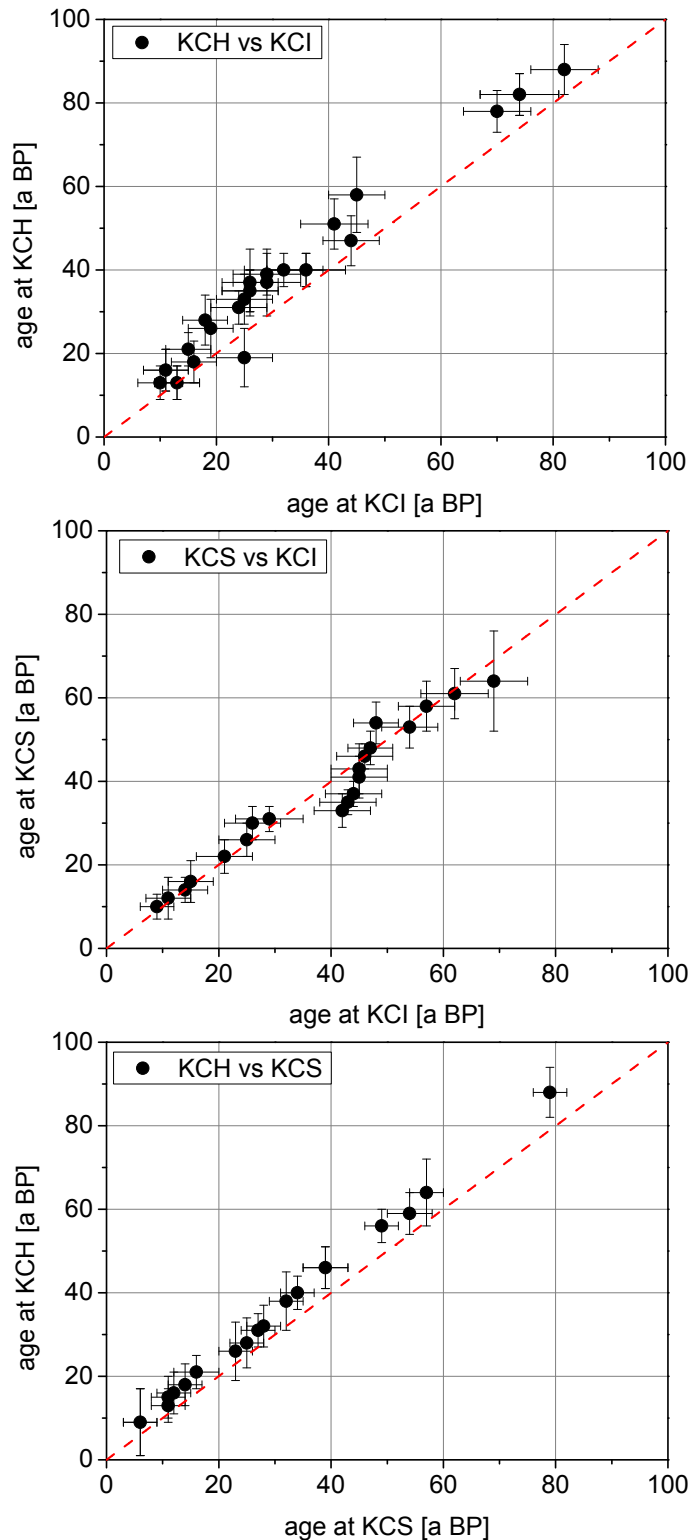


Figure 3.10: Comparison of ages assigned to traced internal reflection horizons by the individual ice core datings. The corresponding ages of each two ice cores are plotted vs each other, including the respective uncertainty estimate. Perfect coherent datings would lie along the bisecting line. Note that a systematic offset towards older ages at KCH seems to be present in comparison with KCI and KCS.

pairwise to KCH and KCS. In a third step, all datings are checked for coherency in a single intercomparison.

KCS-KCH: In order to compare the processing technique deployed here to the previous study by Eisen *et al.* [2003a], it was applied to the raw data of the KCH-KCS profile (dashed grey line in Figure 3.9). At the position of the CC drilling site on the profile, additional output of depth and age according to the CC dating was given for each IRH. Ages assigned to the IRHs at KCS, CC and KCH were all found to agree within their estimated errors. The deepest continuous IRH which could be traced from KCS to KCH in this study was found in 48.3 m depth at KCS and 30.1 m depth at KCH which corresponded to about (79 ± 6) a BP. These findings are consistent with Eisen *et al.* [2003a] and are thus interpreted as a validation of the processing technique used here. It is worth noting that a systematic offset towards older ages was found at KCH, ranging from 2-3 years at the uppermost up to 7-8 years for the deeper IRHs.

KCI-KCH: The deepest traceable continuous IRH was again at 30.0 m depth at KCH corresponding to 16.6 m or about 82 a BP at KCI. In depths corresponding to 22 to 26.5 m at KCH, tracing of IRHs suffered from frequent disturbances and ambiguities in the radargram. Consequently, no inter-core dating agreement was found between 50 and 65 a BP, which is probably a result of the practical difficulties in tracing IRHs. For the remaining IRHs, the assigned ages by the KCI and KCH chronologies were found to agree within their uncertainties, however, KCH ages were again slightly systematically older.

KCI-KCS: Between KCI and KCS, the deepest traceable IRH was found at 43.0 m at KCS corresponding to 15.1 m in KCI and about 69 a BP. The deepest, approximately 80 a BP old, IRH traced along the slope between KCI-KCH and KCS-KCH could not be traced unambiguously in the profile KCI-KCS.

All results of the pairwise dating comparison are given in appendix B.1.3. For a visual overview on the results, the ages of the IRHs coherent between the ice core datings are plotted against each other in Figure 3.10.

3.3.3 Overall inter-core dating coherency

To extend the pairwise dating comparison to a more general consistency evaluation of the ice core chronologies, the GPR-profiles from 2008 and 2000 were linked to form a “closed course” (see Figure 3.11).

By following an IRH corresponding to a certain age it is possible to check if the differences from the pairwise comparison accumulate to a substantial offset in age after a “round trip” in the closed course. Alternatively, if no systematic inconsistencies are present, the age of the IRH returning to the starting point is expected to agree with the age of the IRH with which the round trip was started (within their estimated uncertainties).

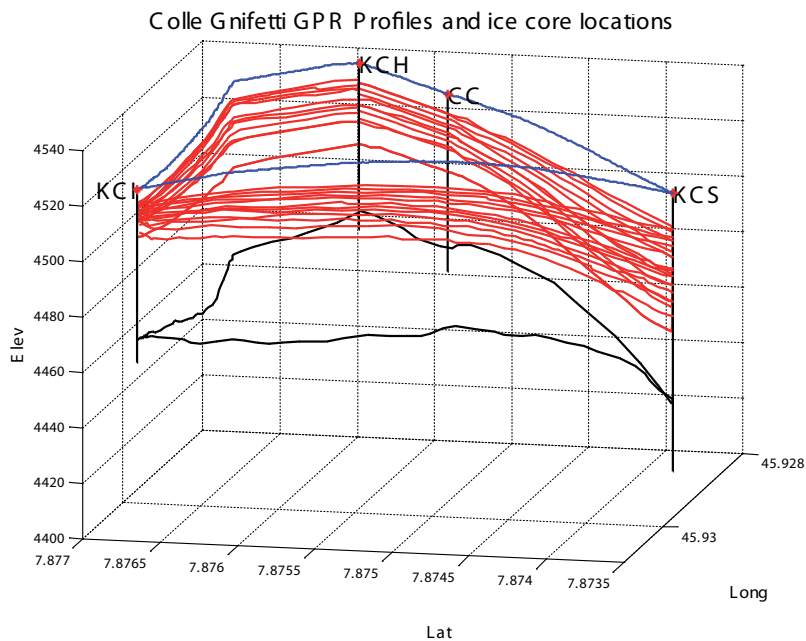


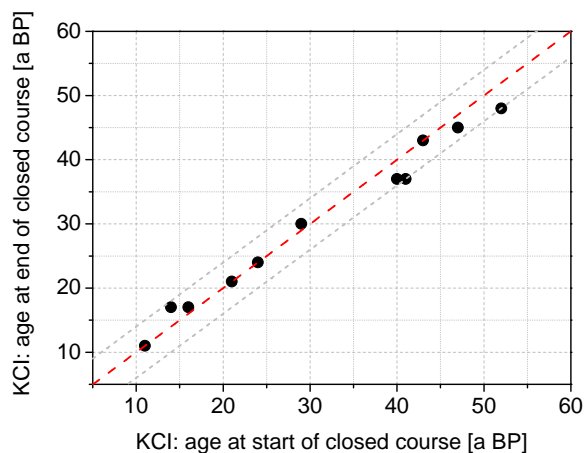
Figure 3.11: Three dimensional map of the traced IRHs between the CG drilling sites. Blue lines: Surface coordinates of the profiles from GPS measurements in WGS84 coordinates. Red lines: IRH featuring consistent ages assigned by the respective ice core datings. Black horizontal lines: Bedrock topography estimated from GPR reflectors. Black vertical lines: Ice core locations.

In detail, this closed course approach consisted of the following steps:

- A drilling site was chosen as a reference point for the closed course, i.e. KCI→KCS →KCH →KCI. Note that the actual tracing of IRHs is always performed in direction of decreasing temporal resolution.
- The most distinct IRHs were chosen and traced along the profiles. At an intersection, the next distinct IRH closest in depth (or TWT, respectively) was chosen which was still within the estimated age uncertainty. Note that between the 2008 and 2000 profiles, the physical origin of an IRH in this round course is most likely different.
- For 10 different ages, distinct IRHs were present in all GPR-profiles within the respective age uncertainty. For these IRHs the starting and ending ages of the course were found consistent with ± 4 a at KCI. The method was also performed with other drilling sites as reference with identical results. The oldest round course that could be completed corresponded to about 50 a BP, see Figure 3.12.

Detailed results of the closed course investigation are shown in the appendix (B.1.4). In a similar strategy by Konrad [2011], IRHs corresponding to a certain age are traced from a starting point along two different directions to a different drilling site as a separate end

Figure 3.12: Results from the closed course dating comparison. The age of the IRH with which the round course was completed is plotted against the age of the IRH with which it was started. Shown here with KCI as a reference point. A perfect match would lie along the (red dashed) bisecting line. For the 10 possible closed course profiles the start and end ages were found consistent with ± 4 a (grey dashed line).



point. There, the ages of the two IRHs coming from two different directions can be compared. The two different strategies yield identical results, and indicate age-depth coherency among the ice cores up to about 50 a BP.

Inter-core dating coherency: Assessment

The minor systematic offset by typically about 4–5 years towards older ages at KCH is present in the comparison with KCI as well as with KCS, and thus not regarded as a property of the new KCI dating, but rather as an effect present at KCH. This anomaly at KCH was also detected independently by Konrad [2011]. Eisen *et al.* [2003a] report a similar systematic effect as their tracing of IRHs corresponding to a certain age at KCS resulted in about 0.8–1.0 m lower depths at KCH than predicted by the KCH age-depth relation. Apart from this minor effect, no pronounced systematic inconsistencies were detected among the CG ice core datings. The KCI dating could be matched up to 82 a BP with KCH and up to 65 a BP with KCS. The pairwise dating comparison between KCI and KCS (Figure 3.10) did not show a systematic offset. Since such an offset would most likely stem from the systematic loss of annual layers by wind erosion across the close-by ice cliff, its absence points towards an intact stratigraphic integrity at KCI. The possibility of a systematic dating error due to missing annual layers could not be excluded so far, as the KCI age-depth relation mostly relied on counting of alleged annual layer signals [Bohleber, 2008].

The overall dating consistency evaluation by the closed course approach comprises a depth limitation (additional to the IRH depth limit) due to the different measurement dates between the GPR-profiles: IRHs in profiles measured in 2000 and 2008 do not have the same physical origin. The detectability of an IRH for a specific age in all profiles is thus somewhat coincidental, and was not given beyond 50 a BP.

The estimated uncertainties in the method range from 3–4 a for the uppermost IRHs up to typically 6–8 a for the lowermost IRHs. With respect to the typical increase in dating uncertainty of the CG ice cores beyond the last 100 a BP [Armbruster, 2000; Bohleber, 2008], an uncertainty of ± 8 a in matching chronologies by this method would still allow for valuable tie points and insights on the consistency of the datings at larger depths.

3.4 Mapping the internal age distribution at the CG drilling area

The results from the closed course comparison indicate coherent age-depth information from the ice cores, at least over the upper depth range of 13 m (KCI) – 39 m (KCS) and the presence of extended isochrone surfaces mapped by GPR within the drilling area of CG. This finding is the basis for a spatial extrapolation of the coherent age information via application of a flow model. The general strategy is to tie the model to boundary conditions derived from ice core data and GPR profiles and to use it for calculating isochrone layers on flow lines. This strategy comprised the following main steps:

- Apply the flow model to a flow line intersecting an ice core drilling site. Use input data (topography, density, accumulation) from ice cores and GPR to predict isochrone layers by the model. Thereby adjust the model to predict isochrone layers in agreement with GPR-IRHs.
- Apply the model to flow lines covered by a GPR-profile attempting a vertical extrapolation of isochrones at greater depths.
- Apply the model to selected flow lines with no additional tie points from ice cores and GPR, thus increasing the spatial density of age information. Based on the age information of all flow lines, isochrone surfaces are to be interpolated.

The actual implementation and evaluation of this strategy was the topic of the diploma thesis by H.Konrad, which was carried out under my supervision. The main results will be discussed here, with more details given in Konrad [2011].

Prior to presenting results from the model application with respect to the above main steps, the following subsection summarizes basic considerations regarding the modelling of alpine glacier flow. Based on fundamental equations of continuum mechanics and the flow law of ice, the stepwise adaption of a simple model to the complex conditions at CG is outlined.

Table 3.1: Quantities in equations (3.3) - (3.5)

ρ	density	\mathbf{g}	gravity acceleration
\mathbf{u}	velocity	T	temperature
τ_{ij}	stress tensor	K	coefficient of heat transfer
$\dot{\epsilon}_{ij}$	strain rate tensor	C	specific heat capacity

3.4.1 Considering ice dynamics for modelling alpine glacier flow

The spatial separation of accumulation and ablation areas of a glacier lead to a net-transport of ice which is achieved via combined flow- and internal deformation processes⁵. In steady-state, the glacier geometry remains constant in time since accumulation and ablation are balanced by the net-transport processes. The local vertical age-distribution at any point, e.g. at the drill-site, can be derived from reciprocal integration of the internal velocity distribution $\mathbf{u}(x,y,z)$ ⁶ along all trajectories leading to the site. Hence, the main goal is to obtain the internal velocity distribution from the glacier-geometry. For this purpose, the main conservation principles of continuum mechanics are generally expressed in the following three fundamental equations (the abbreviations are explained in Table 3.1) regarding the conservation of:

$$\text{mass:} \quad \frac{\partial \rho}{\partial t} + \nabla \cdot (\rho \mathbf{u}) = 0 \quad (3.3)$$

$$\text{momentum:} \quad \rho \underbrace{\frac{d\mathbf{u}}{dt}}_{\approx 0} + \nabla \cdot \underline{\boldsymbol{\tau}} + \rho \mathbf{g} = 0 \quad (3.4)$$

$$\text{internal energy:} \quad \rho C \left(\frac{\partial T}{\partial t} + \mathbf{u} \cdot \nabla T \right) = \text{trace}(\underline{\boldsymbol{\tau}} \dot{\boldsymbol{\epsilon}}) + \nabla \cdot (K \nabla T) \quad (3.5)$$

The acceleration term in equation (3.4) is very small due to the creeping motion of glacier ice and can be neglected. Equation (3.4) constitutes the law of motion of a glacier describing the balance of forces acting on surface ($\nabla \cdot \boldsymbol{\tau}$) and volume ($\rho \mathbf{g}$). Equation (3.5) represents an extended thermal conductivity equation with an additional term describing strain heating ($\text{trace}(\underline{\boldsymbol{\tau}} \dot{\boldsymbol{\epsilon}})$). From a given glacier geometry, equation (3.4) allows to calculate the stress-tensor components τ_{ij} . In order to close the above system of equations (3.3)–(3.5), a constitutive relation $\dot{\epsilon}_{ij} = f(\tau_{ij})$ is needed to link the stress-tensor components τ_{ij} to the actual deformation-rates $\dot{\epsilon}_{ij}$. The respective material-specific flow law of ice is generally expressed as⁷:

$$\dot{\epsilon}_{ij} = A \cdot \tau_{eff}'^{n-1} \cdot \tau_{ij}', \quad (3.6)$$

⁵in the present consideration, sliding motion will be disregarded for the frozen-to-bedrock Colle Gnifetti.

⁶Bold symbols indicate vector quantities. Tensors are marked as bold underlined symbols.

⁷for more details on the subject, refer to a respective textbook, e.g. [Paterson, 1981]

with the effective stress tensor $\tau_{eff}^{\prime 2} = \frac{1}{2} (\tau_{xx}^{\prime 2} + \tau_{yy}^{\prime 2} + \tau_{zz}^{\prime 2}) + \tau_{xy}^{\prime 2} + \tau_{xz}^{\prime 2} + \tau_{yz}^{\prime 2}$, which is invariant regarding choice of coordinate system and based on so-called deviatoric stresses ($\underline{\boldsymbol{\tau}}' = \underline{\boldsymbol{\tau}} - \frac{1}{3} \text{trace}(\underline{\boldsymbol{\tau}}) \cdot \mathbf{1}$), since deformation is not affected by hydrostatic pressure. The ice-specific material parameters A, n have to be determined experimentally, which in most instances is limited to simple laboratory experiments (i.e. in case of uniaxial stress). The flow law exponent, n , is ≈ 3 causing the flow law to be non-linear. The actual velocity components can then be calculated from:

$$\dot{\epsilon}_{ij} = \frac{1}{2} \left[\frac{\partial u_i}{\partial x_j} + \frac{\partial u_j}{\partial x_i} \right] \quad i, j = x, y, z \quad \mathbf{u} = \begin{pmatrix} u \\ v \\ w \end{pmatrix} = \begin{pmatrix} u_x \\ u_y \\ u_z \end{pmatrix}. \quad (3.7)$$

From the velocity distribution \mathbf{u} , the age of a particle moving along a trajectory γ from the surface to a point \mathbf{r} can be derived as:

$$t(\mathbf{r}) = \int_{\gamma} \frac{1}{|\mathbf{u}(\mathbf{r}'(s))|} ds. \quad (3.8)$$

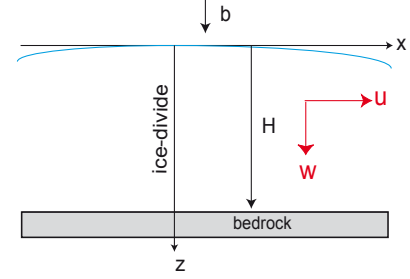
It is important to note that, in a practical application, the velocity field \mathbf{u} , (i.e. the trajectory) is not known, because the system of four partial differential equations (3.3)–(3.6), closely coupled in ρ, τ and T , can not be solved analytically but, at most, numerically. A partial decoupling is possible by neglecting of the firm layers, assuming $\rho = \rho_{ice} = \text{const.}$ (equation (3.3) then reduces to $(\nabla \cdot \mathbf{u}) = 0$) and setting $T = \text{const.}$ (neglecting equation (3.5), although the isothermal approximation $T = \text{const.}$ is reasonable for temperate glaciers only). In thereby avoiding a full thermo-mechanical treatment it must be kept in mind that the flow law itself is also temperature dependent (usually expressed by $A(T)$). Englacial temperature distributions can be obtained experimentally from direct borehole measurements. However, even for this simplified case, solving equations (3.3), (3.4), (3.6) analytically for a real-life glacier breaks down due to the fact that A and n are usually known from simple laboratory experiments only.

The central task of a flow model is thus to approximate the velocity field \mathbf{u} , under certain simplifying assumptions while keeping in mind the fundamental challenges regarding the interpretation of the results with respect to a real-life glacier. Two highly simplified geometries form the basis for the further model-development. Here, only the resulting velocity distributions will be reported for the sake of brevity. A more detailed derivation of the respective equations is given in the appendix (B.1.5).

Nye's model

In its most simple form, Nye's model is essentially build on a 2-D mass balance applied to an ice sheet at its ice divide ($x = 0$). Assuming a most simple geometry (see Figure 3.13) as well as steady state conditions implies for ice thickness H and accumulation rate \dot{b} to be constant in space and time. Additionally, the horizontal velocity \mathbf{u} is regarded

Figure 3.13: The simple geometry of Nye's model. A constant glacier thickness and accumulation rate are assumed.



as independent of depth z . With the boundary conditions of $\rho = \rho_{ice} = \text{constant}$ and $w(0) = \dot{b}$ and $w(H) = 0$ (i.e. ice frozen to bedrock) it follows for horizontal $u(x)$ and vertical $w(x)$ velocities:

$$u(x) = \frac{\dot{b}}{H} x \quad (3.9)$$

$$w(z) = \dot{b} \left(1 - \frac{z}{H}\right) \quad (3.10)$$

Integration of $w = \frac{dz}{dt}$ yields an equation for the age t of the ice in depth z :

$$t(z) = -\frac{H}{\dot{b}} \ln \left(1 - \frac{z}{H}\right) . \quad (3.11)$$

Note that there is a fundamental inconsistency between the assumption of a constant horizontal velocity and the frozen-to-bedrock boundary condition. The purely kinematic approach disregards the constitutive relation (3.6) by assuming constant vertical strain implied in equation (3.10) by $\frac{\partial w}{\partial z} = \text{const}$. Thus, this model is only considered adequate for the comparatively simple conditions within the upper regions (not more than 50%) of an ice sheet, or for rough estimations.

Ice Slab

In a first-order idealisation to the geometry of an alpine glacier, this model treats a parallel sided slab of ice on an inclined plane. Additional assumptions are an infinite extension in y -direction (2D problem), an ice thickness H constant in space and time (steady state) and a constant rate of accumulation (see Figure 3.14). Relying on the flow law of ice with $n = 3$ (equation (3.6)) and with the boundary condition of $u(H) = 0$, $w(H) = 0$ (frozen-to-bedrock ice) and $w(0) = \dot{b}$ it follows that:

$$u(x, z) = \frac{5}{4} \frac{\dot{b} x}{H} \left[1 - \left(\frac{z}{H}\right)^4\right] \quad (3.12)$$

$$w(x, z) = \dot{b} \left(1 - \frac{5}{4} \frac{z}{H} \left[1 - \frac{1}{5} \left(\frac{z}{H}\right)^4\right]\right) . \quad (3.13)$$

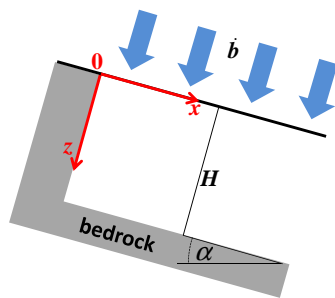


Figure 3.14: Simplified geometry of the ice slab model. Due to the limitation in uphill direction, accumulation is required to maintain a static surface (Figure from Konrad [2011])

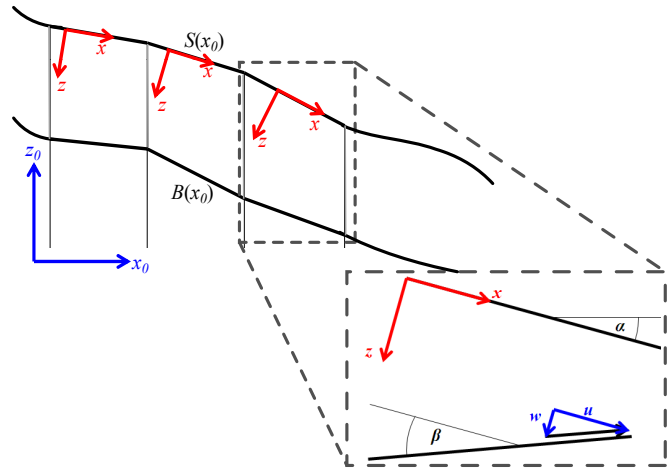
3.4.2 Adaptions of the ice slab for a flow model of an alpine glacier

In the attempt to apply 2D flow models as simple as the ice slab calculations to small scale alpine glaciers like Colle Gnifetti, certain fundamental shortcomings must be kept in mind:

- Evidently, a real alpine glacier typically features a complex geometry, with a non-linear and non-parallel glacier bed and surface.
- There are strong spatial and temporal changes in net accumulation rate. Thus, the parameter \dot{b} must not be treated as a constant.
- Due to the comparatively small thickness (for CG not exceeding much 100 m) the glacier typically consists of a substantial amount of firn, at a spatially varying fraction. The firn densification introduces an additional vertical velocity components and prohibits the use of $\nabla \cdot \mathbf{u} = 0$. Moreover, the flow law of firn is complex to parametrize including large uncertainty [Lüthi, 2000].
- For alpine glaciers, vertical and horizontal scales are usually of comparable order of magnitude, leading to very complex ice flow. Here, the assumption made in the ice slab of an infinite y -component is unjustified. Measured surface flow lines at Colle Gnifetti showed diverging behaviour [Keck, 2001]. A three dimensional flow evaluation is required— at least to some extent.

For these reasons, the prospects of success for a purely theoretical two-dimensional simulation of ice flow and age-depth relationships are very limited— for small scale alpine glaciers in general and especially for CG. Sophisticated three-dimensional flow models have been developed for CG [Wagner, 1996; Lüthi, 2000]. Based on a considerable amount of effort as well as computational knowledge, such models calculate the stress-distribution by finite-element methods solely out of geometric boundary conditions. However, in case of KCS no satisfactory agreement with Armbrusters conventional dating approach was found [Armbruster, 2000]. The following paragraphs briefly describe how the ice slab concept can be refined in a first-order approach to tackling the above shortcomings (a detailed description is found in Konrad [2011]). These considerations form the basis for a still simple, but more adequate flow model for CG.

Figure 3.15: Piecewise linearization of the glacier geometry. In the individual sections with linear, but non-parallel bed and surface, the ice slab model is applied. The according kinematic condition is indicated for an exemplary enlarged section. (Figure modified from Konrad [2011])



Adaption for complex flow line geometry: In a stepwise adaption for a more complex flow line geometry, the first step is to consider a non-parallel glacier bed and surface (Figure 3.15). In this case, the ice thickness H becomes a function of x . In a crude approximation, H is replaced by $H(x)$ in equations (3.12) and (3.13). Glacier surface and bed are linearized piecewise. Then, the modified ice slab model is applied to these linearized subsections. Note that the ice velocity component perpendicular to bedrock must still vanish at the ice-bedrock interface. To fulfill this boundary condition for non-parallel surface and bed, to so-called “kinematic correction” is introduced:

$$w_{corr}(x, z) = w(x, z) - \tan \beta \frac{z}{H(x)} u(x, w) \quad (3.14)$$

where β is the angle between linearized surface S and bedrock B (Figure 3.15). Note that a local coordinate system has to be introduced which may differ from the global coordinate system (here marked with the index 0) in which input and output data of the flow model are defined (shown in Figure 3.15 in red and blue, respectively). However, the velocity components can be transferred from one coordinate system to the other via a respective rotation.

Adaption for spatially variable accumulation rate: If the accumulation rate \dot{b} is not constant but depends on the horizontal coordinate x and for a glacier boundary located somewhere beyond $x = 0$, it follows that the mean ice flux perpendicular to the surface, $q(x)$, can be written as

$$q(x) = \int_0^x \dot{b}(\tilde{x}) d\tilde{x} + q_0 \quad (3.15)$$

Equations (3.12) and (3.13) are still valid if $\dot{b} x$ is replaced by $q(x)$ in equation (3.12) and \dot{b} by $\dot{b}(x)$ in equation (3.13).

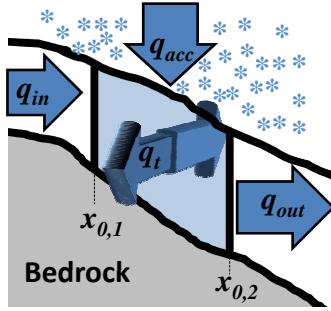


Figure 3.16: Ice flux balance consideration for a longitudinal cross section: without basal melting, as for Colle Gnifetti, there is zero flux at bedrock. Figure from Konrad [2011].

Adaption for density variations: To account for the additional velocity component due to firn densification all depth units are converted to water equivalent (we) units:

$$z_{we} = \int_0^z \frac{\rho(x_0, \tilde{z})}{\rho_w} d\tilde{z}. \quad (3.16)$$

Consequently, velocities are calculated in m w.e./a. Note that this correction does not take into account the different deformation behaviour of firn, which would require the use of a density-dependent flow law.

Adaption for transversal ice flux: The limited glacier extension in transversal direction may not be disregarded in case of small scale alpine glaciers, as it results in stress and velocity gradients and thus in a nonzero velocity component in y -direction. In the present approach, the third dimension is simply parametrized by an additional parameter D for the transversal ice flux divergence. Considering a longitudinal box along a flow line (Figure 3.16), the ice flux balance for a strictly two dimensional model can be written as $q_{out} = q_{acc} + q_{in}$.

In reality, there will be an additional transversal net flux in ($D < 0$) or out ($D > 0$) of the box, and the flux balance can thus be parametrized as (with equation (3.15)):

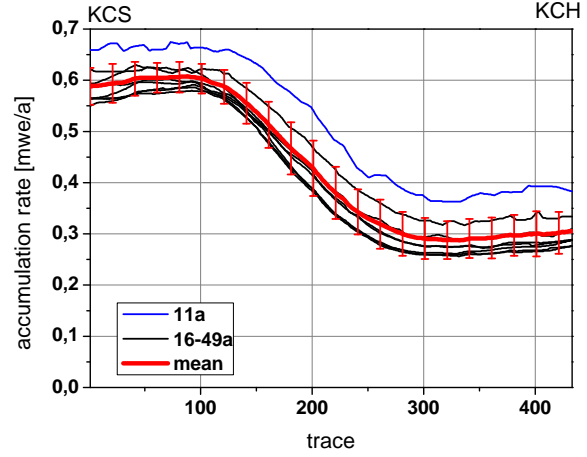
$$q_{out} = (q_{acc} + q_{in}) \cdot (1 - D) = \left(\int_0^x \dot{b}(\tilde{x}) d\tilde{x} + q_0 \right) \cdot (1 - D) \quad (3.17)$$

3.4.3 The ice flow model

Based on the above considerations (section 3.4.1), the model developed here is a refined version of the approach by Vincent *et al.* [1997]. In the following, a brief summary is given regarding required input data, main computational steps as well as output. A thorough discussion is found in Konrad [2011].

Input: The model requires surface and bedrock coordinates (S, B) and accumulation rate \dot{b} as a function of the horizontal coordinate x_0 . Density profiles ρ at two locations $x_{0,D1}$ and $x_{0,D2}$ need to be supplied as a function of depth Z . Finally, the input flux

Figure 3.17: Example of accumulation rate derived from GPR-IRH shown for the profile along the flow line KCH–KCS. The most recent IRH (11 a BP, blue line) shows a systematic offset to higher accumulation rates. Accumulation from older IRHs (black lines) is found more consistent and thus used to compute a mean scenario. The mean and its error are shown in red. Note the substantially higher accumulation at KCS. Figure modified from Konrad [2011].



parameter q_0 at the uphill boundary $x_0 = 0$ and the divergence parameter $D \in [0, 1)$ need to be defined.

Velocity and trajectory computation: The computation of the velocity and trajectory components is performed stepwise for discrete time intervals Δt according to⁸ (conventionally used time increment $\Delta t = 1a$):

- Define starting coordinates $P^{(0)} = (x_0^{(0)}, z_0^{(0)})$ on surface and inside the glacier at starting time $t^{(0)}$ ($t^{(0)} = 0$ if at the surface)
- For each point $P^{(k)}$: Compute velocity components $u_0^{(k)}$ and $w_0^{(k)}$ according to equations (3.12) and (3.14)
- Compute new trajectory coordinates:

$$x_0^{(k+1)} = x_0^{(k)} + u_0^{(k)} \cdot \Delta t$$

$$z_0^{(k+1)} = z_0^{(k)} + w_0^{(k)} \cdot \Delta t$$

$$\text{and age: } t^{(k+1)} = t^{(k)} + \Delta t$$

Output: The model's output is threefold: The output contains data for trajectories computed at a specified horizontal increment, for isochrone layers according to a specified age increment and also a vertical age distribution at a specified horizontal distance.

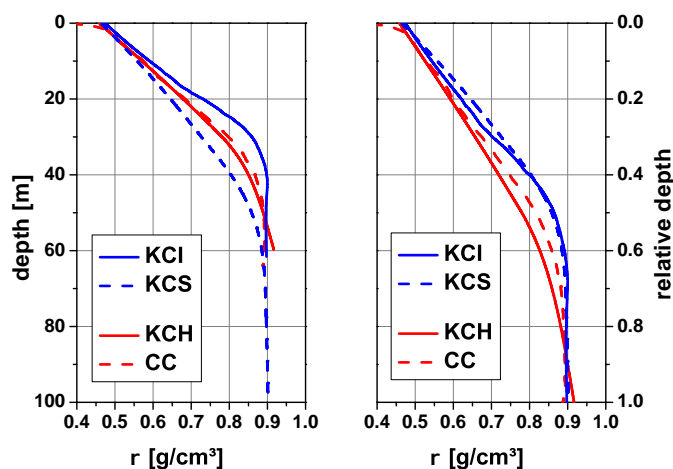


Figure 3.18: CG ice core mean density profiles on absolute (left side) and relative (right side) depth scale. Note that on a relative depth scale, the mean density distribution is similar among the slope cores (KCH and CC) as well as between the saddle cores (KCI and KCS). Figure from Konrad [2011].

3.4.4 Input generation from GPR and ice core data

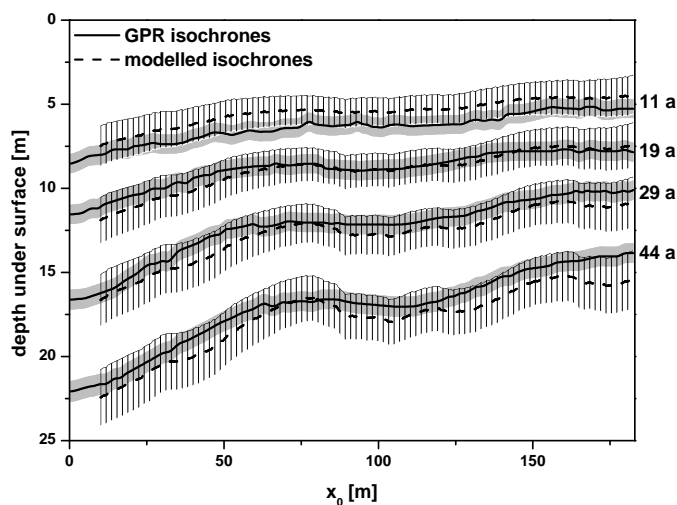
Adequate input data for the application of the model to a specific flow line is derived from ice core data and GPR-profiles. For the case of flow lines which do not coincide with a GPR-profile and do not intersect an ice core drilling site, this comprises the need for spatial interpolation.

Input from GPR-profiles: Coordinates of the surface altitude stem from GPS-measurements along the GPR-profiles. Subtracting the ice thickness obtained from the GPR-bedrock reflection yields the bedrock coordinates. A profile of the mean accumulation rate \dot{b} is obtained from the IRHs coherently dated in the closed course approach (section 3.3, see Figure 3.17 for an example). A first order correction for annual layer thinning is applied to the depth of an IRH as surface accumulation is calculated from equation (3.11).

Input from ice cores: Apart from the age assigned to the IRHs, the ice cores were crucial for supplying density data—not only for the processing of the GPR-data, but also for the model input. Since the local ice core information can only be considered representative of the mean densification behaviour, the density profiles are smoothed accordingly. In a comparison of the smoothed density profiles of all four cores on a relative depth scale (Figure 3.18) similarities become evident between the ice cores located on the saddle and the ones located more up-slope respectively. The “saddle cores” KCI and KCS reach the characteristic close-off density (0.83 g/cm^3) and ice density ($\approx 0.9 \text{ g/cm}^3$) at smaller relative depths than the “slope cores” KCH and CC. To some extent, the different densification patterns go back to less mean insolation on the slope compared to locations on the saddle. For the model input for each flow line, two representative density profiles were derived: One from the average of KCH and CC for a position up-slope on the flow line and one from a distance-weighted average between

⁸Note that the subscript index 0 stands for the global input-output reference frame as described in 3.4.2.

Figure 3.19: Exemplary comparison of GPR-based with flow model based isochrones for the same ages labeled on the right side. Shown here are results for a flow line parallel profile without drilling site, thus illustrating the case where input data for the model had to be interpolated as described in the text. Grey and shaded bands indicate uncertainties for GPR- and model isochrones, respectively. Figure from Konrad [2011].



KCI and KCS for the respective saddle-position on the flow line. For more details on the derivation of density input and the flux parameters, see Konrad [2011].

Spatial interpolation of input data: To apply the model to flow lines which have not been covered by a GPR-profile (so-called “secondary flow lines”) the input data for geometry and accumulation need to be spatially interpolated. Among several tested algorithms, the sophisticated geostatistical method, “kriging”, was eventually found suitable for this purpose. Kriging has been applied successfully for spatial interpolation of bedrock topography from GPR-data in similar studies in Greenland and the Alps [Bamber *et al.*, 2001; Binder *et al.*, 2009]. Interpolation uncertainties were estimated by omitting a subset of input data (e.g. a single GPR-profile) and re-interpolating from the remaining input data. The omitted data is then compared to the result of the interpolation. This method yielded uncertainties of ≈ 1 m for surface altitude, $\approx 1 - 7$ m for ice thickness and $\approx 0.01 - 0.04$ m w.e./a for accumulation rate. For a detailed description concerning the implementation of the method refer to Konrad [2011].

3.4.5 Results

Vertical extrapolation of age information

The model’s capability to predict isochrone layers is validated against IRHs detected in GPR-profiles. This calls for an uncertainty estimation of the model isochrones. For this purpose, a bootstrapping routine was developed by Konrad [2011] which performs a large number of model runs under random variation of input parameters within their associated uncertainties. From these runs, confidence intervals for the model output are derived— increasing with depth from 0.9 to 2.6 m. The respective uncertainty estimate

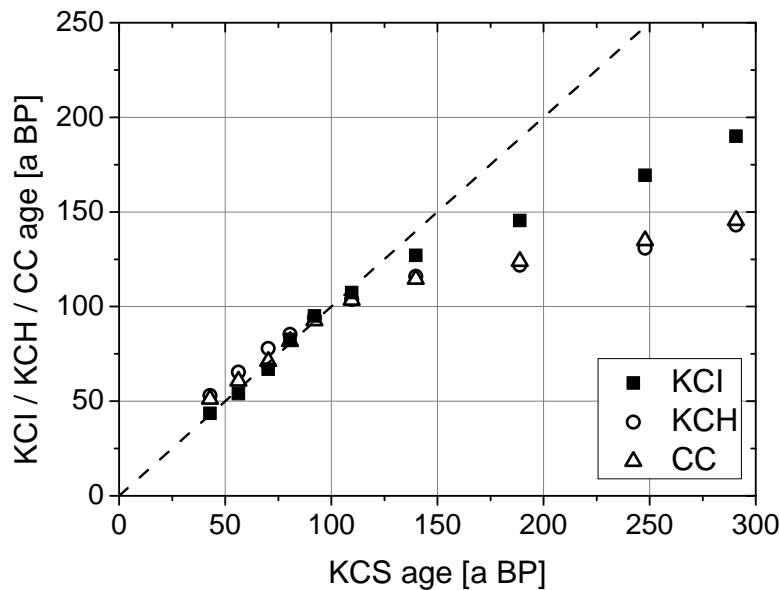


Figure 3.20: Pairwise inter-core dating comparison via flow model isochrones. Isochrone layers were calculated by the flow model and spatial interpolation. For each depth at the respective drilling site, ages were assigned to the layer according to the respective ice core dating. Plotting the resulting ages against ages at KCS as a reference indicate coherence up to ≈ 120 a BP. Beyond, results show a systematic drift to older ages at KCS, however, with large uncertainty (in the order of ± 50 a for ages in KCI and KCS). Figure modified from Konrad [2011].

for the GPR-IRHs ranges around 0.5 – 0.8 m.

Figure 3.19 shows an exemplary comparison on a GPR-profile without intersecting a drilling site. Ages of the GPR-IRHs were obtained from intersections with IRHs from a profile with an ice core, similar to tracing IRHs in a round course. The model isochrones and GPR-IRHs are found in agreement with respect to the comparatively large model uncertainties. Discrepancies were larger for a more steeply inclined bedrock. In general it was found that while the model not always correctly predict the depth of a certain isochrone layer, it much better reproduces the shape of the isochrones and thus their information on the relative subsurface age distribution.

Spatial interpolation of age information

In order to obtain a higher spatial density of age information, 11 secondary flow lines were defined within the drilling area at CG (i.e. between the two dashed lines in Figure 3.9) by approximately tracking the surface altitude gradient. By applying the flow model to these flow lines, isochrone layers were calculated supplementing the IRHs

from GPR-profiles. Moreover, by additionally applying the flow model to slope-parallel GPR-profiles, the isochrone layers could be calculated beyond the depth-limitation of the IRHs. All model isochrone layers according to a specific model-age were gathered and the spatial interpolation routine applied to this subset. In doing so, spatially extended isochrone surfaces were obtained, which were found free of discontinuities or artefacts.

A comparison of a modelled age-depth relation at the KCS drilling site with the respective ice core dating showed that the model itself has only very limited absolute dating capability. However, absolute dating was not intended and, keeping in mind the simplified approach of the model, this limitation comes as no surprise, as similar discrepancies were observed with a full 3D finite-element model [Armbruster, 2000; Konrad, 2011]. The absolute ages of the isochrones are not used for further interpretation and, in the following, will be referred to as the “model ages” as to keep them separate from the ice core based age-information which is considered as most reliable.

Hence, the “absolute ages” were assigned to the extended isochrone surfaces based on the ice core datings. In doing so, it is possible to assess whether the dating consistency known from the GPR-IRH based comparison can be reproduced and hence vertically extrapolated. For this purpose, isochrone layers corresponding to model-ages between 40 – 150 a BP were calculated in a 10 a increment.

Again, a pairwise comparison between KCI and KCS was performed, this time based on the interpolated model isochrone surface. According to the respective depth of the model isochrone at the KCI and KCS drilling site, ages were obtained from the respective ice core dating. The depth error of the spatially interpolated model isochrone layer Δz results in a uncertainty additional to the dating error Δt_{dat} according to the slope of the ice core dating at the respective depth $\frac{dt_{\text{dat}}}{dz}$:

$$\Delta t = \sqrt{(\Delta t_{\text{dat}})^2 + \left(\frac{dt_{\text{dat}}}{dz} \Delta z\right)^2}$$

For KCI and KCS, Δt was found to be in the order of ± 10 a for the last 80 a BP, increasing to ± 50 a around 120 a BP. Figure 3.20 shows the results from plotting again the age of the isochrone according to the KCS dating versus the KCI age. For recent ages, the results lie closely on the bisecting line reproducing the dating coherence between the two ice cores known from GPR-IRH tracing up to 70 a BP. In vertical extrapolation, the model predicts good coherence between the two cores up to about 150 a BP. Beyond, systematic offsets towards older ages at KCS are present going along with a rapid increase in the estimated uncertainties.

An extension of the pairwise dating comparison to the two slope cores KCH and CC proved to be challenging due to their upstream location at the very border of the polygon considered in spatial interpolation. As a result their integration in an intercomparison must be considered preliminary since associated with large and unknown uncertainty. The ages assigned to the model isochrone layers by all four ice core datings were found

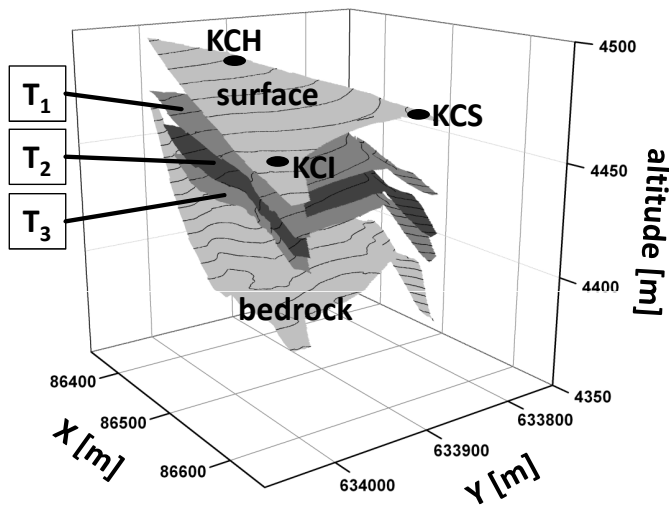


Figure 3.21: 3D age distribution at the CG drilling area. Exemplarily shown are interpolated layers for surface, bedrock and three different isochrones, corresponding to 44, 95 and 169 a BP at KCI. Figure from Konrad [2011].

to indicate agreement up to ≈ 120 a BP (Figure 3.20). Although no concise explanation for the systematic trend to older ages in KCS is readily available at this stage, it seems worth noting that the onset of this trend coincides with a distinct sharp bend in the KCS dating. Below $\approx 50\%$ core depth or around 110 – 120 a BP, the age of the ice increases rapidly with depth, due to a potential upstream-effect (see section 3.5 below) [Armbruster, 2000]. It was shown by Konrad [2011] that the flow model is only able to reproduce this effect under extreme and clearly unrealistic input conditions which were not considered for further model application. The strong non-linearity in the ice core age-depth relation observed at KCS is the result of the large but unknown spatio-temporal variability in accumulation and flow upstream conditions. Since the model cannot fully account for this spatio-temporal upstream variability, the systematic trend in Figure 3.20 may be regarded as in principle associated with this shortcoming.

While the absolute age assigned to the surface by the model must be considered unreliable, ages assigned to the interpolated surfaces from the ice core datings agree up to 120 a BP. Hence, it can be interpreted as a physically reasonable, “best guess” map of the three dimensional age-depth structure within the drilling area. Three exemplary isochrone layers between surface and bedrock are shown Figure 3.21. Two layers are within the age-range where the ice core datings are in agreement, corresponding to ≈ 44 a BP and ≈ 95 a BP. The lowermost layer corresponds to ≈ 169 a BP at KCI.

3.5 Identification of catchment area and upstream-effects

In the context of the spatial accumulation variability at Colle Gnifetti, the relation between the upstream catchment area and depth in an ice core is of special interest. As discussed in chapter 2, the inflow of ice from areas with a systematic offset in seasonal

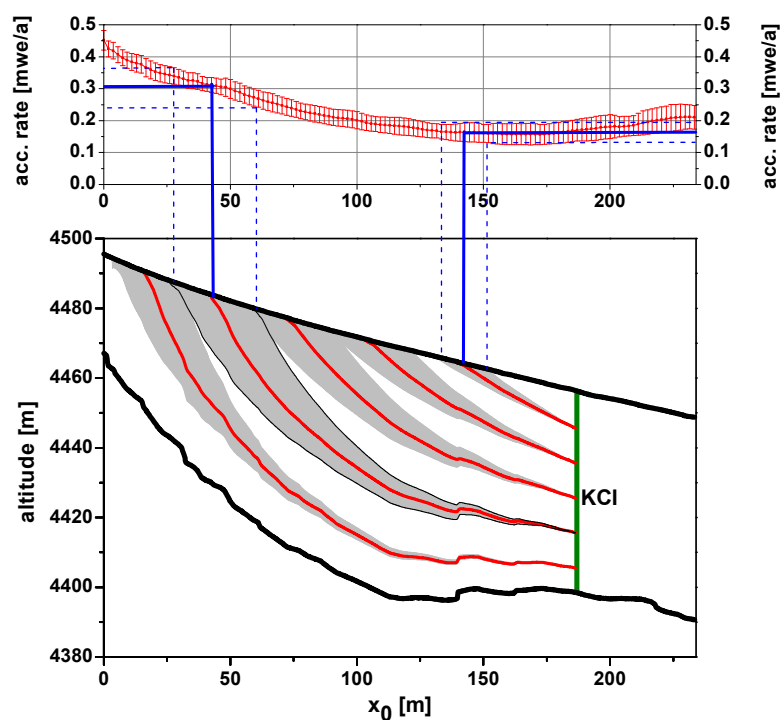


Figure 3.22: Backward trajectories and catchment area identification for KCI (bottom) in relation to upstream-accumulation variation (top). x_0 denotes the horizontal distance from the top of the flow line. From this application of the flow model, a tentative source region for each layer in the ice core and its respective surface accumulation can be identified (blue lines). Note the grey uncertainty bands, resulting in accumulation uncertainty (blue dashed lines). The profile shown here corresponds to the black dashed line in Figure 3.9. Figure modified from Konrad [2011].

net accumulation alters the respective mean $\delta^{18}\text{O}$ -values in the ice core without being directly linked to atmospheric temperature (the so-called “upstream-effects”). Moreover, accumulation at the source region also influences annual layer thickness and thus the dating of the ice core. Obviously, back trajectories from a flow model provide the here needed information to connect any ice core sample to its deposition site.

For the KCS ice core, backward trajectories were calculated by Lüthi [2000]. Based on these trajectories and a large number of shallow ice cores, Keck [2001] investigated the upstream-effect for the KCS $\delta^{18}\text{O}$ -time-series. He concluded that correction for the observed upstream-effect increases the magnitude of long-term isotope-trends within the last 100 a BP. Beyond 100 a BP, the correction is negligible as the accumulation changes only little in the uppermost part (cf. Figure 3.17).

Although not studied in detail so far, different conditions are expected upstream of the

KCI-core, as it was drilled in a small island of exceptional low net accumulation. The accumulation pattern derived from GPR-IRHs show a systematic increase upstream, as shown in Figure 3.22. The backward trajectories obtained from the 2.5 D flow model do not allow for a precise quantitative interpretation due to the considerable uncertainties, indicated by the grey bands in Figure 3.22. Additionally, the exact upstream-variability in mean $\delta^{18}\text{O}$ -values is not known for KCI, as obtained from shallow cores in the quantitative study by Keck [2001]. However, the simple model already provides a number of qualitative insights:

An increase in surface net accumulation upstream by a factor of 2 or more appears present, significantly different in spite of the uncertainties (see blue lines in Figure 3.22). Moreover, the calculated trajectories allow to roughly identify the core depth below which ice from the uppermost source region is contained. This is especially relevant to constrain potential disturbances by the Bergschrund at the top end of the flow line. Regarding the time series of KCI, this preliminary upstream investigation suggests that layers corresponding to roughly 100 a BP stem from more than 100 m upstream where surface accumulation is higher than at KCI by about a factor of 2. Recalling the relation between surface accumulation and mean $\delta^{18}\text{O}$ at Alpine am CG ice cores (cf. Figure 2.3 in section 2.2) it is evident that a change from ≈ 15 cm w.e./a (long-term mean at KCI) to ≈ 30 cm w.e./a (Figure 3.22) may already have a considerable effect on mean $\delta^{18}\text{O}$ values in the KCI ice core. As pointed out in chapter 2, this is especially relevant with respect to the weak long-term isotope variability. Due to the upstream increase in accumulation, the effect on $\delta^{18}\text{O}$ would be opposite at KCI compared to KCS and might contribute to the large $\delta^{18}\text{O}$ -trend observed for KCI and the past 100 a BP.

3.6 Summary and critical assessment

Combining multi-core chronologies with GPR-based IRH-mapping and adapted simple flow modelling resulted in the first comprehensive picture regarding isochrone layering within the drilling area at Colle Gnifetti. Although restricted to approximately the upper half of the glacier thickness, detailed insights could be obtained to what extent coherence between the ice core chronologies may be expected with respect to the spatial distribution of accumulation rate and annual layer thickness, respectively. Tracking of GPR-IRHs between the respective drilling sites showed pairwise consistent ice core datings up to ≈ 80 a BP. Linking GPR-IRHs to a closed course pointed towards an inter-core age coherence, however restricted to 50 a BP. This limitation could be overcome by performing all measurements during one field campaign, which would allow to track IRHs of the same physical origin in a close course. In the present study, the coherence assessment was supplemented with the flow model application for calculating englacial isochrone surfaces within the drilling area. As the model itself has no immediately useful absolute dating abilities, the absolute ages of the isochrone surfaces have

to be determined from the ice core datings. Thereby, the comparison of all four datings indicated reasonable age coherency at least within the past 120 years. However, the still substantial depth- and age-limitation remains a major issue, for which three main causes are identified:

- Missing internal GPR-reflections below the firn-ice transition. At present, this phenomenon is still not fully understood (section 3.7 below) which complicates the potential development of a dedicated technical solution.
- Rapidly increasing model uncertainty, which is not clearly predictable at larger depth.
- The lack of useful ice core age information in the bottom core sections, as well as of unambiguous tie points.

Naturally, this situation calls for improvements, and to continue the promising approach developed here at greater depths. A dedicated technical solution would comprise additional sophisticated GPR deployment, e.g. by means of increasing the signal-to-noise ratio in CO-profiles using high horizontal resolution while stacking a large number of shots (> 100). Moreover, additional information may be obtained using broadband (stepped frequency or FMCW) or even more sophisticated, synthetic aperture radar (pers. communication O.Eisen). As these approaches are very time-consuming, they were not deployed so far in field campaigns mainly dedicated to obtaining extended spatial coverage.

Aiming at greater depths, the help provided by flow models is limited as they certainly become most deficient close to bedrock, since, as a matter of principle, unable to adequately represent the large spatio-temporal variability at CG. Regarding the simple 2.5-dimensional model used in the present study, the kinematic condition demands bedrock-parallel ice flow, whereas the model only considers a 1-dimensional bedrock gradient. While this shortcoming cannot be overcome when avoiding full 3D flow modeling (most likely equally deficient close to bedrock), the existing model could be further improved by using a modified flow law accounting for the deformational behaviour of the large firn fraction. Extended investigations into the flow law of firn were conducted by Lüthi [2000]. In a first order parametrization, the flow law exponent in the flow model used here could be changed from 3 to 1.5. Values close to 1.5 were found most suitable for a firn-ice combination by Wagner [1996] and for parametrizing the vertical velocity profile at KCI [Bohleber, 2008]. As a consequence of the depth limits imposed on the use of flow models and GPR to provide reliable age estimates at larger depth, further age information must come from ice cores.

For this purpose, observational constraints provided by sophisticated dating methods seem most promising. Although potentially influenced by production and reservoir effects, radiocarbon dating of particulate carbon has been used for constraining the age of the lowermost ice at CG [May, 2009; Jenk *et al.*, 2009]. However, this method seems not feasible to provide age information over the last millennium or so. Regarding this

dating gap, complementary information might be provided by investigating ^{10}Be variability (reflecting a precisely dated production signal known from ^{14}C -tree-ring records) and, potentially, by ^{39}Ar -dating performed with atomic trap analysis.

As no absolute dated horizons are provided by the above methods, an adequate strategy is to construct an improved local age–depth relation based on all available age information and associated uncertainties. As these extended chronologies are models in itself, the combination with the adapted flow model presented in this study would be of mutual benefit as to:

1. Further validate and constrain the flow model to observational age information from ice cores at intermediate and larger depths.
2. If 1. is successful, the model-derived isochrones could provide a tentative map of the three dimensional distribution for much older ice layers at CG.
3. Even the improved ice core chronology can not be expected as precise enough to identify volcanic horizons, and thus absolute age markers. Further validation might be obtained if two ice cores with improved chronologies exist. Here, an opportunity for matching is provided by 2., connected to some (undated) outstanding feature in the ice core profiles, thus substituting for the missing IRHs.

In conclusion, the combined approach (GPR, flow model and ice core chronologies) developed in the present study seems feasible to further contribute to the complex task of investigating the age-distribution at deeper layers of Colle Gnifetti. To this end, additional observational age-constraints are called for from sophisticated radiometric methods.

The application of the combined approach to other drilling sites requires at least the presence of a single dated ice core as well as a reasonably dense spatial coverage by GPR-profiles. Naturally, the number of ice cores and GPR-profiles necessary for a successful application depends on the complexity of the site, i.e. regarding scale and sampling trait. Small-scale high alpine drilling sites might profit from an investigation on the internal age-distribution with the combined approach presented here, e.g. Illimani glacier in the Andes [Knüsel *et al.*, 2003] and Belukha glacier in the Himalayan [Fujita *et al.*, 2004; Aizen *et al.*, 2005]. Dating ice cores over a few hundred years is typically regarded as less of a challenge for larger ice-bodies, such as ice caps in the Arctic [Fisher *et al.*, 1998] and at lower latitudes [Thompson *et al.*, 1993]. In this context, the spatial extrapolation of ice properties other than age might appear more interesting, for which the combined approach may be readily adapted. This especially concerns changing physicochemical properties associated with GPR-IRHs.

3.7 Internal GPR–reflections investigated with borehole radar and physical ice core properties

Evidently, the evaluation of ice core records at Colle Gnifetti (and comparable sites) would greatly benefit from the detection of IRHs by GPR at greater depths. Interestingly, a similar phenomenon of an “echo-free zone” (EFZ) is also observed in the lowermost parts of the polar ice-sheets, due to ice-flow induced layer disturbances, as pointed out by Drews *et al.* [2009]. However, the EFZ at Colle Gnifetti is of different origin, not least for the fact that layer disturbances are not observed where IRHs vanish (at much smaller relative depths already). As outlined in section 3.2, the disappearance of IRHs roughly coincides with the firn-ice transition. Although in the focus of ongoing research, direct evidence for changes in crystal orientation fabric (COF) have not been observed at CG so far. Thus, acidity variations are left as the prime reflection mechanism beyond the firn-ice transition. Eisen *et al.* [2003a] put forward that the chemical composition of the ice changes from acidic to slightly alkaline prior to 1950 AD (see Figure 4 in Eisen *et al.* [2003a]) and that pronounced acidity peaks were hardly detected below. For the CG ice cores, the annual layer thickness below the firn-ice transition is typically in the order of a few centimeters only [Bohleber, 2008] which further reduces the strength of dielectric contrast of a potential acidity horizon (of volcanic origin). Altogether, the disappearance of strong density variations seem to coincide at a critical depth with the presence of an alkaline background and small annual layers. The result is a distinct decrease in overall reflection coefficient and hence in the amount of energy reflected to the surface.

In order to investigate the influence of changes in density and acidity as well as annual layer thickness on the GPR return signal, Eisen *et al.* [2003a] suggested forward modeling of radargrams from dielectric profiling (DEP) data [Eisen *et al.*, 2003b]. Unfortunately, no DEP data were obtained from the Colle Gnifetti ice cores at that time. In 2010, Jepsen [2010] performed DEP measurements on the firn core KCO, which was drilled 2 m from KCI. In applying a basic forward model to the DEP-data a number of distinct reflections of a GPR-CO profile could be reproduced, however without a detailed interpretation on their physical origin. Unfortunately, the study remained also restricted to the firn zone since the KCO core only covers the upper 26 m.

Although hypotheses for explaining the depth limitation of IRHs at CG are at hand, the present data seems insufficient to unambiguously decide against or in favour of a specific explanation. With respect to the exceptional density of sub-surface information from firn- and ice cores as well as geophysical measurements, including GPR as well as seismics [Diez, 2010; Hoelzle *et al.*, 2011] the KCI drilling site seems most feasible for a dedicated investigation. Making an attempt to contribute to this ongoing research, the approach of the present study was twofold:

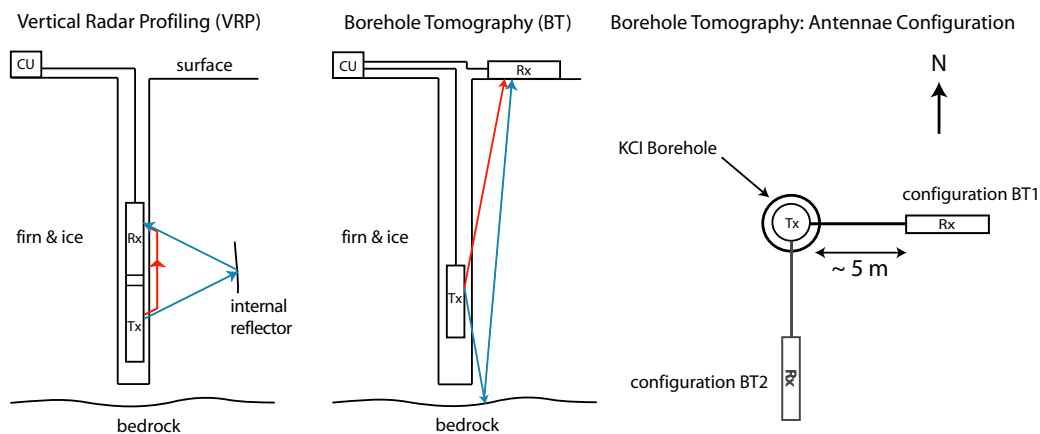


Figure 3.23: Antenna setups used for vertical radar profiling (VRP, left side) and borehole tomography (BT, center). On the right: Different antennae configuration for the two BT profiles. For VRP, receiver (Rx) and transmitter (Tx) were lowered into the borehole together, supported by the cable connection to the control unit (CU). For BT, only Tx was lowered into the hole with Rx kept on the surface. Also shown are two typical ray paths for each profile: Direct wave (red) and reflection (blue).

- In an attempt to deploy a GPR-antenna to the depth-intervals where surface-based GPR fails to supply unambiguous information, the still open KCI-borehole was used to perform a pilot study in borehole radar at CG. Borehole radar surveys have been used for the direct measurement of the propagation velocity of the radar signal in ice caps [Robin, 1975; Jezek and Roeloffs, 1983] and temperate glaciers [Murray *et al.*, 2000]. Depth-dependent velocity profiles obtained by borehole radar at KCI, could be investigated for differences between depth-regions with and without IRHs.
- Additionally, the ice core data of density and acidity obtained from KCI are considered for comparison with local GPR-CO traces. Using the GPR-CO profiles, physical ice properties are compared to distinct IRHs and especially to the lack thereof.

3.7.1 Borehole radar

The top of the KCI-borehole drilled in 2005 was excavated in another field study in 2007. A casing was installed in order to keep the borehole accessible for further studies. During the field campaign in summer 2010, which was primarily focused on performing seismic measurements at CG, a pilot study in borehole radar was carried out at the KCI borehole. Two 250 MHz borehole antennas were deployed in two different setups as shown in Figure 3.23.

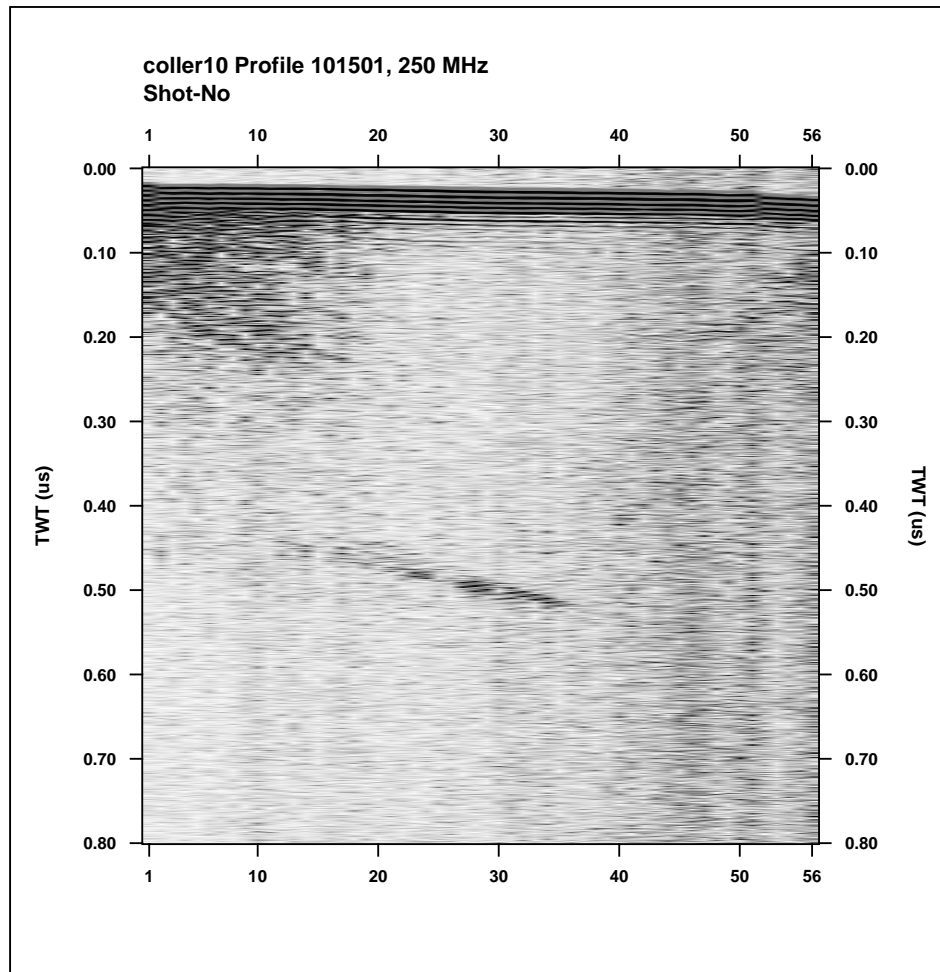


Figure 3.24: Exemplary radargram from vertical radar profiling at KCI. Trace 1 corresponds to Tx and Rx outside of the borehole, which were subsequently lowered down to bedrock at trace 56. Note the distinct reflector between trace 20 and 37, around 400 – 500 ns.

Vertical radar profiling (VRP)

In order to investigate changes in propagation velocity with depth, transmitter (Tx) and receiver (Rx) were lowered into the borehole together. For this purpose, Tx and Rx were joined together by a rigid connector. Lengths of Tx, Rx and the connector were 1.26, 1.23 and 0.5 m, respectively. Measured from the center of the dipole marked on each antenna as 0.35 m from its top end, the fixed separation of Tx and Rx was $\Delta x = 1.73$ m. Measurements were triggered manually at 1 m intervals with the depth-reference point for the recorded measurements set at half the distance between the dipoles, which corresponds to a depth of 1.2 m measured from the top end of Rx (Figure 3.23). A reference measurement was made with the Tx–Rx assembly outside the hole. The 3 m long Tx–Rx assembly could be lowered 56 m into the hole, measured from the very top end of the antenna assembly. A second profile was recorded in 1 m

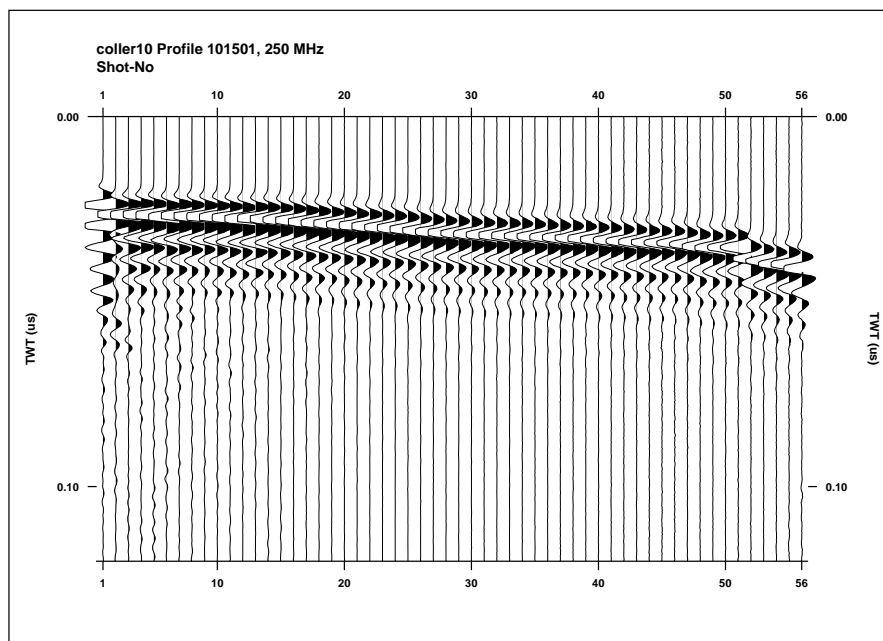


Figure 3.25: Direct wave in vertical radar profiling from figure 3.24. Trace 1 corresponds to the antennae at the surface, trace 56 to the very bottom of the borehole. The vertical axis designates the TWT from Tx to Rx. For further analysis the first maximum of each trace was picked. Note the offset between trace 51 and 52, where measurements were paused for 10 minutes due to a technical problem.

steps while pulling the antennae from the bottom of the hole upwards. An exemplary radargram from vertical radar profiling at KCI is shown in Figure 3.24.

A vertical profile of propagation velocity $v = \Delta x / \Delta t$ is obtained from evaluating the depth-variations in travel-time Δt needed by the direct wave from Tx to Rx. A detailed picture of the direct wave of the profile shown in Figure 3.24 is given in Figure 3.25. At trace 51 measurements had to be stopped for 10 minutes due to a technical problem before they were continued at trace 52. Note in Figure 3.25 that this delay produced a distinct offset between trace 51 and 52. Evidently, this offset does not go back to a sharp change in ice properties (it is missing in the complementary profile pulling the antennae upwards, shown in the appendix B.2) and thus indicates a drift in measurement equipment. In the direct wave signal, this drift is superimposed on effects of vertical variations in propagation velocity. Hence, a correction was necessary but proved to be a challenge. In a first order consideration, the drift was assumed as linear in time with a gradient of 2 ns per 10 minutes, obtained from the offset between trace 51 and 52. An according slope was subtracted from the direct wave (pers. communication M. Eidner, boratec, Weimar). Then, the first maximum of each trace was picked and converted into absolute travel time in ns via the reference measurement in air and assuming the propagation velocity in air to be $v_{\text{air}} = 0.3 \text{ m/ns}$ and with known antennae separation of 1.73 m. Thereby, a vertical profile of potential propagation velocity was obtained. Fig-

Figure 3.26: Vertical profile of propagation velocity derived from VRP at KCI. Results from lowering the antennae into the borehole (bottom plot) are shown in comparison to the KCI density data (top plot, black), subsampled to 1 m resolution (red). Density values were converted into propagation velocity using equation (3.2). Note that the absolute velocities from VRP appear systematically higher.

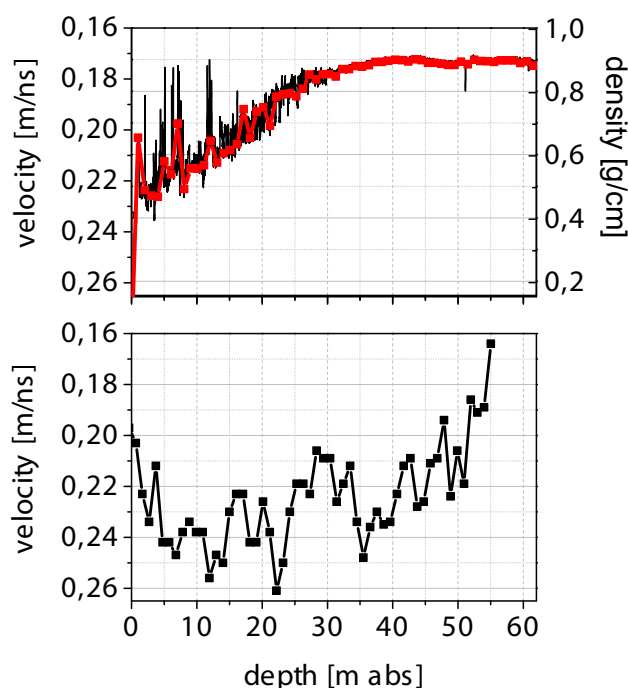


Figure 3.26 shows the comparison with KCI density data with the following main results:

- The absolute velocity values from VRP appear as systematically higher than typical values for firn and ice, e.g. compare 0.22 – 0.17 m/ns obtained with densities from 0.4 to 0.9 g/cm³ and equation (3.2). Due to the substantial air-gap between antennae and the wall of the borehole, this offset most likely results from a contribution by the direct wave also travelling through the air-filled borehole with a larger speed.
- The general trend in the velocity-depth profile is not as expected from the KCI-density profile (note the additional axis for velocity in Figure 3.26). As density and propagation velocity are in an inverse relationship (cf. equation (3.2)), a substantial decrease in velocity is expected up to the firn-ice transition between 25–30 m depth at KCI. Below, density is approximately constant, which should thus also be expected of velocity.

In spite of this discrepancy regarding general trend and absolute values, the relative variations in velocity could still contain relevant information. The comparison with density, also subsampled to 1 m resolution in Figure 3.26 shows no clear signs of the expected inverse relation. No direct information regarding vertical changes in ice properties could be obtained from the VRP-profiles at this stage, which is probably due to the following shortcomings:



Figure 3.27: Ice-cliff at Colle Gnifetti as seen from a helicopter. Note the KCI drilling site as well as a large crevasse in front of the ice-cliff.

- Residual drift effects may hamper the detection of small variations in velocity which are expected from actual changes in physical ice properties. Density anomalies averaged over the antennae separation of 1.73 m are expected to change the measured velocity by less than 0.02 m/ns.
- Potentially large, but hard to estimate variations in velocity potentially stem from relative shifts of the antennae with respect to the borehole-wall. These shifts are especially expected towards the lower depth, where the borehole is most likely inclined.

The VRP-profile was further investigated with respect to the distinct borehole-parallel reflector (Figure 3.24). Note how the reflector can only be detected unambiguously in the middle section roughly between trace 20 and 37. Above trace 20 and below trace 37, a large amount of noise is present in the radargram. In the upper section, these reflections could stem from the same origins that produce the distinct lateral IRHs in the GPR-CO profiles. The noise in the lower section might partially go back to a silty layer above bedrock, but could also be a setup-related artefact, potentially due to cable-elongation (pers. communication M. Eidner, boratec, Weimar).

From calculating the travel-time difference between the direct wave and the reflector, its distance from the borehole can be estimated using the velocity-depth profile based on the KCI density data. This gave a distance between 41 – 42 m. A potential origin for this reflector is the vertical ice-air interface at the ice-cliff close to the KCI drilling site (Figure 3.27). However, a rough estimate indicated the ice-cliff to be at least 80 – 100 m distance from KCI. Alternatively, the reflector could also stem from an air-filled crevasse (known to occur close to the ice-cliff, Figure 3.27) or even a comparatively thin crack.

Borehole tomography (BT)

For the borehole tomography (BT) setup, only Tx was lowered into the hole with Rx kept lying on the surface pointing eastwards and located about 5 m from the hole. Data from this setup will be referred to as profile “BT1”. After lowering Tx to the very bottom, Rx was moved from 5 m distance in eastern direction from the borehole to a location in 5 m distance in southern direction and rotated by 90°. Then, Tx was pulled upwards for the second half of the profile. Data from this setup will be referred to as profile “BT2” (see Figure 3.23). Traces were again recorded at 1 m intervals at equal depths for BT1 and BT2. Note that in earlier borehole-radar studies [Robin, 1975; Murray *et al.*, 2000], the term “vertical radar profiling” mainly referred to this measurement setup, with one antenna kept on the surface. For a nonambiguous terminology, here this setup is referred to as borehole tomography.

Figure 3.28 shows the BT-radargram (an alternative “variable density” plot is shown in the appendix B.2). The first half of the profile down to trace 66 shows profile BT1, the second half BT2. Note the signal from the direct raypath Tx-Rx with increasing travel-time with increasing depth, the so-called “down going wave” [Yilmaz, 2001]. For the raypath from Tx-bedrock-Rx, the overall distance and thus the travel time decreases with lowering Tx producing an arched “upcoming wave” (cf. raypath in Figure 3.23). Obviously, these effects are opposite in the second half of the profile with Tx moved upwards, which leads to the observed “V”-structure of the direct raypath and the hyperbolic shape of the bedrock-reflection. In the lower region of the radargram shown in Figure 3.28, the signal of the direct wave appears much weaker in BT1 compared to BT2. The upper 26 meter of the radargram are missing due to a wrongly placed time-window during data recording. Unfortunately, this restriction hampered the envisaged comparison of propagation characteristics between the upper IRH-zone and the lower glacier parts. Consequently focused solely on the ice part, data evaluation was aimed at calculating an interval velocity profile and estimating the total ice-thickness at KCI.

Calculation of interval velocities: From the direct wave signal, an interval velocity profile can be obtained for the BT-setup [Murray *et al.*, 2000]. For each trace, the first maximum of the direct wave was picked and travel distances between Tx and Rx were calculated including the horizontal offset of Rx. From the difference in travel times Δt and travel distance Δs for each pair of neighbouring traces, interval velocities $v_{\text{int}} = \frac{\Delta s}{\Delta t}$ were calculated for each depth interval. The resulting profile of v_{int} is shown in Figure 3.29. Data from BT1 (grey) are found in overall agreement with BT2. However, both datasets feature a considerable amount of scatter, probably due to the uncertainty in picking the direct wave signal. Most likely, the data scattering among 4–5 different values (Figure 3.29) indicates an influence of limited resolution associated with the respective sampling rate during data recording. This resolution limit was estimated to be of substantial influence: With 2048 samples, a time window of ≈ 800 ns and $\Delta s \approx 1$ m,

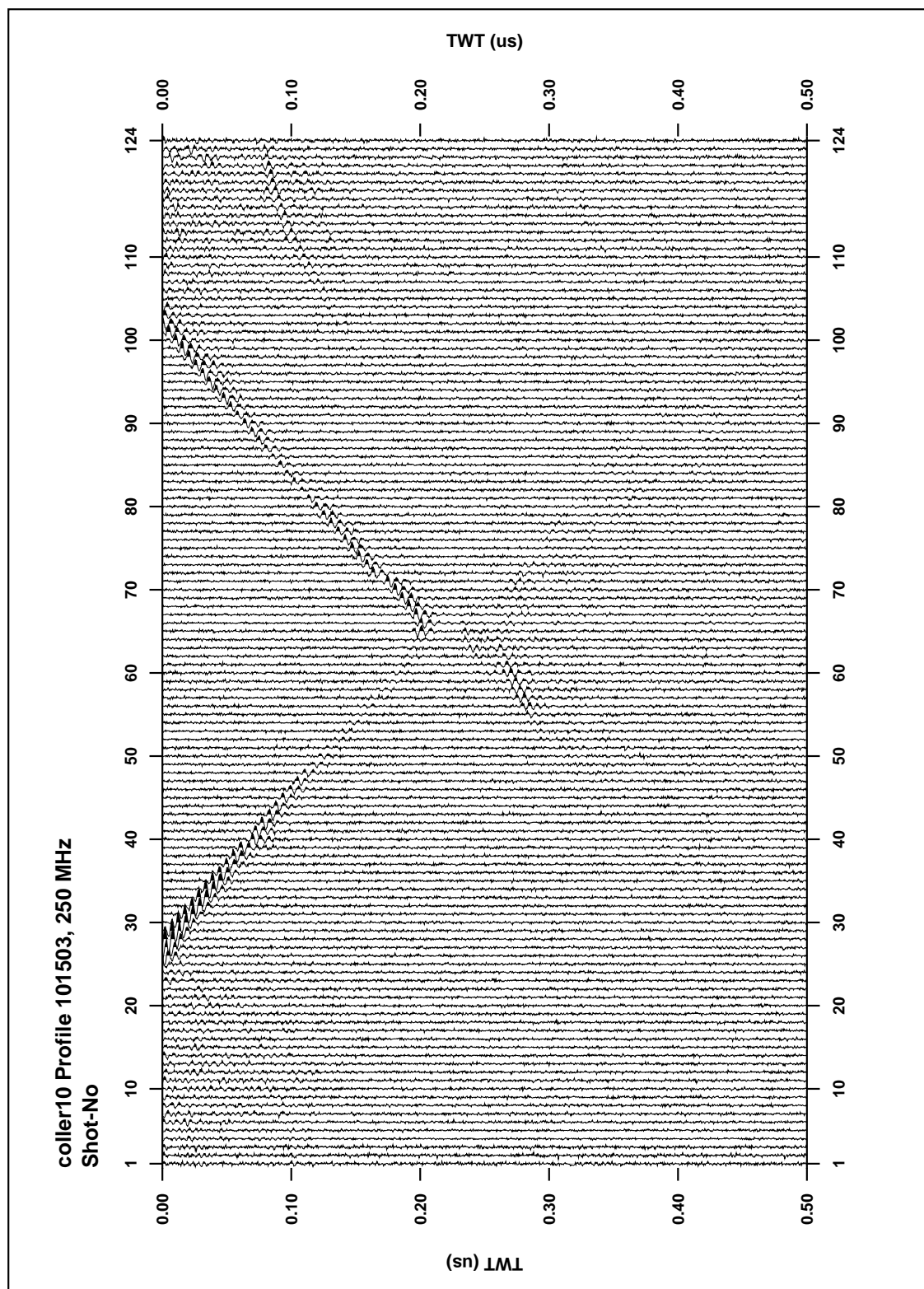
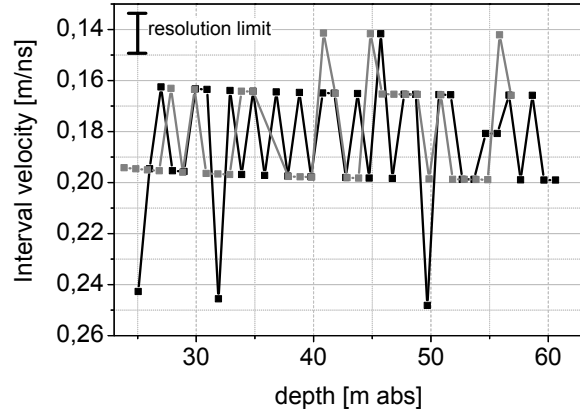


Figure 3.28: Borehole tomography at KCI. The profile concentrates on the ice part as the upper 26 m are missing. Tx was lowered into the borehole from trace 1-66 (profile BT1), and pulled up again during the second half of the profile starting from trace 67 onwards (profile BT2). Clearly seen are the 'V'-structure of the direct raypath Tx-Rx and the hyperbolic shape of the bedrock-reflection. Note that, below trace 52 the amplitude of the direct wave is substantially smaller in the first half of the profile.

Figure 3.29: Interval velocity profile at KCI derived from borehole tomography. Velocities from profile BT1 (lowering Tx) are shown in grey, from BT2 (raising Tx) in black. For BT1, no precise data could be obtained for the lowermost parts due to weak signal amplitude. Note the resolution limit related to sampling rate in data recording.



the uncertainty in v_{int} due to limited resolution is expected to be $\Delta v_{\text{int}} \approx 0.014$ m/ns. Note how nevertheless a slight systematic decrease in velocity seems to be present between 24 and 30 m, potentially the very end of the firn densification. Below the firn-ice transition, the velocity appears constant within uncertainty, with a mean value of (0.18 ± 0.02) m/ns. This value is higher, than the value of ≈ 0.17 m/ns, which would be expected based on the KCI density data and equation (3.2), although both values agree within the respective uncertainty. The estimated errors are similar to uncertainties reported by Murray *et al.* [2000], who report the largest error component to be a result of borehole-inclination, which is most likely also the case at KCI.

Estimation of basal ice thickness: The retrieval of the bottommost, oldest ice was an important objective during the drilling of the KCI ice core. However, in 2005 drilling was stopped due to a gravel stone inside the ice before clear signs of ultimate proximity to bedrock were detected, such as a silt-layer found in CC and KCS cores. Hence, remaining basal ice is expected and envisaged to be retrieved while the borehole is still open. However, the distance to bedrock and thus the amount of ice remained inadequately known due to the large uncertainty in ice thickness estimation using GPR-CO profiles (section 3.3.1). Here, new information can be obtained from the BT-survey.

As the first 6 traces were recorded as a test on the surface, 60 traces could be recorded at 1 m intervals inside the borehole. Adding 1.26 m length of Tx measured from the depth-reference point, this results in an estimated borehole-depth of 61.26 m, which is close to the depth logged for the KCI core of 61.58 m⁹.

A first estimation of the distance to bedrock can be obtained from the difference $\Delta t = t_{\text{bed}} - t_{\text{dw}} \approx 27$ ns between the travel-time of the direct wave Tx-Rx, and the respective bedrock reflection at the lowermost point (trace 66) (t_{dw} and t_{bed} , respectively). t_{dw} and

⁹Note that from the VRP measurements, a smaller depth is estimated: 54 traces inside the borehole plus 3 m antenna length yield 57 m. An already steep borehole inclination would account for the fact that the longer antenna-assembly got stuck earlier and could not be lowered further.

t_{bed} were picked at their lowermost and uppermost reflection, as to obtain a minimal estimation. Using $v_{\text{ice}} \approx 0.17$ m/ns, the distance from the dipole of Tx to bedrock s' can be estimated as:

$$s' = \frac{1}{2} \cdot v_{\text{ice}} \cdot \Delta t \approx 2.30 \text{ m} .$$

Note that in this estimation, the 5 m horizontal distance of Rx on the surface has been neglected. The factor $\frac{1}{2}$ considers the fact that t_{bed} stems from a reflection, not from the direct wave. Additionally considering that the dipole of Tx is positioned 0.91 m above its lower end, one arrives at a distance s between the bottom of the antenna (and thus presumably the borehole) and bedrock:

$$s \approx 0.48 \text{ m} ,$$

indicating that there are at least ca. 50 cm of basal ice remaining in the KCI borehole. With a deeper, but more distinct bedrock reflection signal picked, $\Delta t = t_{\text{bed}} - t_{\text{dw}} \approx 40$ ns results in $s \approx 1.58$ m, giving a rough estimate of the maximum amount of remaining basal ice.

Qualitative indication from BT for vertical changes in COF: As can be seen from Figure 3.28, the signal amplitude of the direct wave below \approx trace 52 is clearly reduced in BT1 compared to BT2. Tx is located at the same position in the borehole for the respective traces, hence this difference should be associated with the different position of Rx relative to Tx. The change in position of Rx comprises a different location and a 90° rotation (cf. Figure 3.23). By this means, Rx was always pointing towards the borehole, resulting in the dipole radiation characteristics of Tx and Rx located in the same plane for both profiles. Changes in transmission characteristics going back to the different location of Rx on the surface would affect the direct wave signal across the entire depth range, which is not observed. Hence, the detected difference should be regarded as an effect of changing the orientation of Rx, thus indicating an dependency of the directional characteristics of the electromagnetic wave in the lowermost ice parts. Due to its crystalline structure, the dielectric properties of a pure mono crystal of ice are not isotropic (for more details, see section 4.2.2). Since glaciers mainly comprise polycrystalline ice with a large number of randomly oriented ice crystals, an isotropic response to electromagnetic radiation should be expected. However, as mentioned in the introduction, internal deformation processes lead anisotropic crystal orientation in the lowermost sections of polar ice sheets. The ice at Colle Gnifetti may experience a similar effect as it is frozen to bedrock [Haerberli and Funk, 1991; Hoelzle *et al.*, 2011] (thus subject to high stresses) and of reasonable old age to provide for a reorientation of ice crystals. With respect to the direction of ice flow at KCI, Rx was perpendicular for BT1 and parallel for BT2, respectively. However, the interpretation of the BT-radargram suggested here can only be regarded as a first hint for potential anisotropic COF in the lowermost parts of CG. Investigations on COF are planned using an automated fabric

analyzer on selected remnant parts of the KCI ice core (pers. communication S. Kipfstuhl, AWI). The qualitative indication for potential changes in COF from the BT survey may be of use for selecting respective ice core samples.

3.7.2 Physical properties in KCI versus internal reflections in GPR

In an alternative approach, data obtained from density and electrical conductivity measurements (ECM) on the KCI ice core were compared to the local signature of the flow line parallel GPR CO-profile (Figure 3.30). The ECM method has been developed to obtain acidity profiles directly from polar ice cores to identify acidity peaks from volcanic eruptions [Hammer *et al.*, 1980]. However, ECM signals are known to fade away below a critical alkalinity level, cf. Greenland ice core data during the last glacial [Taylor *et al.*, 1993]. Within the Holocene, the ECM-acidity peaks have been shown to correlate with GPR reflections [Hempel *et al.*, 2000]. ECM measurements on the KCI ice core comprised the upper 37 m only, performed identically to the recordings of KCH and KCS [Scholze, 1998]. The ECM variability seen at CG is much different from polar ice cores. While minimum levels go back to alkaline mineral dust peaks, the origin of high levels is twofold, as they may indicate (i) very clean conditions in the pre-industrial era, or volcanic horizons during that era or (ii) acid deposition after 1950 AD not disturbed by mineral dust inputs. Consequently, the ECM signal cannot be immediately related to signals of volcanic eruptions, but may nevertheless indicate acidity anomalies above the pre-industrial alkaline background at CG. Hence, in deploying ECM and density datasets, profiles of the two main physical ice properties associated with IRHs are compared to the local GPR signal, as shown in Figure 3.30.

The following datasets were compiled for comparison, shown in plots numbered with (1)-(5): For plot (1), 40 traces around the KCI drilling site were subsampled out of the KCI flow line parallel upstream GPR profile (the black dashed line in Figure 3.9). With a trace spacing of 0.2 m, this corresponds to a horizontal distance of 8 m. A single trace was picked roughly corresponding to the location of the KCI drilling site (2). Note that due to the presence of inclined reflectors, stacking traces may not lead to the desired enhancement in signal-to-noise ratio, but average out relevant information on the IRHs. The mean of the 40 traces was calculated and also used for comparison, but provided no additional insights and hence is not shown in Figure 3.30. The amplitude of the single trace was normalized to its maximum value of the direct wave, the “signal” thus being:

$$\text{signal} = \frac{\text{amplitude}}{\max(\text{amplitude})}$$

Since more representative for the actual energy reflected to the surface, the squared

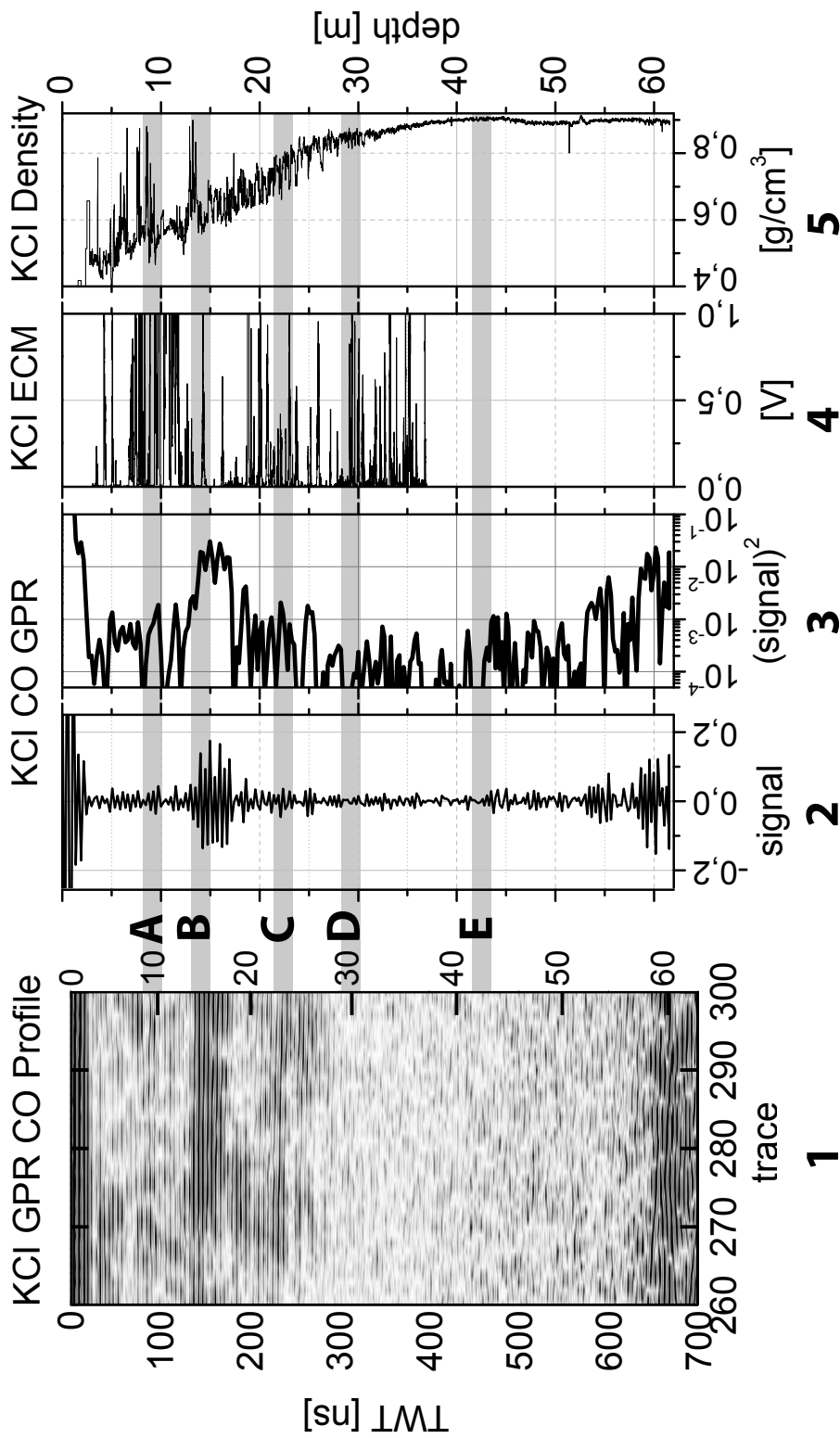


Figure 3.30: Comparison of GPR with ice core data at KCI on a common depth scale. Shown from left to right are: 40 traces of the flow line parallel GPR CO-profile at KCI. Single trace close to the KCI drilling site (black). Squared amplitude of the single GPR-trace (note the logarithmic scale). ECM profile on KCI. Density profile of KCI. For the GPR data, TWT-depth conversion was based on the velocity profile from KCI density data and equation (3.2). Note that the plots have been numbered (1)-(5) and regions of interest have been marked as the grey sections labeled with letters A-F and are discussed in the text.

amplitude of the normalized single trace is also considered (3). In a comparison with a single trace from the GPR-profile at KCI transversal to the slope (see appendix B.2) all major features in Figure 3.30 (discussed below) were present in the traces of both profiles, although differing in relative amplitude.

Regarding ECM (4) and density (5) data, the offset in surface of ≈ 1.6 m (obtained from field measurements) between 2005 (drilling of KCI) and 2008 (GPR measurements) had to be taken into account using equation (3.10).

For the discussion of the comparison, certain regions of interest have been marked with grey bands and labeled with letters A-E:

Region A shows a number of large peaks in (4) and (5). Large ECM-peaks continue below A down to ≈ 14.5 m, corresponding to ca. 1950 AD. A distinct peak appears in (3), although not clearly coherent laterally throughout (1).

Region B is characterized by a pronounced and wide peak in (4) and a more narrow peak in (5). These ice core anomalies correspond to the onset of an IRH in (1-3).

Region C features the deepest continuously traceable IRH in (1-3). Density has almost reached the firn-ice transition and remains somewhat similar to adjacent sections. However, a number of ECM peaks are present in (4).

Region D is just beyond the firn-ice transition. Although coinciding with GPR-peaks for A-C, ECM peaks at depth below the firn-ice transition do not find a respective counterpart in (1-3).

Region E marks the onset of a number anomalies in (3) between 40 and 50 m. Below 50 m, influence from bedrock-reflection is present. It seems worth noting that the uppermost anomaly, somewhat coincides with the by far largest sulphate peak detected in KCI, located roughly at (41.1–41.2) m below the 2008 surface. This large sulphate anomaly is expected to be of volcanic origin, since a respective equal peak in calcium (indicating mineral dust) is absent. The sulphate concentration reaches ≈ 2.5 ppm causing a meltwater conductivity of $\approx 7\mu\text{S}/\text{cm}$, which is above the typical background of meltwater conductivity by a factor of 5 [Bohler, 2008]. In spite of this outstanding event in the ice core record, however, no coherent signal is seen in (1).

The largest GPR-reflector (region B in Figure 3.30) is observed in the slope-parallel as well as transversal GPR-profile and coincides with a wide density anomaly in KCI. Interestingly, this density anomaly is missing in KCO, located in 2 m distance, which indicates a substantial spatial variability in such anomalies. KCO also features a narrow but large peak in DEP-conductivity, which corresponds with the ECM-peak in KCI around 14 m. Below ≈ 14.5 m or 1950 AD, the ECM-baseline is much lower, corresponding to the alkaline background lacking the recent acid deposition. In this region, somewhat smaller but distinct ECM-peaks still appear frequently over broad depth intervals, as in (D). This pattern is seen in the KCS-ECM profile throughout pre-industrial depths and can thus be expected to continue at KCI also below 37 m. However, no match

for the pronounced ECM-peaks ((D) and below) could be detected in the GPR-signal.

3.7.3 Critical assessment and future perspective

The results from the pilot study in borehole-radar motivate further effort to retrieve the remaining basal ice at KCI, and to investigate the crystal orientation fabric of the KCI ice core. The findings of the borehole tomography survey may serve as a reference not only for the ice core investigations but also for further evaluation of internal reflections found in seismic measurements [Diez, 2010]. While the VRP-setup appears limited regarding its uncertainties, especially from the unknown antenna position inside the borehole, the borehole tomography array seems promising to obtain velocity information with depth. In contrast to uncertainties associated with potential borehole inclination, the substantial resolution limit in v_{int} could be further reduced by interpolating the recorded data as to facilitate a more precise detection of the first maximum of the direct wave. A computation of a mean velocity over increasing depth intervals from a certain starting point (e.g. the uppermost) seems also interesting, as to investigate the resulting average velocity for trends. Obtaining a complete depth-profile including the firn part would require a new BT-measurement, where special care should be assigned to high resolution data recording and a proper time window. A continuous recording of data while steadily lowering the antenna inside the borehole at constant speed may supplement measurements at discrete intervals for better spatial resolution.

The comparison of physical ice properties with local GPR-traces clearly demonstrates the different frequency structures in both data sets. This is especially evident in comparison with the ECM-data. The CG ECM profiles feature a large abundance of distinct peaks occurring at high frequency, which can not be resolved by GPR, dedicated to the decimeter-to-meter scale, depending on frequency [Navarro and Eisen, 2009]. In this respect, the better correspondence of GPR reflector with ECM-data from polar ice cores comes as no surprise, since in polar cores, large ECM anomalies are distinctly separated by several meters over large depth intervals [Hempel *et al.*, 2000]. Moreover, the comparison of density profiles from the KCI and KCO ice cores drilled 2 m apart reveals a pronounced spatial variability introducing additional noise and further reducing the dielectric contrast seen by GPR. While GPR with a lower frequency features a larger penetration depth but also a greater spatial averaging by the respective wavelet, the above mentioned fundamental shortcomings do also apply, and a similar IRH-free zone was observed accordingly by Böhlert [2005].

Based on dielectric ice core profiles, GPR and ice core properties could be compared more adequately by means of forward modelling of synthetic GPR traces. As mentioned above, DEP-measurements were performed on the firn-core KCO only. A complete dielectric profile of the down-to-bedrock KCI would allow for extending forward modelling to the entire depth range. The results would be of special interest for further investigating the influence of acidity within the ice-part, especially the large volcanic

signature is detected in KCI chemical impurities. For a better understanding of the ECM signal in the CG ice cores from a dielectric perspective, a comparison with dielectric data obtained from the same ice core appears feasible. To this end, it would be desirable to complete ECM measurements over the entire KCI. With respect to these requirements, the DEP-technique can not be readily applied, as it requires an entire cylindrical ice core sample, whereas for KCI, only a residual fraction of the cross-section is available.

Although no definite explanation for the depth limitation of IRHs can be given so far, the present survey not only indicates potential contributions by borehole GPR but also illustrates the need for dielectric measurements, directly on ice cores and at the decimeter scale. Approaching the latter task with an alternative measurement technique is the topic of the next chapter.

4 The Permittivity of Ice in the MHz-range

4.1 Introductory remarks

Precise knowledge of the dielectric properties of ice in the MHz-range is of central importance for the analysis of ground-penetrating radar data from glaciers and ice sheets. In the wide-spread use of GPR for investigating the internal structure of polar ice sheets, identifying the physical cause of an internal reflection allows to extrapolate the respective ice property over the comparatively large spatial distances (e.g. Hempel *et al.* [2000]; Matsuoka *et al.* [2003]; Jacobel and Welch [2005]). Within this context, the complex valued permittivity is the essential material parameter in two ways: It depends on physical ice properties and determines the propagation speed, reflection and attenuation of radio waves in ice. Hence, the dielectric permittivity provides the fundamental link between ice cores and GPR.

However, in the range of radio-frequencies, present knowledge on the permittivity of ice relies on sparse data associated with large uncertainties [Fujita *et al.*, 2000]. Thus, it cannot be determined at this stage if the observed scatter in the sparse data stems from experimental errors or from actual dispersion in the MHz-range. Compensating for this uncertainty by using standard values for the wave speeds in travel-time–depth conversion can lead to relative depth errors of several per cent, even when accounting for the firn-column and temperature variations [Dowdeswell and Evans, 2004]. Consequently, the uncertainty in permittivity alone entails a depth-uncertainty of an internal reflection horizon (IRH) which may be in the order of several tens to hundred meters at larger depths, thereby hampering its interpretation for the synchronisation of ice cores. Dielectric profiling (DEP), routinely employed in polar ice core studies, nowadays allows to account for the contribution of air inclusions in order to determine the permittivity of pure ice only [Wilhelms, 2005]. However, the required transfer of DEP-data from kHz- to GPR-frequencies is basically flawed by insufficient permittivity-knowledge in the MHz-range, not least concerning its exact frequency dependence.

In this context, remedy may be provided by additional laboratory measurements on ice encompassing the MHz-range. At MHz-frequencies, the complex permittivity of pure ice features a very small imaginary part. Thus, the predominant role is played by the (almost frequency-independent) real part, e.g. regarding propagation velocity. Consequently, measurements should focus first on determining the real part at high accuracy. With respect to the background of glaciological research, the envisaged setup should

additionally allow for measuring artificial as well as natural ice samples, e.g. prepared from a cylindrical ice core without melting.

The present part of this thesis is dedicated to approaching this task with laboratory ice measurements using a coaxial transmission line cell originally designed for soil samples. Accordingly, the main goal was to assess the potential of the coaxial transmission line method for permittivity measurements on artificial and also natural ice samples. With respect to the required high accuracy and the broad differences in dielectric characteristics between soil and ice, a substantial refinement of the original setup was inevitable. This task included a dedicated assessment of measurement accuracy and of the permittivity calculation algorithm. The results of the setup refinement and reassessment are presented in section 4.3 below, which is recommended to the reader generally interested in coaxial transmission line measurements on low-loss dielectrics. The reader mainly interested in the results and implications from measurements on artificial and natural ice is advised to focus on sections 4.6 and 4.7, respectively.

The following section 4.2 attempts to provide a concise introduction to the topic, including relevant basics from electromagnetic theory and ice physics, as well as a brief overview on the present state of knowledge regarding the permittivity of ice.

4.2 A brief introduction to the permittivity of ice

4.2.1 Considerations from electromagnetic theory and ice physics

Ice in its prevalent form on earth is a hexagonal crystal with uniaxial symmetry, often referred to as “Ice I_h ”¹⁰. In case of mono crystalline ice, its physical properties depend on the orientation relative to the c-axis, the direction normal to the basal planes. Polycrystalline ice, when including a large number of randomly oriented ice crystals, can be regarded as having bulk isotropic properties.

When subject to an external, time-varying electric field, several processes occur in an ice sample, with their relative contribution depending on frequency (e.g. see Bogorodsky *et al.* [1985]; Petrenko and Whitworth [1999]):

Atomic and electronic polarisation: The electric field leads to polarization effects within the constituent water molecules. This comprises the distortion of electronic as well as molecular charge distributions. The response of these mechanisms is very rapid, which are thus independent of frequency up to ca. 10^{11} Hz.

Orientational polarisation: Due to the permanent dipole moment of the water molecules, there will be a tendency to align the dipoles with the electric field. It is important to note that this dielectric relaxation process essentially goes back to

¹⁰In the following, only Ice I_h is considered.

the density and migration of defects (Bjerrum as well as ionic) within the crystal lattice [Gränicher *et al.*, 1957; Glen and Paren, 1975; Geil *et al.*, 2005]. This effect dominates the interaction of ice with an electric field below the MHz-range (see section 4.2.2).

Conduction: The diffusion of defects also facilitates an ohmic (d.c.) and dielectric conductivity through ice. Ohmic conduction occurs even at zero frequency.

In general, a comprehensive description of any electromagnetic phenomenon in matter is given by the macroscopic Maxwell equations, stated here with \mathbf{E} and \mathbf{H} being the electric and magnetic field, \mathbf{D} and \mathbf{B} the electric and magnetic flux density and ρ and \mathbf{J} the electric charge and flux density, respectively¹¹ (e.g. Jackson [1962]).

$$\nabla \times \mathbf{E} = -\frac{\partial \mathbf{B}}{\partial t} \quad \nabla \cdot \mathbf{D} = \rho \quad (4.1)$$

$$\nabla \times \mathbf{H} = \frac{\partial \mathbf{D}}{\partial t} + \mathbf{J} \quad \nabla \cdot \mathbf{B} = 0 \quad (4.2)$$

In order to obtain a detailed solution, however, the equations in (4.1) and (4.2) need to be supplemented by constitutive relations, which relate the (macroscopic) flux densities to the (microscopic) effective fields. The electromagnetic properties of the material in which the fields exist are expressed through the functional dependence of these constitutive relations. In case of ice, as with many other materials, linear response can be assumed (i.e. a linear relation between \mathbf{D} and \mathbf{E}). However, the dielectric properties of an ice crystal are generally anisotropic and dispersive. Because of the latter, the constitutive relations are conveniently formulated in the frequency-domain:

$$\mathbf{D}(\omega) = \boldsymbol{\varepsilon}^*(\omega) \mathbf{E}(\omega) \quad (4.3)$$

$$\mathbf{H}(\omega) = \boldsymbol{\mu}^*(\omega) \mathbf{B}(\omega) \quad (4.4)$$

with angular frequency $\omega = 2\pi f$. To describe effects related to conductivity $\boldsymbol{\sigma}^*$ equations (4.3) and (4.4) are supplemented by Ohm's law relating current density \mathbf{J} and electric field \mathbf{E} as $\mathbf{J} = \boldsymbol{\sigma}^* \mathbf{E}$. The dielectric permittivity $\boldsymbol{\varepsilon}^*$ is the central parameter of interest here, as it describes the dielectric response of the material (as ice is generally non-magnetic, $\boldsymbol{\mu}^*$ will not be further considered here). Note that for anisotropic media, $\boldsymbol{\varepsilon}^*$ and $\boldsymbol{\sigma}^*$ are not scalar quantities but tensors of rank 2, which is in case of the uniaxial symmetry of ice (for a single crystal):

$$\boldsymbol{\varepsilon}^* = \begin{pmatrix} \varepsilon_{\perp}^* & 0 & 0 \\ 0 & \varepsilon_{\perp}^* & 0 \\ 0 & 0 & \varepsilon_{\parallel}^* \end{pmatrix} \quad (4.5)$$

¹¹As in chapter 3, bold symbols refer to vector quantities, complex valued quantities will be marked with a **,

where ε_{\perp}^* and $\varepsilon_{\parallel}^*$ are the components for the electrical field vector perpendicular and parallel to the c-axis, respectively. Note that for polycrystalline isotropic ice and wavelengths sufficiently larger than the size of individual crystal grains, the macroscopic permittivity amounts to [Fujita *et al.*, 2000]:

$$\varepsilon^* = \frac{2}{3}\varepsilon_{\perp}^* + \frac{1}{3}\varepsilon_{\parallel}^*. \quad (4.6)$$

In the following, effective scalar components will be considered, the results being valid for ε_{\perp}^* and $\varepsilon_{\parallel}^*$ likewise. With time-harmonic electric fields $\mathbf{E} = \mathbf{E}_0 \exp(j\omega t)$, the permittivity is generally complex¹², and is usually reported as a dimensionless quantity ε_r^* , relative to vacuum permittivity ε_0 ¹³:

$$\varepsilon^*(\omega) = \varepsilon_0 \varepsilon_r^*(\omega) = \varepsilon_0 (\varepsilon_r'(\omega) - j\varepsilon_r''(\omega)) \quad (4.7)$$

with the imaginary unit $j = \sqrt{-1}$. It is important to note that $\varepsilon_r'(\omega)$ and $\varepsilon_r''(\omega)$ may depend not only on frequency, but also on additional parameters, e.g. temperature. The use of complex quantities is convenient as it allows to include a description of conductivity in a generalized effective complex permittivity $\varepsilon_{\text{eff}}^*$, as with Ohm's law it follows from Maxwells equations that:

$$\nabla \times \mathbf{H} = \mathbf{J} + \frac{\partial \mathbf{D}}{\partial t} = \sigma^* \mathbf{E} + j\omega \varepsilon^* \mathbf{E} = j\omega \varepsilon_0 \left(\varepsilon_r^* - \frac{j\sigma^*}{\omega \varepsilon_0} \right) \mathbf{E} = j\omega \varepsilon_{\text{eff}}^* \mathbf{E} \quad (4.8)$$

Note that its is basically also possible to likewise define a generalized conductivity function σ_{eff}^* [Wagner *et al.*, 2011]. As ice generally behaves as a dielectric, $\varepsilon_{\text{eff}}^*$ is used here to include a separate representation for ohmic (d.c.) conductivity with $\sigma^* = \sigma \in \mathbb{R}$:

$$\varepsilon_{\text{eff}}^* = \varepsilon_0 \left(\varepsilon_r' - j \left(\varepsilon_r'' + \frac{\sigma}{\omega \varepsilon_0} \right) \right). \quad (4.9)$$

In a general physical interpretation of $\varepsilon_{\text{eff}}^*$,

- its real part, $\varepsilon_{\text{eff}}'$, describes the above mentioned various molecular polarization mechanisms, i.e. the displacement of internal charge distributions.
- the imaginary part, $\varepsilon_{\text{eff}}''$, describes dissipative losses. It is important to note that two different physical loss-mechanisms are involved: Ohmic losses are due to conduction currents and occur even at zero frequency. Dielectric losses, however, require a time-dependent field, converting electromagnetic into thermal energy due to friction involved in polarization. The relative strength of the losses is usually expressed as the loss tangent:

$$\tan \delta = \varepsilon_{\text{eff}}'' / \varepsilon_{\text{eff}}'.$$

¹²Note that for conductivity σ^* analogue expressions to equations (4.5), (4.6) and (4.7) can be formulated, σ^* generally also being a complex, tensorial quantity.

¹³the same is valid for permeability $\mu^* = \mu_r^* \mu_0$ with relative permeability μ_r^* and permeability of vacuum μ_0

4.2.2 General ice characteristics up to GHz-frequencies

Due to the permanent dipole moment of the water molecule, the permittivity of ice is high at very low frequencies, for which almost all dipoles are aligned with the electric field (the so-called “static” permittivity). For very high frequencies, the apparent dipole reorientation caused by defect migration cannot follow the electric field, and thus the permittivity will be determined by atomic and molecular polarisation alone (the high-frequency limit permittivity). The transition between these limits is characterised by the “relaxation frequency”, f_r , which is related to the kinetics of the defect migration. For pure ice, f_r typically lies in the low- to mid-kHz-range, dependent on temperature and impurity concentration (e.g. see Auty and Cole [1952]; Gränicher *et al.* [1957]; von Hippel *et al.* [1972]; Mätzler and Wegmüller [1987]). Consequently, the permittivity of ice is dominated up to MHz-frequencies by the general relaxation behaviour characteristic for materials with permanent dipole moment (for more details see the reviews by Johari [1981]; Warren [1984]; Fujita *et al.* [2000]).

Although somewhat phenomenological with respect to the underlying mechanisms in ice, this relaxation behaviour can be described in the frequency-domain with the Debye model [Debye, 1929; Bogorodsky *et al.*, 1985; Petrenko and Whitworth, 1999]:

$$\varepsilon_r(\omega) = \varepsilon_\infty + \frac{\varepsilon_{\text{static}} - \varepsilon_\infty}{1 + j\omega\tau} \quad (4.10)$$

with real and imaginary part:

$$\varepsilon'_r(\omega) = \varepsilon_\infty + \frac{\varepsilon_{\text{static}} - \varepsilon_\infty}{1 + \omega^2\tau^2}, \quad \varepsilon''_r(\omega) = \omega\tau \frac{\varepsilon_{\text{static}} - \varepsilon_\infty}{1 + \omega^2\tau^2} \quad (4.11)$$

Here, parameters (all $\in \mathbb{R}$) are: $\tau = \frac{1}{2\pi f_r}$ the relaxation time, f_r the relaxation frequency, ε_∞ the relative high-frequency-limit permittivity and $\varepsilon_{\text{static}}$ the relative¹⁴ static permittivity. The Debye-model for the permittivity of ice is shown in Figure 4.1, with a closer look at the MHz-range on its right hand side. Following the Debye-picture, the general dielectric characteristics of ice at MHz-frequencies can be summarized as follows:

- Above the high frequency end of the Debye-relaxation, the real part of the permittivity is determined by the contribution of atomic and electronic polarisation which remain frequency independent far into the GHz-range and thus: $\varepsilon'_r(\omega) = \varepsilon_\infty$
- Beyond the Debye-relaxation (i.e. for $f > f_r$), the imaginary part decreases with frequency as $\varepsilon''_r \propto f^{-1}$ and becomes very small, typically around 10^{-2} . It reaches a minimum around 1 GHz, where it starts to rise again due to the infrared absorption.
- Consequently, pure ice is a pronounced low-loss dielectric in the MHz-range.

¹⁴For the sake of clarity, the subscript r will be omitted for these quantities

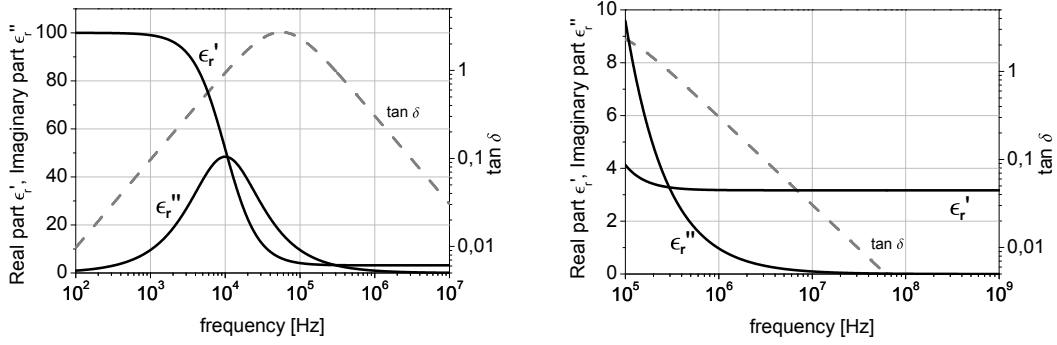


Figure 4.1: Debye-model of the permittivity of ice, up to 10 MHz (left) with an additional plot covering the MHz-range (right). Real and imaginary parts are shown as black curves, the grey dashed curve indicates the loss tangent. Typical values were used for the Debye-parameters: 100, 3.17 and 10 kHz for ϵ_{static} , ϵ_{∞} and f_r , respectively. No d.c.-conductivity σ was considered, as it only affects the low-frequency characteristics of ϵ_r'' [Moore and Fujita, 1993].

4.2.3 Implications for the interaction of ice with electromagnetic radiation

The dielectric permittivity plays a central role in describing the propagation of an GPR-signal in ice. Due to the low-loss dielectric characteristic of ice, the (phase) propagation speed v of the GPR-signal can be calculated as [Bogorodsky *et al.*, 1985]:

$$v = \frac{c_0}{\sqrt{\epsilon_r'}} \quad (4.12)$$

where c_0 denotes the speed of light in vacuum.

For non-magnetic media (like ice), complex permittivity ϵ^* and complex refractive index n^* are connected as: $n^* = \sqrt{\epsilon^*}$. Thus, the amplitude reflection coefficient R for perpendicular incidence of the GPR-wave on a boundary between two layers of different permittivities in the ice (denoted by indices 1 and 2, respectively) is:

$$R = \frac{n_1^* - n_2^*}{n_2^* + n_1^*} = \frac{\sqrt{\epsilon_1^*} - \sqrt{\epsilon_2^*}}{\sqrt{\epsilon_2^*} + \sqrt{\epsilon_1^*}} \quad (4.13)$$

From this expression it becomes evident that generally, a distinct change in ice permittivity will cause a reflection of the GPR wave and thus an IRH. For small changes in ϵ^* due to changes in real and imaginary part, simplified expressions exist to calculate R (and thus also the power reflection coefficient $PRC = PRC(|R|^2)$) [Paren and Robin, 1975; Paren, 1981; Fujita and Mae, 1994]. In glaciers and ice sheets, three physical ice properties have been identified to produce internal reflections by causing respective changes in ϵ^* (e.g. Fujita *et al.* [2000]):

1. Density: Snow, firn and to some extent glacier ice, can be regarded as mixture of the dielectric materials air and pure ice where density ρ basically renders the volume fraction of ice. This mixture between air and ice can be treated as a two-phase composite. The effective real relative permittivity of the composite ε'_c is expressed as a power law with the permittivities ε'_i of the constituent phases [Roth *et al.*, 1990]:

$$\varepsilon'_c{}^\alpha = \sum_i \nu_i \varepsilon'_i{}^\alpha, \quad (4.14)$$

where ν_i is the volume fraction of phase i and $\alpha \in [-1, 1]$. The influence of density variations on the permittivity of firn and ice has been studied in detail theoretically and empirically [Glen and Paren, 1975; Kovacs *et al.*, 1995; Wilhelms, 2005]. Following Looyenga [1965], who proposed a power law for the permittivity of heterogenous mixtures based on spherical inclusions, i.e. equation (4.14) with $\alpha = 1/3$, firn is treated as a mixture of ice and air [Glen and Paren, 1975]:

$$\varepsilon'_F = ((\varepsilon_I'^{1/3} - \varepsilon_A'^{1/3})\nu_I + \varepsilon_A'^{1/3})^3, \quad (4.15)$$

with ν_I being the ice volume fraction and the indices F, I, A indicating firn, ice and air, respectively. As pointed out by Wilhelms [2005], equation (4.15) may also be used for complex permittivities, although the direct influence of density variations on ε''_r is negligible compared to ε'_r [Fujita *et al.*, 2000]. Kovacs *et al.* [1995] used equation (4.14) with $\alpha = 0.5$ to fit empirical data and derived a relation that is nowadays widely used to describe the density-dependency of ε'_r :

$$\varepsilon'_r = \left(1 + 0.845 \frac{\text{cm}^3}{\text{g}} \rho\right)^2 \quad (4.16)$$

Note that equations (4.12) and (4.16) lead to equation (3.2) used to calculate wave speeds in chapter 3.

2. Acidity: The permittivity of ice in presence of acidity, e.g. from snow containing aerosols, deposited after volcanic eruptions, has been the subject of a number of semi-empirical and theoretical investigations [von Hippel *et al.*, 1972; Glen and Paren, 1975; Champlin *et al.*, 1978; Gross *et al.*, 1978; Nagle, 1979]. Laboratory measurements of the permittivity of acidity-doped ice have been performed at various frequencies (e.g. Gross *et al.* [1978]; Fujita *et al.* [1992]; Moore [1993]). The doping of ice with acids such as hydrofluoric (HF) and hydrochloric (HCl) acid results in an increase of defects in the ice lattice. The according rise in conductivity evidently affects the imaginary part of ε^* (equation (4.9)). However, the real part ε'_r was also found affected, and to depend linearly on the acid concentration, with the gradient itself being frequency dependent [Matsuoka *et al.*, 1996, 1997a]. As pointed out by Fujita *et al.* [2000], the effect of acidity on ε' potentially stems from interfacial polarisation (Maxwell-Wagner-effect) and from the presence of liquid acid-water mixture above the respective eutectic point (the

latter was also suggested by Wolff and Paren [1984] for polar ice).

3. Dielectric anisotropy: For the imaginary part, anisotropy could only be detected up to the high frequency Debye tail, however not at microwave frequencies [Fujita *et al.*, 2000]. For the real part, Matsuoka *et al.* [1997b] concluded from their measurements at 1 MHz and 39 GHz that a frequency independent anisotropy $\Delta\epsilon' = \epsilon'_{\parallel} - \epsilon'_{\perp}$ of a little more than 1% exists- in agreement with an earlier study at 9.7 GHz by Fujita *et al.* [1993]. Fujita and Mae [1994] showed that internal reflections are possible due to changes in crystal-orientation fabrics (COF). Recently, direct evidence for a continuous GPR-reflector caused by changes in COF were reported by Eisen *et al.* [2007].

It is important to note that the reflections based on (1.) and (3.) go back to variations in the real part in permittivity, which is allegedly constant at radio-frequencies. Consequently, the amplitude of the complex reflection coefficient is independent of frequency used for GPR. In contrast, the amplitude of reflections from (2.) stem from changes in ϵ'' and are thus basically inversely proportional to frequency. Moreover, only reflections from (2.) show a distinct temperature dependency. Elaborate multi-frequency GPR-experiments aim at identifying the origin of an IRH by exploiting these different frequency dependencies [Fujita *et al.*, 1999; Fujita *et al.*, 2006]. Within the context of these sophisticated GPR-measurements, a precise knowledge of the real part in the MHz-range becomes important, including the potential small frequency dependence of $\epsilon'_r(\omega)$.

4.2.4 Permittivity measurements on ice in and around the MHz-range

As mentioned above, the imaginary part ϵ''_r of ice is very small within the MHz-range. As a result, precise absolute measurements of ϵ''_r are difficult and were not intended within the present work. Accordingly, the following overview focuses on the real part ϵ'_r .

Figure 4.2 shows a compilation by Fujita *et al.* [2000] of the knowledge on ϵ'_r around the MHz-range (before this study). In the kHz-range, data on the permittivity of ice mainly stem from dielectric profiling (DEP, see Moore and Paren [1987]; Moore *et al.* [1989]; Moore [1993], Wilhelms [2000]) and other capacitive measurement techniques on coaxial or disk-shaped ice samples [Auty and Cole, 1952; Gough, 1972; Matsuoka *et al.*, 1996; Fujita *et al.*, 2000]. In the GHz-range, the permittivity of ice is typically measured with the resonator method (e.g. by Matsuoka *et al.* [1997b] with an open resonator and by Matsuoka *et al.* [1997a] with a cavity resonator). Mätzler and Wegmüller [1987] additionally used a radiometric method (at 10–100 GHz) and Fujita *et al.* [1993] the standing wave method in a waveguide at 9.7 GHz. For frequencies adjacent to radio

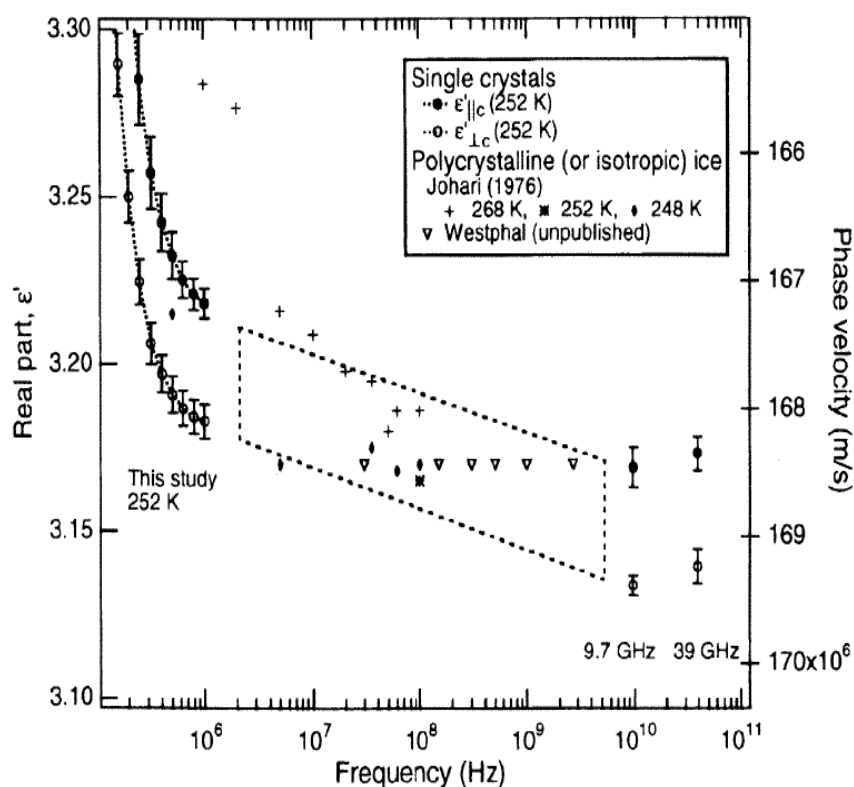


Figure 4.2: Compilation of available data on the permittivity of ice at MHz-frequencies. The decrease at frequencies below 1 MHz is the high frequency end of the Debye-dispersion (Figure 4.1). Note the distinct anisotropy of ca. 1% and the gap from 1 MHz to ≈ 10 GHz with only sparse data without uncertainty estimates. Figure from Fujita *et al.* [2000].

frequencies (i.e. 500 kHz–1 MHz and 9.7 GHz), these laboratory measurements are typically associated with less than 1% relative uncertainty [Fujita *et al.*, 2000].

Measuring velocities of radio waves in a borehole [Robin, 1975] or wide angle radar measurements [Jezek *et al.*, 1978] allow for permittivity measurements in-situ. However, these measurements in principle average over a comparatively large sample volume and the respective natural variability. Laboratory data sets are especially sparse from 1 MHz to ≈ 10 GHz. Johari [1976] used a two-port coaxial capacitor as a dielectric cell with an RX-meter for measurements up to 100 MHz and reports uncertainties between 0.3-2%. A similar setup was used by Johari and Charette [1975] for measurements at 35 and 60 MHz. Between 100 MHz and 1 GHz present knowledge relies on measurements made by Westphal, which were reported in Evans [1965], however without details on the measurements and associated uncertainties.

From these data, the high frequency end of the Debye-dispersion (cf. Figure 4.1) appears at frequencies below 1 MHz in Figure 4.2. Precise and well documented measurements start again at 9.7 GHz and are found significantly lower than at 1 MHz by at least

0.04, indicating a small dispersion. At the present stage, it remains unclear as to what extent the difference in ε_r' between 1 MHz and 9.7 GHz can be explained solely with the Debye-dispersion extending into the MHz-range. The distinct anisotropy of ca. 1% has not been observed at MHz-frequencies, although precisely measured below 1 MHz and in the GHz-range.

A valuable contribution from a new attempt at laboratory ice measurements would stem from a technique allowing for (i) frequency-dependent measurements encompassing the MHz-range and (ii) high accuracy for the real part (around 1%). With respect to envisaged later application of this technique in glaciological research, additional requirements arise from the need to not only measure pure, artificial but also natural (i.e. glacier-) ice samples: (iii) Sample volume has to be large enough and thus representative with respect to typical wavelength involved in electromagnetic remote sensing (i.e. on the decimeter-scale). (iv) Natural ice samples (e.g. from ice cores) must not be melted in order to preserve their unique properties regarding air-inclusions, location of impurities in the grain-boundary network and crystal orientation. With a suitable measurement setup, the following central questions are to be addressed:

- What is $\varepsilon_r'(\omega)$ of pure ice at MHz-frequencies? Is this information consistent with existing values, especially with the observed offset between values at 1 MHz and 9.7 GHz (cf. Figure 4.2)?
- Are there systematic differences between artificial and natural ice samples?
- What is the influence of density, acidity and crystal orientation on ε_r' at MHz-frequencies?

Specifically dedicated to addressing these questions with respect to requirements (i-iv), the present study is aiming at investigating the potential of the coaxial transmission line cell technique for ice measurements.

A large coaxial cell transmission line developed by Oswald [2000] was established at the Institute of Environmental Physics (IUP) in 2005 for measurements of soil samples and high-loss materials. From soil physical applications, coaxial transmission line cells were introduced by Topp *et al.* [1980] for one port time domain reflectometry (TDR) measurements on different soil types. In investigations by Shang *et al.* [1999]; Rowe *et al.* [2001]; Gorriti and Slob [2005a]; Wagner *et al.* [2007] and Wagner *et al.* [2011] two-port coaxial transmission line cells in combination with a vector network analyzer technique were used to determine the frequency dependent complex permittivity of soils in the MHz-range. In these soil-related studies, the focus lies on an accurate determination of dispersion and absorption of electromagnetic waves rather than the determination of low permittivities of lossless materials with high accuracy [Wagner *et al.*, 2011]. However, as pointed out by Baker-Jarvis *et al.* [1990] in investigations on PTFE (Teflon) and Folgero [1996] and Folgero [1998] on low-loss liquids, the coaxial transmission line cells are also adequate for the determination of frequency dependent permittivity of low-

loss materials. Fujita *et al.* [2000] reported the use of a coaxial transmission line cell to investigate the influence of acidity on ε'_r of ice samples between 100–600 MHz. For zero acidity, however, their measurements resulted in ε'_r between 3.0 and 3.2, and could thus not provide additional information regarding the present state of knowledge shown in Figure 4.2.

Consequently, the present study aimed at adapting the IUP coaxial cell transmission line setup for measuring ε'_r of ice at high accuracy. As a first step, this includes the need for a detailed assessment of the setup's measurement characteristics.

4.3 Coaxial Transmission Line Cell Measurements

4.3.1 The Setup

The three main parts of the coaxial setup were manufactured at the IUP comprising the main cylindrical sample holder (length 20 cm) and two conic transition units. The inner and outer diameter ($d_{\text{in}} = 26$ mm, and $d_{\text{out}} = 60$ mm) yield a 50Ω impedance for the empty sample holder. The diameters of the conic transition units decrease accordingly to maintain the 50Ω impedance. The setup is connected to the two ports of an Agilent ET 8714 vector network analyzer (NWA) via two standard 7/16–N adapters and RG 58 coaxial cables. The general principle of a permittivity measurement with this setup is as follows:

- Inserting a dielectric material into the sample holder will change the impedance of this transmission line segment. Consequently, the electromagnetic wave travelling through the transmission line will be partially reflected at the planes where impedance jumps occur.
- The reflection/transmission behaviour of the setup is characterised with the NWA by measuring so-called “scattering parameters” (S-parameters). For a two-port network (such as the present setup), S-parameters can be written as a matrix:

$$\begin{pmatrix} b_1 \\ b_2 \end{pmatrix} = \begin{pmatrix} S_{11} & S_{12} \\ S_{21} & S_{22} \end{pmatrix} \begin{pmatrix} a_1 \\ a_2 \end{pmatrix}. \quad (4.17)$$

Here, the indices 1 and 2 refer to the respective port at the NWA (Figure 4.3). The vector $\mathbf{a} = (a_1, a_2)$ represents the electromagnetic waves incident on the sample holder from the respective port side. Similarly, the vector $\mathbf{b} = (b_1, b_2)$ represents the waves reflected from the sample holder to the respective port. Thus, \mathbf{b} may be regarded as the response of the transmission element upon electromagnetic excitation by \mathbf{a} . The scattering behaviour, and thus the response, can be characterized by the respective S-parameters. The parameters S_{ii} ($i = 1, 2$) represent reflection, and S_{ij} ($i = 1, 2; j = 1, 2, i \neq j$) transmission¹⁵, respectively (e.g. S_{21} character-

¹⁵If not stated otherwise, S_{ij} will always imply $i \neq j$ in the following.

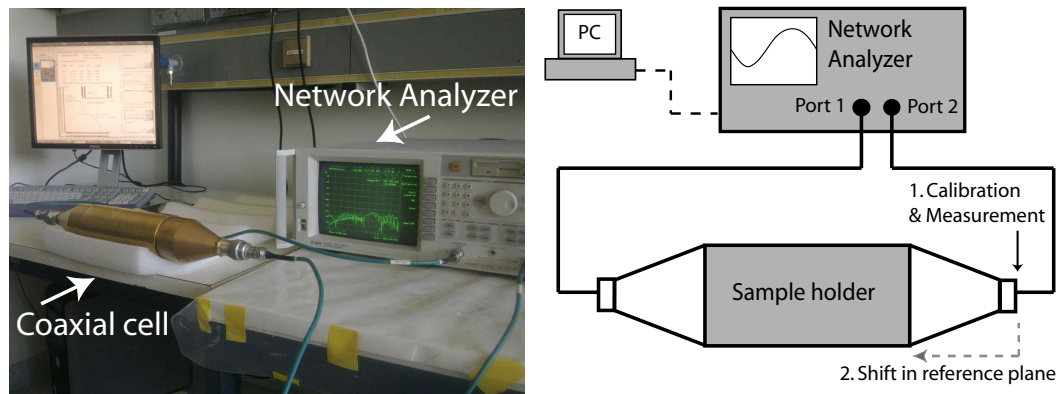


Figure 4.3: The IUP coaxial cell setup. Left: Picture of the setup. Right: Schematic view of the coaxial setup. The sample holder contains the dielectric probe. Each end of the sample holder is connected to the respective port of the Agilent ET8714 Network analyzer via a conical coaxial transition unit, a 7/16-N connector and a standard RG58 coaxial cable. After calibration, measurement and shift of reference planes, permittivity is inferred from S-parameters by means of an optimisation algorithm.

izes the response at port 2 due to a signal at port 1). It is important to note that, although the term “parameters” might suggest a scalar, S-parameters are actually frequency-dependent as well as complex quantities (the electromagnetic waves, a and b are also complex). For more details refer to a respective textbook (e.g. Zhang and Li [2008])

- Based on the scattering parameters measured with the NWA, the frequency dependent permittivity of the sample is inferred by means of an optimisation algorithm: A modified Debye-type relaxation model is assumed and used for forward modelling of S-parameters. Using a genetic optimisation routine, the Debye-model is adjusted to minimize the difference between measured and forward modeled S-parameters [Oswald *et al.*, 2006]. A detailed assessment of this permittivity computation including a comparison with alternative algorithms is given in section 4.4.

4.3.2 Calibration and measurement

Figure 4.4 shows the individual parts of the coaxial cell setup. The inner conductor is supported by Teflon discs. The sample holder is sealed watertight by rubber sealings facilitating measurements on liquids. All parts are connected by screw threads. In general, impedance jumps may arise at discontinuities such as connections between individual parts (which may not be exactly of 50Ω impedance). In order to remove the influence of the coaxial cables and the probe parts from the measured scattering parameters, calibration is performed on the empty cell prior to measurement. To this end, the

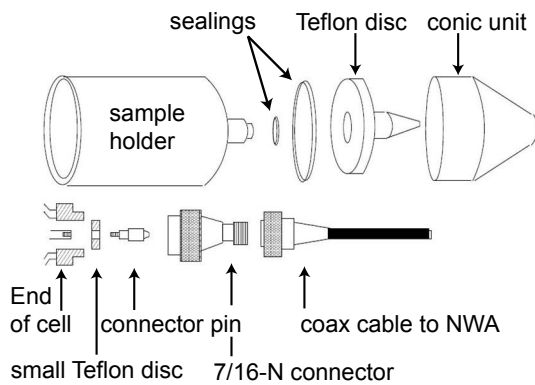


Figure 4.4: Detailed view of the setup components. The inner conductor is supported by four Teflon discs, one at each of the smaller ends of the conical units and one at each end of the sample holder. The sample holder is watertight due to rubber sealings at the inner and outer contacts with the Teflon discs. All components are connected via screw threads. Figure personal communication K.Roth, IUP, subsequently modified.

NWA supplies a 1-port calibration for reflection: Different terminations (open, short, and $50\text{-}\Omega$ -match of the Agilent Calibration Kit 85020E) are connected to the 7/16-N-end behind the coaxial cell and measured. In doing so, the reflection scattering to port 1 of the empty setup is corrected. For transmission, the NWA supplies an enhanced response option, which includes a “through” measurement, with the setup connected to both ports. However, as a calibration from port 2 is omitted, this is not a full 2-port calibration.

In order to still obtain a full set of S-parameters, the entire probe is disconnected from the coaxial cables after measuring reflection S_{11} and transmission S_{21} and reconnected in reversed orientation in order to measure S_{22} and S_{12} of the sample. To account for potential anisotropic scattering behaviour of the cell, a separate calibration is recorded for each direction of measurement through the probe. Reflection measurements are recorded with the match-termination connected to the end of the probe. After calibration, it was ensured that S_{ii} of the empty cell in-between the two coaxial cables remained well below -20 dB, indicating that no major reflections of the setup have been left unaccounted for by calibration. The NWA records S-Parameters between 300 kHz and 3 GHz in a linear sweep. For the subsequent application of the permittivity computation algorithm, a pre-processing routine shifts the reference planes from the end of the probe to the sample holder, where the actual impedance jump due to the measured dielectric occurs (as indicated in Figure 4.3). In the following the above procedure is referred to as the “standard measurement routine”.

4.3.3 Setup refinements

At the beginning of the present study, a number of experimental shortcomings in the setup hampered its deployment for reliable ice measurements. Neither reproducible measurements nor a meaningful application of the permittivity calculation algorithm were possible at this stage. Regardless of the measured dielectric (air, water, ethanol),

two major artefacts occurred in the S-Parameters (an example of S-Parameters disturbed by these artefacts is shown in the appendix C.1 — for more details, see Hoppe [2009]):

- An unreasonable large artefact-peak around 1 GHz in S_{ii} , dominant over all other features in the spectrum.
- Time-dependent fluctuating noise, completely masking the signal in S_{ii} and S_{ij} below 500 MHz.

Identifying and eventually overcoming these shortcomings was a labor-intensive, time-consuming process which was not envisaged in the original outline of this work. Here, the consultation with C. Schindler (University of Marburg) and especially N. Wagner (Institute of Material Research and Testing (MFPA), Bauhaus University, Weimar) was crucial and resulted in the following assessment and eventual refinement of the setup: Unscrewing and reassembling the entire probe is necessary for inserting the sample into the sample holder. This can result in a slight alteration of the contacts between the numerous parts (cf. Figure 4.4). Since these changes have not been accounted by the calibration, their scattering effects bias the recorded S-parameters. In the original setup, the contact between the inner conductor and the N-7/16 adapter was flawed and suspected to be the main reason for the above mentioned artefacts. New connector pins were crafted to ensure faultless contacts. Moreover, all parts made of aluminium were replaced by identical brass components, since aluminium oxide within the screw threads can produce additional flawed contacts (pers. communication, C. Schindler). As a result of these modifications, the S-parameter measurements improved to be very stable and reproducible, even after unscrewing and reassembling the probe. However, between 1.5 – 2 GHz, the reproducibility was observed to become somewhat weaker (a detailed examination of this effect is given in section 4.5 below). In a coaxial waveguide, only the TEM-mode¹⁶ can propagate below a certain cut-off frequency in which the electric field is directed perpendicular to the symmetry axis of the cylindrical waveguide. f_{cutoff} depends on the permittivity of the material and the radii of the conductors (outer radius of inner conductor r_{in} and inner radius of outer conductor r_{out}) and can be estimated for non-magnetic material as [Zhang and Li, 2008]:

$$f_{\text{cutoff}} = \frac{c_0}{\pi(r_{\text{in}} + r_{\text{out}})\sqrt{\varepsilon_r'}} \quad (4.18)$$

For the present coaxial cell and assuming $\varepsilon_r' \approx 3.17$ for ice, it was estimated that $f_{\text{cutoff}} \approx 1.3$ GHz. With respect to the envisaged high measurement accuracy and the fact that the used permittivity calculation algorithms (see section 4.4 below) consider TEM-mode propagation only, the measurements were focused on the frequency interval below 1.5 GHz.

Aimed at an in-depth assessment of the refined setup's capability for reliable S-parameter measurements, two additional refinements were developed:

¹⁶TEM: transversal electromagnetic mode

- To allow for routine reference measurements, a hollow Teflon cylinder was crafted to precisely match the sample holder's geometry. Teflon is a low-loss material of constant permittivity of $\varepsilon'_r = 2 - 2.1$ [Riddle *et al.*, 2003]. The similarity in dielectric properties compared to ice in the MHz-range make Teflon an ideal standard with respect to the envisaged use of the setup for ice measurements. The Teflon standard was used to check the reproducibility of our measurements and was routinely measured after calibration.
- To obtain reference S-parameters from solving the forward problem, as well as to study the influence of faults on the S-parameters, a dedicated forward model was developed for the setup.

4.3.4 The forward model

The forward calculation used in the algorithm by Oswald *et al.* [2006] was further extended to simulate the entire setup based on a transmission-matrix approach. Figure 4.5 shows measured (grey line) and forward calculated (grey dashed line) S-parameters S_{11} and S_{12} for the Teflon standard. Note how the transmission line segment is in resonance as reflections $|S_{11}|$ approaches zero at quasi-periodic intervals. A number of features in the measured data remain unexplained by the initially used simple forward calculation:

- the damping and frequency-shift in resonance frequencies in reflection $|S_{11}|$ (plot 'a' in Figure 4.5).
- the high-frequency variability ("ripples") in transmission measurements $|S_{21}|$ (plot 'b' in Figure 4.5).
- the small trends increasing with frequency for $|S_{11}|$ and decreasing for $|S_{21}|$, respectively (plots 'a', 'b' in Figure 4.5).

In order to obtain an at least qualitative understanding of the origin of these artefacts, the forward calculation was extended to simulate the additional components of the assembly (Figure 4.4) in a transmission matrix approach. Alternative to the use of S-parameters (equation (4.17)), two-port networks may be characterized by expressing the inward (\mathbf{a}) and outward waves (\mathbf{b}) at the output port (port 2) in terms of the respective waves at the input port (port 1):

$$\begin{pmatrix} b_2 \\ a_2 \end{pmatrix} = \begin{pmatrix} T_{11} & T_{12} \\ T_{21} & T_{22} \end{pmatrix} \begin{pmatrix} b_1 \\ a_1 \end{pmatrix}, \quad \text{where } T = \begin{pmatrix} T_{11} & T_{12} \\ T_{21} & T_{22} \end{pmatrix} \quad (4.19)$$

is the transmission matrix (T-matrix) comprising the complex T-parameters. The convenient property of T-matrices is that a cascade-connected network can be described by a single T-matrix T equal to the product of the T-matrices of all elementary segments:

$$T = T_1 T_2 \dots T_N. \quad (4.20)$$

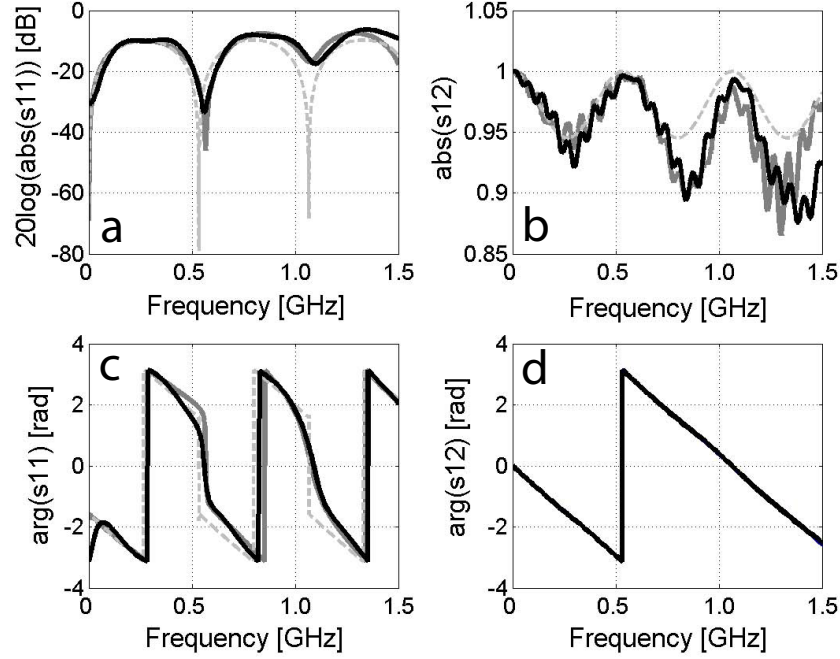


Figure 4.5: Teflon scattering parameters as measured (grey line) compared to the simple (grey dashed line, [Oswald *et al.*, 2006]) and extended forward model (black line, present work). The complex S-parameters are plotted against frequency as absolute value and phase in 'a' and 'c' for reflection $|S_{11}|$, and 'b' and 'd' for transmission $|S_{12}|$, respectively.

Transmission matrices can be converted into S-parameters via the following relation (for more details, see e.g. Zhang and Li [2008]):

$$\begin{pmatrix} S_{11} & S_{12} \\ S_{21} & S_{22} \end{pmatrix} = \frac{1}{T_{11}} \begin{pmatrix} T_{21} & \det(T) \\ 1 & -T_{12} \end{pmatrix}. \quad (4.21)$$

In the forward model, each fixture component is represented by an according transmission matrix of a transmission line segment T_{seg} , considering a potential impedance discontinuity between the components by a transmission matrix for a transmission line connection t_{con} .

$$T_{\text{seg}_p} = \begin{pmatrix} e^{\gamma_p l_p} & 0 \\ 0 & e^{-\gamma_p l_p} \end{pmatrix}, \quad t_{\text{con}_{p \rightarrow q}} = \frac{1}{2\sqrt{Z_q Z_p}} \begin{pmatrix} Z_q + Z_p & Z_q - Z_p \\ Z_q - Z_p & Z_q + Z_p \end{pmatrix} \quad (4.22)$$

with γ_p being the complex propagation factor of transmission line segment p and $Z_{p,q}$ the complex impedance of segment p and q , respectively. Transmission line theory yields

the following general equations for γ and Z ¹⁷,

$$\gamma = \sqrt{(R' + j\omega L')(G' + j\omega C')}, \quad Z = \sqrt{\frac{R' + j\omega L'}{G' + j\omega C'}}, \quad (4.23)$$

resistance R' , inductance L' , conductance G' and capacitance C' are determined by the geometry of the transmission line and the dielectric material properties $\varepsilon^* = \varepsilon_0(\varepsilon_r' - j\varepsilon_r'')$ and $\mu^* = \mu_r^* \mu_0$ ¹⁸.

$$\begin{aligned} L' &= \frac{\mu}{2\pi} \ln\left(\frac{r_{\text{out}}}{r_{\text{in}}}\right) & C' &= \frac{2\pi\varepsilon_r'\varepsilon_0}{\ln\left(\frac{r_{\text{out}}}{r_{\text{in}}}\right)} \\ R' &= \frac{1}{2\pi} \left(\frac{1}{r_{\text{out}}} + \frac{1}{r_{\text{in}}}\right) \sqrt{\omega\mu\sigma/2} & G' &= \frac{2\pi}{\ln\left(\frac{r_{\text{out}}}{r_{\text{in}}}\right)} (\varepsilon_r''\varepsilon_0\omega + \sigma). \end{aligned} \quad (4.24)$$

The initially used forward calculation of Oswald *et al.* [2006] considers the sample holder only (cf. Figure 4.3) and can be expressed in transmission matrix formulation accordingly as:

$$T_{\text{holder}} = t_{\text{con1}} T_{\text{sample}} t_{\text{con2}}. \quad (4.25)$$

The forward calculation was extended to the setup components on the right hand side of the sample holder (cf. Figure 4.4), including transmission matrices for the Teflon disc T_{tef} , the conic coaxial connector T_{cone} and the 7/16-N adaptor T_{N} and the respective connecting matrices t_i , numbered in consecutive order. Since the left hand side of the sample holder is made up by identical components, at first only the right hand side was considered in order to keep the introduced parameters to a minimum. The T-matrix of the coaxial probe¹⁹ T_{probe} can thus be expressed as (going from left to right):

$$T_{\text{probe}} = T_{\text{holder}} T_{\text{tef}} t_{\text{con3}} T_{\text{cone}} t_{\text{con4}} T_{\text{N}} \quad (4.26)$$

The transmission matrix expression for the total setup, T_{tot} , depends on the different terminations used for reflection and transmission measurements via the T-matrix of the 50 Ω matched termination, T_{match} , or the connecting cable to port 2, T_{cable} , respectively:

$$\text{Reflection:} \quad T_{\text{tot}} = T_{\text{probe}} t_{\text{con5}} T_{\text{match}} \quad (4.27)$$

$$\text{Transmission:} \quad T_{\text{tot}} = T_{\text{probe}} t_{\text{con5}} T_{\text{cable}} t_{\text{con6}} \quad (4.28)$$

The forward calculated transmission matrices are then converted into S-parameters via equation (4.21). The extended forward model was deployed to qualitatively study the

¹⁷Quantities per unit length of transmission line are primed ($'$). With angular frequency $\omega = 2\pi f$, imaginary unit $j = \sqrt{-1}$ and d.c. conductivity σ .

¹⁸Here, in case of non-magnetic ice and Teflon $\mu_r^* = \mu_r = 1$ and hence $\mu^* = \mu = \mu_0$

¹⁹In this context, the term ‘‘probe’’ refers to the setup components within the coaxial cell and the conical units (see Figure 4.4), i.e. excluding the coaxial cables.

influence of changing the propagation characteristics (γ_i , Z_i) of the setup components on the S-parameters. The complexity of the model was increased stepwise, starting with lossless, 50Ω characteristics for all components. A single impedance mismatch at one of the setup components in the model already reproduces the observed damping and slight shift in resonance frequencies in reflection (e.g. compare S_{11} in Figure 4.5). If the coaxial cable behind the probe is assigned a nonzero length in the model, the observed “ripples” are reproduced in the forward calculated transmission S-parameters (e.g. compare S_{12} in Figure 4.5). This indicates that the “ripples” result from the lack of a full 2-port calibration, and the fact that the second coaxial cable necessary for transmission measurements is not completely accounted for by the standard measurement routine (see section 4.3.2). An exemplary result of the forward model is shown as the black curve in Figure 4.5, which is in good agreement with the actual measured S-parameters (a detailed description of the model code is given in the appendix D). In summary, although it is not possible to pinpoint the exact origin of the artefacts in the probe components, it becomes evident from the forward model based investigation that they are not part of the signal from the dielectric sample.

4.4 Permittivity computation from S-parameters

In order to investigate on the influence of the above mentioned artefacts on permittivity calculation and to validate the application of the Debye-based optimisation to low-loss materials, a comparison to other dedicated permittivity computation algorithms is called for. Within the present thesis, a close cooperation was started with N. Wagner²⁰ (MFPA Weimar), whose support included providing the alternative permittivity computation algorithms used in the following (BJI, CCPM, see below). Moreover, for additional validation, measurements on Teflon and artificial ice were performed at the MFPA Weimar using the IUP coaxial cell setup (section 4.4.2). By this means, a detailed performance assessment of the setup and the Debye-based algorithm was obtained. The results of this assessment are presented in the following.

4.4.1 Overview

For a brief overview on how the frequency dependent permittivity can generally be calculated from S-parameters measured with a coaxial transmission line, the existing techniques can be roughly divided into two categories:

²⁰in the framework of the DFG project Wa-2112/2-1 concerning dielectric relaxation studies on fine grained soil.

Quasi-analytical

Quasi-analytical techniques are used to obtain the complex impedance Z_S or complex propagation factor γ_S of a coaxial transmission line from measured S-parameters. As shown in Gorriti and Slob [2005c], the different approaches (assuming propagation in TEM mode in an ideal coaxial transmission line) all lead to one of the following relations linking Z_S and γ_S to the relative complex permittivity ε_r^* of a non-magnetic sample [Nicolson and Ross, 1970; Baker-Jarvis *et al.*, 2004; Gorriti and Slob, 2005b; Wagner *et al.*, 2010]:

$$\varepsilon_r^* = \left(\frac{Z_0}{Z_S} \right)^2, \quad \varepsilon_r^* = \left(\frac{c_0 \gamma_S}{j\omega} \right)^2, \quad \varepsilon_r^* = \frac{c_0 Z_0}{j\omega} \left(\frac{\gamma_S}{Z_S} \right). \quad (4.29)$$

Herein Z_0 is the characteristic impedance of the empty transmission line and c_0 the speed of light in vacuum. However, Baker-Jarvis [1990] derived equations for the determination of the broadband electromagnetic material properties with coaxial transmission line cells and revisited the classical quasi-analytical algorithm according to Nicolson and Ross [1970] and Weir [1974] (NRW). On this basis, an iterative inversion technique, called BJI, was introduced [Baker-Jarvis *et al.*, 2004; Baker-Jarvis, 1990; Baker-Jarvis *et al.*, 1990]. The BJI method can be applied to all S-parameters separately or simultaneously. The drawbacks of the BJI are the high sensitivity to uncertainties of the cell design or used calibration as well as the necessary starting guess to ensure stable convergence. A brief overview on the computational principles of the BJI-algorithm used within the present chapter is given in the appendix C.2.

Forward model based

These inverse modelling techniques are based on the numerical calculation of S-parameters with a forward model (mostly TEM based). The model considers the used coaxial transmission line cell in combination with a Debye-type relaxation function [Oswald *et al.*, 2006], a generalized dielectric relaxation model (GDR, [Wagner *et al.*, 2007, 2011]) or a broadband transfer function (complex conductivity and permittivity model (CCPM), [Börner, 2006; Wagner *et al.*, 2007, 2011]) for the expected permittivity. The advantage of the techniques of this category is that unrealistic results due to the cell design or calibration can be avoided by means of stabilizing implicit boundaries (such as by implicitly satisfying the Kramers – Kronig relations between $\varepsilon_r'(\omega)$ and $\varepsilon_r''(\omega)$, see e.g. Jackson [1962]). A substantial drawback is the lack of knowledge of the complexity of expected relaxation processes.

The forward model based algorithm used in the present work relies on a modified Debye-type relaxation function. Modified to include ohmic conductivity (cf. equation (4.9)), equations (4.10) are supplemented with a separate parameter for ohmic conduc-

tivity, σ , which contributes to the imaginary part of $\varepsilon_r^*(\omega)$:

$$\varepsilon_r^*(\omega) = \varepsilon_\infty + \frac{\varepsilon_{\text{static}} - \varepsilon_\infty}{1 + j\omega\tau} - j\frac{\sigma}{\omega\varepsilon_0}. \quad (4.30)$$

The algorithm performs a forward calculation based on equations (4.21), (4.22) – (4.25) and (4.30). Best values for the model parameters ε_∞ , $\varepsilon_{\text{static}}$, f_r and σ are extracted by minimizing the difference between forward calculated and measured scattering parameters using a global optimisation approach based on a genetic algorithm²¹. The algorithm does not require a starting guess. Instead, physically reasonable boundaries are imposed on the model parameters (see Oswald *et al.* [2006] for more details on the algorithm).

With respect to the envisaged deployment for calculating the frequency dependent permittivity for ice measurements, the following fundamental difficulty arises: As outlined in section 4.2.2, the Debye-relaxation frequency of ice is located in the lower-to-mid kHz-range ($10^3 - 10^4$ Hz). With the present setup, S-parameters can be measured down to 300 kHz only. Thus only the high-frequency limit of the Debye-dispersion may be covered, primarily described by ε_∞ while the remaining parameters f_r and $\varepsilon_{\text{static}}$ are most likely not fully constrained from the input-data. In this context, it remains to be assessed to what extent the optimisation algorithm can be used for materials featuring a non-Debye-type permittivity distribution within in the measured frequency range. For this purpose, the genetic algorithm was tested against the alternative permittivity computational methods BJI and CCPM. In the following comparison with the Debye-based optimisation, but also for the later processing of ice S-parameters, the main focus was on the BJI-method (the CCPM-method was used for additional validation). In doing so, all important measurements were processed by one method of each of the above categories, quasi-analytical and forward model based.

4.4.2 Validation of the Debye-model optimisation

The Debye-based optimisation, the BJI and CCPM methods were all applied to the same set of S-parameters measured on the Teflon-standard. The BJI method was used considering the full set of S-parameters and additionally with the transmission parameters S_{ij} only. The genetic optimisation produced a large scatter in the values of f_r (located far below the measured frequency interval), and $\varepsilon_{\text{static}}$ but highly stable and reproducible values for ε_∞ , thereby giving a constant real part around (1.99 ± 0.2). This value is in good agreement with the mean values for ε_r' (over the respective frequency range) obtained by the other methods. A comparison of the results for ε_r' is given in Table 4.1. As a consequence of the large scatter in $\varepsilon_{\text{static}}$ and f_r , no precise values for the small imaginary part of the Teflon sample can be calculated from equation (4.30).

²¹In the following, if not stated otherwise, the parameter σ was always found set to almost zero, as the d.c. conductivity of the measured samples was generally very low.

Table 4.1: Intercomparison of inversion techniques on one data set of Teflon S-parameters. For 2), 3) and 4) mean values for ε'_r over the frequency range (1 MHz - 1.5 GHz) are reported with their respective standard deviations ($\Delta\varepsilon'_r$). For more details on the uncertainty estimate of 1), see section 4.5

	Algorithm	ε'_r	$\Delta\varepsilon'_r$
1)	Debye-Model based Genetic Optimisation	1.99	0.02
2)	Baker-Jarvis Iterative	1.98	0.05
3)	Baker-Jarvis Iterative Transmission only	1.99	0.04
4)	Complex Conductivity and Permittivity Model	1.994	0.005

Influence of calibration artefacts

For frequencies below ≈ 10 MHz, measured data points are sparse due to the linear sweep sampling of the NWA. Consequently, the BJI-result must be regarded on a tentative basis only for these low frequencies, and 10 MHz were set as a lower boundary for a definite data interpretation from the BJI-method (section 4.5). Figure 4.6 gives an overview on the BJI-results for $\varepsilon'_r(\omega)$. Shown is the mean from processing 8 separate Teflon measurements, including an indication of the typical scatter (grey curve with dashed error curves). Also shown is the range of ε_∞ obtained from processing 8 separate Teflon measurements with the Debye-based optimisation (black dashed lines). As expected from the results shown in Table 4.1, the two methods yield almost identical mean values of $\varepsilon'_r(\omega)$ over the frequency range 10 MHz – 1.5 GHz. However, the $\varepsilon'_r(\omega)$ -distribution calculated with the BJI-method is not entirely constant with frequency, but can be regarded as comprising three separate signal components:

1. A stationary mean value.
2. An oscillating pattern with a comparatively large frequency causing three distinct local minima in the considered frequency range.
3. A high-frequency oscillation somewhat similar to the “ripples” observed in the S-parameter input (cf. Figure 4.5).

Since Teflon is expected to exhibit a frequency-independent permittivity, signal components 2 and 3 are suspected to be artefacts potentially caused by deficits in the cell design and imperfect calibration. The latter has already been shown to be associated with the “ripples” in transmission S-parameters (see section 4.3.4). The approach to investigate the origin of signal components 2 and 3 is two-fold: (i) Eliminate the influence of imperfect calibration by using a full 2-port calibration. (ii) further deploy the forward model to investigate the sensitivity of the permittivity reconstruction with respect to deficits in cell design.

Regarding examination step i, supplementary measurements were performed at the MFPA, Weimar. With an Agilent PNA E8363B network analyzer and using a full 2-port calibration, S-parameters were recorded for the Teflon standard (and also for an

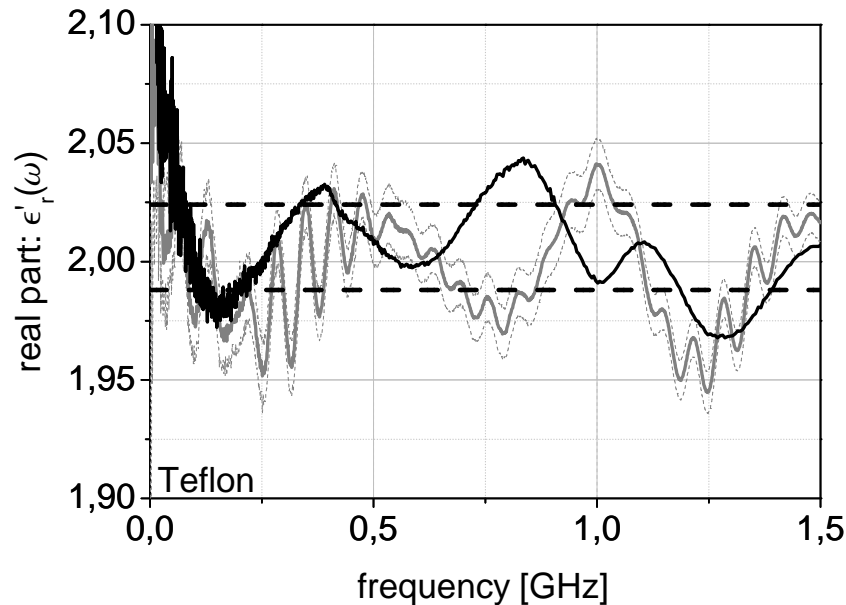


Figure 4.6: Intercomparison of permittivity computation algorithms for eight separate S-parameter measurements on the Teflon standard. Grey curve: Mean of ϵ'_r from BJI at the respective frequency. Dashed grey curves indicate ± 1 standard deviation around the mean. Black dashed lines: Range in $\epsilon'_r(\omega)$ obtained from the Debye-based optimisation. Black curve: BJI results from S-parameters measured after full 2-port calibration (see text). Note that permittivity computation is associated with large uncertainty for frequencies smaller than 10 MHz, and was only performed down to 300 kHz at maximum.

artificial ice sample, section 4.7) in linear and also logarithmic frequency sweep up to 16 GHz (the respective S-parameter plots are shown in the appendix (C.3)). As expected, in this case no “ripples” were found in the transmission S-parameters, although the damping and shift in resonance peaks remained present. To ensure comparability to our standard measurement routine (see section 4.3.2), S-parameters up to 1.5 GHz were considered and reference planes were shifted to the ends of the sample holder. Then, the Debye-based optimisation and the BJI-technique were applied. For Teflon, the genetic optimisation output for ϵ_∞ was again (1.99 ± 0.2) and unchanged for data from the logarithmic sweep. The BJI-technique yields a mean value for the real part of (2.02 ± 0.3) — the resulting $\epsilon'_r(\omega)$ is included in Figure 4.6 (black curve). The BJI- $\epsilon'_r(\omega)$ now showed no sign of signal component 3, but still featured component 2.

Regarding examination step ii, the forward model was employed to calculate synthetic S-parameters for a frequency independent permittivity of $\epsilon'_r = 2$, $\epsilon''_r = 0$. The synthetic S-parameters were then processed with the BJI-algorithm. Thereby, the effects of

various deficits in cell design (e.g. an impedance jump) on the S-parameters and on the respective output for $\varepsilon_r'(\omega)$ from the BJI-method could be investigated. In agreement with examination step i, it was found that an imperfect calibration (represented by non-zero cable length in equation (4.28)) corresponds with the appearance of “ripples” in the S-parameters as well as in the BJI- $\varepsilon_r'(\omega)$. The integration of an impedance jump altered the S-parameters (e.g. the above mentioned damping and shift in resonance peaks) and, moreover, the oscillations (component 2) were reproduced in the BJI- $\varepsilon_r'(\omega)$. More details of this investigation are shown in the appendix C.4.

In an additional attempt to investigate the link between signal components 2 and 3 and the disturbances in S-parameters, the BJI-calculated permittivity distribution was used as input for a simple backward calculation of S-parameters using equation (4.25). Using the BJI- $\varepsilon_r^*(\omega)$ (which includes the effects of signal components 1, 2 and 3) resulted in backward calculated S-parameters, featuring the disturbances “damping in resonance peaks” and “the ripples” (section 4.3.4) to the same extent as the measured S-parameters. Including only signal component 1, i.e. using a constant input values (e.g. $\varepsilon_r' = 2$, $\varepsilon_r'' = 0$;) resulted in backward calculated S-parameters lacking any of the disturbances described in section 4.3.4. Exemplary results of this investigation are shown in the appendix C.5.

As a result of the approach made by examination steps i and ii, the components 2 and 3 are not regarded as a signal from the dielectric sample but as measurement artefacts.

Permittivity inferred from S-parameters without computational algorithms

By means of the more sophisticated NWA used at the MFPA Weimar (regarding its large bandwidth (up to 16 GHz)) a detailed picture of the Time Domain Reflectometry (TDR) signals was obtained for the Teflon (Figure 4.7) and ice measurements (Figure C.7 in the appendix (C.6)). The TDR signal allows to inspect the cell assembly for impedance discontinuities in the time domain. In Figure 4.7, in addition to the distinct reflection of to the sample, two distinct impedance jumps can be identified, estimated from their reflection times as most likely corresponding to the 7/16-N adapters. The TDR signals analyzed in each direction of the coaxial cell (black and grey curves) are almost identical showing that the cell assembly appears as almost symmetric.

Moreover, the TDR signal allows for a direct estimation of the mean permittivity without deploying a computational algorithm. For a low-loss dielectric, ε' is related to the travel time Δt between the front and rear end of the sample (see arrows in the TDR-reflection signal in Figure 4.7) via equation (4.12), and may thus be calculated as:

$$\varepsilon_r' = \left(\frac{c_0 \Delta t}{\Delta l}\right)^2 \quad (4.31)$$

where Δl is the known sample length. From the Teflon TDR signal, ε_r' was estimated as (1.96 ± 0.1) , in agreement with the computational algorithms. The comparatively large

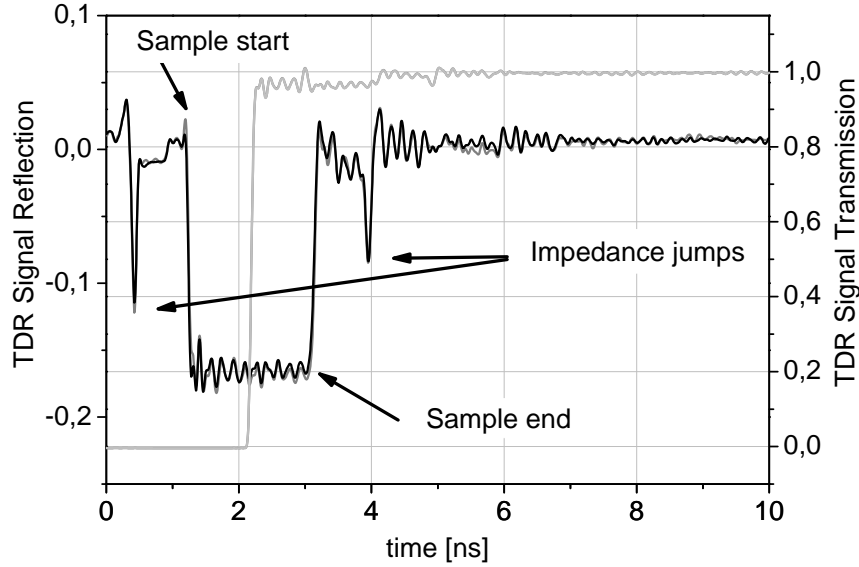


Figure 4.7: Time Domain Reflectometry (TDR) signal obtained from S-parameter measurements on the Teflon standard. Measurements were performed with an Agilent PNA E8363B network analyzer up to 16 GHz (at MFPA, Weimar). Black and dark grey curves show the reflection signal in each direction of the coaxial cell. The light grey curve shows the transmission signal. Indicated are the start and end of the sample in the reflection signal. Also note the two distinct signals of impedance discontinuities.

error results from the uncertainty in detecting the front and rear end of the sample. An additional alternative method for a direct permittivity estimation based on the S-parameters alone was used by Gorriti and Slob [2005b]. For non-dispersive lossless materials ($\varepsilon_r^*(\omega) = \varepsilon_r'$) the reflections S_{ii} become (close to) zero at periodic frequencies f_k ($k=1,2,\dots$) from which ε_r' can be calculated:

$$\varepsilon_r' = \left(\frac{k c_0}{2f_k \Delta l} \right)^2. \quad (4.32)$$

In case of the Teflon standard, to which the above requirements concerning the permittivity of the material should apply, ε_r' was calculated by this method to be (1.95 ± 0.18) . The large uncertainty stems from the observed damping hampering the detection of resonance minima. As already discussed in section 4.3.4, the forward model indicates a small impedance discontinuity to be responsible for the observed damping, which goes along with a slight shift towards larger frequencies in the model. This could explain the systematic underestimation of ε_r' by this method.

Due to their large uncertainties, the two “direct” methods for estimating ε_r' (TDR, equation (4.31) and resonance minima, equation (4.32)) were only used as an initial consistency check for the Debye-based permittivity reconstruction algorithm.

4.5 Performance assessment of the coaxial cell setup

4.5.1 Reproducibility of S-parameter measurements

The TDR inspection showed no asymmetric scattering or unknown impedance discontinuities. Hence, after the setup refinements discussed in section 4.3.3, no substantial inadequacies in the cell design were detected. S-parameter measurements with the refined setup proved to be very reproducible. Routine measurements of the Teflon standard showed very little scatter in the S-parameters. An overview on the respective S-parameter plots is given in the appendix C.7. In order to further assess the reproducibility, a frequency-dependent quantity representative for the relative data scatter was calculated as:

$$\Delta S_{ij}(\omega) = \frac{\text{std}(|S_{ij}(\omega)|)}{\text{mean}(|S_{ij}(\omega)|)}, \quad (4.33)$$

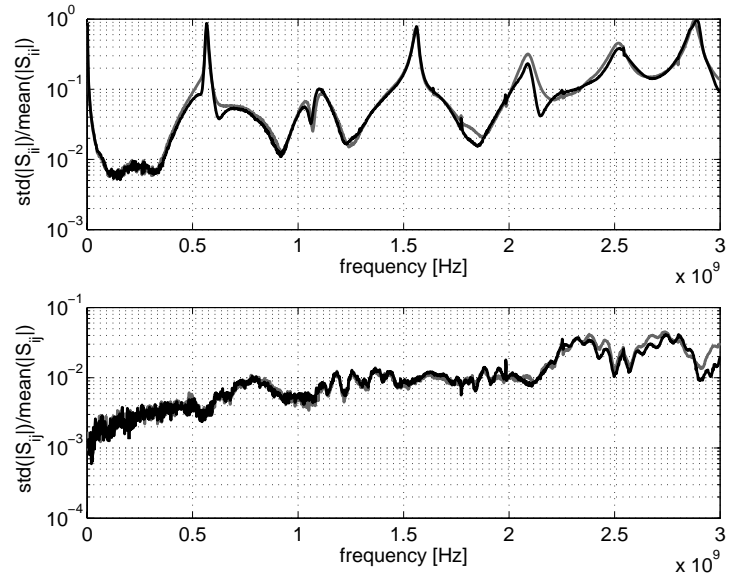
where, in this case, the indices ij indicate reflection S_{ii} as well as transmission S_{ij} measurements. Figure 4.8 shows $\Delta S(\omega)$ calculated from 9 Teflon measurements that were performed up to 3 GHz. Evidently, $\Delta S_{ii}(\omega)$ becomes large at the quasi-periodic resonance peaks, where $|S_{ii}(\omega)|$ values are very small. Up to 1.5 GHz the reproducibility is highest, with $\Delta S_{ii}(\omega) < 10^{-1}$ and $\Delta S_{ij}(\omega) < 10^{-2}$, respectively. Beyond 1.5 GHz, $\Delta S(\omega)$ increases by up to an order of magnitude. Hence, in addition to the considerations of section 4.3.3 it still seems reasonable to confine the measurements to frequencies below 1.5 GHz to ensure the highest possible accuracy in S-parameter measurements.

4.5.2 Uncertainty in permittivity estimation

The general strategy for an overall uncertainty estimation in permittivity reconstruction is to consider the Teflon-measurements and to assign quantitative uncertainties to each contribution of: 1) the coaxial cell, 2) the optimisation routine and 3) the sample.

Assuming the Teflon standard to be identical for all measurements, the resulting variability in calculated permittivities is a result of contribution 1) and 2). For a total of 17 measurements of the Teflon standard (up to 1.5 GHz), the Debye-based optimisation yields a mean value for ε_∞ of (2.016 ± 0.016) , or $\approx 0.8\%$ mean relative scatter and an absolute range of 1.988-2.024. The optimisation algorithm does not produce continuously distributed values for ε_∞ but converges to discrete values. However, the observed increment is small, e.g. 1.988 to 2.002. To investigate the influence of 2) separately, the extended forward model was again employed to simulate S-parameters including the same artefacts as in the standard measurement routine (section 4.3.4 and Figure 4.5). As input for the model, frequency independent values of ε'_r between 1 and 4 in steps

Figure 4.8: Illustration of the high reproducibility in S-parameter measurements performed on the Teflon standard. For the absolute values of reflection (top) and transmission (bottom) the standard deviation (std) of 9 Teflon datasets was divided by the respective mean for each measured frequency. Black and grey curve indicate the two respective measurements (e.g. S_{11} and S_{22}).



of 0.1 were used. The reconstructed values for ϵ_∞ from the genetic optimisation were found to differ from the input values by less than 0.5%. This is not surprising regarding the stability of the Debye-based optimisation with respect to the S-parameter disturbances (section 4.4.2) and also the apparent discretization in output values of ϵ_∞ .

Uncertainties from sample variations are negligible for the Teflon standard. However, the influence of variations in sample geometry becomes important for the envisaged ice measurements. This especially concerns the sample length, which has to be provided as a parameter for permittivity calculation, regardless of the choice of algorithm. To investigate the sensitivity of the Debye-based optimisation on sample length, the algorithm was applied to the same set of S-parameters while solely changing the sample length input parameter. The Debye-parameter ϵ_∞ was found to depend linearly on the sample length, with a sensitivity of $-(0.354 \pm 0.001)$ per cm.

Taking all these contributions into account, an uncertainty in ϵ'_r of around 1% appears reasonable based on the measurements of the Teflon standard. For ice samples, a detailed uncertainty estimation is given below (section 4.6).

4.5.3 Validation with reference materials

In order to further assess the setup's capability for adequate permittivity detection, reference materials of known permittivity were measured in addition to the Teflon laboratory standard. Air, water and ethanol were selected for this purpose. While the permittivity of air is frequency independent, water and ethanol follow a Debye-relaxation, with their relaxation frequency close to (water) or within (ethanol) the measured frequency range (300 kHz – 1.5 GHz) [Kaatze, 2007; Gregory and Clarke, 2009]. A detailed comparison

with the reference values is given in Table 4.2. In case of water and ethanol, a full set of Debye-parameters is reported. The uncertainties for air, water and ethanol indicate the amount of scattering in Debye-parameters (i.e. their standard deviation) observed in multiple runs ($n \approx 10$) of the optimisation routine for the same sample. The value for Teflon is reported with the uncertainty of 1% as estimated in section 4.5.2. Parameters dominating the permittivity distribution within the measured frequency range can be fitted precisely by the algorithm. In contrast, Debye-parameters relevant to ε_r^* far outside the frequency range typically show a large scatter since they are not adequately constrained by the S-parameters. Consequently, only values which could be adequately constrained within the measured frequency interval can be reasonably compared to references.

For water, $\varepsilon_{\text{static}}$ is close to the reference, however, outside of the estimated uncertainty. In case of water and ethanol measurements, the standard deviation from multiple optimisation runs may not be appropriate to fully capture uncertainties related to the ambient temperature and the sample: Measurements were performed at room temperature ($\approx (23 - 25)^\circ\text{C}$, reference values at 25°C). However, at this stage no precise temperature control at the sample inside the coaxial cell was possible. An additional uncertainty might stem from incomplete filling of the cell with the respective liquid, and thus a potential bias by air inclusions.

The results obtained with air were extremely stable, with same values $\varepsilon_\infty = 0.993$ for all runs, and for different routine measurements. For measurements on air, the cell could be used directly after calibration—hence, potential small changes in cell geometry and contact due to sample insertion were not an issue. For Teflon, $\varepsilon_\infty = (2.02 \pm 0.02)$ is consistent with reference values between 2–2.1 reported in other studies [Riddle *et al.*, 2003].

4.5.4 Critical assessment and future perspective

Measurements on air and the Teflon laboratory standard showed that the Debye-model based genetic optimisation yields reliable results also for low-loss, non-Debye type materials. For these materials, the Debye-parameter ε_∞ determines the real part of the permittivity over the measured frequency range. In case of water and ethanol, both featuring a Debye-type permittivity distribution, the Debye-parameters determining ε_r^* mostly outside the measured frequency range feature a large scatter in optimisation output, since only insufficiently constrained by measurements. This is also expected to be the case for f_r and $\varepsilon_{\text{static}}$ for the envisaged ice measurements. The expected data scatter in f_r and $\varepsilon_{\text{static}}$ would hamper the use of the Debye optimisation for a precise determination of ε_r'' (equation (4.11)). However, with a relative uncertainty for ε_r' estimated for Teflon in the order of 1%, the present setup seems feasible with respect to the aim of high accuracy measurements of ε_r' on ice samples.

With respect to the observed disturbances in S-parameters, the present refined setup

Table 4.2: Debye-parameters for the investigated reference materials obtained with the genetic optimisation algorithm from measured S-parameters. For water, ethanol and air, uncertainties are reported as standard deviations from multiple optimisation runs ($n \approx 10$). Debye-parameters relevant outside the measured frequency range feature a large scatter in optimisation output. Reference values for water, ethanol and Teflon are from Kaatz [2007] ($T = 25^\circ\text{C}$), Gregory and Clarke [2009] and Riddle *et al.* [2003] respectively.

Sample	Debye-Parameter	Optimisation output	Reference values
water	$\varepsilon_{\text{static}}$	79.7 ± 0.1	78.35 ± 0.05
	ε_{∞}	10.4 ± 11.4	5.2 ± 0.4
	f_r [GHz]	15.6 ± 2.6	19.3 ± 0.1
ethanol	$\varepsilon_{\text{static}}$	24.1 ± 0.5	24.43 ± 0.04
	ε_{∞}	3.7 ± 1.5	4.505 ± 0.033
	f_r [GHz]	0.97 ± 0.07	0.964 ± 0.005
air	ε_{∞}	0.99 ± 0.00	1
Teflon	ε_{∞}	2.02 ± 0.02	2–2.1

appears capable of even higher accuracy by means of improving the S-parameter measurements. The extended forward model reproduces the disturbances as due to the lack of a full 2-port calibration (“the ripples”) and impedance mismatch in the cell components (“damping” in S_{ii} -resonance peaks). It could be shown that as a consequence of these disturbances, the BJI-method features oscillating patterns in $\varepsilon'_r(\omega)$ instead of a stationary mean value. Hence, the oscillations in $\varepsilon'_r(\omega)$ must not be interpreted as an actual frequency dependent signal, but have to be regarded as artefacts. From Teflon measurements, the Debye optimisation method appeared somewhat more robust against the artefacts than the BJI-method although the value of ε_{∞} showed an absolute scatter of 1.988-2.024.

The exemplary comparison with S-parameters measured with a full 2-port calibration showed that by this means the high-frequency disturbance (“the ripples”) are absent. No precise localisation for the impedance discontinuity associated with the remaining oscillation of larger frequency in $\varepsilon'_r(\omega)$ could be obtained. Taking into account the TDR-signal, however, it seems plausible the 7/16-N-adapters are a potential origin of the observed impedance jumps. The high reproducibility in S-parameters up to 1.5 GHz indicates that this impedance jump is compensated to a large extent by the calibration. After taking the cell apart and reassembling the empty cell, the reflection-signal in $|S_{ii}|$ was found slightly altered but remained below -20 dB, hence only of minor disturbance to the actual signal. The exact cell geometry may be altered to a larger extent when inserting a sample. Uncertainty in the precise cell geometry mostly arises from the use of screw threads, which should be replaced by flange joints in the prospective building of a new cell. With such a future setup, it would be desirable to perform the calibration

routine directly at the end of the sample in the cell. Thereby, the present pre-processing shift in reference planes would not be needed. Misplaced reference planes result in erroneous sample length, which has a substantial influence on permittivity computation as shown in section 4.5.2. In this context, a continuative approach would be the deployment of a 3D full-wave electromagnetic field simulation (such as HFSS by Ansys Software) as to obtain a better understanding of the exact origin of artefacts and effects of altering the cell geometry.

Further refinement of the existing setup might be achieved by means of the extended forward model. At present, the model has three main parameters to simulate potential flaws in cell design: The magnitude in impedance discontinuity and losses as well as the length of the cable connecting the cell to port 2 of the NWA. Using measurements of reference materials such as air, water and Teflon, the model parameters could be optimized accordingly. Thus having “tuned” the forward model to adequately describe the cell characteristics, the permittivity computation could be refined in two ways:

- With respective T-matrices describing the individual setup components, a so-called “de-embedding” procedure can be performed. The T-matrices of the components are inverted and multiplied to T_{tot} (e.g. equation (4.28) and (4.26)) in order to extract all additional scattering effects but the dielectric sample in the sample holder (see Agilent [2004] for a detailed description of this procedure).
- Alternatively, the adjusted forward model could be integrated directly in the genetic optimisation routine. This would mean to replace equation (4.25) in the algorithm by equation (4.28). In doing so, S-parameters more representative for the entire setup can be fitted to the measurements.

For further measurements at still higher accuracy, a full 2-port calibration will be required eventually. As deployed exemplarily in the present study, a full 2-port calibration is possible using a sophisticated NWA. However, the use of manually defined calibration schemes is an alternative, e.g. based on measurements of various standard materials as suggested by Schwing *et al.* [2010]. Suitable standard materials should preferably feature low-loss permittivities similar to ice, such as Teflon or, possibly, the liquid toluene²² (with $\epsilon'_r \approx 2.4$ [Wohlfarth and Lechner, 2008]).

In conclusion, the successful validation of the coaxial cell transmission line setup with Teflon is an important result regarding its envisaged application for measurement of ϵ'_r for ice. The total uncertainty for the Teflon standard estimated around 1% fulfills the initial requirements, with respect to the deployment for ice.

²²although toluene and liquids of similar permittivity (e.g. cyclohexane, 1,4-dioxane) can be measured in principle with the present setup, they were not used in the present study as they are potentially harmful and need to be handled with special care compared to the easy-to-use Teflon standard.

4.6 Permittivity of artificial ice

In order to employ the refined setup for measurements on artificial ice samples, an according sample preparation procedure had to be developed. This task includes the need to precisely characterize the sample with regards to its crystal orientation distribution, which is addressed in section 4.6.1.

The present investigation did not aim at studying the complex mechanisms in the interaction of ice permittivity and acid concentration yet, but primarily focused on deploying the acidity and temperature dependence for manipulations on ε'_r of the artificial samples (section 4.6.3). In an attempt to reproduce the linear relation of ε'_r on acidity, the sensitivity of the present setup to determine acidity-based changes in ε'_r (and qualitatively also ε''_r) is assessed.

The relation between density and ε'_r is studied using natural firn and ice samples, see section 4.7 below.

4.6.1 Sample preparation and characteristics

Evidently, artificial and natural ice samples had to be prepared as to fit the coaxial cell geometry as precisely as possible. This especially concerned avoiding air gaps, which would bias the measured permittivity. In contrast, the influence of air enclosed in the ice sample and its relative contribution to ε'_r , is a desired measurement signal. Moreover, natural ice samples (e.g. from ice cores) must not be melted and have to be preserved for further analyses. To this end, two different sample preparation methods have been developed for artificial and natural ice samples. The latter will be presented in section 4.7.1.

Pure²³ artificial ice samples were prepared by freezing water inside the cell: The sample holder can be sealed watertight with the help of the rubber sealings and a screw cap. The inner conductor remains supported by the Teflon discs. The sample holder is filled with degassed, ultra-pure water and left in the cold room (-20°C) standing upright. The freezing process of the water inside the cell progresses from the outer conductor towards the center cylindrical axis. This method produced very homogenous clear ice with virtually no cracks and only few thin radially oriented air inclusions remaining (Figure 4.9). The upward facing end of the sample in the upright standing sample holder showed a non-planar, rough surface which resulted in an uncertainty in sample length of about 0.5 mm. With a sensitivity on sample length of $-(0.354 \pm 0.001)$ per cm, this uncertainty results in a relative contribution to $\Delta\varepsilon'_r$ of $\approx 0.6\%$, in addition to the contributions discussed in section 4.5.2. In absolute values, the uncertainty for a single ice measurement was thus estimated as $\Delta\varepsilon'_r = \pm 0.03$.

The crystal orientation distribution of two exemplary ice samples was investigated at the

²³Here, “pure” ice means ice prepared from ultra-pure water

Alfred Wegener Institute (AWI), Bremerhaven, using an automated crystal fabric analyzer [Wilson *et al.*, 2003; Wilen *et al.*, 2003]. A standard coaxial ice sample was cut along the inner conductor (“vertical cut”). An additional sample was prepared by freezing water inside the sample holder without the inner conductor. The resulting solid ice cylinder was cut perpendicular to the symmetry axis (“horizontal cut”). Two thin sections for the automatic fabric analyzer were prepared from each sample. Measurement results are given as Schmidt diagrams (shown in the appendix C.8) and as c-axis distribution vs. “latitude”–angle (shown in Figure 4.9). In this context, “latitude” measures the c-axis orientation relative to the symmetry axis of the cylindrical cell (as illustrated in Figure 4.9): 0° defines an “equatorial” position of the c-axis, i.e. perpendicular to the symmetry axis, whereas 90° is for a c-axis orientation parallel to the symmetry axis. While no clear preference in orientation was found in the vertical cuts, the crystals in the horizontal cuts showed a clear preference for a radial orientation of c-axes, i.e. perpendicular to the symmetry axis (Figure 4.9). The preference for a radial orientation of c-axes is most likely due to the slow and directional freezing process resulting in the large lamellar single crystals, seen on the left in Figure 4.9 (pers. communication S. Kipfstuhl, AWI). Under the assumption of TEM-mode propagation only, as discussed in section 4.3.3, the electric field vector is perpendicular to the symmetry axis of the cylindrical waveguide. Consequently, for the artificial ice samples, c-axes and electric field vector are mostly parallel, and the main contribution to the measured value of ε'_r will stem from ε'_\parallel . From the measured distribution of crystal orientation in the artificial samples, a correction can be calculated for the contribution of the crystals with their c-axis non-parallel to the electric field as pointed out by Fujita and Mae [1994]. To do so, the measured value $\varepsilon'_{\text{meas}}$ is assumed to consist of:

$$\varepsilon'_{\text{meas}} = \varepsilon_\perp + \Delta\varepsilon' D_a, \quad (4.34)$$

$$D_a = \frac{1}{N} \sum_{j=1}^N \cos\theta_j, \quad (4.35)$$

with a frequency-independent anisotropy $\Delta\varepsilon'_r = \varepsilon_\parallel - \varepsilon_\perp$, N being the total number of crystals and the factor D_a describing the degree of contribution of $\Delta\varepsilon'_r$ ($D_a = 0 \Leftrightarrow \varepsilon'_{\text{meas}} = \varepsilon_\perp$ and $D_a = 1 \Leftrightarrow \varepsilon'_{\text{meas}} = \varepsilon_\parallel$). The number of crystals with an orientation θ_j can be calculated from the binned distribution of crystal orientation shown in Figure 4.9. Due to the preferred radial orientation in the synthetic ice samples, D_a is close to one, with the average from two horizontal cuts $D_a = 0.959$.

4.6.2 Permittivity of pure artificial ice

Out of over 30 different samples, 8 different synthetic ice samples could be measured at highest possible accuracy. These measurements were performed with the coax-

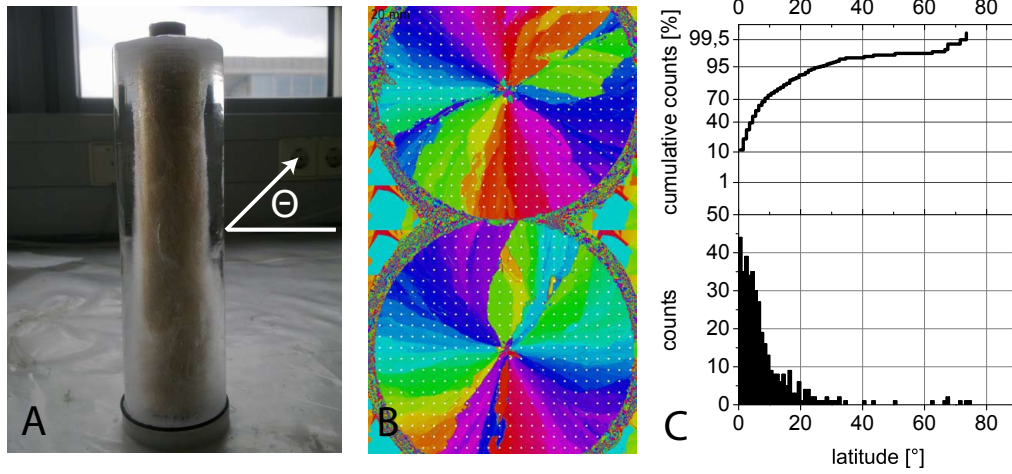


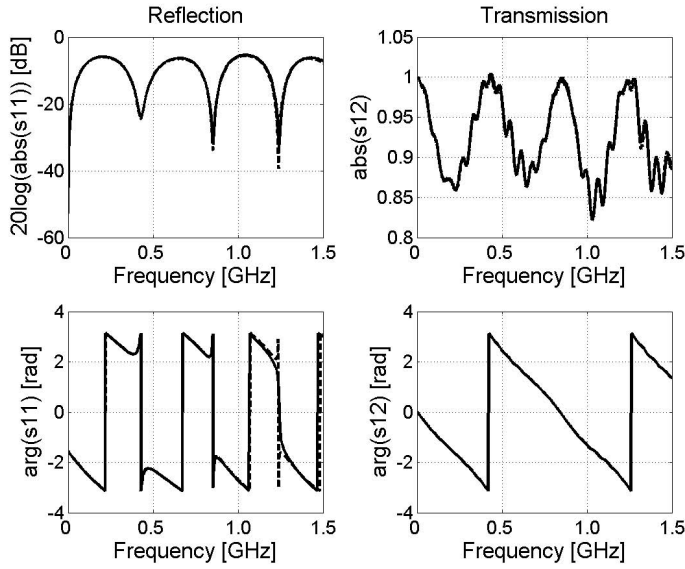
Figure 4.9: Characterisation of an artificial ice sample. From left to right: A. An artificial ice sample prepared by freezing water inside the upright standing sample holder. Very few air inclusions are remaining. Note the “latitude” angle θ . B. Artificial ice samples prepared without inner conductor, cut perpendicular to the symmetry axis and viewed under crossed polarized filters. Note the lamellar crystal structure due to directional freezing. Each color corresponds to a respective c-axis orientation. C: Result from using an automated fabric analyzer on the samples shown in B. C-axis distribution is plotted against “latitude”-angle binned in 1° intervals. “Latitude” measures the angle from the symmetry axis of the cylindrical cell (see text).

ial cell inside an insulating styrofoam box stabilizing the ambient temperature around $(-20 \pm 2)^\circ\text{C}$. S-Parameters of these samples are highly reproducible just as for Teflon (see section 4.5), with $\Delta S_{ii}(\omega) = 10^{-2} - 10^{-1}$ and $\Delta S_{ij}(\omega) = 10^{-3} - 10^{-2}$ between 1 MHz and 1.5 GHz. An exemplary set of S-parameters for artificial ice is shown in Figure 4.10.

From multiple runs on the same S-parameter set, the Debye-based genetic optimisation algorithm produced a large scatter in f_r and $\varepsilon_{\text{static}}$. From the S-parameters in the MHz-range, only insufficient experimental constraint can be obtained for f_r and $\varepsilon_{\text{static}}$. Appropriate boundary conditions for the optimisation algorithm were investigated in the following scenarios:

Intermediate boundary conditions: Imposing reasonable boundaries (e.g. following Fujita *et al.* [2000]) that $\varepsilon_{\text{static}} > \varepsilon_\infty$ by at least an order of magnitude, the relaxation frequency was found between $10^3 - 10^4$ Hz and $\varepsilon_{\text{static}}$ ranged $\approx 90 - 120$. A similar picture was found when constraining f_r to $10^2 - 10^4$ Hz. The parameter ε_∞ ranged between 3.188 and 3.153.

Restrictive boundary conditions: Setting f_r between $10^3 - 10^4$ Hz, $\varepsilon_{\text{static}}$ between 100 - 120 and ε_∞ between 1 - 5, the parameter ε_∞ was 3.180, f_r and $\varepsilon_{\text{static}}$ were frequently set to the respective limits of the boundaries.

**Figure 4.10:**

Scattering parameters of an artificial ice sample. Dashed lines: S-Parameters from reversed direction, i.e. S_{22} and S_{12} . Note the quasi-periodic resonance minima in $|S_{ii}|$ typical for a low-loss dielectric.

No boundary conditions: Without boundaries, values of $\varepsilon_{\text{static}}$ were in some cases found close to ε_{∞} . In this case, f_r tended to large values around 10^5 Hz. The parameter ε_{∞} was again between 3.188 and 3.153.

Multiple relaxation frequencies: The algorithm in principle allows for using multiple relaxation frequencies [Oswald *et al.*, 2006]. However, in exemplary test runs, a second relaxation frequency was always set outside the measured frequency range (e.g. around 10^{11} Hz).

Qualitatively, all of the above scenarios reproduced an almost identical distribution of ε'_r at MHz frequencies, with a slight decrease between 300 kHz and 10 MHz due to the high-frequency end of the Debye-relaxation and a constant value from 10 MHz – 1.5 GHz. None of the above scenarios featured a distinct better quality of fit between forward calculated and measured S-parameters. Hence, the intermediate boundary conditions of the first scenario were adapted as standard constraints. If necessary, the results were additionally compared to the other settings.

With f_r far below the measured frequency interval, the Debye-based reconstruction yields a constant ε'_r above ≈ 10 MHz given by ε_{∞} . The values obtained for ε_{∞} were (3.188 ± 0.03) (6 samples) and (3.153 ± 0.03) (2 samples). The effect of occasionally occurring slightly lower outcomes for ε_{∞} from the optimisation routine has also appeared in processing measurements of the Teflon standard at a similar rate (2 out of 8 samples with $\varepsilon_{\infty}=1.988$ compared to $\varepsilon_{\infty}=2.024$ respectively). The samples with the slightly smaller values for ε_{∞} showed no irregularities during measurement or upon visual inspection. As discussed in section 4.5.4, this scatter is most likely the product of disturbed S-parameters. However, at this stage there is no firm evidence to disregard the smaller values. The respective mean value of all 8 measurements is: $\bar{\varepsilon}_{\infty} = (3.18 \pm 0.01)$. Although experimental errors are expected to increase above 1.5

Table 4.3: Intercomparison of ε'_r obtained by different methods and algorithms for an exemplary S-parameter set of an artificial ice sample (1-4)). For 2), 3) and 4) mean values over the entire frequency range (1 MHz – 1.5 GHz) are reported with their respective standard deviations. Also shown: Alternative permittivity estimation methods (5-6)) discussed in the text.

	Algorithm / Method	ε'_r	$\Delta\varepsilon'_r$
1)	Debye-Model based Genetic Optimisation	3.188	0.03
2)	Baker-Jarvis Iterative	3.169	0.04
3)	Baker-Jarvis Iterative Transmission only	3.198	0.04
4)	Complex Conductivity and Permittivity Model	3.192	0.01
5)	TDR	3.12	0.15
6)	Resonant Frequencies	3.13	0.10

GHz, the measurement of S-parameters were tentatively extended to the full range of the NWA up to 3 GHz. Additionally, permittivity computation was performed in a number of overlapping frequency intervals (0.2–0.8, 0.5–1, 0.8–1.5 and 1.25–2 GHz). This was to check for changes in ε_∞ , potentially indicating dispersive effects. However, for the full range and all windows, the Debye-parameters from the optimisation algorithm remained unchanged, with $\varepsilon'_r = \varepsilon_\infty = (3.188 \pm 0.03)$ above ≈ 10 MHz.

Permittivity computation was also performed with the BJI-method. A frequency dependent comparison of the results from both methods is shown in Figure 4.11. The BJI reconstruction again features ripples and oscillations around a mean value close to the Debye-based optimisation. The oscillations seem to co-vary with the ones in the Teflon data and were identified as artefacts (section 4.5.4). Thus, they are not interpreted as actual frequency dependent variations of the permittivity of ice. The BJI-results also lacked clear evidence for dispersion— which was also checked for the full measurement range up to 3 GHz. Hence, the permittivity calculation algorithms agree within their uncertainties— not only regarding mean values of $\varepsilon'_r(\omega)$, which are shown in Table 4.3, but also in the lack of a systematic frequency dependency above 10 MHz. Below 10 MHz, both algorithms show a trend in $\varepsilon'_r(\omega)$ decreasing with frequency. However, uncertainties are somewhat larger due to the scatter in f_r and $\varepsilon_{\text{static}}$ for the Debye-optimisation and due to the low data density (linear sweep by the NWA) for the BJI-method. Using the exemplary MFPA Weimar ice measurement featuring a logarithmic sweep provided by the MFPA-NWA, no substantially different results were obtained. Additional measurements, specifically dedicated to the lower MHz-range, should be performed in the future also with the IUP-NWA, ensuring a higher density of recorded data points for subsequent permittivity calculation.

Alternative permittivity calculation methods were used for a broad consistency check. The TDR signal obtained from a exemplary measurement of an artificial ice sample at the MFPA was used with equation (4.31). Additionally, resonant frequencies in S_{ii} were

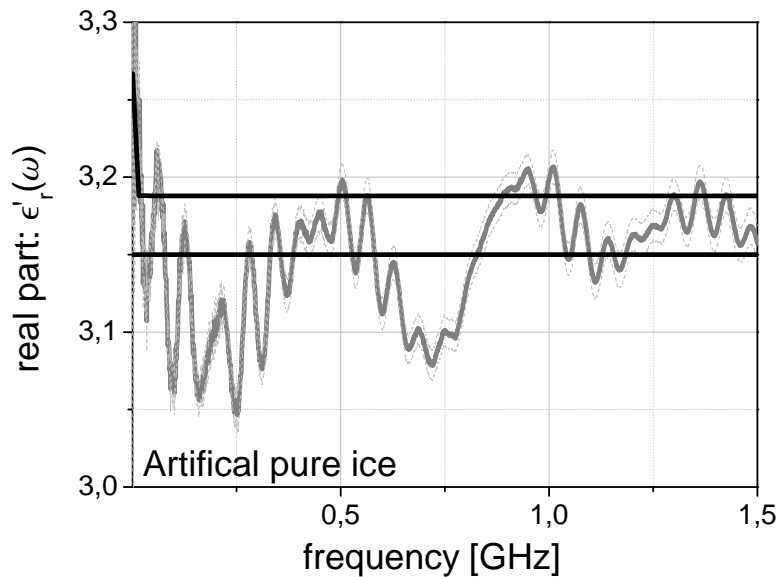


Figure 4.11: Permittivity computation by the Debye-based optimisation (two black lines, indicating the absolute range) and the BJI-method (grey line). Dashed lines indicate the standard deviation in BJI from processing 8 samples. According to the optimisation method, the relaxation frequency is far below the measured frequency interval resulting in constant ϵ'_r . The oscillations in BJI- ϵ'_r were identified as setup related artefacts (cf. section 4.4.2).

used with equation (4.32) for multiple S-parameter data sets. The results agree within their large error but again tend to systematically underestimate the absolute values from the algorithms (Table 4.3).

From the measured crystal orientation distribution ($D_a = 0.959$) and using a value for $\Delta\epsilon' = \epsilon'_{\parallel} - \epsilon'_{\perp} = 0.037$ reported by Fujita and Mae [1994] with the average value of the measurements of the present work $\epsilon'_{\text{meas}} = (3.18 \pm 0.01)$, applying equations (4.34) and (4.35) yields a value perpendicular $\epsilon'_{\perp} = (3.14 \pm 0.01)$ and parallel to c-axes $\epsilon'_{\parallel} = (3.18 \pm 0.01)$, respectively. Thereby a mean value for isotropic bulk ice can be derived from equation (4.6): $\epsilon'_{\text{iso}} \approx (3.16 \pm 0.01)$. Using the presumably most accurate value of a single measurement, $\epsilon'_{\text{meas}} = 3.188$, this procedure yields $\epsilon'_{\text{iso}} = 3.17$.

4.6.3 Influence of acidity and temperature

From previous laboratory measurements, ϵ'_r has been shown to feature a quasi-linear dependency on acidity and temperature of the sample (e.g. Fujita *et al.* [2000]). The goal of the pilot investigation presented here was to further assess the sensitivity of the setup (including the Debye-based algorithm), as to which extent dielectric sample

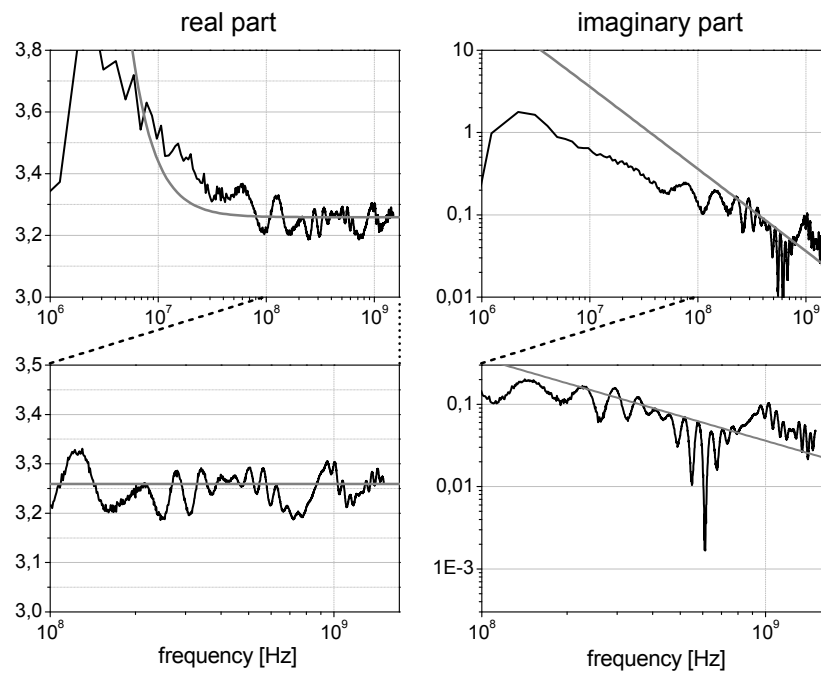


Figure 4.12: Exemplary comparison of permittivities for an artificial ice sample with an acidity of 10^{-3}M . Black curve: Results from the BJI-algorithm. The uncertainty for the BJI-method is highest in the frequency range below ≈ 50 MHz. The bold grey line shows the principal output of the optimisation, with f_r in the order of $10^5 - 10^6$ Hz. Above ≈ 100 MHz the Debye-model optimisation and the BJI-method consistently yield a constant value for ϵ_r' of 3.26, and a qualitative agreement on ϵ_r'' .

properties changed by different acid concentration or temperature can be adequately resolved.

Measurement of acid-doped ice

Four different degassed water samples were prepared with a known concentration of hydrochloric acid (HCl). The acidity of the samples ranged from $2 \cdot 10^{-4}$ to $1 \cdot 10^{-2}\text{M}$. Conductivity ranged from 9.3 to 395 mS/cm respectively. From these solutions, ice samples were prepared by freezing inside the sample holder. The large acidity of the ice samples caused pronounced changes in the S-parameters compared to the pure ice samples. Transmission S-parameters now showed a distinct decreasing trend in amplitude with increasing frequency— with the opposite effect present in reflection S-parameters (an example is shown in the appendix C.9). In the forward model, these trends can be reproduced in two ways: Either by increasing the value of σ or by setting f_r to higher frequencies. Generally, the Debye-model based optimisation showed a clear tendency

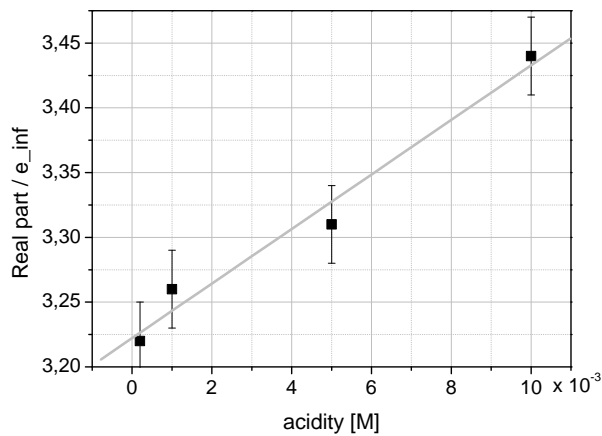


Figure 4.13: Linear relation between ε_{∞} and the acidity of the ice sample doped with HCl. Grey line: Linear regression. The slope is $\frac{d\varepsilon'_r}{dC} = (21.1 \pm 3.9)[1/M]$. Extrapolation to zero acidity yields $\varepsilon'_r = (3.21 \pm 0.02)$. Temperature was held constant at $\approx -20^{\circ}\text{C}$.

for an increase in the value of f_r only, the conductivity parameter remaining $\sigma \approx 0$. Qualitatively, the decrease of the high-frequency tail of the Debye-relaxation now extended into 10–100 MHz. The value of f_r and thus the extension of the Debye-tail increased with increasing acidity. However, the large scatter in $\varepsilon_{\text{static}}$ and f_r remained present and still hampered a unequivocal detection of f_r . Even when f_r was constrained to values below 10^4 Hz, the optimisation did not produce an increase in σ , but attempted to fit S-parameters lacking the respective trends. Further investigation regarding the parameter σ in the Debye-model optimisation is necessary.

The results were again cross-checked with the non-parametric BJI-algorithm. An exemplary comparison is shown in Figure 4.12, including the imaginary part. The BJI-method showed a similar extension of the decreasing trend at low frequencies. For all acidity samples and regardless of the exact value of the parameter f_r , ε'_r was constant above 100 MHz and consistent between the Debye-model optimisation and the BJI-method. In this frequency range, a close to linear relationship was found between the constant real part ε'_r and the acidity of the original water sample (see Figure 4.13). The slope of the linear relationship, also called molar permittivity, was $(21.1 \pm 3.9) [1/M]$. The imaginary part showed a systematic increase with acidity and was also consistent between both algorithms for frequencies above 100 MHz.

Qualitative investigation on temperature influence

By means of the insulating styrofoam box and a number of thermal packs, the ambient temperature at the coaxial cell could be held constant around $(-20 \pm 2)^{\circ}\text{C}$ during measurement. However, it was not possible to precisely manipulate the temperature inside the box. Consequently, the influence of temperature on ε'_r could only be investigated qualitatively in an exemplary experiment. For this purpose, the lid of the box was removed and the ambient temperature around the cell rose to roughly room temperature

((20 ± 2)°C) over a time period of ≈ 20 minutes. Meanwhile, no distinct changes were observed in S-parameters and calculated permittivity values. After 60 minutes, ε_∞ increased in a single step by about 0.035. No changes could be detected unambiguously for the imaginary part. After 80 minutes, S-parameters became clearly disturbed and meltwater was found inside the sample holder.

4.6.4 Discussion: The permittivity of artificial ice in the MHz-range

Under reasonable boundary conditions, f_r and $\varepsilon_{\text{static}}$ were found somewhat close to the values of previous studies (e.g. by Johari and Jones [1978]; Johari [1981]; Fujita *et al.* [2000]). However, since f_r and $\varepsilon_{\text{static}}$ are only insufficiently constrained by measurement and dependent on the imposed boundary conditions, a meaningful comparison of these values is not intended here— the focus remaining on $\varepsilon'_r(\omega)$ the MHz-range.

In Figure 4.14, $\varepsilon'_r(\omega)$ calculated from both algorithms is plotted as a function of frequency. In case of the Debye-based optimisation, the Debye-parameter triple (f_r , $\varepsilon_{\text{static}}$, ε_∞) is used to calculate ε'_r via equation (4.11). For the 8 ice samples measured at highest accuracy, the Debye-based optimisation yields ε'_r in between the black and dark grey curve, which result from Debye parameters ($f_r \approx 63$ kHz, $\varepsilon_{\text{static}} = 116.4$, $\varepsilon_\infty = 3.188$) and ($f_r \approx 10$ kHz, $\varepsilon_{\text{static}} = 74.1$, $\varepsilon_\infty = 3.188$) respectively. The black, grey and grey dashed curves are drawn in order to illustrate the typical range in results from the Debye-based optimisation. The BJI-based $\varepsilon'_r(\omega)$ is in somewhat better agreement with the black Debye-curve, but is also associated with large uncertainty for frequencies below 50 MHz.

Improvements with respect to previous studies on pure ice

The most obvious direct reference values for the results of the present investigation is the study by T. Ishida reported in Fujita *et al.* [2000], which also relied on a coaxial transmission line cell setup for measurements on acid-doped artificial ice. For pure ice, however, only a range of $\varepsilon'_r = 3.0 - 3.2$ and an experimental error of ± 0.1 is reported. Although it seems worth noting that the uncertainty of the present setup is about an order of magnitude lower, a further detailed comparison is not attempted due to the lack of more details concerning S-parameter measurements and permittivity computation in Fujita *et al.* [2000].

In the lower MHz-range, the results from the present study indicate the high-frequency tail of the Debye-relaxation to range up to roughly 10 MHz. The Debye-tail calculated by both algorithms lies in-between the data of Fujita *et al.* [2000] (squares in Figure 4.14, measured at 252 K) and Johari [1976] (crosses in Figure 4.14, measured at 268 K). A precise interpretation of the Debye-tail would require additional measurements at

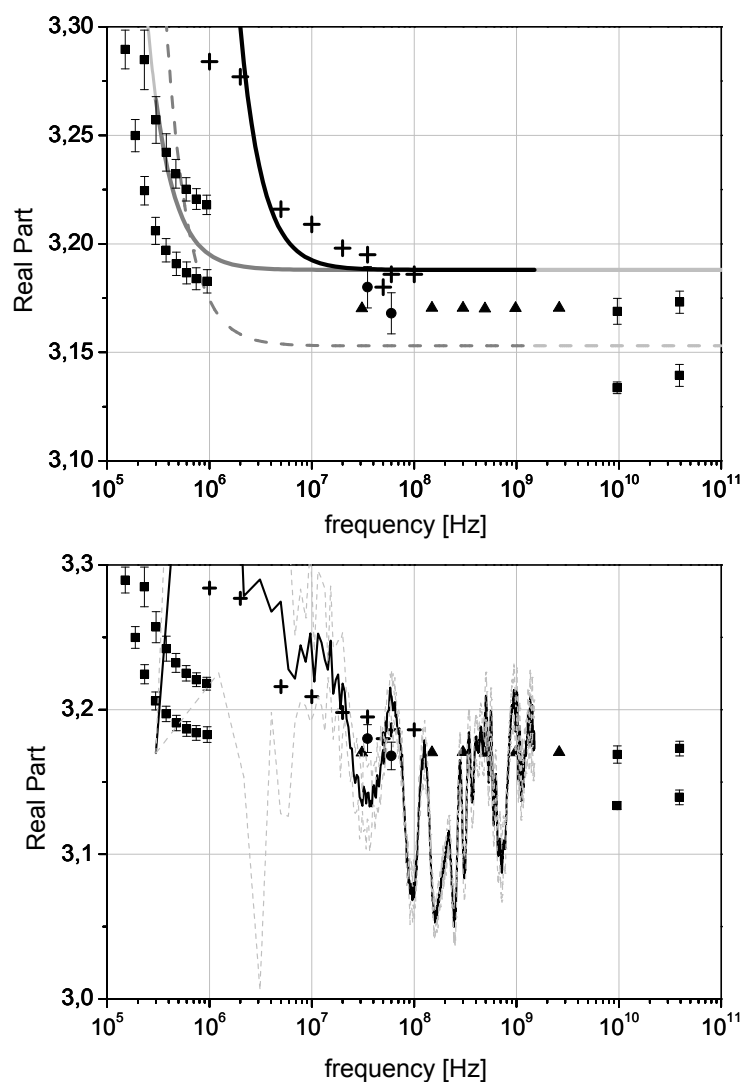


Figure 4.14: Real part of the complex permittivity of ice reconstructed with the Debye-model based optimisation (upper graph) and the BJI-method (lower graph). Also shown: Data from Fujita *et al.* [2000, 1993]; Matsuoka *et al.* [1997b] (squares, at 252K), Johari and Charette [1975] (dots, at 253K), Johari [1976] (cross, at 268K) and Westphal in Evans [1965] (triangles). Upper graph: The majority of artificial ice samples yielded Debye-parameters resulting in the black curve. Also shown are two grey curves to indicate the maximum uncertainty range due to scatter in f_r (grey curve) and in ϵ_∞ (dashed grey curve). All curves are extended beyond the frequency interval of actual measurements, indicated by light grey shading. Lower graph: Permittivity from the BJI-method (black line) with an estimated uncertainty range as dashed grey lines. Uncertainty is largest below 10 MHz, due to a low density of recorded data points.

lower frequencies, however.

A more detailed intercomparison with existing data is possible within 10 MHz – 1.5 GHz. Here, the constant ε'_r shows an absolute range between (3.188 ± 0.03) and (3.153 ± 0.03) . The difference in these absolute values is most likely a result from experimental uncertainties, with values of 3.188 observed more regularly and hence a mean value of (3.18 ± 0.01) . Due to the preferred radial crystal orientation observed in the synthetic ice samples, this value is considered representative for ε'_{\parallel} . Based on the crystal orientation distribution and a frequency-independent anisotropy of roughly 1%, a value for isotropic ice was calculated as (3.16 ± 0.01) . This finding is in agreement with the isotropic value reported by Westphal of $\varepsilon'_r = 3.17$, while the values of Johari [1976] are systematically slightly larger. This offset may be explained by the difference in temperature during measurements of -5°C [Johari, 1976] and $-20 \pm 2^{\circ}\text{C}$ (present study). Mätzler and Wegmüller [1987] report a sensitivity of ε'_r on temperature of $9.1 \cdot 10^{-4}[1/^{\circ}\text{C}]$, which would account for a positive offset of about 0.014. Consequently, values of Johari [1976] at 60 MHz and 100 MHz corrected to -20°C are 3.172. Johari and Charette [1975] report $\varepsilon'_r = 3.180$ at 35 MHz and $\varepsilon'_r = 3.168$ at 60 MHz with 0.3% relative uncertainty at -20°C .

Interestingly, a similar sample preparation was used by Johari [1976] and Johari and Charette [1975], where alleged polycrystalline ice samples were prepared from degassed water poured into a coaxial dielectric cell and left for freezing at -5°C . The authors analysed the ice samples under crossed polarizing filters but did not observe any obvious c-axis orientation. Similar results were obtained in the present study using crossed polarizing filters which only showed the lamellar coaxial crystal arrangement due to the directional freezing (Figure 4.9). Only by using an automated fabric analyzer it was possible to detect the radial anisotropy in our samples and to quantify the crystal orientation distribution. Thus, a preferred radial orientation of the ice crystals inside the dielectric cell might also have occurred in Johari [1976] and Johari and Charette [1975] and contributed to measured values somewhat more representative of ε'_{\parallel} .

Dispersion in the MHz-range

At 1 MHz, ε'_r was previously measured to be larger by about 0.044 than at 39 GHz [Matsuoka *et al.*, 1997b] and at 9.7 GHz [Fujita *et al.*, 1993]- indicating a small dispersion. The value for $\varepsilon'_{\parallel} = 3.17$ reported by Fujita *et al.* [1993] at 9.7 GHz and 252 K lies within the error of the mean value for $\varepsilon'_{\parallel} = 3.18 \pm 0.01$ of the present study, as well as within the estimated uncertainty of a single measurement. Hence, the present results point towards a frequency-dependence in ε'_r only below 10 MHz. Within the estimated uncertainties, no evidence for dispersion was detected between 10 MHz and 1.5 GHz, and even up to 3 GHz. This results fits with the argument made by Mätzler [2006], who rejects the hypothesis of a small decrease of 1% in ε'_r spread-out between 2 MHz and 5 GHz on the ground that such a dispersion would imply higher dielectric losses than

observed around 1 GHz.

The estimated uncertainties of the present work impose additional experimental limitation on the potential dispersion-strength in the upper MHz-range. A small dispersion is most likely difficult to detect with the Debye-type permittivity model, as it implicitly assumes a constant value $\varepsilon'_r = \varepsilon_\infty$ at high frequencies. However, the artefact-oscillations in the BJI-method indicate a limit for potential dispersive effects to be less than ≈ 0.04 (being the typical amplitude in oscillation around a mean value). Evidently, a further investigation on dispersive effects in the upper MHz-range would require an adequate reduction in artefact-oscillations.

In conclusion, according to the preliminary synopsis proposed here based on the new results of the present study, no additional frequency-dependent effects apart from the high-frequency end of the Debye relaxation have to be taken into account within the MHz-range.

Acidity and temperature influence

The preliminary experiment performed in the present study focused on assessing the potential of the present setup to determine the molar permittivity of HCl doped ice over a broad range in HCl-concentrations and frequencies (100 MHz–1.5 GHz). Note that the concentrations used go beyond the maximum range representative for typical glacier ice ($\approx 10^{-5}\text{M}^{-1}$, [Matsuoka *et al.*, 1997a]). The large range in acid concentrations was intended to yield ε'_r values distinctly separable with regards to our uncertainties. A concentration of $2 \cdot 10^{-4}\text{M}^{-1}$ already resulted in a high-frequency limit value of ε'_r of (3.22 ± 0.03) . Large acidity events in glacier ice seem potentially detectable as small, but systematic changes in ε'_r .

As the main reference for the present results serves again the study by T. Ishida in Fujita *et al.* [2000], in which the molar permittivity $\frac{d\varepsilon'_r}{dC}$ (i.e. the linear gradient) of ε'_r of ice samples doped with various concentrations of different acids was measured with a coaxial transmission line cell between 100–600 MHz. The linear gradient of $\frac{d\varepsilon'_r}{dC} = (21.1 \pm 3.9)[1/\text{M}]$ obtained from linear regression on the present results is close to the values reported in Fujita *et al.* [2000]. The authors additionally give an empirical relationship between molar permittivity and frequency, valid up to 9.7 GHz. Using their relation to calculate a mean value for the frequency interval measured in the present work gives $\frac{d\varepsilon'_r}{dC} = 20.9$ for $T = -10^\circ$ and $\frac{d\varepsilon'_r}{dC} = 14.5$ for $T = -20^\circ$. A validation of this empirical relation in the previously unmeasured frequency range from 600 MHz up to 1.5 GHz seems at reach deploying the present setup, but would require a precise temperature control.

Qualitatively regarding the imaginary part, a clear rise in ε''_r with increasing acidity is observed here. From the Debye-optimisation, f_r is also observed to rise, which extends the Debye-tail further into the MHz-range. Hence, the BJI-method as well as the Debye-optimisation consistently point towards dispersive effects due to the presence of acidity

extending up to ca. 100 MHz. Above, ϵ'_r is constant with frequency but dependent on acidity concentration. As pointed out by Fujita *et al.* [2000], both interfacial polarisation and reorientation of water molecules in the liquid phase due to the presence of acidity can lead to dispersion in the MHz-range.

From the present preliminary experiment the linear relation between ϵ'_r and acidity could be confirmed over the measured frequency range, with $\frac{d\epsilon'_r}{dC}$ close to reference values. A more in-depth investigation on molar permittivity with the present setup seems feasible at this point. Of special interest would be further investigations on acidity-related dispersion in the MHz-range as well as the influence of small, ice-core representative, acidity concentrations.

In the preliminary temperature experiment, the small, but systematic effect of a large temperature increase could not be detected unambiguously, e.g. $+15^\circ\text{C}$ roughly correspond to $+0.014$ in ϵ'_r , as discussed above. The preliminary experiment showed only little qualitative effect of a rising ambient temperature on ϵ'_r , before disturbances due to meltwater became dominant. At this stage, the primary purpose of the insulating box was to preserve the cold room temperature to $-20 \pm 2^\circ\text{C}$, which sufficed for a precise measurement of ϵ'_r . With a sensitivity of $9.1 \cdot 10^{-4} [1/^\circ\text{C}]$ [Mätzler and Wegmüller, 1987] variations in ϵ'_r less than 0.002 are expected for $\pm 2^\circ\text{C}$, which is far below the estimated measurement uncertainty. For future work, a better temperature control at the ice sample is called for. A precise temperature control would allow for a more precise intercomparison with previous measurements on pure ice, especially with the values of Johari [1976] below 10 MHz. Moreover, temperature control would allow to study in more detail the temperature dependency of ϵ'_r , and also the influence of acidity on ϵ'_r in relation to temperature. An adequate temperature control seems to be achievable by comparatively simple means (e.g. by placing the coaxial cell in a low temperature cabinet) but would also require an assessment of the effect of temperature on the setup components (e.g. cables), which may corrupt the use of a single calibration made at a specific temperature. In the end, the small but systematic effects on ϵ'_r due to its comparatively weak dependency on temperature would presently remain a challenge to detect. Evidently, the envisaged future investigations on acidity-related dispersion, small acidity concentrations and temperature influence would greatly benefit from the suggested further setup refinements (section 4.5.4) and thus increased measurement accuracy.

4.7 Permittivity of natural ice

Measurements of natural ice sample were aimed at investigating as to what extent the results obtained from artificial samples may be representative for real glacier ice. For this purpose, natural samples of firn and ice from two Alpine glaciers, were used. A set of natural ice samples was originally retrieved from Grenzgletscher (Monte Rosa massif, Swiss-Italian Alps), where bottom layers of cold, pre-industrial ice resurface

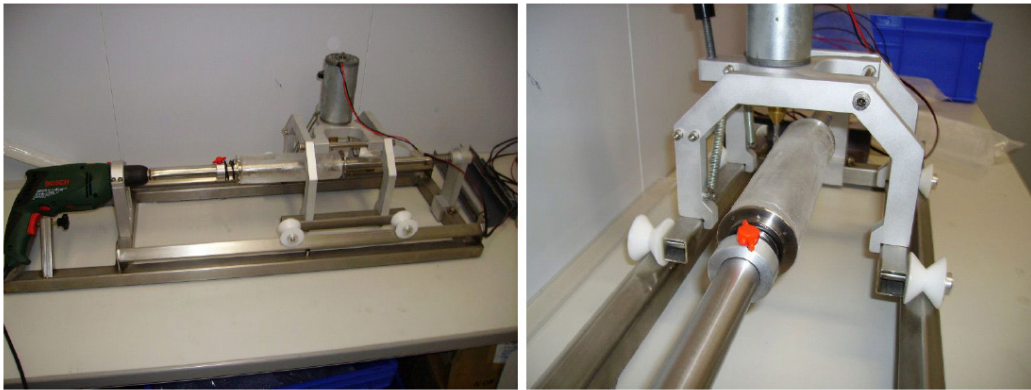


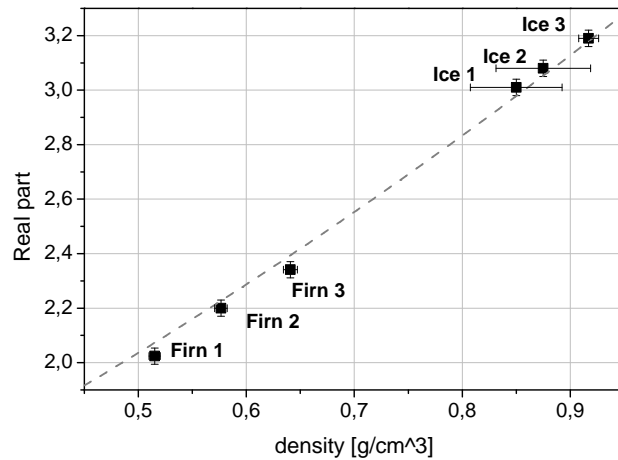
Figure 4.15: Setup for preparing natural ice samples as cylindrical rods to precisely fit the coaxial cell. Left: A hole is drilled for the inner conductor. Right: The inner conductor serves as a axis of rotation for milling the outside of sample while rotating it. Thereby, the cylindrical geometry is achieved. Figure from Hoppe [2009].

[Pichlmayer *et al.*, 1998; Steier *et al.*, 2006]. As discussed in chapter 3 (section 3.7) these bottom layers have undergone a history of different stresses and might thus contain an anisotropic crystal orientation distribution. A second set consisting of firm samples was measured in order to assess the sensitivity of the present setup to determine the natural variability in ϵ'_r due to density variations. The according firm samples were obtained from snow pits at the cold firm saddle Colle Gnifetti (CG).

4.7.1 Sample preparation and characteristics

Since the natural samples must not be melted for sample preparation, they need to be adjusted mechanically for the coaxial cell geometry. In doing so, the resulting samples will not feature the same preference for a radial c-axis orientation as with the artificial ice samples. In mechanical adjustment, the real challenge lies in achieving an adequate fit to the cell's geometry, hence avoiding air gaps. For this purpose, a dedicated setup was developed with a diploma thesis under my supervision comprising the following work flow [Hoppe, 2009]: The sample is first cut to the length of the sample holder. Next, a hole is drilled for the inner conductor which is inserted and then serves as a axis of rotation. By gradually milling the outside of sample while rotating it, the cylindrical geometry of the cell is achieved. This method is time consuming and sub-mm air gaps, especially towards the outer conductor, cannot be avoided. If large air gaps were observed, meltwater from the same sample was used to fill the gaps. In order to investigate if the potential crystal anisotropy in the Grenzgletscher-samples can be detected in different values of ϵ'_r , two ice samples were cut perpendicular to each other out of a larger block and shaped into cylindrical rods via the above milling-procedure. For a reference measurement, a third sample was prepared via the freezing method: Ice from this block was melted, degassed and frozen inside the sample holder. The two ice sam-

Figure 4.16: The real part, ε'_r of firn and ice plotted against the density of the samples. Temperature was held constant $\approx -20^\circ \text{C}$. Dashed line: The empirical relation for ε'_r of polar firn (equation (4.16)) by Kovacs *et al.* [1995].



ples prepared by mechanical adjustment showed a large number of small air bubbles, whereas the ice sample prepared by melting and refreezing was close to bubble free. For a density estimation of the ice samples, small cuboids were cut out of the samples and weighed. This can only be considered a rough estimate, with a relative uncertainty close to 5%. For this sample, density of pure ice was assumed, i.e. 0.917 g/cm^3 . The firn was too brittle for mechanical adjustment with the milling-procedure. Thus, it was simply pushed into the sample holder and subsequently further compacted in two steps, resulting in a total of three firn samples of variable density. The sample density ρ was estimated for the firn samples by weighing the total amount of firn filled into the volume of the sample holder, with a mean uncertainty for ρ of 1%.

4.7.2 Permittivity of natural firn and ice

Figure 4.16 shows the real part, ε'_r , of the natural firn and ice samples plotted against their estimated densities. All samples were measured by means of the “standard routine” (cf. section 4.3.2). The two ice samples (“Ice 1” and “Ice 2”) prepared by mechanical adjustment showed a large number of small air bubbles. In contrast, the ice sample prepared by melting, degassing and refreezing (“Ice 3”) was close to air-free and yielded a value of $\varepsilon'_r = (3.188 \pm 0.03)$, identical to the laboratory ice samples. The conductivity of the meltwater of “Ice 3” was $2.4 \mu\text{S/cm}$. From the investigations in section 4.6.3, this conductivity seems too low as to have an detectable influence on ε'_r . However, the value lies within the typical conductivity range measured in ice cores from Colle Gnifetti [Wagenbach *et al.*, 1988]. In order to correct for the different densities of the samples, as to compare the respective values for pure ice, the measured densities can be used in combination with equation (4.15). To this end, the ice volume fraction can be

Table 4.4: Results from measuring ε'_r of natural firn and ice samples. Based on density (ρ) measurements, equation (4.36) was used to calculate values for pure ice, ε'_I . The respective uncertainty $\Delta\varepsilon'_I$ was obtained by error propagation.

Sample	ρ [g/cm ³]	$\Delta\rho$	ε'_r	$\Delta\varepsilon'_r$	ε'_I	$\Delta\varepsilon'_I$
Firn 1	0.515	0.005	2.02	0.02	3.19	0.02
Firn 2	0.577	0.006	2.20	0.02	3.23	0.03
Firn 3	0.641	0.006	2.34	0.02	3.17	0.03
Ice 1	0.850	0.043	3.01	0.03	3.23	0.14
Ice 2	0.875	0.044	3.08	0.03	3.22	0.15
Ice 3	0.917	0.009	3.19	0.03	3.19	0.03

approximated as $\nu_I = \rho_F/\rho_I$ [Wilhelms, 2005]. Relying on the original approach by Looyenga [1965] (with $\alpha = 1/3$, cf. equation (4.15)) and additionally assuming $\varepsilon'_A = 1$ leads to:

$$\varepsilon'_I = \left(\frac{1}{\nu_I} (\varepsilon'_F)^{1/3} - 1 \right) + 1)^3. \quad (4.36)$$

Using equation (4.36), the respective value of ε'_I was calculated from all natural samples. The results are shown in Table 4.4. An according uncertainty $\Delta\varepsilon'_I$ was estimated based on the uncertainties in density $\Delta\rho$ and permittivity $\Delta\varepsilon'_r$ using error propagation. Note the large errors for “Ice 2” and “Ice 3” resulting from the respective larger density uncertainties. For “Ice 3”, no density error was assumed in order to compute an uncertainty based on $\Delta\varepsilon'_r$ only.

4.7.3 Discussion: Permittivity of natural firn and ice

The different densities of the 6 measured firn and ice samples cover almost the entire density spectrum encountered in a glacier or ice sheet. When plotted against density (Figure 4.16), the results from the present study are in close agreement with the widely used empirical relation between density ρ and ε'_r of polar firn, equation (4.16), which is reported to be associated with a standard error of ± 0.03 in ε'_r [Kovacs *et al.*, 1995]. The pronounced dielectric contrast due to density variations in firn can be expected to be reliably resolved using the present setup, which is important for a potential application to firn- and ice cores.

Regarding potential differences between natural and artificial ice samples, the same values of ε'_r were found when using an identical sample preparation procedure. In this case, residual air content, crystal orientation and stress states are expected to be identical to the artificial samples. Since impurities are very low in the natural and artificial ice samples, as indicated by comparable meltwater conductivities (1.7 $\mu\text{S}/\text{cm}$ and 2.4 $\mu\text{S}/\text{cm}$ of artificial and natural ice samples respectively), the observed identical values for ε'_r are not surprising.

In order to investigate on differences between natural and artificial samples (e.g. regarding crystal orientation and residual stresses), the influence of enclosed air bubbles has to be accounted for as to compare values for ε'_r of ice only. The accordingly corrected values agree within their error with the value obtained from using the artificial sample preparation method (“Ice 3”). However, for the ice samples (“Ice 1” and “Ice 2”), the error in density estimation results in a large uncertainty in ε'_r . Hence, no significant differences in ε'_r between artificial and natural ice samples could be detected so far. The ε'_r values for the natural ice samples are well within the range known from in-situ measurements [Jezek *et al.*, 1978; Robin, 1975].

The maximum anisotropy in ε'_r due to different crystal orientations of the samples is expected to be about 0.034 (Matsuoka *et al.* [1997b]), which is in principle close to the estimated uncertainty of our method. However, since it is a systematic effect, i.e. frequency-independent, it might still be detectable. In this preliminary investigation, a potential difference in ε'_r due to different crystal orientation between “Ice 1” and “Ice 2” could not be detected due to the large density errors. For future measurements, high-precision density data could be provided by means of gamma ray absorption measurements [Wilhelms, 1996]. Based on a further reduction of artefact disturbances in ε'_r as well as high-accuracy density data, repeating measurements on natural ice samples with a potential anisotropic crystal orientation fabric seems feasible.

4.8 Future perspective

Within the present work, the potential of the coaxial transmission line cell method has been demonstrated to determine ε'_r of pure ice at close to 1% accuracy. The coaxial cell setup was successfully adapted and refined for ice measurements in the MHz-range. Supplementing existing sparse data, new results for ε'_r of pure ice indicated the high-frequency end of the Debye-relaxation up to 10 MHz, but featured no evidence for additional dispersive effects within the range of uncertainty. In the upper MHz-range, results gave a constant value of $\varepsilon'_{||} = (3.18 \pm 0.01)$. The sensitivity of the present setup regarding variations in acidity and density of the sample has been demonstrated. Further refinements of the setup have been suggested, primarily aiming at (i) enhanced accuracy by reducing measurement artefacts and (ii) improving the permittivity computation by integrating the developed forward model. These refinements should allow for a even more accurate investigation on $\varepsilon'_r(\omega)$ in the MHz-range, and potentially even $\varepsilon''_r(\omega)$. An adequate temperature control would provide a detailed investigation on the influence of acidity, temperature, and their combined effects, especially regarding shifts in relaxation frequency and dispersive effects in the MHz-range.

The present operational coaxial transmission line as well as a future refined version may contribute in the context of a continuative, instrumentally improved study on dielectric

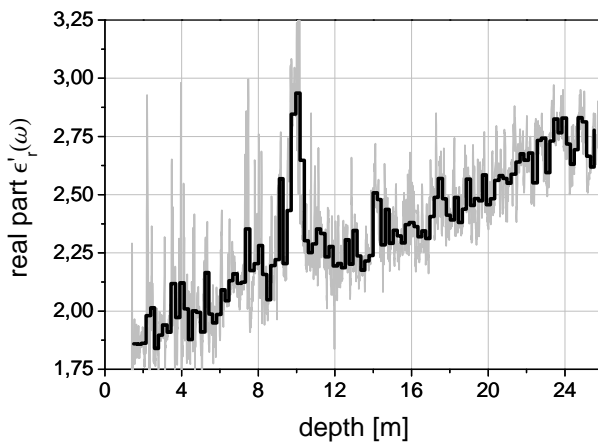


Figure 4.17: Permittivity of the Colle Gnifetti firn core KCO. Shown is the ϵ'_r -profile obtained from high-resolution DEP measurements (gray, data from Jepsen [2010]). The high-resolution data were subsampled to a depth-resolution of 20 cm, the length of the coaxial cell sample holder (black).

ice properties (including studying the influence of different physical parameters). For this purpose, a combination of electromagnetic methods seems promising, dedicated to performing measurements over a broad frequency range (e.g. Hz-GHz). Aimed at a further improved investigation on $\epsilon_r^*(\omega)$ in the MHz-window of such a study, a feasible combination of methods could comprise the present coaxial transmission line for frequency-dependent measurements together with high-accuracy, but narrow-band resonator and waveguide measurements. The suggested broadband, multi-method approach to ice permittivity would reflect the importance of ice within the wide context of electromagnetic remote sensing techniques in environmental applications. This wide context comprises not only glaciological applications, but also investigations of permafrost soils (e.g. Wollschläger *et al.* [2010]) and planetary research, e.g. of Mars, such as satellite-based GPR (i.e. the MARSIS and SHARAD projects) [Picardi *et al.*, 2004; Seu *et al.*, 2007] as well as the characterisation of the binding state of water under martian conditions with dielectric spectroscopy [Lorek, 2008; Lorek *et al.*, 2011].

Regarding further contribution of the present setup within glaciological applications, a dedicated sample preparation procedure has been developed for measuring natural firn and ice samples. The naturally occurring variability of ϵ'_r due to density variations can be adequately resolved. On this basis, a first deployment of the present setup on firn- and ice cores appears feasible. Ice core measurements could provide a direct validation against the established dielectric profiling technique (DEP), in a mutual sense:

- The permittivity-data obtained from DEP and the present method would allow for an assessment of the conventional transfer of the kHz-DEP data into the MHz-range.
- The DEP measurements would comprise an adequate benchmark to assess the potential of the present method for deployment on ice cores, especially in polar studies.

A first possibility for such a validation is provided by the firn core KCO from Colle Gnifetti, which still exists as an entire cylindrical core, on which DEP- and high-resolution density measurements have already been performed [Jepsen, 2010]. Sub-sampling the DEP-data to the 20 cm depth resolution of the coaxial cell determined by the length of the sample holder, shows that most of the natural variability in ϵ'_r could be successfully resolved by the present method (Figure 4.17). In combination with further refinements of the method, its application to the KCO firn core would be an adequate next step. Based on the findings of the present study and the experience from the envisaged firn core measurements, a new dedicated cell may be eventually manufactured specifically designed for frequency dependent permittivity measurements on ice cores.

Bibliography

- [Agilent 2004] Agilent: De-embedding and Embedding S-parameter Networks Using a Vector Network Analyzer. *Application note* 1364-1 . 2004
- [Aizen *et al.* 2005] Aizen, V. ; Aizen, E. ; Fujita, K. ; ; Nikitin, S. ; Kreutz, K. ; Takeuchi, N.: Stable-Isotope time series and precipitation origin from firn-core and snow samples, Altai glaciers, Siberia. *Journal of Glaciology* 175 , p. 637–655. 2005
- [Alean *et al.* 1983] Alean, J. ; Haeberli, W. ; Schädler, B.: Snow accumulation, firn temperature and solar radiation in the area of the Colle Gnifetti core drilling site (Monte Rosa, Swiss Alps): distribution patterns and interrelationships. *Zeitschrift für Gletscherkunde und Glazialgeologie* 19(2) , p. 131–147. 1983
- [Allen and Smith 1996] Allen, M. R. ; Smith, L. A.: Monte Carlo SSA: Detecting irregular oscillations in the presence of colored noise. *Journal of Climate* 9 , p. 3373–3404. 1996
- [Andersen *et al.* 2004] Andersen, K. K. ; Azuma, N. ; Barnola, J.-M. ; Bigler, M. ; Biscaye, P. ; Caillon, N. ; Chappellaz, J. ; Clausen, H. B. ; Dahl-Jensen, D. ; Fischer, H. ; Flückiger, J. ; Fritzsche, D. ; Fujii, Y. ; Goto-Azuma, K. ; Gronvold, K. ; Gundestrup, N. S. ; Hansson, M. ; Huber, C. ; Hvidberg, C. S. ; Johnsen, S. J. ; Jonsell, U. ; Jouzel, J. ; Kipfstuhl, S. ; Landais, A. ; Leuenberger, M. ; Lorrain, R. ; Masson-Delmotte, V. ; Miller, H. ; Motoyama, H. ; Narita, H. ; Popp, T. ; Rasmussen, S. O. ; Raynaud, D. ; Röthlisberger, R. ; Ruth, U. ; Samyn, D. ; Schwander, J. ; Shoji, H. ; L., Siggard-Andersen M. ; Steffensen, J. P. ; Stocker, T. F. ; Sveinbjörnsdottir, A. E. ; Svensson, A. ; Takata, M. ; Tison, J.-L. ; Thorsteinsson, Th. ; Watanabe, O. ; Wilhelm, F. ; White, J. W. C.: High-resolution record of Northern Hemisphere climate extending into the last interglacial period. *Nature* 431 , p. 147–151. 2004
- [Andersen *et al.* 2006] Andersen, K. K. ; Ditlevsen, P. D. ; Rasmussen, S. O. ; Clausen, H. B. ; Vinther, B. M. ; Johnsen, S. J. ; Steffensen, J. P.: Retrieving a common accumulation record from Greenland ice cores for the past 1800 years. *Journal of Geophysical Research (Atmospheres)* 111 , p. D15106. 2006
- [Armbruster 2000] Armbruster, M.: Stratigraphische Datierung hoch-alpiner Eisbohrkerne über die letzten 1000 Jahre, IUP Heidelberg, Diploma thesis, 2000

- [Auer *et al.* 2007] Auer, I. ; Böhm, R. ; Jurkovic, A. ; Lipa, W. ; Orlik, A. ; Potzmann, R. ; Schöner, W. ; Ungersböck, M. ; Matulla, C. ; Briffa, K. ; Jones, P. ; Efthymiadis, D. ; Brunetti, M. ; Nanni, T. ; Maugeri, M. ; Mercalli, L. ; Mestre, O. ; Moisselin, J.-M. ; Begert, M. ; Müller-Westermeier, G. ; Kveton, V. ; Bochnicek, O. ; Stastny, P. ; Lapin, M. ; Szalai, S. ; Szentimrey, T. ; Cegnar, T. ; Dolinar, M. ; Gajic-Capka, M. ; Zaninovic, K. ; Majstorovic, Z. ; Nieplova, E.: HISTALP - historical instrumental climatological surface time series of the Greater Alpine Region. *International Journal of Climatology* 27 , p. 17–46. 2007
- [Auty and Cole 1952] Auty, R.P. ; Cole, R. H.: Dielectric Properties of Ice and D₂O. *Journal of Chemical Physics* 20(8) , p. 1309–1314. 1952
- [Azuma *et al.* 2000] Azuma, N. ; Wang, Y. ; Yoshida, Y. ; Narita, H. ; Hondoh, T. ; Shoji, H. ; Watanabe, O.: *The Physics of Ice Core Records*. chap. Crystallographic analysis of the Dome Fuji ice core, p. 45–61, Hokkaido University Press, Sapporo, Japan, 2000
- [Baisch and Bokelmann 1999] Baisch, S. ; Bokelmann, G.H.R.: Spectral analysis with incomplete time series: an example from seismology. *Computers & Geoscience* 255 , p. 739–750. 1999
- [Baker-Jarvis *et al.* 1990] Baker-Jarvis, J. ; Vanzura, E. J. ; Kissick, W. A.: Improved technique for determining complex permittivity with the transmission/reflection method. *IEEE Transactions on Microwave Theory and Techniques* 38(8) , p. 1096–1103. 1990
- [Baker-Jarvis 1990] Baker-Jarvis, James: Transmission/Reflection and short circuit line permittivity measurements / National Institute of Standards and Technology - NIST TN1341. 1990. – research report
- [Baker-Jarvis *et al.* 2004] Baker-Jarvis, James ; Janezic, Michael D. ; Riddle, Bill ; Johnk, Robert T. ; Kabos, Pavel ; Holloway, Christopher L. ; Geyer, Richard G. ; Grosvenor, Chriss A.: Measuring the Permittivity and Permeability of Lossy Materials: Solids, Liquids, Metals, Building Materials, and Negative-Index Materials / National Institute of Standards and Technology - NIST TN1536. 2004. – research report
- [Bamber *et al.* 2001] Bamber, J.L. ; Layberry, R.L. ; Gogineni, S.P.: A new ice thickness and bed dataset for the Greenland ice sheet. 1. Measurement, data reduction, and errors. *Journal of Geophysical Research* 106(D24) , p. 33,773–33,780. 2001
- [Binder *et al.* 2009] Binder, D. ; Brückel, E. ; Roch, K.H. ; Behm, M. ; Schöner, W. ; Hynek, B.: Determination of total ice volume and ice-thickness distribution of two glaciers in the Hohe Tauern region, Eastern Alps, from GPR data. *Annals of Glaciology* 50(51) , p. 71–79. 2009

- [Bogorodsky *et al.* 1985] Bogorodsky, V.V. ; Bentley, C.R. ; Gudmandsen, P. E.: Radioglaciology. D. Reidel, 1985
- [Bohleber 2008] Bohleber, P.: Age distribution and $\delta^{18}O$ variability in a low accumulation Alpine ice core: perspective for paleoclimate studies, IUP Heidelberg, Diploma thesis, 2008
- [Böhlert 2005] Böhlert, R.: Glaziologische Untersuchungen auf dem Colle Gnifetti und auf dem Mt. Blanc: Ermittlung der Eisdickenverteilung und interner Schichten mittels Georadar, Geographisches Institut der Universität Zürich, Diploma thesis, 2005
- [Böhm *et al.* 2010] Böhm, R. ; Jones, P.D. ; J., Hiebl ; Frank, D. ; Brunetti, M. ; Mageri, M.: The early instrumental warm-bias: a solution for long central european temperature series 1760-2007. *Climatic Change* 101 , p. 41–67. 2010
- [Börner 2006] Börner, F.: *Groundwater Geophysics, A Tool for Hydrogeology*. chap. Complex Conductivity Measurements, p. 119–153, Springer, 2006
- [Champlin *et al.* 1978] Champlin, G.C. ; Glen, J.W. ; Paren, J.G.: Theoretical models for interpreting the electric behaviour of HF-doped ice. *Journal of Glaciology* 21(85) , p. 123–142. 1978
- [Chaudhuri and Marron 1999] Chaudhuri, P. ; Marron, J. S.: SiZer for exploration of structures in curves. *J. Amer. Statistical Assoc.* 94(447) , p. 807–823. 1999
- [Chimani *et al.* 2011] Chimani, B. ; Böhm, R. ; Matulla, C. ; Ganekind, M.: Development of a longterm dataset of solid/liquid precipitation. *Advances in Science and Research* 6 , p. 39–43. 2011
- [Clausen and Hammer 1988] Clausen, H.B. ; Hammer, C.U.: The Laki and Tambora eruptions as revealed in Greenland ice cores from 11 locations. *Annals of Glaciology* 10(55) , p. 16–22. 1988
- [Crüger *et al.* 2004] Crüger, T. ; Fischer, H. ; Storch, H. von: What do accumulation records of single ice cores in Greenland represent? *Journal of Geophysical Research* 109(D21110) . 2004
- [Dansgaard 1964] Dansgaard, W.: Stable isotopes in precipitation. *Tellus* 16 , p. 436–468. 1964
- [Debye 1929] Debye, P.: Polare molekeln. S. Hirzel, 1929
- [Diez 2010] Diez, A.: Ice properties derived from reflection seismics at a cold alpine saddle and a local antarctic dome, Karlsruher Institut für Technologie, Diploma thesis, 2010

- [Dowdeswell and Evans 2004] Dowdeswell, J.A. ; Evans, S.: Investigations on the form and flow of ice sheets and glaciers using radio-echo sounding. *Rep. Prog. Phys.* 67 , p. 1821–1861. 2004
- [Drews *et al.* 2009] Drews, R. ; Eisen, O. ; Weikusat, I. ; Kipfstuhl, S. ; Lambrecht, A. ; Steinhage, D. ; Wilhelms, F. ; Miller, H.: Layer disturbances and the radio-echo free zone in ice sheets. *The Cryosphere* 3 , p. 195–203. 2009
- [Ebisuzaki 1997] Ebisuzaki, W.: A Method to Estimate the Statistical Significance of a Correlation When the Data Are Serially Correlated. *Journal of Climate* 10(3) , p. 2147–2153. 1997
- [Efron 1979] Efron, B.: The 1977 Riez Lecture, Bootstrap methods: Another look at the jackknife. *The Annals of Statistics* 7(1) , p. 1–26. 1979
- [Efthymiadis *et al.* 2006] Efthymiadis, D. ; Jones, P.D. ; Briffa, K.R. ; Auer, I. ; Böhm, R. ; Schöner, W. ; Frei, C. ; Schmidli, J.: Construction of a 10-min-gridded precipitation data set for the Greater Alpine Region for 1800-2003. *Journal of Geophysical Research* 110(D01105) . 2006
- [Eichler *et al.* 2000] Eichler, A. ; Schwikowski, M. ; Gäggeler, H.W. ; Furrer, V. ; Synal, H.-A. ; Beer, J. ; Saurer, M. ; Funk, M.: Glaciochemical dating of an ice core from upper Grenzgletscher (4200 m a.s.l.). *Journal of Glaciology* 46(154) , p. 507–515. 2000
- [Eisen *et al.* 2007] Eisen, O. ; Hamann, I. ; Kipfstuhl, S. ; Steinhage, D. ; Wilhelms, F.: Direct evidence for continuous radar reflector originating from changes in crystal-orientation fabric. *The Cryosphere* 1 , p. 1–10. 2007
- [Eisen *et al.* 2003a] Eisen, O. ; Nixdorf, U. ; Keck, L. ; Wagenbach, D.: Alpine ice cores and ground penetrating radar: combined investigations for glaciological and climatic interpretations of a cold Alpine ice body. *Tellus* 55B , p. 1007–1017. 2003
- [Eisen *et al.* 2003b] Eisen, O. ; Wilhelms, F. ; Nixdorf, U. ; Miller, H.: Revealing the nature of radar reflections in ice: DEP-based FDTD forward modeling. *Geophysical Research Letters* 30(5) , p. 22–122–4. 2003
- [Eisen *et al.* 2006] Eisen, O. ; Wilhelms, F. ; Steinhage, D. ; Schwander, J.: Improved method to determine radio-echo sounding reflector depths from ice-core profiles of permittivity and conductivity. *Journal of Glaciology* 52(177) , p. 229–310. 2006
- [Elsässer *et al.* 2011] Elsässer, C. ; Wagenbach, D. ; Weller, R. ; Auer, M. ; Wallner, A. ; Christl, M.: Continuous 25-yr aerosol records at coastal Antarctica. *Tellus B* (. 2011

- [Evans 1965] Evans, S.: Dielectric properties of ice and snow - a review. *Journal of Glaciology* 5 (42) , p. 773–792. 1965
- [Fahnestock *et al.* 2001] Fahnestock, M. ; Abdalati, W. ; Luo, S. ; Gogineni, S.: Internal layer tracing and age-depth-accumulation relationships for the northern Greenland ice sheet. *Journal of Geophysical Research* 106(D24) , p. 33,789–33,797. 2001
- [Fischer *et al.* 1998] Fischer, H. ; Werner, M. ; Wagenbach, D. ; Schwager, M. ; Thorsteinsson, T. ; Wilhelms, F. ; Kipfstuhl, J. ; Sommer, S.: Little Ice Age Clearly Recorded in Northern Greenland Ice Cores. *Geophysical Research Letters* 25(10) , p. 1749–1752. 1998
- [Fisher and Koerner 1988] Fisher, D. A. ; Koerner, R. M.: The effects of wind on $\delta(^{18}O)$ and accumulation give an inferred record of seasonal δ amplitude from the Agassiz ice cap, Ellesmere Island, Canada. *Annals of Glaciology* 10 , p. 34–37. 1988
- [Fisher and Koerner 1994] Fisher, D. A. ; Koerner, R. M.: Signal and noise in four ice-core records from the Agassiz Ice Cap, Ellesmere Island, Canada: details of the last millennium for stable isotopes, melt and solid conductivity. *The Holocene* 4(2) , p. 113–120. 1994
- [Fisher *et al.* 1998] Fisher, D. A. ; Koerner, R. M. ; Bourgeois, J. C. ; Zielinski, G. ; Wake, C. ; Hammer, C. U. ; Clausen, H. B. ; Gundestrup, N. ; Johnsen, S. ; Goto-Azuma, K. ; Hondoh, T. ; Blake, E. ; Gerasimoff, M.: Penny Ice Cap Cores, Baffin Island, Canada, and the Wisconsinan Foxe Dome Connection: Two States of Hudson Bay Ice Cover. *Science* 279(5351) , p. 692–695. 1998
- [Fisher *et al.* 1983] Fisher, D. A. ; Koerner, R. M. ; Paterson, W. S. B. ; Dansgaard, W. ; Gundestrup, N. ; Reeh, N.: Effect of wind scouring on climatic records from ice-core oxygen-isotope profiles. *Nature* 301 , p. 205–209. 1983
- [Fisher *et al.* 1985] Fisher, D.A. ; Reeh, N. ; Clausen, H.B.: Stratigraphic noise in time series derived from ice cores. *Annals of Glaciology* 7 , p. 76–83. 1985
- [Folgero 1996] Folgero, K.: Bilinear calibration of coaxial transmission/reflection cells for permittivity measurement of low-loss liquids. *Measurement Science and Technology* 7(9) , p. 1260–1269. 1996
- [Folgero 1998] Folgero, K.: Broad-band dielectric spectroscopy of low-permittivity fluids using one measurement cell. *IEEE Transactions on Instrumentation and Measurement* 47(4) , p. 881–885. 1998
- [Fricke and O’Neil 1999] Fricke, H. ; O’Neil, J.: The correlation between $^{18}O/^{16}O$ ratios of meteoric water and surface temperature: its use in investigating terrestrial climate change over geologic time. *Earth Planet. Sci. Lett.* 170 , p. 181–196. 1999

- [Fujita *et al.* 2004] Fujita, K. ; Takeuchi, N. ; Aizen, V. ; Nikitin, S.: Glaciological observations on the plateau of Belukha Glacier in the Altai Mountains, Russia from 2001-2003. *Bulletin of Glaciological Research* 21 , p. 57–64. 2004
- [Fujita and Mae 1994] Fujita, S. ; Mae, S.: Causes and nature of ice-sheet radio-echo internal reflections estimated from the dielectric properties of ice. *Annals of Glaciology* 20 , p. 80–86. 1994
- [Fujita *et al.* 1993] Fujita, S. ; Mae, S. ; Matsuoka, T.: Dielectric anisotropy in ice Ih at 9.7 GHz. *Annals of Glaciology* 17 , p. 276–280. 1993
- [Fujita *et al.* 2006] Fujita, S. ; Maeno, H. ; Matsuoka, K.: Radio-wave depolarization and scattering within ice sheets: a matrix based model to link radar and ice-core measurements and its application. *Journal of Glaciology* 52(178) , p. 407–425. 2006
- [Fujita *et al.* 1999] Fujita, S. ; Maeno, H. ; Uratsuka, S. ; Furukawa, T. ; Mae, S. ; Fujii, Y. ; Watanabe, O.: Nature of radio echo layering in the Antarctic ice sheet detected by a two-frequency experiment. *Journal of Geophysical Research* 104(B6) , p. 13,013–13,024. 1999
- [Fujita *et al.* 2000] Fujita, S. ; Matsuoka, T. ; Ishida, T. ; Matsuoka, K. ; Mae, S.: *The Physics of Ice Core Records*. chap. A summary of the complex dielectric permittivity of ice in the megahertz range and its application for radar sounding of polar ice sheets, p. 185–212, Hokkaido University Press, Sapporo, Japan, 2000
- [Fujita *et al.* 1992] Fujita, S. ; Shiraishi, M. ; Mae, S.: Measurement on the dielectric properties of acid-doped ice at 9.7 GHz. *IEEE Transactions on Geoscience and Remote Sensing* 30(4) , p. 799–803. 1992
- [Geil *et al.* 2005] Geil, B. ; Kirschgen, T.M. ; Fujara, F.: Mechanism of proton transport in hexagonal ice. *Physical Review B* 72 , p. 014304 1–10. 2005
- [Glen and Paren 1975] Glen, J.W. ; Paren, J.G.: The electrical properties of snow and ice. *Journal of Glaciology* 15(73) , p. 15–38. 1975
- [Gorriti and Slob 2005a] Gorriti, A. ; Slob, E.: A new tool for S-parameters measurements and permittivity reconstruction. *IEEE Transactions on Geoscience and Remote Sensing* 43(8) , p. 1727–1735. 2005
- [Gorriti and Slob 2005b] Gorriti, A.G. ; Slob, E.C.: Comparison of the different reconstruction techniques of permittivity from S-parameters. *IEEE Transactions on Geoscience and Remote Sensing* 43(9) , p. 2051–2057. 2005
- [Gorriti and Slob 2005c] Gorriti, A.G. ; Slob, E.C.: Synthesis of all known analytical permittivity reconstruction techniques of nonmagnetic materials from reflection and

- transmission measurements. *IEEE Geosci. Remote Sens. Lett.* 2(4) , p. 433–436. 2005
- [Gough 1972] Gough, S.R.: A Low Temperature Dielectric Cell and the Permittivity of Hexagonal Ice to 2K. *Canadian Journal of Chemistry* 50 , p. 3046–3051. 1972
- [Gränicher *et al.* 1957] Gränicher, H. ; Jaccard, C. ; Scherrer, P. ; Steinemann, A.: Dielectric relaxation and the electrical conductivity of ice crystals. *Discussions of the Faraday Society* 23 , p. 50–62. 1957
- [Gregory and Clarke 2009] Gregory, A.P. ; Clarke, R.N.: Tables of the Complex Permittivity of Dielectric Reference Liquids at Frequencies up to 5 GHz / National Physical Laboratory. 2009. – research report
- [Gross *et al.* 1978] Gross, W. ; Hayslip, I.C. ; Hoy, R. N.: Electrical conductivity and relaxation in ice crystals with known impurity content. *Journal of Glaciology* 21(85) , p. 143–160. 1978
- [Gudmandsen 1975] Gudmandsen, P.: Layer echos in polar ice sheets. *Journal of Glaciology* 15(73) , p. 95–101. 1975
- [Haeberli and Funk 1991] Haeberli, W. ; Funk, M.: Borehole temperatures at the Colle Gnifetti core-drilling site (Monte Rosa, Swiss Alps). *Journal of Glaciology* 37(125) , p. 37–46. 1991
- [Haeberli *et al.* 1988] Haeberli, W. ; Schmid, W. ; Wagenbach, D.: On the geometry, flow and age of firn and ice at the Colle Gnifetti core drilling site (Monte Rosa, Swiss Alps). *Zeitschrift für Gletscherkunde und Glazialgeologie* 24/1 , p. 1–19. 1988
- [Hammer *et al.* 1980] Hammer, C.U. ; Clausen, H.B. ; Dansgaard, W.: Greenland ice sheet evidence of post-glacial volcanism and its climatic impact. *Nature* 288 , p. 230–235. 1980
- [Hempel *et al.* 2000] Hempel, L. ; Thyssen, F. ; Gundestrup, N. ; Clausen, H.B. ; Miller, H.: A comparison of radio-echo sounding data and electrical conductivity of the GRIP ice core. *Journal of Glaciology* 46 , p. 369–374. 2000
- [Hiebl *et al.* 2009] Hiebl, J. ; Auer, I. ; Böhm, R. ; Schöner, W. ; Maugeri, M. ; Lentini, G. ; Spinoni, J. ; Brunetti, M. ; Nanni, T. ; Tadic, M.P. ; Bihari, Z. ; Dolinar, M. ; Müller-Westermeier, G.: A high-resolution 1961-1990 monthly temperature climatology for the greater Alpine region. *Meteorologische Zeitschrift* 18(5) , p. 507–530. 2009
- [von Hippel *et al.* 1972] Hippel, A. von ; Mykolajewycz, R. ; Runck, A. H. ; Westphal, W. B.: Dielectric and Mechanical Response of Ice Ih Single Crystals and Its Interpretation. 57(6) , p. 2560–2571. 1972

- [Hoelzle *et al.* 2011] Hoelzle, M. ; Darms, G. ; Lüthi, M. P. ; Suter, S.: Evidence of accelerated englacial warming in the Monte Rosa area, Switzerland/Italy. *The Cryosphere* 5(1) , p. 231–243. 2011
- [Hoffmann *et al.* 2006] Hoffmann, G. ; Cuntz, M. ; Jouzel, J. ; Werner, M.: A systematic comparison between the IAEA/GNIP isotope network and Atmospheric General Circulation Models: How much climate information is in the water isotopes? Aggarwal, P.K. (ed.) ; Gat, J.R. (ed.) ; Froehlich, K.F.O. (ed.): *Isotopes in the Water Cycle – Past, Present and Future of a Developing Science*, Springer, 2006
- [Hoppe 2009] Hoppe, M.: Frequenzabhängige Messungen der dielektrischen Eigenschaften von Eis mit einer Koaxial-Zelle, IUP Heidelberg, Diploma thesis, 2009
- [Jackson 1962] Jackson, J. D.: *Classical electrodynamics*. Wiley, 1962
- [Jackson and Dunlevy 1988] Jackson, J. D. ; Dunlevy, J. A.: Orthogonal Least Squares and the Interchangeability of Alternative Proxy Variables in the Social Sciences. *Journal of the Royal Statistical Society. Series D (The Statistician)* 37(1) , p. 7–14. 1988
- [Jacobel and Welch 2005] Jacobel, R.W. ; Welch, B.C: A time marker at 17.5 kyr BP detected throughout West Antarctica. *Annals of Glaciology* 41(1) , p. 47–51. 2005
- [Jenk *et al.* 2009] Jenk, T. M. ; Szidat, S. ; Bolius, D. ; Sigl, M. ; Gäggeler, H. W. ; Wacker, L. ; Ruff, M. ; Barbante, C. ; Boutron, C. F. ; Schwikowski, M.: A novel radiocarbon dating technique applied to an ice core from the Alps indicating late Pleistocene ages. *Journal of Geophysical Research* 114 , p. D14305. 2009
- [Jepsen 2010] Jepsen, K.: Leitfähigkeits- und Dichtemessungen an einem alpinen Eiskern, Georg-August-Universität Göttingen, Bachelor thesis, 2010
- [Jezek *et al.* 1978] Jezek, K.C. ; Clough, J.W. ; Bentley, C.R. ; Shabtaie, S.: Dielectric Permittivity of Glacier Ice Measured in situ by Radar Wide-angle Reflection. *Journal of Glaciology* 21(85) , p. 315–329. 1978
- [Jezek and Roeloffs 1983] Jezek, K.C. ; Roeloffs, E.A.: Measurements of radar wave speeds in polar glaciers using a down-hole radar target technique. *Cold Regions Science and Technology* 8 , p. 199–208. 1983
- [Johari 1976] Johari, G.P.: The dielectric properties of H₂O and D₂O Ice Ih at MHz frequencies. *Journal of Chemical Physics* 64 , p. 3998–4005. 1976
- [Johari and Charette 1975] Johari, G.P. ; Charette, P.A.: The Permittivity and Attenuation in Polycrystalline and single-crystal ice Ih at 35 and 60 MHz. *Journal of Glaciology* 71 , p. 293–303. 1975

- [Johari and Jones 1978] Johari, G.P. ; Jones, S.J.: The Orientation Polarization in Hexagonal Ice Parallel and Perpendicular to the c-axis. *Journal of Glaciology* 21 (85) , p. 259–276. 1978
- [Johari 1981] Johari, U.P.: The spectrum of ice. *Contemporary Physics*, 22, 1981. – 613–642 S
- [Johnsen *et al.* 1989] Johnsen, S. J. ; Dansgaard, W. ; White, J. W. C.: The origin of Arctic precipitation under present and glacial conditions. 4, p. 452–468. 1989
- [Johnsen *et al.* 2000] Johnsen, S.J. ; Clausen, H.B. ; Cuffey, K.M. ; Hoffmann, G. ; Schwander, J. ; Creyts, T.: *The Physics of Ice Core Records*. chap. Diffusion of stable isotopes in polar firn and ice: The isotope effect in firn diffusion, p. 121–140, Hokkaido University Press, Sapporo, Japan, 2000
- [Jouzel *et al.* 1997] Jouzel, J. ; Alley, R. B. ; Cuffey, K. M. ; Dansgaard, W. ; Grootes, P. ; Hoffmann, S. J. ; Koster, R. D. ; Shurman, C. A. ; Stievenard, M. ; Stuiver, M. ; White, J.: Validity of the temperature reconstruction from water isotopes in ice cores. *C12*, p. 26471–26487. 1997
- [Kaatze 2007] Kaatze, U.: Reference liquids for the calibrations of dielectric sensors and measurement instruments. *Measurement Science and Technology* 18 , p. 967–976. 2007
- [Keck 2001] Keck, L.: Climate significance of stable isotope records from Alpine ice cores, IUP Heidelberg, PhD thesis, 2001
- [Knüsel *et al.* 2003] Knüsel, S. ; Ginot, P. ; Schotterer, U. ; Schwikowski, M. ; Gäggeler, H. W. ; Francou, B. ; Petit, J. R. ; Simões, J. C. ; Taupin, J. D.: Dating of two nearby ice cores from the Illimani, Bolivia. *Journal of Geophysical Research (Atmospheres)* 108 , p. 4181. 2003
- [Konrad 2011] Konrad, H.: Characterization of the age distribution and the flow field of an Alpine glacier by a combination of simple flow modeling and ground-penetrating radar, IUP Heidelberg, Diploma thesis, 2011
- [Kovacs *et al.* 1995] Kovacs, A. ; Gow, A.J. ; Morey, R.M.: The in-situ dielectric constant of polar firn revisited. *Cold Regions Science and Technology* 23 , p. 245–256. 1995
- [Lambert *et al.* 2008] Lambert, F. ; Delmonte, B. ; Petit, J. R. ; Bigler, M. ; Kaufmann, P. R. ; Hutterli, M. A. ; Stocker, T. F. ; Ruth, U. ; Steffensen, J. P. ; Maggi, V.: Dust-climate couplings over the past 800,000 years from the EPICA Dome C ice core. *Nature* 452 , p. 616–619. 2008

- [Langway *et al.* 1988] Langway, C.C. ; Clausen, H.B. ; Hammer, C.U.: An inter-hemispheric volcanic time-marker in ice cores from Greenland and Antarctica. *Annals of Glaciology* 10(55) , p. 102–108. 1988
- [Levenberg 1944] Levenberg, K.: A Method for the Solution of Certain Problems in Least Squares. *Quart. Appl. Math.* 2 , p. 164–168. 1944
- [Leysinger-Vieli *et al.* 2007] Leysinger-Vieli, G.J.-M.C. ; Hindmarsh, R.C.A. ; Siegert, M. J.: Three-dimensional flow influences on radar layer stratigraphy. *Annals of Glaciology* 46 , p. 22–28. 2007
- [Leysinger-Vieli *et al.* 2011] Leysinger-Vieli, G.J.-M.C. ; Hindmarsh, R.C.A. ; Siegert, M. J. ; Bo, Sun: Time-dependence of the spatial pattern of accumulation rate in East Antarctica deduced from isochronic radar layers using a 3-D numerical ice flow model. *Journal of Geophysical Research* 116 . 2011
- [Leysinger-Vieli *et al.* 2004] Leysinger-Vieli, G.J.-M.C. ; Siegert, M. J. ; Payne, A.J.: Reconstructing ice-sheet accumulation rates at ridge B, East Antarctica. *Annals of Glaciology* 39 , p. 326–330. 2004
- [Looyenga 1965] Looyenga, H.: Dielectric Constants of Heterogenous Mixtures. *Physica* 31 , p. 401–406. 1965
- [Lorek 2008] Lorek, A.: Flüssiges unterkühltes Grenzflächenwasser in der Marsoberfläche, University of Potsdam, PhD thesis, in German, 2008
- [Lorek *et al.* 2011] Lorek, A. ; Wagner, N. ; deVera, J. P. P.: Estimation of ice and liquid water content of two martian analogue soils in a temperature range from 0°C to –70°C by means of dielectric spectroscopy. *7th European Conference on Mineralogy and Spectroscopy (4th – 7th September, 2011)*, Helmholtz-Zentrum, Potsdam, Deutsches GeoForschungsZentrum, 2011
- [Lüthi *et al.* 2008] Lüthi, D. ; Le Floc, M. ; Bereiter, B. ; Blunier, T. ; Barnola, J.-M. ; Siegenthaler, U. ; Raynaud, D. ; Jouzel, J. ; Fischer, H. ; Kawamura, K. ; Stocker, T. F.: High-resolution carbon dioxide concentration record 650,000–800,000 years before present. *Nature* 453 , p. 379–382. 2008
- [Lüthi and Funk 2000] Lüthi, M. ; Funk, M.: Dating ice cores from a high Alpine glacier with a flow model for cold firn. *Annals of Glaciology* 31 , p. 69–79. 2000
- [Lüthi 2000] Lüthi, M. P.: Rheology of cold firn and dynamics of a polythermal ice stream, Versuchsanstalt für Wasserbau, Hydrologie und Glaziologie der ETH Zürich, PhD thesis, 2000
- [Marquardt 1963] Marquardt, D.: An algorithm for least-squares estimation of non-linear parameters. *SIAM J. Applied Math* 11 , p. 431–441. 1963

- [Matsuoka *et al.* 1996] Matsuoka, K. ; Fujita, S. ; Matsuoka, T. ; Ishida, T. ; Hondoh, T. ; Mae, S.: Measurements of the complex permittivity of acid-doped ice from 1 kHz to 30 MHz -New data set for developing ice radar and dielectric analysis of ice cores-. *Proc. NIPR Symp. Polar Meteorol. Glaciol.* 10 , p. 25–35. 1996
- [Matsuoka *et al.* 2003] Matsuoka, K. ; Furukawa, T. ; Fujita, S. ; Maeno, H. ; Uratsuka, S. ; Naruse, R. ; Watanabe, O.: Crystal orientation fabrics within the Antarctic ice sheet revealed by a multipolarization plane and dual-frequency radar survey. *Journal of Geophysical Research (Solid Earth)* 108 , p. 2499. 2003
- [Matsuoka *et al.* 1997a] Matsuoka, T. ; Fujita, S. ; Mae, S.: Dielectric Properties of Ice Containing Ionic Impurities at Microwave Frequencies. *J. Phys. Chem. B* 101 , p. 6219–6222. 1997
- [Matsuoka *et al.* 1997b] Matsuoka, T. ; Fujita, S. ; Morishima, S. ; Mae, S.: Precise measurement of dielectric anisotropy in ice Ih at 39 GHz. *Journal of Applied Physics* 81(5) , p. 2344–2348. 1997
- [Mätzler 2006] Mätzler, C. ; Mätzler, C. (ed.) ; Rosenkranz, P.W. (ed.) ; Battaglia, A. (ed.) ; Wigneron, J.P. (ed.): *Thermal Microwave Radiation: Application from Remote Sensing*. Institute of Engineering and Technology, Stevenage, U.K., 2006
- [Mätzler and Wegmüller 1987] Mätzler, C. ; Wegmüller, U.: Dielectric properties of fresh-water ice at microwave frequencies. *J. Phys. D: Appl. Phys.* 20 , p. 1623–1630. 1987
- [May 2009] May, B.: Radiocarbon microanalysis on ice impurities for dating of Alpine glaciers, IUP Heidelberg, PhD thesis, 2009
- [Millar 1981] Millar, D.H.M.: Radio-echo layering in polar ice sheets and past volcanic activity. *Nature* 292(1) , p. 441–443. 1981
- [Miners *et al.* 2002] Miners, W.D. ; Wolff, E.W. ; Moore, J.C. ; Jacobel, R. ; Hempel, L.: Modelling the radio echo reflections inside the ice sheet at Summit, Greenland. *Journal of Geophysical Research* 107(B8) , p. 6–1–11. 2002
- [Mook 2006] Mook, W. G.: *Introduction to isotope hydrology*. Taylor & Francis Group, London, 2006
- [Moore and Paren 1987] Moore, J. C. ; Paren, J. G.: New technique for dielectric logging of Antarctic ice cores. *Journal de Physique (Colloque C1)* 48(3) , p. 155–160. 1987
- [Moore 1993] Moore, J.C.: High-resolution dielectric profiling of ice cores. *Journal of Glaciology* 132 , p. 245–248. 1993

- [Moore and Fujita 1993] Moore, J.C. ; Fujita, S.: Dielectric Properties of Ice Containing Acid and Sali Impurities at Microwave and Low Frequencies. *Journal of Geophysical Research* 98(B6) , p. 9769–9780. 1993
- [Moore *et al.* 1989] Moore, J.C. ; Mulvaney, R. ; Paren, J.G.: Dielectric stratigraphy of ice: A new technique for determining total ionic concentrations in polar ice cores. *Geophysical Research Letters* 16 (10) , p. 1177–1180. 1989
- [Moran *et al.* 2000] Moran, M. L. ; Greenfield, R. J. ; Arcone, S. A. ; Delaney, A. J.: Delineation of a complexly dipping temperate glacier bed using short-pulse radar arrays. 153, p. 274–286. 2000
- [Mudelsee 2003] Mudelsee, M.: Estimating Pearson's Correlation Coefficient With Bootstrap Confidence Interval From Serially Dependent Time Series. *Mathematical Geology* 35(6) , p. 651–665. 2003
- [Mudelsee 2010] Mudelsee, M.: Climate Time Series Analysis. Springer, 2010
- [Müller *et al.* 2010] Müller, K. ; Sinisalo, A. ; Anschütz, H. ; Hamran, S.-E. ; Hagen, J.-O. ; McConnell, J.R. ; Pasteris, D.R.: An 860 km surface mass-balance profile on the East Antarctic plateau derived by GPR. *Annals of Glaciology* 51(55) . 2010
- [Murray *et al.* 2000] Murray, T. ; Stuart, G.W. ; Fry, M. ; Gamble, N.H. ; Crabtree, M.D.: Englacial water distribution in a temperate glacier from surface and borehole radar velocity analysis. *Journal of Glaciology* 46(154) , p. 389–397. 2000
- [Nagle 1979] Nagle, J.F.: Theory of the dielectric constant of ice. *Chemical Physics* 43 , p. 317–328. 1979
- [Navarro and Eisen 2009] Navarro, F. ; Eisen, O.: Ground-penetrating radar in glaciological applications. Pellika, P. (ed.) ; Rees, G. (ed.): *Remote Sensing of Glaciers*. chapter 11. Taylor and Francis, 2009
- [Nicolson and Ross 1970] Nicolson, A.M. ; Ross, G.F.: Measurement of the Intrinsic Properties of Materials by Time Domain Techniques. *IEEE Trans. Instrum. Meas* IM-19 , p. 377–382. 1970
- [Oeschger *et al.* 1977] Oeschger, H. ; Schotterer, U. ; Haeberli, W. ; Röthlisberger, H.: First results from Alpine core drilling projects. *Zeitschrift für Gletscherkunde und Glazialgeologie* 13(1/2) , p. 193–208. 1977
- [Oswald 2000] Oswald, B.: Full wave solution of inverse electromagnetic problems - Application in environmental measurement techniques, Swiss Federal Institute of Technology, Dissertation, 2000

- [Oswald *et al.* 2006] Oswald, B. ; Doetsch, J. ; Roth, K.: A new computational technique for processing transmission-line measurements to determine dispersive dielectric properties. *Geophysics* 71(2) , p. K31–K35. 2006
- [Pälli *et al.* 2002] Pälli, A. ; Kohler, J.C. ; Isaksson, E. ; Moore, J.C. ; Pinglot, J.F. ; Pohjola, V.A. ; Samuelsson, H.: Spatial and temporal variability of snow accumulation using ground-penetrating radar and ice cores on a svalbard glacier. *Journal of Glaciology* 48 , p. 417–424. 2002
- [Paren 1981] Paren, J.G.: Reflection coefficient at a dielectric interface. *Journal of Glaciology* 27(95) , p. 203–204. 1981
- [Paren and Robin 1975] Paren, J.G. ; Robin, G. de Q.: Internal reflections in polar ice sheets. *Journal of Glaciology* 14(71) , p. 251–259. 1975
- [Paterson 1981] Paterson, W.S.B.: The physics of glaciers. 2nd edition. Pergamon Press, 1981
- [Pearson 1901] Pearson, K.: On Lines and Planes of Closest Fit to Systems of Points in Space. *Philosophical Magazine* 2 (6) , p. 559–572. 1901
- [Petit *et al.* 1999] Petit, J. R. ; Jouzel, J. ; Raynaud, D. ; Barkov, N. I. ; Barnola, J. M. ; Basile, I. ; Benders, M. ; Chappellaz, J. ; Davis, M. ; Delaygue, G. ; Delmotte, M. ; Kotlyakov, V. M. ; Legrand, L. ; Lipenkov, V. Y. ; Lorius, C. ; Pepin, L. ; Ritz, C. ; Saltzman, E. ; Stievenard, M.: Climate and atmospheric history of the past 420,000 years from the Vostok ice core, Antarctica. *Nature* 399 , p. 429 ff. 1999
- [Petrenko and Whitworth 1999] Petrenko, V.F. ; Whitworth, R.W.: The Physics of Glaciers. Oxford University Press, 1999
- [Picardi *et al.* 2004] Picardi, G. ; Biccari, D. ; Seu, R. ; Plaut, J. ; Johnson, W. T. K. ; Jordan, R. L. ; Safaeinili, A. ; Gurnett, D. A. ; Huff, R. ; Orosei, R. ; Bombaci, O. ; Calabrese, D. ; Zampolini, E.: MARSIS: Mars Advanced Radar for Subsurface and Ionosphere Sounding. A. Wilson & A. Chicarro (ed.): *Mars Express: the Scientific Payload* Vol. 1240, 2004, p. 51–69
- [Pichlmayer *et al.* 1998] Pichlmayer, F. ; Schöner, W. ; Seibert, P. ; Stichler, W. ; Wagenbach, D.: Stable isotope analysis for characterization of pollutants at high elevation Alpine sites. *Atmospheric Environment* 32 , p. 4075–4085. 1998
- [Preunkert 1994] Preunkert, S.: Glazio-chemische Verhältnisse des Colle Gnifetti im Vergleich zu seiner regionalen Umgebung, IUP Heidelberg, Diploma thesis, 1994
- [Preunkert *et al.* 2001] Preunkert, S. ; Legrand, M. ; Wagenbach, D.: Sulfate Trends in a Col du Dôme (French Alps) Ice Core: A Record of Anthropogenic Sulfate Levels in the European Mid-Troposphere. *J. Geophys. Res.* 106(D23) , p. 31991–32004. 2001

- [Preunkert *et al.* 2000] Preunkert, S. ; Wagenbach, D. ; Legrand, L. ; Vincent, C.: Col du Dôme (Mt Blanc Massif, French Alps) suitability for ice-core studies in relation with past atmospheric chemistry over Europe. *Tellus* 52B , p. 993–1012. 2000
- [Riddle *et al.* 2003] Riddle, B. ; Baker-Jarvis, J. ; Krupka, J.: Complex Permittivity Measurements of Common Plastics Over Variable Temperatures. *IEEE Transactions on microwave theory and techniques* 51(3) , p. 727–733. 2003
- [Robin 1975] Robin, G.Q.: Velocity of Radio Waves in Ice by Means of a Bore-hole Interferometric Technique. *Journal of Glaciology* 15(73) , p. 151–159. 1975
- [Robin *et al.* 1969] Robin, G.Q. ; Evans, S. ; Bailey, J.T.: Interpretation of radio echo sounding in polar ice sheets. *Philos. Trans. R. Soc. London Ser. A* 146 , p. 437–505. 1969
- [Roth *et al.* 1990] Roth, K. ; Schulin, R. ; Flühler, H. ; Attinger, W.: Calibration of Time Domain Reflectometry for Water Content Measurement Using a Composite Dielectric Approach. *Water Resources Research* 26(10) , p. 2267–2273. 1990
- [Rowe *et al.* 2001] Rowe, R.K. ; Shang, J.Q. ; Xie, Y.: Complex permittivity measurement system for detecting soil contamination. *Canadian Geotechnical Journal* 38(3) , p. 498–506. 2001
- [Rozanski *et al.* 1992] Rozanski, K. ; Araguas-Araguas, L. ; Gonfiantini, R.: Relation Between Long-Term Trends of Oxygen-18 Isotope Composition of Precipitation and Climate. *Science* 258(5084) , p. 981–985. 1992
- [Scargle 1989] Scargle, J.: Studies in astronomical time series analysis. III. Fourier transforms, Autocorrelation functions, and cross-correlation functions of unevenly spaced data. *The Astrophysical Journal* 343 , p. 874–887. 1989
- [Schäfer 1995] Schäfer, J.: Rekonstruktion bio-chemischer Spurenstoffkreisläufe anhand eines alpinen Eisbohrkerns, IUP Heidelberg, Diploma thesis, 1995
- [Scholze 1998] Scholze, M.: Analyse der visuellen Stratigraphie alpiner Eisbohrkerne mittels digitaler Bildverarbeitung, IUP Heidelberg, Diploma thesis, 1998
- [Schotterer *et al.* 1978] Schotterer, U. ; Haeblerli, W. ; Good, W.: Datierung von kaltem Firn und Eis in einem Bohrkern vom Colle Gnifetti, Monte Rosa. Birkhäuser, 1978
- [Schulz and Mudelsee 2002] Schulz, M. ; Mudelsee, M.: REDFIT: estimating red-noise spectra directly from unevenly spaced paleoclimatic time series. *Computers & Geoscience* 28 , p. 421–426. 2002

- [Schulz and Stattegger 1997] Schulz, M. ; Stattegger, K.: SPECTRUM: Spectral Analysis of unevenly spaced paleoclimatic time series. *Computers & Geoscience* 23(9) , p. 929–945. 1997
- [Schwerzmann *et al.* 2006] Schwerzmann, A. ; Funk, M. ; Blatter, H. ; Lüthi, M. ; Schwikowski, M. ; Palmer, A.: A method to reconstruct past accumulation rates in alpine firn regions: A study on Fiescherhorn, Swiss Alps. *Journal of Geophysical Research* 111 , p. F01014. 2006
- [Schwing *et al.* 2010] Schwing, M. ; Scheuermann, A. ; Wagner, N.: Experimental investigation of dielectric parameters of soil during shrinkage. Kupfer, K. (ed.): *Proc 1st European Conference on Moisture Measurement, Aquametry 2010*, MFPA, Weimar, 2010, p. 511–519
- [SeaSolve 2003] SeaSolve, Software Inc.: AutoSignal - User's Guide, 2003
- [Seu *et al.* 2007] Seu, R. ; Phillips, R. J. ; Alberti, G. ; Biccari, D. ; Bonaventura, F. ; Bortone, M. ; Calabrese, D. ; Campbell, B. A. ; Cartacci, M. ; Carter, L. M. ; Catallo, C. ; Croce, A. ; Croci, R. ; Cutigni, M. ; Placido, A. D. ; Dinardo, S. ; Federico, C. ; Flamini, E. ; Fois, F. ; Frigeri, A. ; Fuga, O. ; Giacomoni, E. ; Gim, Y. ; Guelfi, M. ; Holt, J. W. ; Kofman, W. ; Leuschen, C. J. ; Marinangeli, L. ; Marras, P. ; Masdea, A. ; Mattei, S. ; Mecozzi, R. ; Milkovich, S. M. ; Morlupi, A. ; Mougino, J. ; Orosei, R. ; Papa, C. ; Paterno, T. ; Marmo, P. P. del ; Pettinelli, E. ; Pica, G. ; Picardi, G. ; Plaut, J. J. ; Provenziani, M. ; Putzig, N. E. ; Russo, F. ; Safaeinili, A. ; Salzill: Accumulation and Erosion of Mars' South Polar Layered Deposits. *Science* 317(5845) , p. 1715–1718. 2007
- [Shang *et al.* 1999] Shang, J.Q. ; Rowe, R.K. ; Umana, J.A. ; Scholte, J.W.: A Complex Permittivity Measurement System for Undisturbed/Compacted Soils. *Geotechnical Testing Journal* 22(2) , p. 165–174. 1999
- [Siegert 1999] Siegert, M.J.: On the origin, nature and uses of Antarctic ice-sheet radio-echo layering. *Progress in Physical Geography* 23(2) , p. 159–179. 1999
- [Steier *et al.* 2006] Steier, P. ; Drogg, R. ; Fedi, M. ; Kutschera, W. ; Schock, M. ; Wagnenbach, D. ; Wild, E.M.: Radiocarbon determination of particulate organic carbon in non-temperated, Alpine glacier ice. *Radiocarbon* 48(1) . 2006
- [Taylor *et al.* 1993] Taylor, K. C. ; Hammer, C. U. ; Alley, R. B. ; Clausen, H. B. ; Dahl-Jensen, D. ; J., Gow. A. ; Gundestrup, N. S. ; Kipfstuhl, J. ; Moore, J. C. ; Waddington, E. D.: Electrical conductivity measurements from the GISP2 and GRIP Greenland ice cores. *Nature* 366 , p. 549–554. 1993
- [Thompson *et al.* 1993] Thompson, L.G. ; Mosley-Thompson, E. ; Davis, M. ; Lin, P.N. ; Yao, T. ; Dyurgerov, M. ; Dai, J.: Recent warming: ice core evidence from

- tropical ice cores with emphasis on Central Asia. *Global and Planetary Change* 7(1-3) , p. 145 – 156. 1993
- [Topp *et al.* 1980] Topp, G. C. ; Davis, J. L. ; Annan, A.P.: Electromagnetic determination of soil water content: Measurement in coaxial transmission lines. *Water Resources Research* 16(3) , p. 574–582. 1980
- [Usoskin *et al.* 2009] Usoskin, I. G. ; Horiuchi, K. ; Solanki, S. ; Kovaltsov, G. A. ; Bard, E.: On the common solar signal in different cosmogenic isotope data sets. *Journal of Geophysical Research (Space Physics)* 114 , p. A03112. 2009
- [Vincent *et al.* 1997] Vincent, C. ; Vallon, M. ; Pinglot, J. F. ; Funk, M. ; Reynaud, L.: Snow accumulation and ice flow at Dôme du Goûter (4300m), Mont Blanc, French Alps. *Journal of Glaciology* 43(145) , p. 513–521. 1997
- [Vinther *et al.* 2006] Vinther, B.M. ; Clausen, H.B. ; Johnsen, S.J. ; Rasmussen, S.O. ; Andersen, K.K. ; Buchardt, L. ; Dahl-Jensen, D. ; I.K., Seierstad ; Siggard-Andersen, M.-L. ; Steffensen, J.P. ; Svensson, A. ; Olsen, J. ; Heinemeier, J.: A synchronized dating of three Greenland ice cores throughout the Holocene. *Journal of Geophysical Research* 111(D6) , p. 1–16. 2006
- [von Storch and Zwiers 2002] von Storch, H. ; Zwiers, F. W.: Statistical Analysis in Climate Research. 2002
- [Wagenbach 1989] Wagenbach, D.: Environmental Records in Alpine Glaciers. Oeschger, H. (ed.) ; C. C. Langway, Jr. (ed.): *The Environmental Record in Glaciers and Ice Sheets*, John Wiley and Sons, 1989, p. 69–83
- [Wagenbach 1992] Wagenbach, D. ; Haeberli, W. (ed.) ; Stauffer, B. (ed.): Special problems of mid-latitude glacier ice-core research. In: Greenhouse Gases, Isotopes and Trace Elements in Glaciers as Climatic Evidence of the Holocene. Versuchsanstalt für Wasserbau, Hydrologie und Glaziologie der Eidgenössischen Technischen Hochschule Zürich, 1992
- [Wagenbach 2001] Wagenbach, D. (ed.): Environmental and Climatic Records from High Elevation Alpine Glaciers (ALPCLIM). Final Report, 2001
- [Wagenbach *et al.* 1988] Wagenbach, D. ; Münnich, K. O. ; Schotterer, U. ; Oeschger, H.: The anthropogenic impact on snow chemistry at Colle Gnifetti, Swiss Alps. *Annals of Glaciology* 10 , p. 183–187. 1988
- [Wagner *et al.* 2011] Wagner, N. ; Emmerich, K. ; Bonitz, F. ; Kupfer, K.: Experimental investigations on the frequency and temperature dependent dielectric material properties of soil. *IEEE Transactions on Geoscience and Remote Sensing* 49(8) , p. in print. 2011

- [Wagner *et al.* 2007] Wagner, N. ; Kupfer, K. ; Trinks, E.: A broadband dielectric spectroscopy study of the relaxation behaviour of subsoil. Okamura, Seichi (ed.): *Proc. of the 7th International Conference on Electromagnetic Wave Interaction with Water and Moist Substances*, 2007, p. 31–38
- [Wagner *et al.* 2010] Wagner, N. ; Mueller, B. ; Kupfer, K. ; Schwing, M. ; Scheuermann, A.: Broadband electromagnetic characterization of two-port rod based transmission lines for dielectric spectroscopy of soil. Kupfer, Klaus (ed.): *Proceedings, 1th European Conference on Moisture Measurement, Aquametry 2010 in Weimar*, 2010, p. 228–237
- [Wagner 1996] Wagner, S.: Dreidimensionale Modellierung zweier Gletscher und Deformationsanalyse von eisreichem Permafrost, Versuchsanstalt für Wasserbau, Hydrologie und Glaziologie der ETH Zürich, PhD thesis, 1996
- [Warren 1984] Warren, S.G.: Optical Constants of ice from the ultraviolet to the microwave. *Applied Optics* 23 (8) , p. 1206–1225. 1984
- [Weikusat *et al.* 2009] Weikusat, I. ; Kipfstuhl, S. ; Azuma, N. ; Faria, S.H. ; Miyamoto, A.: *The Physics of Ice Core Records II.* chap. Deformation microstructures in an Antarctic ice core (EDML) and in experimentally deformed artificial ice, p. 115–123, Hokkaido University Press, Sapporo, Japan, 2009
- [Weir 1974] Weir, W.B.: Automatic Measurement of Complex Dielectric Constant and Permeability at Microwave Frequencies. *Proceedings of the IEEE* 62(1) , p. 33–36. 1974
- [Wilen *et al.* 2003] Wilen, L.A. ; Diprinzio, C.L. ; Alley, R.B. ; Azuma, N.: Development, Principles, and Applications of Automated Ice Fabric Analyzers. *Microscopy Research and Techniques* 62 , p. 2–18. 2003
- [Wilhelms 1996] Wilhelms, F.: Leitfähigkeits- und Dichtemessung an Eisbohrkernen. *Berichte zur Polarforschung* 191 . 1996
- [Wilhelms 2000] Wilhelms, F.: Measuring the Dielectric Properties of Polar Ice Cores. *Berichte zur Polarforschung* 367 . 2000
- [Wilhelms 2005] Wilhelms, F.: Explaining the dielectric properties of firn as a density-and-conductivity mixed permittivity (DECOMP). *Geophysical Research Letters* 32 . 2005
- [Wilson *et al.* 2003] Wilson, C.J.L. ; Russel-Head, D. ; Sim, H.M.: The application of an automated fabric analyzer system to the textural evolution of folded ice layers in shear zones. *Annals of Glaciology* 37 (11) , p. 7–17. 2003

- [Wohlfarth and Lechner 2008] Wohlfarth, C. (ed.) ; Lechner, M. D. (ed.): Static Dielectric Constants of Pure Liquids and Binary Liquid Mixtures. Springer, 2008
- [Wolff and Paren 1984] Wolff, E.W. ; Paren, J.G.: A two-phase model of electrical conduction in polar ice sheets. *Journal of Geophysical Research* 89(B11) , p. 9433–9438. 1984
- [Wollschläger *et al.* 2010] Wollschläger, U. ; Gerhards, H. ; Yu, Q. ; Roth, K.: Multi-channel ground-penetrating radar to explore spatial variations in thaw depth and moisture content in the active layer of a permafrost site. *The Cryosphere* 4(3) , p. 269–283. 2010
- [Yilmaz 2001] Yilmaz, Ö.: Seismic data analysis: processing, inversion, and interpretation of seismic data. 2nd. Society of Exploration Geophysicists, 2001 (Investigations in geophysics 10)
- [Zhang and Li 2008] Zhang, K. ; Li, D.: Electromagnetic Theory for Microwaves and Optoelectronics. 2nd edition. Springer-Verlag Berlin Heidelberg, 2008

Lists

List of Figures

2.1	Colle Gnifetti ice core array	7
2.2	Centennial trends in Colle Gnifetti isotope records	9
2.3	Snow sampling influence on $\delta^{18}\text{O}$ mean values	11
2.4	Colle Gnifetti ice core raw isotope records	13
2.5	Colle Gnifetti isotope time series for past 120 a	14
2.6	Binned correlation coefficient of CG $\delta^{18}\text{O}$ time series	16
2.7	Mean binned correlation coefficient of CG $\delta^{18}\text{O}$ time series	17
2.8	Decadal common record compilation of CG $\delta^{18}\text{O}$ time series	19
2.9	Mean weights for subsampling the instrumental temperature data	21
2.10	Ice core representative modified instrumental temperature	23
2.11	Decadal time series intercomparison $\delta^{18}\text{O}$ common record vs. instru- mental temperature	24
2.12	Centennial trend intercomparison $\delta^{18}\text{O}$ common record vs. instrumental temperature	25
2.13	Binned correlation of CG $\delta^{18}\text{O}$ time series 1880-1760 AD	27
3.1	Principle of GPR measurement	31
3.2	GPR: Derivation of reflector depth	31
3.3	KCI density profile	32
3.4	GPR CO-measurements at Colle Gnifetti	33
3.5	Reflection-hyperbolae in a CO-radargram	34
3.6	Shortcoming in GPR-reflector position allocation	34
3.7	Exemplary Colle Gnifetti GPR profile	36
3.8	Ambiguity in GPR bedrock reflection detection	37
3.9	Colle Gnifetti GPR profiles and ice core locations	38
3.10	Pairwise dating comparison of the CG ice cores via GPR-IRHs	39
3.11	Map of traced IRHs between the CG drilling sites	41
3.12	Results from closed course dating comparison	42
3.13	Nye's simple flow model of an ice sheet at the ice divide	46
3.14	Simplified geometry of the ice slab model	47
3.15	Piecewise ice slab model	48

3.16	Ice flux balance consideration	49
3.17	Example of accumulation rate derived from GPR-IRH	50
3.18	CG ice core mean density profiles	51
3.19	Comparison of GPR-based with flow model based isochrones	52
3.20	Pairwise inter-core dating comparison by flow model integration	53
3.21	Exemplary 3D age distribution at the CG drilling area	55
3.22	Trajectories and catchment area for KCI	56
3.23	Antenna setups in vertical radar profiling and borehole tomography	61
3.24	Vertical radar profiling at the KCI borehole	62
3.25	Direct wave in vertical radar profiling	63
3.26	Vertical profile of propagation velocity at KCI	64
3.27	Ice-cliff at Colle Gnifetti close to KCI	65
3.28	Borehole tomography at KCI	67
3.29	Interval velocity profile at KCI	68
3.30	GPR CO-profile compared with KCI ice core data	71
4.1	Debye-model of the permittivity of ice	80
4.2	Permittivity of ice in the MHz-range	83
4.3	The IUP coaxial cell setup	86
4.4	Detailed schematic view of the coaxial probe parts	87
4.5	The extended forward model of scattering parameters	90
4.6	Intercomparison of permittivity computation algorithms	96
4.7	Time Domain Reflectometry: Teflon standard	98
4.8	Variability in Teflon-S-parameters	100
4.9	Characterisation of an artificial ice sample	106
4.10	S-parameters of an artificial ice sample	107
4.11	Artificial ice ϵ'_r : comparison of algorithms	109
4.12	Permittivity distribution of acid-doped ice	110
4.13	Results of ϵ'_r for acid-doped ice	111
4.14	Artificial ice ϵ'_r : comparison with previous data	113
4.15	Setup for preparing natural ice samples	117
4.16	Permittivity of natural firn and ice	118
4.17	Permittivity of Colle Gnifetti firn core	121
A.1	Synthetic time series	147
A.2	Coherence between CG time series	148
A.3	Lomb-Scargle Periogram of the CG $\delta^{18}\text{O}$ time series	149
B.1	Exemplary comparison of raw and processed radargram	150
B.2	Vertical radar profile at the KCI borehole (bottom->top)	158
B.3	Borehole tomography at KCI (variable density plot)	159
B.4	GPR traces in slope-parallel and isohypse-parallel profiles	160

C.1	Artefacts in S-parameters measured with the original setup	161
C.2	Pure Teflon and ice S-parameters: IUP vs. MFPA measurements	163
C.3	Foward simulation of S-parameters biased by artefacts: Model runs 0,1 .	165
C.4	Foward simulation of S-parameters biased by artefacts: Model runs 2,3 .	166
C.5	Foward simulation of S-parameters biased by artefacts: Model runs 4,5 .	167
C.6	Backward calculation of S-parameters from permittivity distribution . .	168
C.7	Time Domain Reflectometry (TDR) in the coaxial cell	169
C.8	Reproducibility of Teflon and Ice S-parameter measurements	170
C.9	Schmidt plots of crystal orientation in artificial ice samples	171
C.10	Distribution of c-axes in vertical cuts	172
C.11	S-parameters of HCL-doped ice	172

List of Tables

2.1	Characteristic parameters of the Colle Gnifetti ice cores	8
3.1	Quantities in equations (3.3) - (3.5)	44
4.1	Intercomparison of inversion techniques on Teflon S-parameters	95
4.2	Debye-parameters of reference materials	102
4.3	Artificial ice ϵ'_r obtained by different methods and algorithms	108
4.4	Real part ϵ'_r of natural firm and ice samples	119
A.1	Parameters according to the CG ice-cores used for synthesizing four artificial time series with alike properties. The decay time τ and the amplitude of the noise were estimated directly from the original time series. The values of τ are close to the persistence times of the time series estimated following Mudelsee [2010].	147
C.1	Model parameter for foward simulation of S-parameters biased by artefacts	164

List of abbreviations

AD	(year) anno Domini
AWI	Alfred Wegener Institute for Polar and Marine Research, Bremerhaven
BJI	Baker-Jarvis iterative
BP	before present
BT	borehole tomography
CC	deep ice core at Colle Gnifetti
CCPM	complex conductivity and permittivity model
CG	Colle Gnifetti
CO	common offset
COF	crystal orientation fabric
ECM	electric conductivity measurement
FMCW	frequency-modulated continuous wave
GPR	Ground-penetrating radar
IRH	internal reflection horizon
IUP	Institute of Environmental Physics, University of Heidelberg
KCH	deep ice core at Colle Gnifetti
KCI	deep ice core at Colle Gnifetti
KCS	deep ice core at Colle Gnifetti
MFPA	Institute of Material Research and Testing, Bauhaus University, Weimar
NRW	Nicholson-Ross-Weir
NWA	network analyzer
SSA	singular spectrum analysis
TDR	time domain reflectometry
TEM	transversal electromagnetic mode
TWT	two-way travel time
VRP	vertical radar profiling
w.e.	water equivalent

Appendices

A Appendix to chapter 2

A.1 Artificial time series

The construction of the artificial time series was performed in four main steps:

- 1. Define ice-core specific parameters.** See Table A.1.
- 2. Calculate signal components:** Common signal = trend + harmonic oscillations osz40 and osz10. Individual signal = Mean + Damped short-term (e.g. seasonal) oscillation (osz1) + noise (white noise of amplitude “noise” (see Table A.1))

$$\begin{aligned}\text{osz40} &= 0.5 \sin((2\pi/40)t) \\ \text{osz10} &= \cos((2\pi/10)t) \\ \text{osz1} &= 8 e^{-t/\tau} \sin(2\pi t) \\ \text{trend} &= (0.0003(t - 110)^2) - 3\end{aligned}$$

with t = time in years, from 1 to 120 a BP.

- 3. Add common and individual signal components**
- 4. Subsample according to individual time scale and resolution:** (cf. equation (3.11))

$$t(z) = -\frac{H}{A} \ln \left(1 - \frac{z}{H} \right) \quad (0 < z < H) \quad (\text{A.1})$$

This procedure results in the four time series shown in Figure A.1 below.

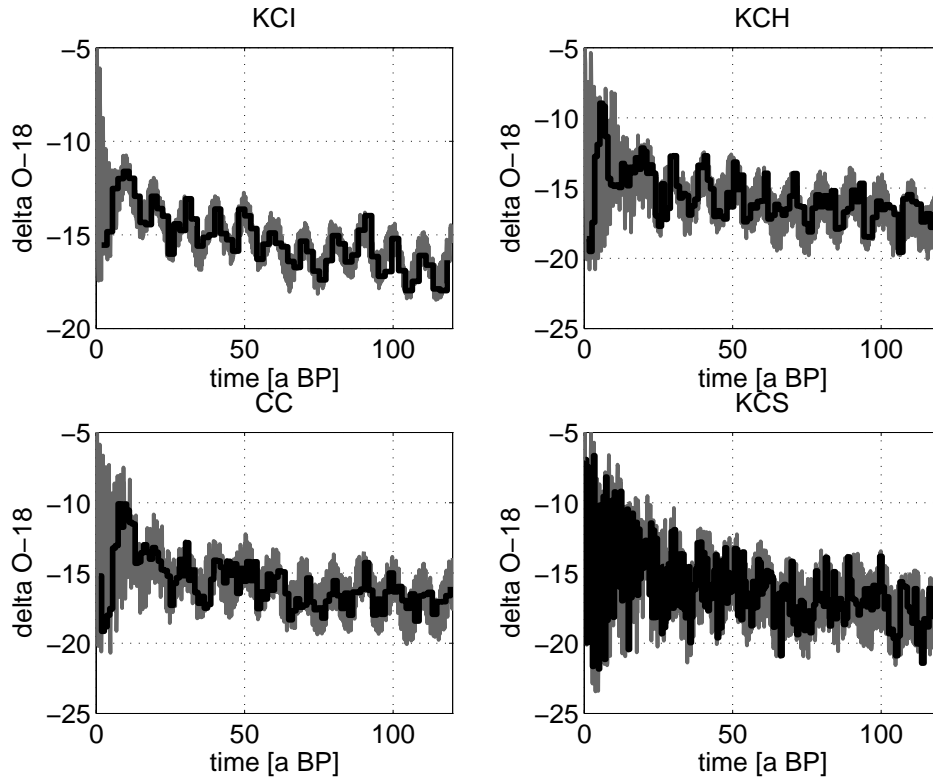


Figure A.1: Synthetic time series resembling the individual characteristics of the CG $\delta^{18}\text{O}$ time series. Grey: Original high resolution data. Black: Subsampled time series according to individual analytical age-depth relation.

Table A.1: Parameters according to the CG ice-cores used for synthesizing four artificial time series with alike properties. The decay time τ and the amplitude of the noise were estimated directly from the original time series. The values of τ are close to the persistence times of the time series estimated following Mudelsee [2010].

Parameter	Value for [KCI KCH CC KCS]
Total depth [m w.e.]	$H = [48.44; 45.02; 49.85; 78.65]$
Accumulation [m w.e./a]	$A = [0.11; 0.23; 0.22; 0.51]$
$\delta^{18}\text{O}$ mean [‰]	mean = $[-13.3; -13.9; -13.8; -14.4]$
Characteristic decay time of short-term oscillations [a]	$\tau = [3; 10; 10; 20]$
Amplitude of short time scale noise [‰]	noise = $[2; 4; 4; 6]$

A.2 Common signal analysis

Coherence estimation

The standard magnitude squared coherence, $C_{xy}(f)$, measures the agreement between two time series x and y at frequency f and is defined as:

$$C_{xy}(f) = \frac{|S_{xy}(f)|^2}{S_{xx}(f)S_{yy}(f)}$$

where S is the power spectral density of the cross spectrum ($S_{xy}(f)$) or the individual time series ($S_{xx}(f), S_{yy}(f)$) [von Storch and Zwiers, 2002]. $C_{xy} = 0$ corresponds to no coherence, $C_{xy} = 1$ to perfect coherence, respectively.

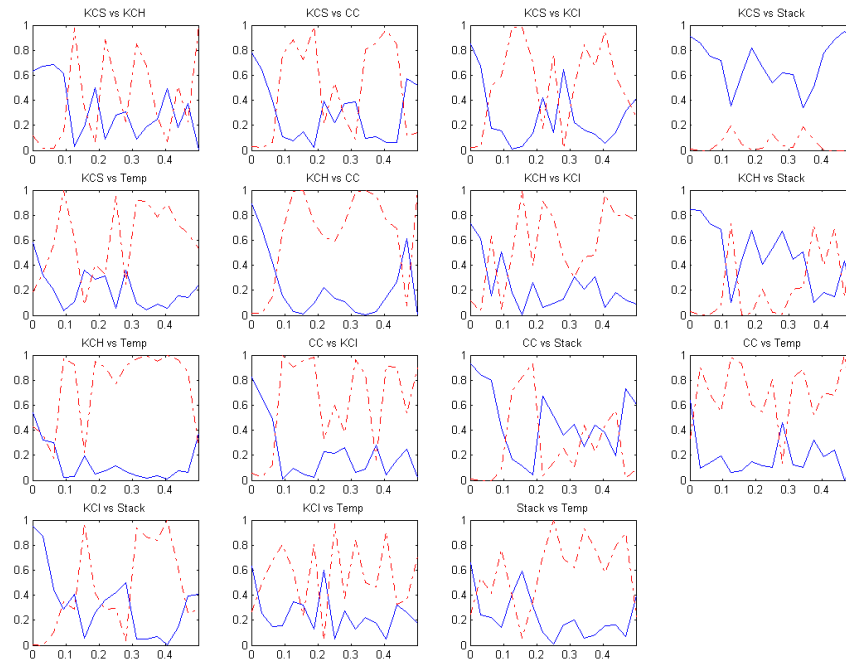


Figure A.2: Coherence between CG time series plotted against frequency (in [1/year], blue lines). Considered are all ice core $\delta^{18}\text{O}$ time and additionally, the stack and the modified temperature T_{mod} . Also shown: Preliminary significance estimate (red dashed lines) based on the method proposed by Ebisuzaki [1997] for serially correlated data.

Lomb-Scargle Periogram Analysis

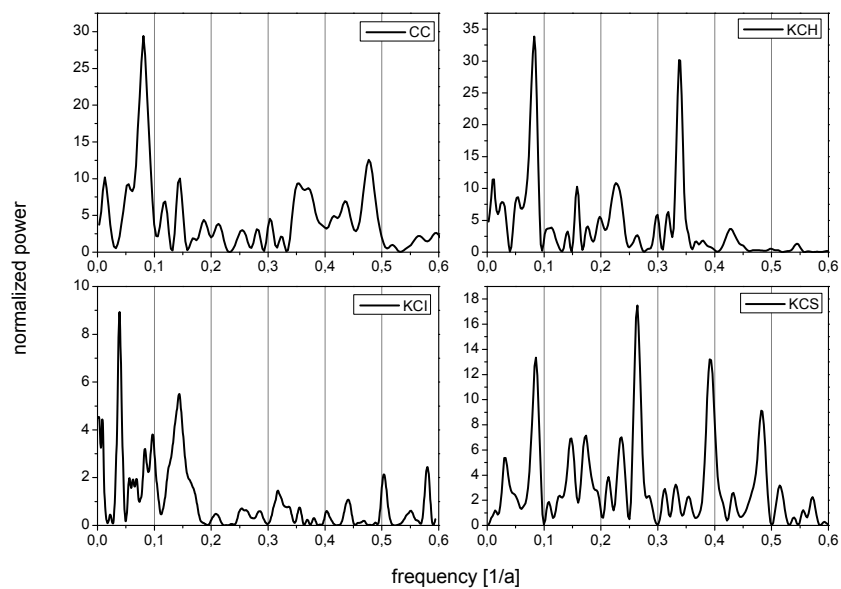


Figure A.3: Lomb-Scargle Periogram of the CG $\delta^{18}\text{O}$ time series back to 1880 AD. The mean of the respective time period was subtracted. Note the abundance of high frequency components in the high resolution KCS core, and the lack thereof in the low accumulation KCI, respectively.

B Appendix to chapter 3

B.1 GPR raw data processing

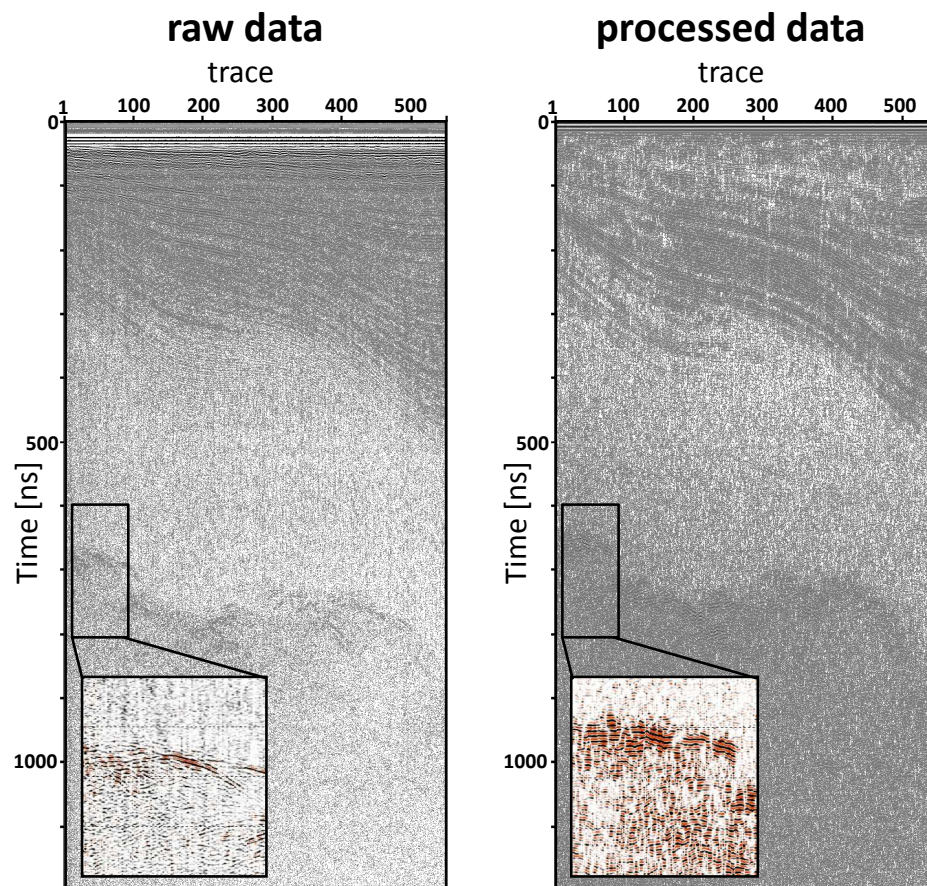


Figure B.1: Exemplary comparison between raw and processed data of the GPR-profile linking the drilling sites of KCI (close to trace 1) and KCS (close to trace 550)). Static correction, trapezoidal bandpass filtering, migration and gain correction were applied. Signal strength is shown in grey color scale. Note the IRHs present down to roughly 400 ns and the bedrock reflection around 650 ns. The effect of migration is illustrated in the enlarged section. Figure from Konrad [2011].

B.1.1 TWT-depth conversion, density interpolation methods

Two different methods were deployed for TWT-depth conversion during post-processing of the GPR-IRHs:

1. In an initially developed scheme, the mean density distributions are interpolated in absolute depth coordinates. Beyond the core depth, density values are set to their constant maximum value of $\approx 0.9 \frac{g}{cm^3}$. This ensures that density profiles can be interpolated to depths larger than at the drilling sites. By means of the velocity profiles based on the interpolated density data, the depth of any internal reflector z^{IRH} at each trace can be calculated from the according TWT t_{TWT}^{IRH} by integrating

$$t_{TWT} = 2 \int_0^z \frac{1}{c(\tilde{z})} d\tilde{z}$$

until $t_{TWT} = t_{TWT}^{IRH}$ and thus $z^{IRH} = z$.

2. In a refined approach used by Konrad [2011], the mean density distributions at the drilling sites are converted in units of relative depth $z \rightarrow \Sigma = z/H, \Sigma \in [0, 1]$ and subsequently linearly interpolated. The ice thickness H at each trace can then be calculated from the according TWT t_{TWT}^H by solving:

$$t_{TWT}^H = 2 H \int_0^1 \frac{1}{c(\rho(\Sigma))} d\Sigma \quad (B.1)$$

With known ice thickness H, the interpolated relative density profiles are rescaled to absolute depths.

The two methods were found to produce virtually identical values for the TWT-depth conversion.

B.1.2 Uncertainty estimation in IRH processing

Δz^{IRH} is related to the vertical resolution of the GPR wavelet for detecting an IRH, which can be estimated as half of its envelope ($\approx 2\lambda$) and thus: $\Delta z_1 \approx \lambda$ Navarro and Eisen [2009]. An additional contribution stems from potential errors in manually tracing an IRH in the time domain: In regions of the profile where continuity of phases is disturbed an accidental 'shift' to picking an adjacent phase may occur. For most instances these shifts can be limited by additionally tracing neighbouring continuous phases as upper and lower boundaries for the disturbed phase. The resulting uncertainty of the two above contributions is estimated as $\Delta t_{TWT} \approx 5ns$.

In the subsequent conversion from two-way travel times to depth Δz_2 and additional contribution due to the uncertainty in the velocity profile goes back to uncertainty in density $\Delta\rho$, derived from interpolation between mean ice-core profiles. The following error propagation follows the description given by Konrad [2011]:

Wave speed

$$c(\rho(z)) = \frac{c_0}{1 + 0.845 \frac{cm^3}{g} \cdot \rho(z)} \quad (\text{cf. equations (3.2) and (4.7)})$$

$$\Rightarrow \Delta c(\rho(z)) = \frac{c_0 \cdot 0.845 \frac{cm^3}{g}}{\left(1 + 0.845 \frac{cm^3}{g} \cdot \rho(z)\right)^2} \cdot \Delta \rho(z) \quad (\text{B.2})$$

where $\Delta \rho$ is composite of the potential error due to smoothing, i.e. considering only the mean density distribution as shown in Figure 3.18, and the spatial interpolation uncertainty.

Depth of internal reflection horizons

Here, c and Δc are functions of z . The IRH depth z^{IRH} is not calculated explicitly (as for instance H) but implicitly:

$$t_{\text{TWT}} = 2 \int_0^z \frac{1}{c(\rho(\tilde{z}))} d\tilde{z}.$$

The integration is carried out until $t_{\text{TWT}} = t_{\text{TWT}}^{\text{IRH}}$. Then it is $z^{\text{IRH}} = z$. The problem of error propagation is solved by rearranging this relation as follows:

$$t_{\text{TWT}}^{\text{IRH}} = 2 z^{\text{IRH}} F' \quad \Leftrightarrow \quad z^{\text{IRH}} = \frac{t_{\text{TWT}}^{\text{IRH}}}{2 F'} \quad \text{where } F' = \frac{1}{z^{\text{IRH}}} \int_0^{z^{\text{IRH}}} \frac{1}{c(\rho(\tilde{z}))} d\tilde{z}.$$

The IRH depth z^{IRH} is assumed to be without uncertainty in the expression for F' . Otherwise, the error must be calculated by iteration due to the implicit calculation. Δz^{IRH} is calculated in accordance with the error of ice thickness:

$$\Delta z_{\text{TWT}}^{\text{IRH}} = \frac{\Delta t_{\text{TWT}}^{\text{IRH}}}{2 F'} \quad (\Delta t_{\text{TWT}}^{\text{IRH}} = 5ns)$$

$$\Delta z_c^{\text{IRH}} = \frac{t_{\text{TWT}}^{\text{IRH}}}{2} \frac{\Delta F'}{F'^2} \quad \left(\Delta F' = \frac{1}{c_0} \int_0^{z^{\text{IRH}}} 0.845 \frac{cm^3}{g} \cdot \Delta \rho(\tilde{z}) d\tilde{z} \right)$$

$$\Delta z^{\text{IRH}} = \sqrt{(\Delta z_{\text{TWT}}^{\text{IRH}})^2 + (\Delta z_c^{\text{IRH}})^2}$$

IRH age

The IRH dating error results from

- dating error of the cores: $\Delta t_{\text{dat}}^{\text{dat}} = 3$ a in the relevant time interval ($t_{\text{dat}}(z)$ is the core dating).
- depth error of the IRH: $\Delta t_z^{\text{dat}} = \left. \frac{dt_{\text{dat}}(z)}{dz} \right|_{z=z^{\text{IRH}}} \Delta z^{\text{IRH}}$

$$\Rightarrow \Delta t^{\text{dat}} = \sqrt{(\Delta t_{\text{dat}}^{\text{dat}})^2 + (\Delta t_z^{\text{dat}})^2}$$

Ice thickness

Here, c and Δc are functions of the relative depth Σ , not of absolute depth z .

$$H = \frac{t_{\text{TWT}}^H}{2} \left[\underbrace{\int_0^1 \frac{1}{c(\rho(\Sigma))} d\Sigma}_F \right]^{-1} \quad (\text{cf. equation (B.1)})$$

There are two independent error sources: Δt_{TWT}^H and $\Delta c(\rho(\Sigma))$.

$$\Delta H_{\text{TWT}} = \frac{\Delta t_{\text{TWT}}^H}{2} \int_0^1 \frac{1}{c(\rho(\Sigma))} d\Sigma \quad (\Delta t_{\text{TWT}}^H = 20 \text{ ns})$$

$$\Delta H_c = \frac{t_{\text{TWT}}^H}{2} \cdot \frac{\Delta F}{F^2}$$

$$\text{where } \Delta F = \int_0^1 \frac{\Delta c(\rho(\Sigma))}{c(\rho(\Sigma))^2} d\Sigma \stackrel{\text{eq. (B.2)}}{=} \frac{1}{c_0} \int_0^1 0.845 \frac{\text{cm}^3}{\text{g}} \cdot \Delta \rho(\Sigma) d\Sigma$$

$$\Delta H = \sqrt{(\Delta H_{\text{TWT}})^2 + (\Delta H_c)^2}$$

B.1.3 Pairwise inter-core dating comparison

KCI					KCS							
TWT [ns]	depth [m]	depth [m we]	age [a BP]	Err [a]	TWT [ns]	depth [m]	depth [m we]	age [a BP]	Err [a]	Iso?	Agediff	
3.70E-08	3.87		1,85	9	3	1.02E-07	10,34	5,23	10	3	1	-1
4.80E-08	4.78		2,34	11	4	1.31E-07	13,09	6,81	12	5	1	-1
5.80E-08	5.91		2,96	14	4	1.57E-07	15,50	8,28	14	3	1	0
6.40E-08	6.23		3,15	15	4	1.72E-07	16,87	9,12	16	5	1	-1
7.50E-08	7.51		3,93	21	5	2.01E-07	19,47	10,78	22	4	1	-1
8.00E-08	8.21		4,32	25	5	2.34E-07	22,37	12,67	26	4	1	-1
8.50E-08	8.57		4,52	26	5	2.64E-07	24,95	14,43	30	4	1	-4
9.00E-08	9.05		4,80	29	6	2.86E-07	26,81	15,68	31	3	1	-2
1.06E-07	10,69		5,75	42	5	2.99E-07	27,91	16,42	33	4	1	9
1.07E-07	10,89		5,86	43	5	3.18E-07	29,48	17,52	35	3	1	8
1.09E-07	11,07		5,96	44	5	3.34E-07	30,79	18,47	37	3	1	7
1.12E-07	11,23		6,05	45	5	3.64E-07	33,22	20,26	41	5	1	4
1.15E-07	11,35		6,12	45	5	3.78E-07	34,33	21,10	43	6	1	2
1.21E-07	11,57		6,26	46	5	3.92E-07	35,44	21,94	46	3	1	0
1.22E-07	11,62		6,29	47	4	4.04E-07	36,39	22,70	48	4	1	-1
1.26E-07	11,88		6,47	48	4	4.36E-07	38,90	24,71	54	5	1	-6
1.31E-07	13,06		7,24	54	5	4.35E-07	38,82	24,65	53	5	1	1
1.41E-07	13,59		7,56	57	5	4.65E-07	41,16	26,53	58	6	1	-1
1.49E-07	14,32		8,04	62	6	4.84E-07	42,64	27,75	61	6	1	1
1.55E-07	15,11		8,54	69	6	4.89E-07	43,03	28,08	64	12	1	5
1.76E-07	16,71		9,58	83	6	5.22E-07	45,60	30,25	71	3	0	12
1.92E-07	18,25		10,63	95	5	5.50E-07	47,76	32,07	77	4	0	18
2.06E-07	19,32		11,38	102	6	5.50E-07	47,79	32,10	77	4	0	25
6.37E-07	54,02		41,31	2128	97	8.73E-07	74,15	55,48	644	62	0	
KCS					KCH							
TWT [ns]	depth [m]	depth [m we]	age [a BP]	Err [a]	TWT [ns]	depth [m]	depth [m we]	age [a BP]	Err [a]	Iso?	Agediff	
6.10E-08	6.32		3,01	6	3	3.60E-08	3,78	1,77	9	8	1	-3
6.40E-08	6.62		3,17	6	3	3.60E-08	3,78	1,77	9	8	1	-3
1.18E-07	11,86		6,10	11	3	6.10E-08	6,30	3,03	13	4	1	-2
1.22E-07	12,24		6,32	11	3	7.00E-08	7,18	3,50	15	5	1	-4
1.34E-07	13,37		6,98	12	3	7.40E-08	7,57	3,71	16	5	1	-4
1.54E-07	15,22		8,12	14	3	8.40E-08	8,54	4,25	18	5	1	-4
1.70E-07	16,69		9,01	16	4	9.60E-08	9,69	4,92	21	4	1	-5
2.09E-07	20,18		11,24	23	3	1.12E-07	11,20	5,79	26	7	1	-3
2.24E-07	21,50		12,10	25	3	1.19E-07	11,85	6,17	28	6	1	-3
2.36E-07	22,54		12,78	27	3	1.30E-07	12,87	6,78	31	4	1	-4
2.45E-07	23,32		13,32	28	3	1.35E-07	13,32	7,05	32	5	1	-4
2.98E-07	27,82		16,36	32	3	1.58E-07	15,40	8,32	38	7	1	-6
3.10E-07	28,82		17,06	34	3	1.84E-07	15,93	8,67	40	4	1	-6
3.51E-07	32,17		19,48	39	4	1.87E-07	17,95	9,99	46	5	1	-7
3.52E-07	32,25		19,54	39	4	1.88E-07	18,04	10,05	46	5	1	-7
4.15E-07	37,25		23,39	49	3	2.22E-07	20,95	12,02	57	4	0	-8
4.16E-07	37,33		23,45	49	3	2.17E-07	20,53	11,73	56	4	1	-7
4.38E-07	39,05		24,83	54	4	2.32E-07	21,79	12,61	59	5	1	-8
4.51E-07	40,07		25,64	57	3	2.47E-07	23,04	13,48	64	8	1	-7
5.56E-07	48,26		32,50	79	3	3.35E-07	30,11	18,68	88	6	1	-9
8.88E-07	75,41		56,61	710	30	6.25E-07	53,02	38,46	484	62	0	
KCH					KCI							
TWT [ns]	depth [m]	depth [m we]	age [a BP]	Err [a]	TWT [ns]	depth [m]	depth [m we]	age [a BP]	Err [a]	Iso?	Agediff	
5.60E-08	5,80		2,77	13	4	4.20E-08	4,30	2,06	10	4	1	3
7.20E-08	7,38		3,60	16	5	4.80E-08	4,78	2,34	11	4	1	5
7.50E-08	7,67		3,76	16	5	4.80E-08	4,78	2,34	11	4	1	5
5.60E-08	5,80		2,77	13	4	5.30E-08	5,52	2,76	13	4	1	0
5.60E-08	5,80		2,77	13	4	5.30E-08	5,52	2,76	13	4	1	0
9.50E-08	9,60		4,86	21	4	6.30E-08	6,17	3,11	15	4	1	6
8.50E-08	8,64		4,31	18	5	6.40E-08	6,28	3,19	16	4	1	2
1.19E-07	11,85		6,17	28	6	6.90E-08	6,88	3,54	18	4	1	10
1.13E-07	11,29		5,85	26	7	7.40E-08	7,17	3,72	19	4	1	7
1.33E-07	13,14		6,94	31	4	7.90E-08	8,11	4,27	24	5	1	7
1.44E-07	14,14		7,55	33	6	8.00E-08	8,21	4,32	25	5	1	8
8.90E-08	9,03		4,53	19	7	8.00E-08	8,21	4,32	25	5	1	-6
1.49E-07	14,59		7,82	35	5	8.40E-08	8,50	4,48	26	5	1	9
1.50E-07	14,68		7,88	35	5	8.50E-08	8,57	4,52	26	5	1	9
1.57E-07	15,31		8,27	37	8	8.50E-08	8,57	4,52	26	5	1	11
1.56E-07	15,22		8,21	37	8	9.00E-08	9,05	4,80	29	6	1	8
1.62E-07	15,76		8,56	39	5	9.00E-08	9,05	4,80	29	6	1	10
1.68E-07	16,29		8,90	40	4	9.30E-08	9,35	4,97	32	7	1	8
1.67E-07	16,20		8,85	40	4	9.90E-08	9,92	5,31	36	7	1	4
1.68E-07	16,29		8,90	40	4	9.90E-08	9,92	5,31	36	7	1	4
2.03E-07	19,33		10,94	51	6	1.04E-07	10,46	5,62	41	6	1	10
1.89E-07	18,13		10,11	47	6	1.09E-07	11,07	5,96	44	5	1	3
2.27E-07	21,37		12,32	58	9	1.12E-07	11,23	6,05	45	5	1	13
2.17E-07	20,53		11,74	56	4	1.15E-07	11,35	6,12	45	5	0	11
2.32E-07	21,79		12,61	59	5	1.19E-07	11,49	6,21	46	5	0	13
2.59E-07	24,03		14,17	69	4	1.28E-07	12,02	6,57	49	4	0	20
2.55E-07	23,71		13,94	68	7	1.33E-07	13,21	7,33	55	5	0	13
2.65E-07	24,52		14,51	70	6	1.34E-07	13,27	7,36	55	5	0	15
2.94E-07	26,87		16,22	78	5	1.52E-07	14,70	8,29	65	6	0	13
2.89E-07	26,47		15,92	77	5	1.52E-07	14,70	8,29	65	6	0	12
3.13E-07	28,38		17,35	82	5	1.57E-07	15,26	8,64	70	6	0	12
2.94E-07	26,87		16,22	78	5	1.57E-07	15,26	8,64	70	6	1	8
3.13E-07	28,38		17,35	82	5	1.63E-07	15,76	8,96	74	7	1	8
3.13E-07	28,38		17,35	82	5	1.63E-07	15,76	8,96	74	7	1	8
3.33E-07	29,95		18,56	88	6	1.74E-07	16,63	9,52	82	6	1	6
6.44E-07	54,52		39,80	594	120	6.40E-07	54,28	41,54	2181	97	0	

B.1.4 Closed course dating comparison

Nr.	KCI -> KCS				KCS -> KCH				KCH -> KCI				
	TWT [ns]	depth [m]	age [a BP]	start	TWT [ns]	depth [m]	age [a BP]	end	TWT [ns]	depth [m]	age [a BP]	end	start
1	48	4.9	11	131	134	13.7	15	74	74	75	7.6	16	11
2	58	5.9	14	157	154	15.6	15	84	84	85	8.5	18	14
3	64	6.5	16	172	170	17.1	16	96	95	95	9.5	21	16
4	75	7.5	21	201	209	20.7	24	112	10.9	113	11.1	25	21
5	80	8.0	24	234	236	23.2	28	130	12.5	133	13.0	31	24
6	90	8.9	29	286	298	28.7	34	156	14.9	156	15.1	37	30
7	107	10.5	41	318	310	29.8	35	164	15.5	167	16.0	40	37
8	112	10.9	43	364	352	33.4	41	188	17.5	189	17.8	45	43
9	121	11.8	47	392	415	38.7	53	222	20.2	227	20.7	56	48
10	131	12.6	52	435	438	40.6	57	232	21.0	232	21.0	57	52

B.1.5 Velocity distributions from simplified geometries

Nye's model

In its most simple form, Nye's model is essentially build on a 2-D mass balance applied to an ice sheet at its ice divide ($x = 0$). Assuming a most simple geometry (see Figure 3.13) as well as steady state conditions implies for ice thickness H and accumulation rate \dot{b} to be constant in space and time. Additionally, the horizontal velocity u is regarded as independent of depth z . The 2-D mass balance then yields:

$$\frac{\partial(uH)}{\partial x} = \dot{b} \quad \Rightarrow \quad u(x) = \frac{\dot{b}}{H} x \quad (\text{B.3})$$

From here, the vertical velocity profile $w(z)$ can be calculated assuming $\rho = \rho_{ice} = \text{constant}$ and the boundary conditions $w(0) = \dot{b}$ and $w(H) = 0$ (i.e. ice frozen to bedrock).

$$\frac{\partial w}{\partial z} = -\frac{\partial u}{\partial x} \quad \Rightarrow \quad w(z) = \dot{b} \left(1 - \frac{z}{H}\right) \quad (\text{B.4})$$

Integration of $w = \frac{dz}{dt}$ yields an equation for the age of the ice in depth z :

$$t(z) = -\frac{H}{\dot{b}} \ln \left(1 - \frac{z}{H}\right) . \quad (\text{B.5})$$

Ice Slap

In a first-order idealisation to the geometry of an alpine glacier, this model treats a parallel sided slap of ice on an inclined plane. Additional assumptions are an infinite extension in y -direction (2-D problem), an ice thickness H constant in space and time (steady state) and a constant rate of accumulation (see Figure 3.14). This results in the only non-zero component of the stress tensor τ_{ij} to be, according to (3.4):

$$\tau_{xz} = -\rho g \sin \alpha \cdot z = \text{const.} \cdot z \quad (\text{B.6})$$

In this two-dimensional case with constant rate of accumulation, the vertical velocities are independent of x , and thus: $\dot{\epsilon}_{xz} = \frac{1}{2} \frac{\partial u}{\partial z}$. The tensor-invariant reduces to: $\tau' = |\tau_{xz}|$ (convention: $\tau \geq 0$). With the boundary condition of frozen-to-bedrock ice ($u(H) = 0$), it follows from (3.6) that:

$$\dot{\epsilon}_{xz} = \frac{1}{2} \frac{\partial u}{\partial z} = -A (\rho g \sin \alpha z)^n = \text{const.} \cdot z^n \quad (\text{B.7})$$

$$u(z) = u(0) \left(1 - \left(\frac{z}{H}\right)^{n+1}\right) \quad (\text{B.8})$$

The constant horizontal velocity at surface $u(0)$ contains the contribution of all constant factors. (B.8) is an expression for the dependency of the horizontal velocity on depth z

at a fixed point x at the surface. At any variable surface point x the ice flux accumulated uphill must account to: $q_{acc}(x) = \dot{b} x$. It follows that the mean ice flux perpendicular to the surface at that x is

$$q(x) = \int_0^H u(x, z) dz = \bar{u}(x) H$$

and with (B.8):

$$\bar{u}(x) = \frac{n+1}{n+2} u(x, 0) \quad \Rightarrow \quad q(x) = \frac{n+1}{n+2} u(x, 0) H$$

From a mass balance consideration follows that at every x , the ice flux through the glacier cross section must equal the accumulation uphill:

$$q(x) = q_{acc}(x) \quad \Rightarrow \quad u(x, 0) = \frac{n+2}{n+1} \frac{\dot{b} x}{H} \quad (\text{B.9})$$

$$\Rightarrow \quad u(x, z) = \frac{n+2}{n+1} \frac{\dot{b} x}{H} \left[1 - \left(\frac{z}{H} \right)^{n+1} \right] \quad (\text{B.10})$$

Deploying again that $\frac{\partial w}{\partial z} = -\frac{\partial u}{\partial x}$ and respecting the boundary conditions $w(H) = 0, w(0) = \dot{b}$ it follows for the vertical velocity profile:

$$w(x, z) = \dot{b} \left(1 - \frac{n+2}{n+1} \frac{z}{H} \left[1 - \frac{1}{n+2} \left(\frac{z}{H} \right)^{n+1} \right] \right) \quad (\text{B.11})$$

In case of $n = 3$:

$$u(x, z) = \frac{5}{4} \frac{\dot{b} x}{H} \left[1 - \left(\frac{z}{H} \right)^4 \right] \quad (\text{B.12})$$

$$w(x, z) = \dot{b} \left(1 - \frac{5}{4} \frac{z}{H} \left[1 - \frac{1}{5} \left(\frac{z}{H} \right)^4 \right] \right) . \quad (\text{B.13})$$

B.2 Investigation on IRHs with borehole radar and physical ice core properties

Supplementary borehole radar profiles

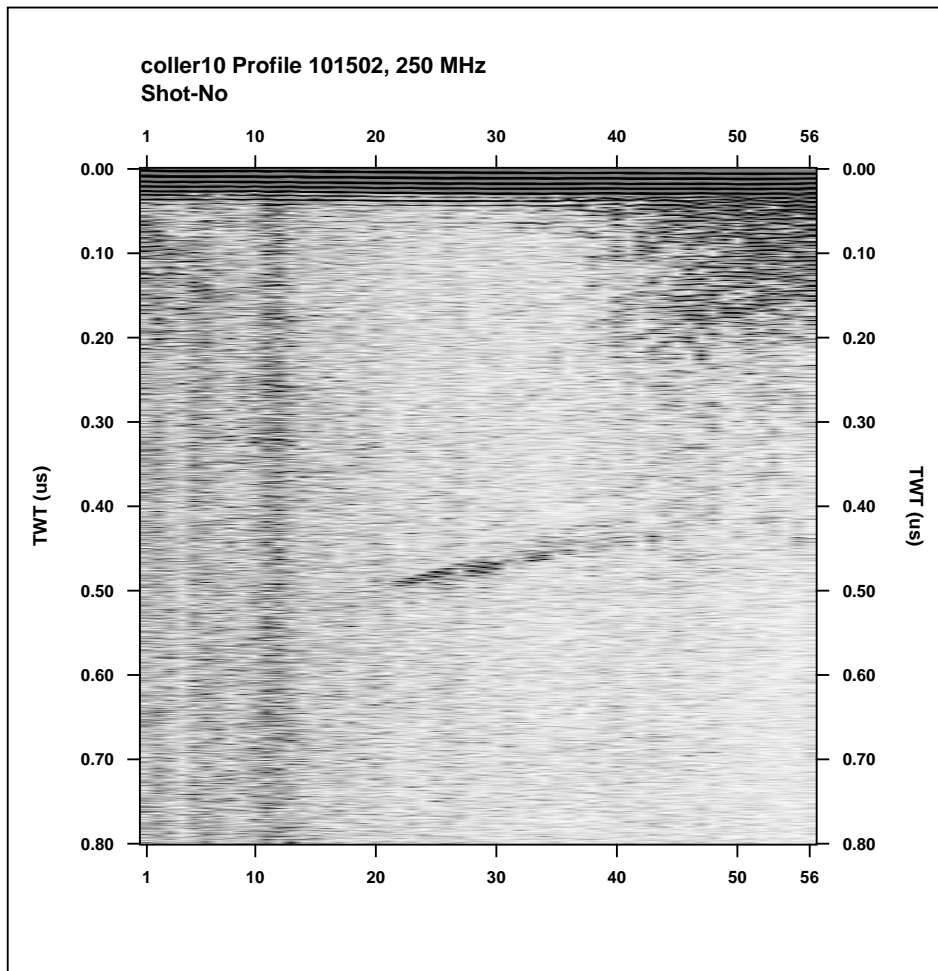


Figure B.2: Radargram from vertical radar profiling at KCI. Trace 1 corresponds to Tx and Rx at their bottommost point in the borehole. They were subsequently pulled back upwards with traces recorded in 1 m intervals.

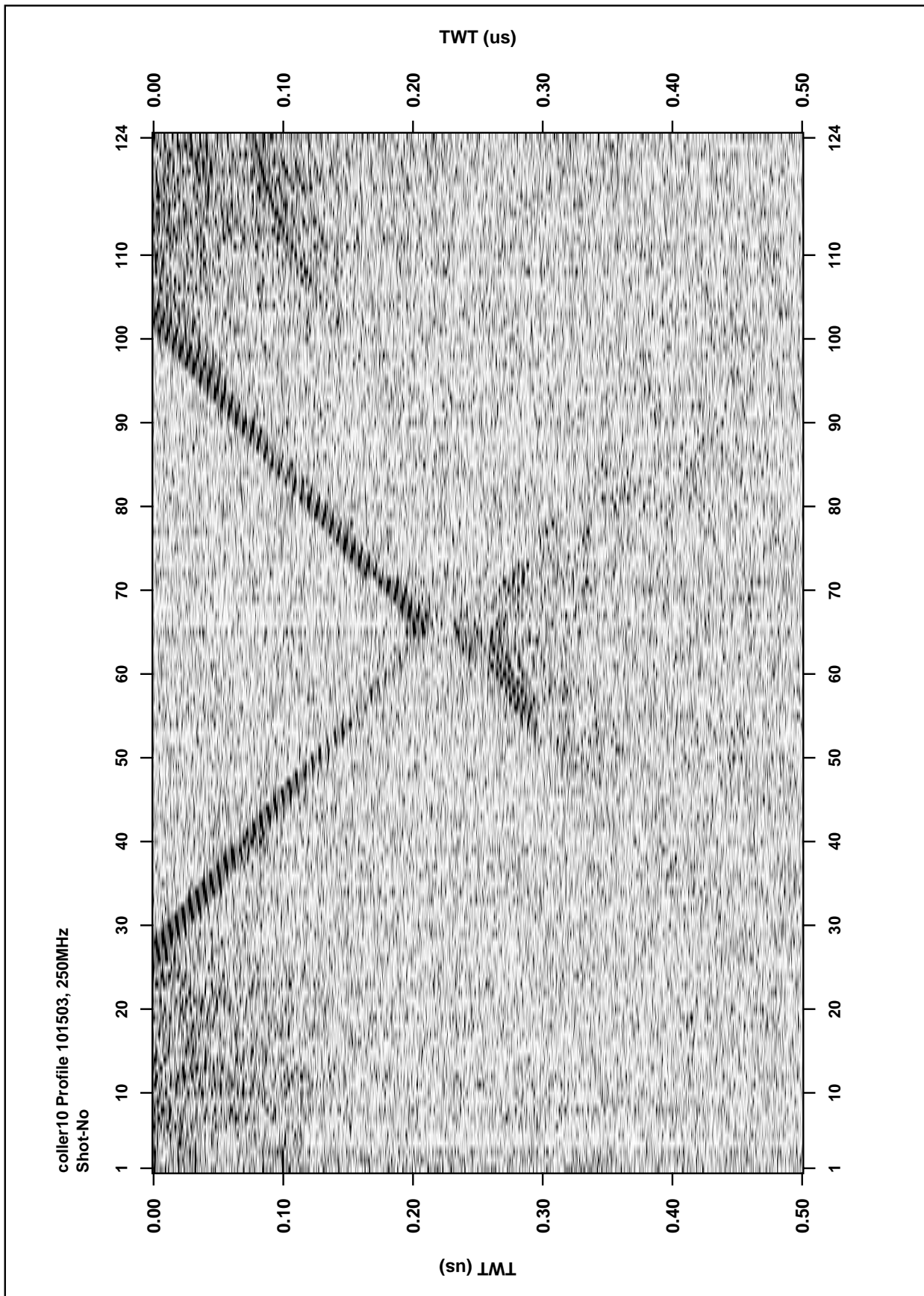


Figure B.3: Borehole tomography at KCI. The profile shows the same data as Figure 3.28, here as a variable density plot.

GPR traces in slope-parallel and isohypse-parallel profiles

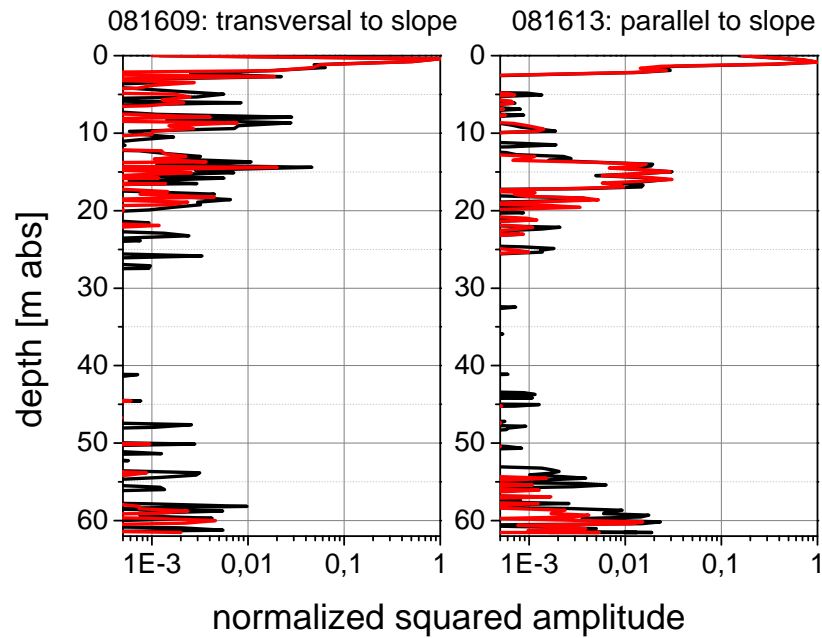


Figure B.4: Intercomparison of GPR traces in slope-parallel (left) and isohypse-parallel (denoted here as “transversal”, right side) profiles. Single traces are plotted in black, the stack of ≈ 20 traces in red, respectively. Note that feature may be different in amplitude, however, the large features are common to both profiles, e.g. the distinct reflector around 15 m.

C Appendix to chapter 4

C.1 Initial experimental shortcomings

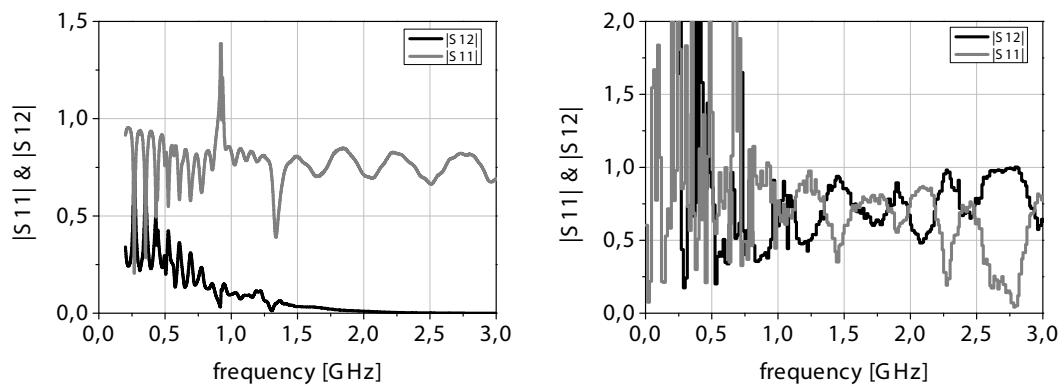


Figure C.1: Artefacts in S-parameters measured with the original setup. Left side: Measurement of distilled water inside the cell. Note the large artefact peak shortly before 1 GHz in reflection $|S_{11}|$ (grey curve), unreasonably high above 1. Right side: Measurement of artificial ice sample inside the cell. Note the large amount of noise up to 1 GHz in $|S_{11}|$ (grey) and $|S_{12}|$ (black). The noise disturbance was additionally found fluctuating in time. Figures modified from Hoppe [2009].

C.2 Permittivity computation with the BJI-technique

The implementation of the BJI-technique was developed by N. Wagner (MFPA, Weimar) and provided for validation of the Debye-based optimisation algorithm. In the following, a brief overview on the computational method is given (N. Wagner, personal communication).

Nicolson and Ross [1970] and Weir [1974] introduced a quasi analytical inversion procedure (NRW) to obtain the frequency dependent permittivity of low permittivity and low loss materials from measured S-parameters. However, for low loss materials, the NRW solution is divergent at integral multiples of one-half wavelength in the sample,

where the absolute value of the scattering parameter S_{ii} gets very small (see Figure 4.5). The BJI-method remained stable in the complete frequency range measured in the present study.

To obtain the permittivity with the BJI-technique in a first step calibrated and preprocessed S-parameters are used with NRW. The determined mean relative effective complex permittivity is used as starting guess for BJI. The permittivity $\varepsilon_{r,\text{eff}}^*$ is then obtained iteratively for every frequency by minimizing the objective function F determined with measured and numerical calculated S-parameters by means of a Levenberg-Marquardt algorithm [Levenberg, 1944; Marquardt, 1963] in MATLAB[®] based on the following equations:

$$f_1 = S_{11}S_{22} - S_{21}S_{12} - \frac{\Gamma^2 - T^2}{1 - T^2\Gamma^2}, \quad (\text{C.1})$$

$$f_2 = \frac{w_1(S_{21} + S_{12}) + (1 - w_1)(S_{11} + S_{22})}{2} - \frac{w_1T(1 - \Gamma^2) + (1 - w_1)\Gamma(1 - T^2)}{1 - \Gamma^2T^2} \quad (\text{C.2})$$

and

$$F = \frac{w_2f_1 + (1 - w_2)f_2}{2}. \quad (\text{C.3})$$

with weighting factors $0 \leq w_i \leq 1$, ideal reflection factor Γ and ideal transmission factor T of a sample with length d in the coaxial transmission line defined as follows:

$$\Gamma = \frac{Z_S - Z_0}{Z_S + Z_0} \quad (\text{C.4})$$

$$T = \exp(-\gamma_S d); \quad (\text{C.5})$$

and the relations between the complex effective relative permittivity $\varepsilon_{r,\text{eff}}^*$ and the complex impedance Z and complex propagation constant γ of vacuum Z_0, γ_0 and the waveguide Z_S, γ_S , respectively:

$$\varepsilon_{r,\text{eff}}^* = \left(\frac{Z_0}{Z_S} \right)^2, \quad (\text{C.6})$$

$$\varepsilon_{r,\text{eff}}^* = \left(\frac{c_0 \gamma_S}{j\omega} \right)^2, \quad (\text{C.7})$$

$$(\text{C.8})$$

with c_0 being the speed of light in vacuum and ω the angular frequency. The Jacobian of the system is approximated using finite differences. To ensure stable results after the first 10 frequencies the appropriate starting guess for the next frequency is calculated with the median of the previous 10 results.

C.3 Comparison of S-parameter measurements with the IUP and MFPA-NWA

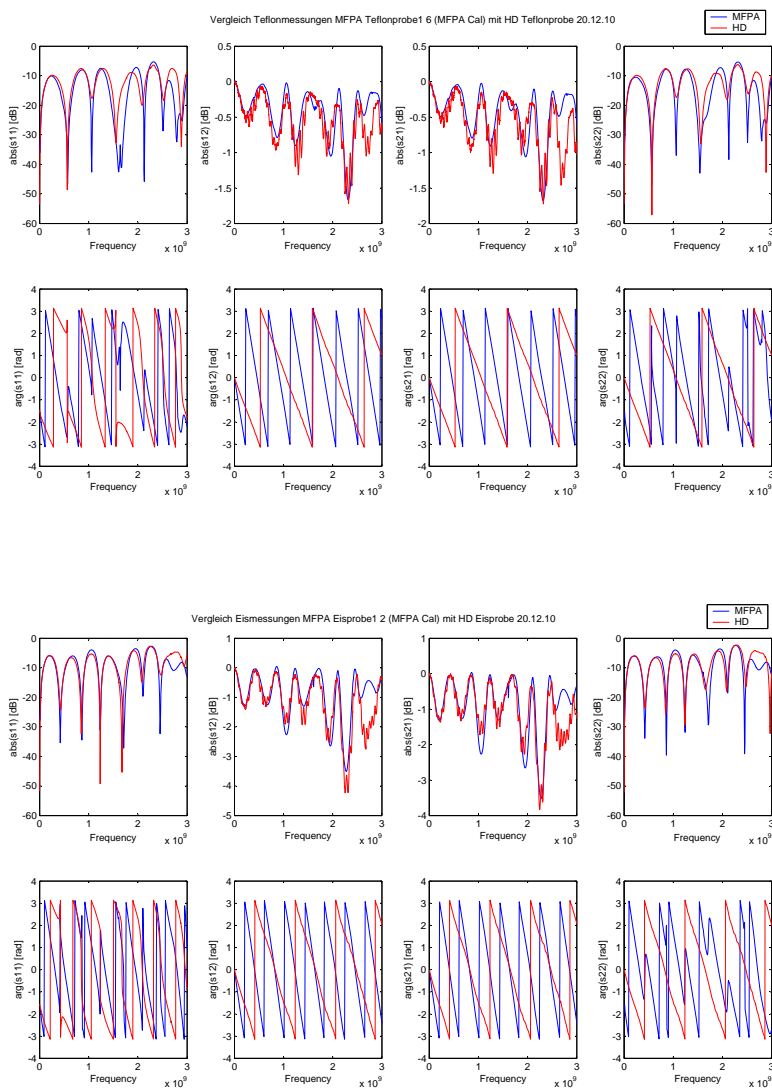


Figure C.2: Teflon (top) and pure ice (bottom) S-parameters plotted against frequency in GHz: IUP (red) vs. MFPA (blue) measurements. Note how the “ripples” are absent in the MFPA S-parameters, even in transmission $|S_{12}|$. The differences in phase (bottom rows) are due to different reference planes used by the IUP and MFPA calibration schemes.

C.4 Forward modelled artefact bias investigation

As described in section 4.4.2, the forward model was used to simulate the observed artefacts in synthetic S-parameters. Subsequently, these synthetic (i.e. forward modelled) S-parameters were used for permittivity calculation with the BJI-algorithm. The following plots show the results of six different S-parameter sets, with the forward model configuration shown in Table C.1 below.

Table C.1: Model parameter for forward simulation of S-parameters biased by artefacts. 'x' denotes a non-zero value of the respective model parameter. The according values in the model of (Cable length, Loss, Impedance jump) were (1.3,1.8,13) and tuned to match the observed artefacts in measured S-parameters.

Model run	Cable	Loss	Impedance jump
0	-	-	-
1	x	-	-
2	-	x	-
3	-	-	x
4	-	x	x
5	x	x	x

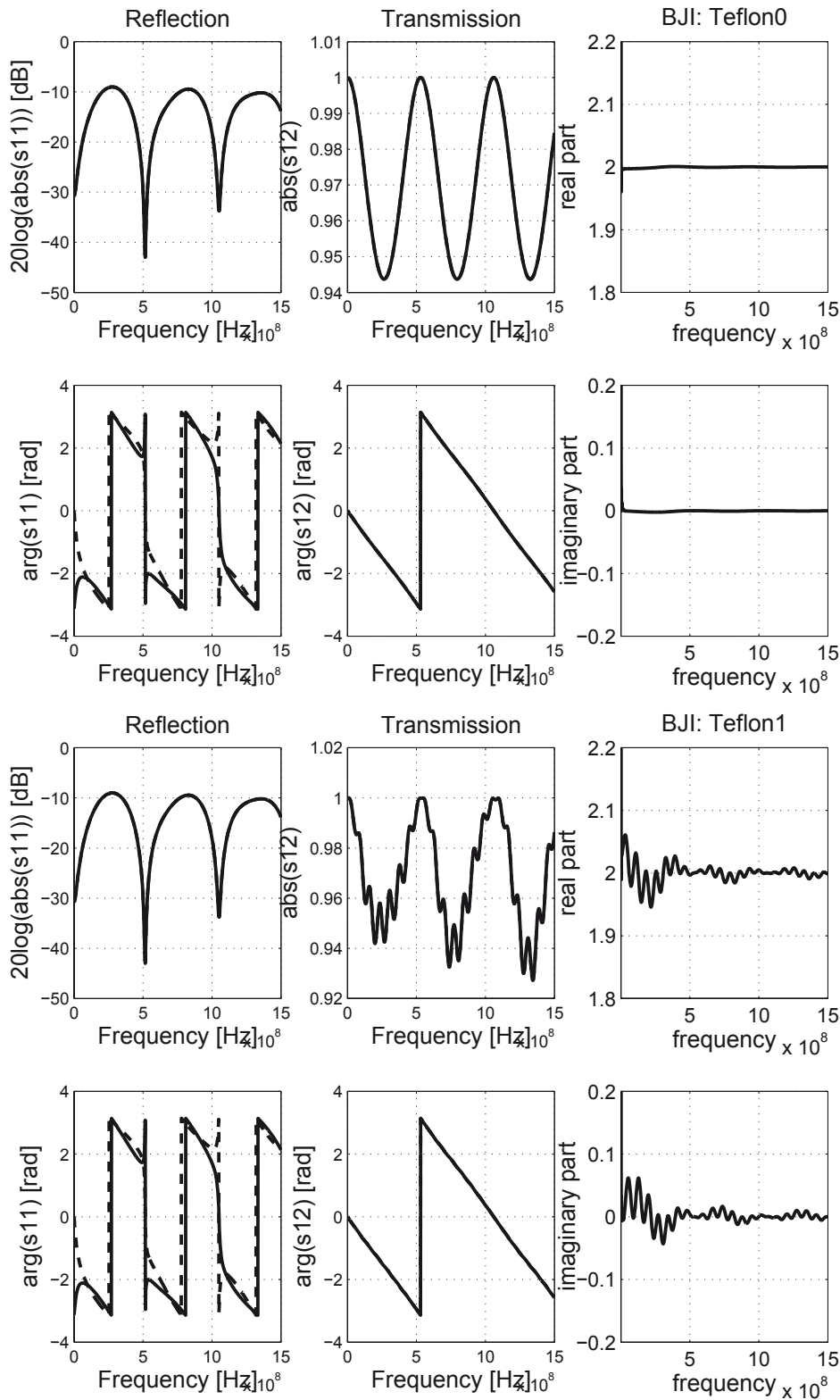


Figure C.3: Forward simulation of S-parameters biased by artefacts: Model runs 0 (top), 1 (bottom). Dashed lines indicate S-parameters measured in reverse direction (i.e. S_{11} and S_{22} , and S_{21} and S_{12} respectively). For the respective model configuration, see Table C.1.

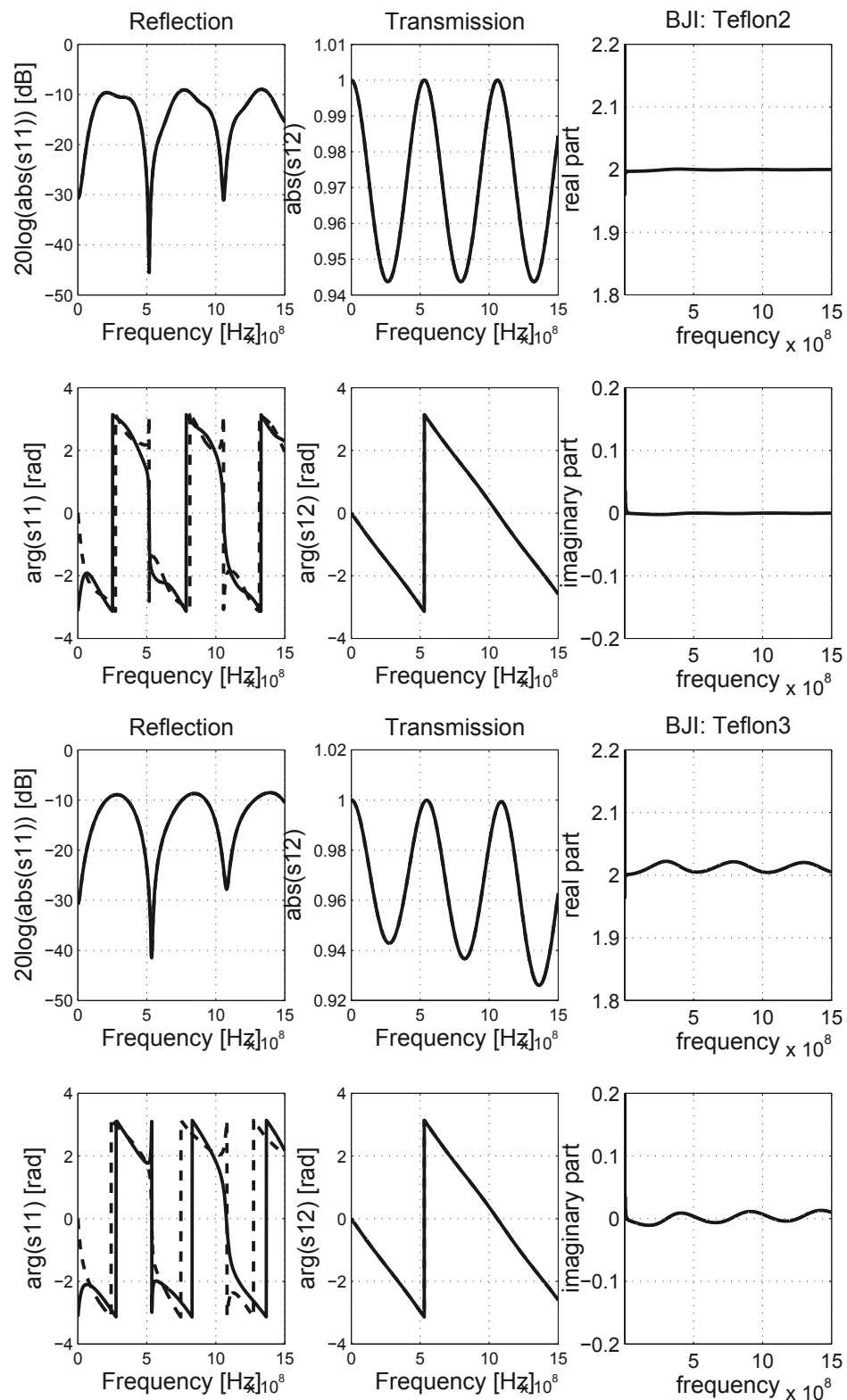


Figure C.4: Forward simulation of S-parameters biased by artefacts: Model runs 2 (top), 3 (bottom). Dashed lines indicate S-parameters measured in reverse direction (i.e. S_{11} and S_{22} , and S_{21} and S_{12} respectively). For the respective model configuration, see Table C.1.

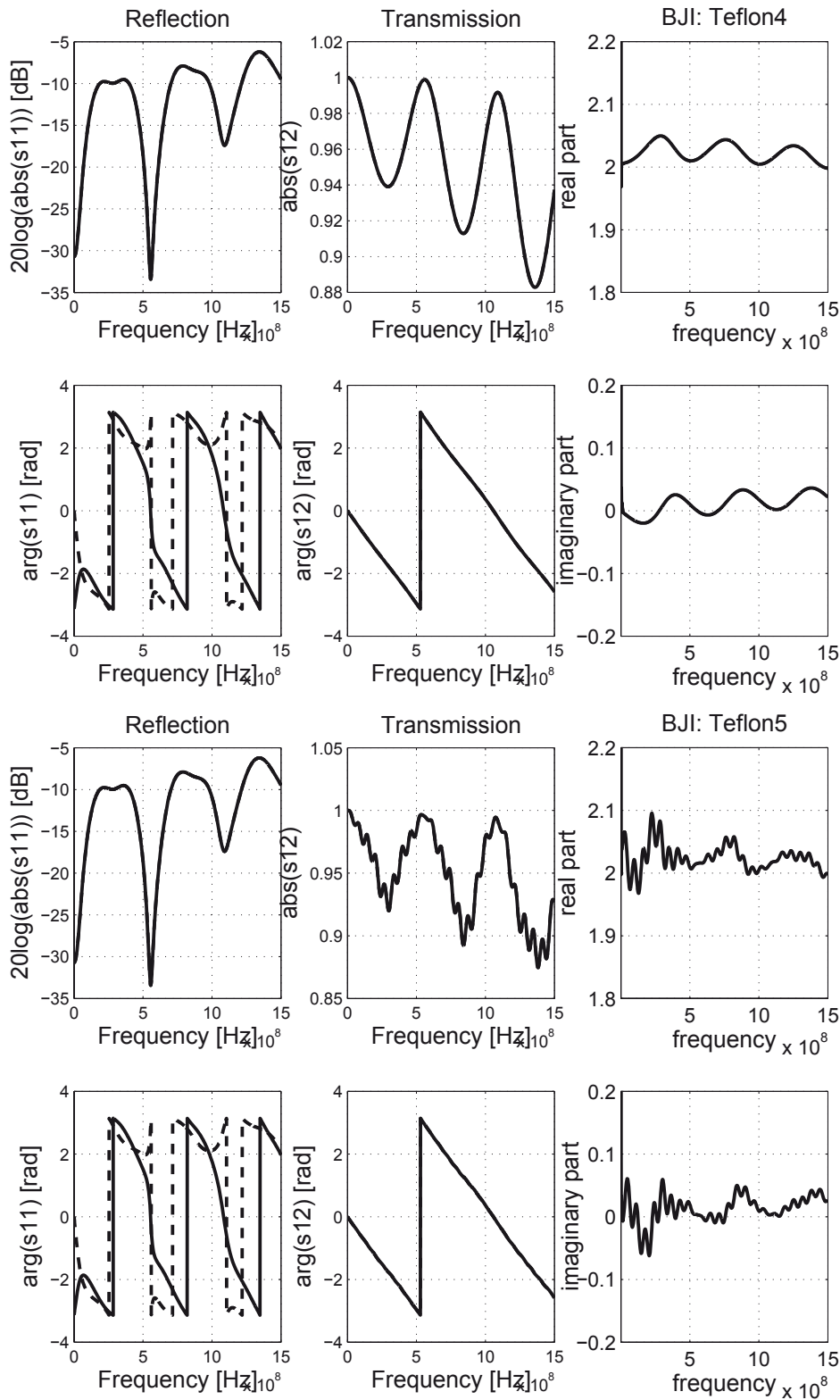


Figure C.5: Forward simulation of S-parameters biased by artefacts: Model runs 4 (top), 5 (bottom). Dashed lines indicate S-parameters measured in reverse direction (i.e. S_{11} and S_{22} , and S_{21} and S_{12} respectively). For the respective model configuration, see Table C.1.

C.5 Backward calculation of S-parameters from permittivity distribution

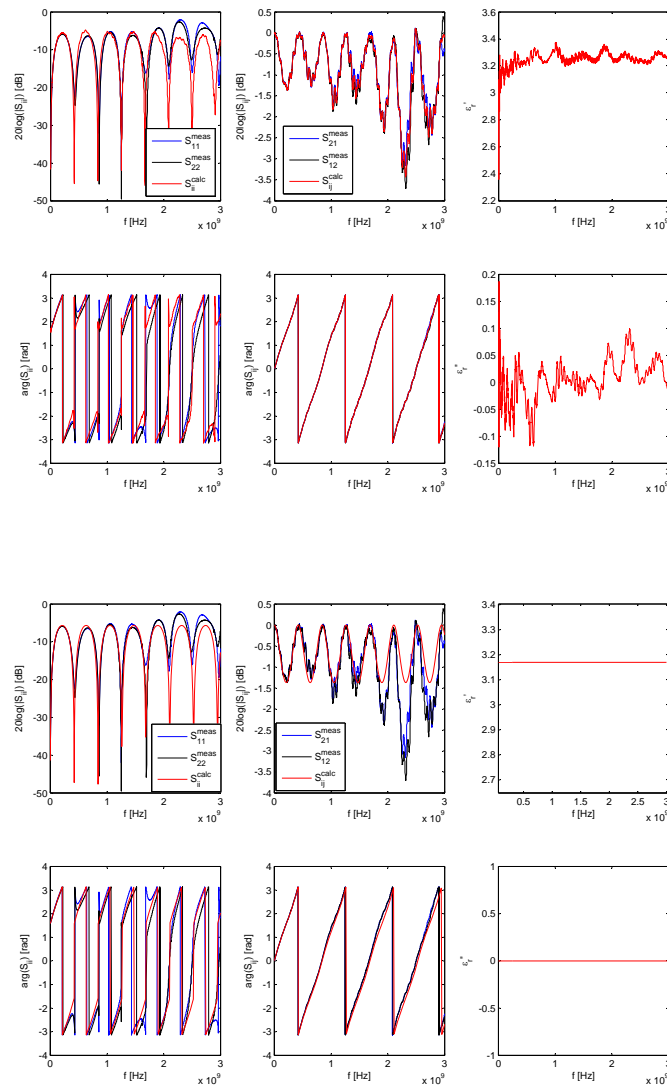


Figure C.6: Backward calculated S-parameters based permittivity distribution (in red) derived from: Pure ice measurements (top plot), with S-parameters featuring the respective artefacts discussed in the text (see section 4.4.2) and with a hypothetical frequency-independent permittivity distribution for comparison (bottom plot). Also shown are measured S-parameters in black and blue (for S_{11} and S_{22} , and S_{21} and S_{12} respectively). Figures personal communication N. Wagner.

C.6 TDR of an artificial ice sample in the coaxial cell

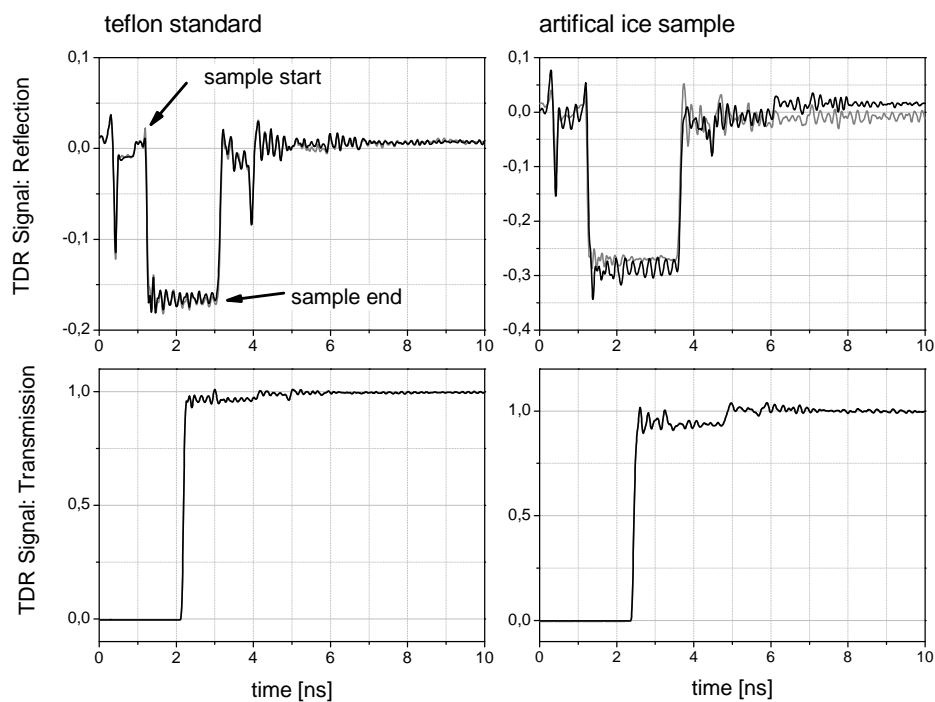


Figure C.7: Time Domain Reflectometry (TDR) signal obtained from S-parameter measurements on an artificial ice sample. Measurements were performed with an Agilent PNA E8363B network analyzer up to 16 GHz. Indicated are the start (t_{start}) and end (t_{end}) of the sample in the time domain. From $\Delta t = t_{\text{start}} - t_{\text{end}}$ a first order permittivity estimate can be obtained.

C.7 Reproducibility of S-parameter measurements up to 3 GHz

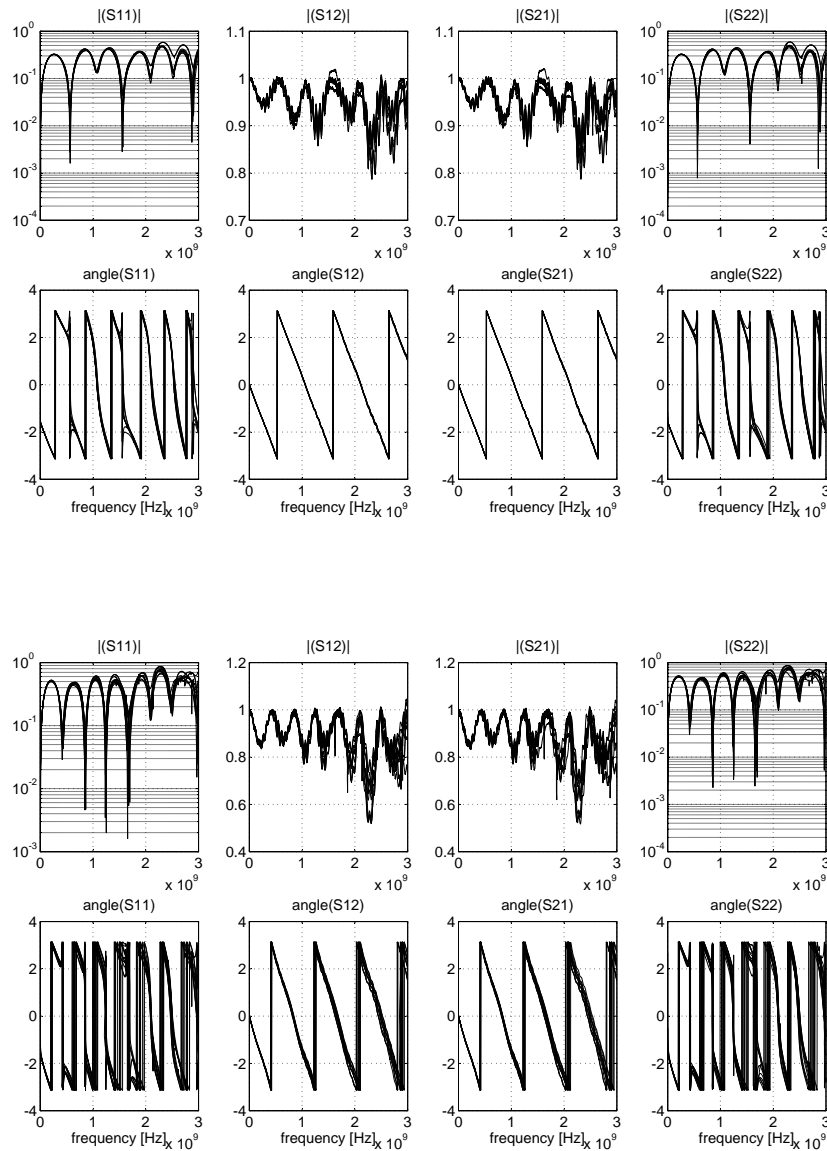


Figure C.8: Reproducibility of Teflon and Ice S-parameter measurements up to 3 GHz. Shown are the S-parameters of 9 measurements of the Teflon standard (top plot) and 8 different artificial pure ice samples (bottom plot). The reproducibility becomes weaker for frequencies above 1.5 GHz.

C.8 Investigation of crystal orientation in artificial ice samples

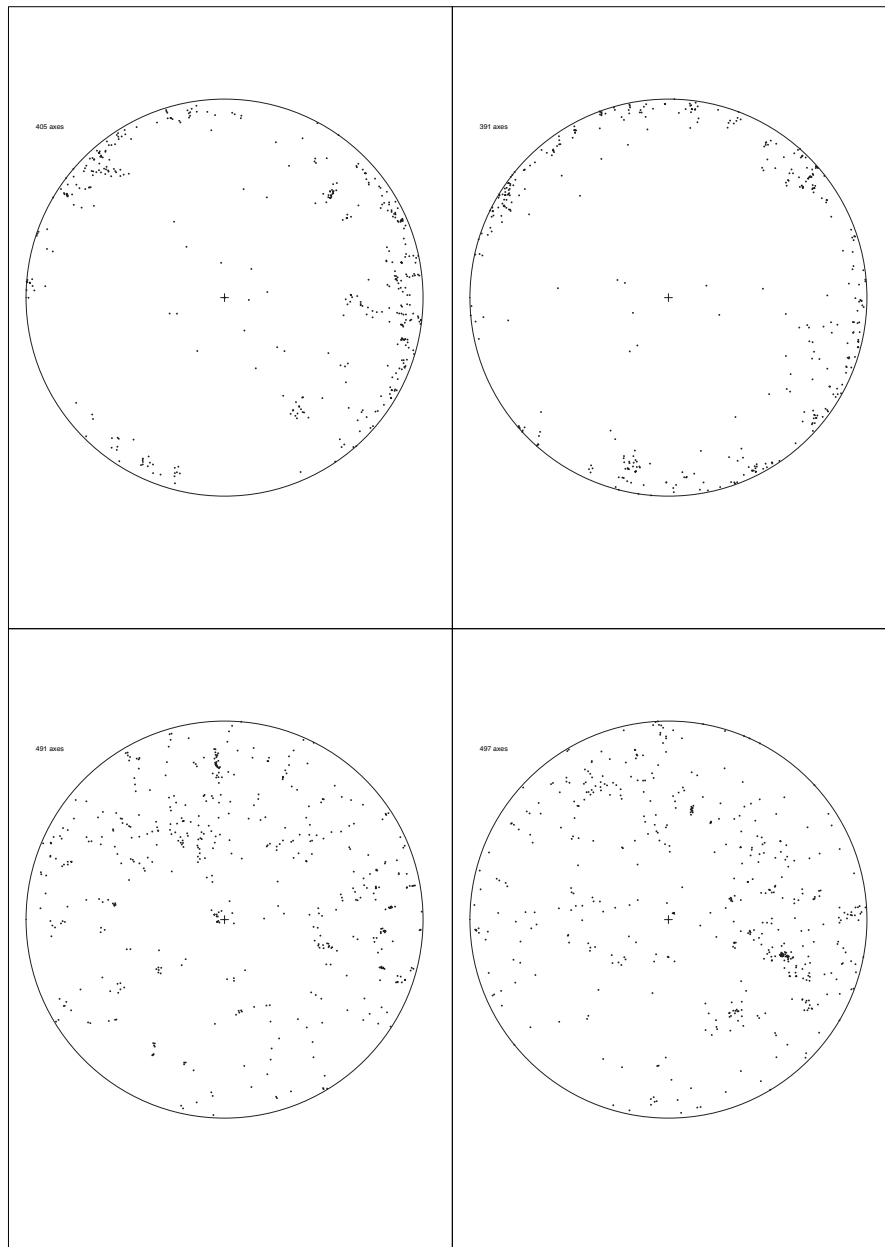
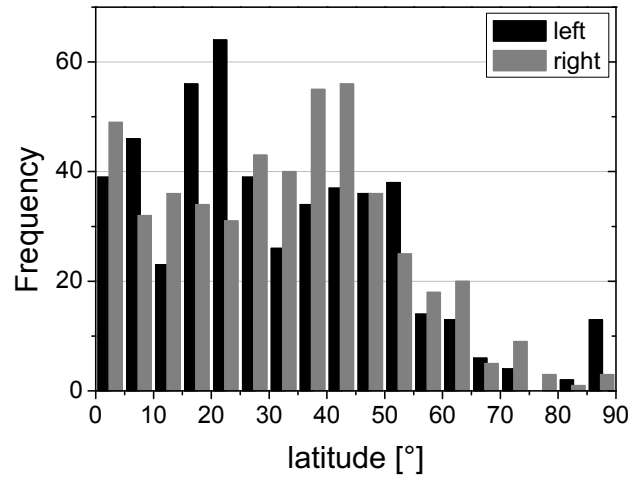


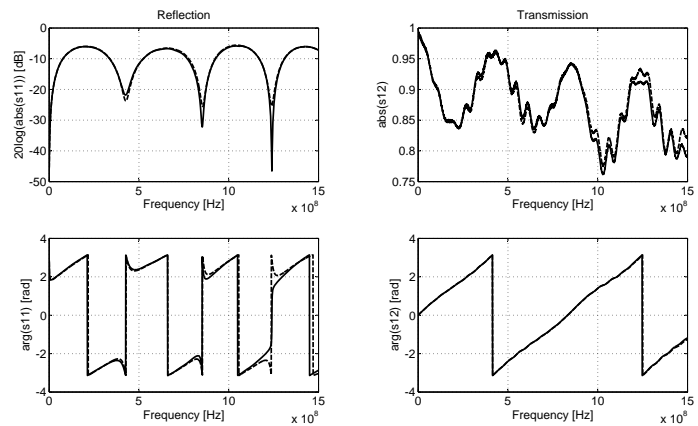
Figure C.9: Schmidt plot of crystal orientation in artificial ice samples. Upper row: Two horizontal cuts, bottom row: Two vertical cuts. The dots in the Schmidt plots mark the intersection of the c-axes with the hemisphere in horizontal (upper row) or vertical direction (bottom row). For more details on Schmidt plots, see Wilen *et al.* [2003].

Figure C.10: Distribution of c -axes in vertical cuts. Note that no clear preference in crystal orientation is detected (cf. Figure 4.9). For the definition of the “latitude” angle, see text.



C.9 S-parameters of HCL-doped ice

Figure C.11: Exemplary S-parameters of HCL-doped ice. Shown here is sample no.2 with an acidity of 10^{-3} resulting in $\epsilon_{\infty} = 3.26$. Note the distinct decreasing trend in transmission, e.g. $|S_{21}|$. The S-parameters in reverse direction, e.g. $|S_{12}|$ are shown as dashed lines.



D Code

D.1	Binned correlation	page 173	(developed with H.Konrad)
D.2	Bootstrap:	page 175	
D.3	Postprocessing routine of GPR-IRHs	page 176	
D.4	Forward model of coaxial cell setup:	page 180	

```

C:\MATLAB65\work\bin\correlation\bin\cor_mc_cg_plot.m Page 2
'Color','grey','LineWidth',2);grid on;set(gca,'FontSize',14);xlabel('Window length',\
'fontSize',14);ylabel('R','fontSize',14);title('KCS-CC','fontSize',14);
subplot(2,3,5)plot(Fenster,KCHRCI(:,1),'k','LineWidth',3);hold on;plot(Fenster,KCHCC(:,\
1)-KCHRCI(:,2)),'--','Color','grey','LineWidth',2);plot(Fenster,KCHCC(:,1)-KCHRCI(:,2)),'--',\
'Color','grey','LineWidth',2);grid on;set(gca,'FontSize',14);xlabel('Window length',font\
size,14);ylabel('R','fontSize',14);title('KCH-CC','fontSize',14);
subplot(2,3,6)plot(Fenster,KSCC(:,1),'k','LineWidth',3);hold on;plot(Fenster,KSCC(:,\
1)-KSCC(:,2)),'--','Color','grey','LineWidth',2);plot(Fenster,KSCC(:,1)-KSCC(:,2)),'--',\
'Color','grey','LineWidth',2);grid on;set(gca,'FontSize',14);xlabel('Window length',font\
size,14);ylabel('R','fontSize',14);title('KCS-CC','fontSize',14);
figure
subplot(2,3,1)plot(Fenster,KCHRCI(:,3),'k','LineWidth',3);hold on;plot(Fenster,KCHRCI(:,\
3)-KCHRCI(:,4)),'--','Color','grey','LineWidth',2);plot(Fenster,KCHRCI(:,3)-KCHRCI(:,4)),'\
--','Color','grey','LineWidth',2);grid on;set(gca,'FontSize',14);xlabel('Window length',\
'fontSize',14);ylabel('F','fontSize',14);title('KCH-KCI','fontSize',14);ylim([-10 10]);
subplot(2,3,2)plot(Fenster,KCSKCI(:,3),'k','LineWidth',3);hold on;plot(Fenster,KCSKCI(:,\
3)-KCSKCI(:,4)),'--','Color','grey','LineWidth',2);plot(Fenster,KCSKCI(:,3)-KCSKCI(:,4)),'\
--','Color','grey','LineWidth',2);grid on;set(gca,'FontSize',14);xlabel('Window length',\
'fontSize',14);ylabel('F','fontSize',14);title('KCS-KCI','fontSize',14);ylim([-10 10]);
subplot(2,3,3)plot(Fenster,CKKCI(:,3),'k','LineWidth',3);hold on;plot(Fenster,CKKCI(:,\
3)-CKKCI(:,4)),'--','Color','grey','LineWidth',2);plot(Fenster,CKKCI(:,3)-CKKCI(:,4)),'--',\
'Color','grey','LineWidth',2);grid on;set(gca,'FontSize',14);xlabel('Window length',font\
size,14);ylabel('F','fontSize',14);title('CC-KCI','fontSize',14);ylim([-10 10]);
subplot(2,3,4)plot(Fenster,KCHRCIS(:,3),'k','LineWidth',3);hold on;plot(Fenster,KCHRCIS(:,\
3)-KCHRCIS(:,4)),'--','Color','grey','LineWidth',2);plot(Fenster,KCHRCIS(:,3)-KCHRCIS(:,4)),'\
--','Color','grey','LineWidth',2);grid on;set(gca,'FontSize',14);xlabel('Window length',\
'fontSize',14);ylabel('F','fontSize',14);title('KCH-KCS','fontSize',14);ylim([-10 10]);
subplot(2,3,5)plot(Fenster,KCHCCI(:,3),'k','LineWidth',3);hold on;plot(Fenster,KCHCCI(:,\
3)-KCHCCI(:,4)),'--','Color','grey','LineWidth',2);plot(Fenster,KCHCCI(:,3)-KCHCCI(:,4)),'--',\
'Color','grey','LineWidth',2);grid on;set(gca,'FontSize',14);xlabel('Window length',font\
size,14);ylabel('F','fontSize',14);title('KCS-CC','fontSize',14);ylim([-10 10]);
% Mean values for R und F
R=[KCHRCI(:,1) KCSKCI(:,1) CKKCI(:,1) KCHRCIS(:,1) KCHCCI(:,1) KSCCC(:,1)]; R_err=[KCHRCI(:,\
2) KCSKCI(:,2) CKKCI(:,2) KCHRCIS(:,2) KCHCCI(:,2) KSCCC(:,2)];
F=[KCHRCI(:,3) KCSKCI(:,3) CKKCI(:,3) KCHRCIS(:,3) KCHCCI(:,3) KSCCC(:,3)]; F_err=[KCHRCI(:,\
4) KCSKCI(:,4) CKKCI(:,4) KCHRCIS(:,4) KCHCCI(:,4) KSCCC(:,4)];
figure
subplot(2,1,1)plot(Fenster,mean(R,2),'k','LineWidth',3);hold on;plot(Fenster,mean(R,2)\
-std(R,0,2)),'--','Color','grey','LineWidth',2);plot(Fenster,mean(R,2)-std(R,0,2)),'--',\
'Color','grey','LineWidth',2);grid on;set(gca,'FontSize',14);xlabel('Window length',fontsize\
e,14);ylabel('mean(R)','fontSize',14);
subplot(2,1,2)plot(Fenster,mean(F,2),'k','LineWidth',3);hold on;plot(Fenster,mean(F,2)\
-std(F,0,2)),'--','Color','grey','LineWidth',2);plot(Fenster,mean(F,2)-std(F,0,2)),'--',\
'Color','grey','LineWidth',2);grid on;set(gca,'FontSize',14);xlabel('Window length',fontsize\
e,14);ylabel('mean(F)','fontSize',14);ylim([-10 10]);
Rout=[Fenster' R R_err];
Fout=[Fenster' F F_err];
save Rout Rout -ascii
save Fout Fout -ascii

```

```

C:\MATLAB65\work\bin\correlation\bin\cor_mc_cg_plot.m Page 1
% Binned correlation for the delta 0-18 time series of the CG ice cores
% Input:
% 1. number (see binned cor mc.m)
% 2. T_ende (see binned cor mc.m)
% 3. T_start (see binned cor mc.m)
% 4. T_min (deltaT_min_start_deltaT_min: see binned cor mc.m)
% 5. T_max (deltaT_min_end_deltaT_max: binned cor mc.m)
% 6. deltaT: increment for 4. and 5.
function binned_cor_mc_cg_plot(number,T_anfng,T_ende,T_min,T_max,deltaT)
i=1;
for k=T_min:deltaT:T_max
    deltaT_min=i;
    deltaT_max=k+deltaT;
    R_err=binned_cor_mc_cg(number,T_anfng,T_ende,deltaT_min,deltaT_max);
    % Calculate F=R/(1-R) for all pairs
    KCHRCI(1,1)=R_err(2,1); KCHRCI(1,2)=R_err(2,5); KCHRCI(1,3)=R_err(2,1)/(1-R_err(2,1)); KCHRCI(
    1,4)=R_err(2,5)/(1-R_err(2,1))-2);
    KCSKCI(1,1)=R_err(3,1); KCSKCI(1,2)=R_err(3,5); KCSKCI(1,3)=R_err(3,1)/(1-R_err(3,1)); KCSKCI(
    1,4)=R_err(3,5)/(1-R_err(3,1))-2);
    CKKCI(1,1)=R_err(4,1); CKKCI(1,2)=R_err(4,5); CKKCI(1,3)=R_err(4,1)/(1-R_err(4,1)); CKKCI(1,4)
    =R_err(4,5)/(1-R_err(4,1))-2);
    KCHRCIS(1,1)=R_err(3,2); KCHRCIS(1,2)=R_err(3,6); KCHRCIS(1,3)=R_err(3,2)/(1-R_err(3,2)); KCHRCIS(
    1,4)=R_err(3,6)/(1-R_err(3,2))-2);
    KCHCCI(1,1)=R_err(4,2); KCHCCI(1,2)=R_err(4,6); KCHCCI(1,3)=R_err(4,2)/(1-R_err(4,2)); KCHCCI(1,4)
    =R_err(4,6)/(1-R_err(4,2))-2);
    KSCCC(1,1)=R_err(4,3); KSCCC(1,2)=R_err(4,7); KSCCC(1,3)=R_err(4,3)/(1-R_err(4,3)); KSCCC(1,4)
    =R_err(4,7)/(1-R_err(4,3))-2);
    Fenster(i)=(deltaT_min+deltaT_max)/2;
    i=i+1;
end
% Make plots
grey = [0.4,0.4,0.4];
figure
subplot(2,3,1)plot(Fenster,KCHRCI(:,1),'k','LineWidth',3);hold on;plot(Fenster,KCHRCI(:,\
1)-KCHRCI(:,2)),'--','Color','grey','LineWidth',2);plot(Fenster,KCHRCI(:,1)-KCHRCI(:,2)),'\
--','Color','grey','LineWidth',2);grid on;set(gca,'FontSize',14);xlabel('Window length',\
'fontSize',14);ylabel('R','fontSize',14);title('KCH-KCI','fontSize',14);
subplot(2,3,2)plot(Fenster,KCSKCI(:,1),'k','LineWidth',3);hold on;plot(Fenster,KCSKCI(:,\
1)-KCSKCI(:,2)),'--','Color','grey','LineWidth',2);plot(Fenster,KCSKCI(:,1)-KCSKCI(:,2)),'\
--','Color','grey','LineWidth',2);grid on;set(gca,'FontSize',14);xlabel('Window length',\
'fontSize',14);ylabel('R','fontSize',14);title('KCS-KCI','fontSize',14);
subplot(2,3,3)plot(Fenster,CKKCI(:,1),'k','LineWidth',3);hold on;plot(Fenster,CKKCI(:,\
1)-CKKCI(:,2)),'--','Color','grey','LineWidth',2);plot(Fenster,CKKCI(:,1)-CKKCI(:,2)),'--',\
'Color','grey','LineWidth',2);grid on;set(gca,'FontSize',14);xlabel('Window length',font\
size,14);ylabel('R','fontSize',14);title('CC-KCI','fontSize',14);
subplot(2,3,4)plot(Fenster,KCHRCIS(:,1),'k','LineWidth',3);hold on;plot(Fenster,KCHRCIS(:,\
1)-KCHRCIS(:,2)),'--','Color','grey','LineWidth',2);plot(Fenster,KCHRCIS(:,1)-KCHRCIS(:,2)),'

```


C:\MATLAB65\work\Produktion\bootstrap\bootstrap2.m

```

Pdown=10;
P= prctile(Filterresults, [Pdown Pup]);
Percentile=P;

Result=zeros(M,3);
Result(:,1)=Gaussstack;
Result(:,2)=Gaussstack;
Result(:,3)=Percentile(:,2);

figure;
plot(Result(:,1),'b');hold on
plot(Result(:,2),'r');hold on
plot(Result(:,3),'b');hold on
hold off

save bootstrapresults Result;
out= Result;

```

C:\MATLAB65\work\Produktion\bootstrap\bootstrap2.m

```

% Ice core=Bootstrap
% Pascal Rohleber, 27.08.2009
% Goal: Uncertainty estimation for decadal trends in ice core stack
% Input: Matrix with normalized ice core time series as columns
% Output: File "bootstrapresults.mat", plots
function out= bootstrap2(file)

% 1. Read data, calculate stack und matrix of the residuals (individual ice
% core minus stack)
In= file;
Stack= mean(In, 2);
[M, N] = size(In);
Residuen= zeros(M, N);
[Gaussstack]=Gaussfilter(Stack);

for i=1:M
    for j=1:N
        Residuen(i,j)= file(i,j)-Stack(i);
    end
end

% 2. Bootstrap
Runs=10000;
Filterresults= zeros(M, Runs);

% 2.1 Generate random numbers (needs improvement!)
for k=1:Runs
    randn('seed', 0);
    X=zeros(1,4);
    X(1,:)=mod(randperm(4),5);
    Y=zeros(1,4);
    Y(1,:)=mod(randperm(4),5);

% 2.2 Matrix with reconstructed series: Allow to randomly pick residuals
% from all cores.
Recons= zeros(M, N);
for i=1:M
    for j=1:N
        Recon(i,j)= Stack(i)+ Residuen(X(4), Y(3));
    end
end

% 2.3 Calculate New Stack
NewStack= mean(Recon, 2);

% 2.4 Filter New Stack
[Gaussfilter]= Gaussfilter(NewStack);
%plot(Gaussfilter); hold on;

% 2.5 Save filtered results as column in Filterresults- then repeat 2.1-2.5
% until number Runs is reached.
for i=1:M
    Filterresults(i,k)=Gaussfilter(i);
end
end

% 3. Calculate Percentiles from bootstrap series- to be used as "confidence
% intervals"
Pup=90;

```

Page 1	Page 2
<pre> C:\WATLAB6p5\work\CollRad\Version5und6\horzprocess6.m ----- GPR horizon processing ----- % Version 6.0, Pascal Bohleber, 16.06.10 (1st version 14.12.09) % - Converts trace-TWT into trace-depth based on interpolation between density profiles at start and end of profile. % - Calculates age in Year BP at start and end of each horizon based on the according ge-depth relationships. % INPUT: horzprocess(GPR-Data, Ice-core data start = density file 1, dating file 1, Ice core data end = density file 2, dating file 2) % i.e. horzprocess('081609.txt', 'KCI_density.txt', 'KCI_dating.txt', 'KCS_density.txt', 'KCS_dating.txt') % GPR-Data: Picked horizons, Last horizon = bedrock!, produced by "mute2tx.sh" (Olaf Eh sen). Conversion from unix to dos ascii needed (i.e. "unix2dos.sh"). % File structure: Delimiter: space, 1st column: trace nr., 2nd column: TWT, delimiter-c haracter after end of horizon: ">". % Ice core data: I. Density file: Column 1: Absolute depth [m], Column2: Density [g/cm3] , II. Dating file: Column 1: Absolute depth [m], % Column 2: depth [m.w.e.], Column 3: year BP % OUTPUT: 1 txt-file for each individual horizon. File structure: Delimiter: space, 1st column: trace nr., 2nd column: TWT, % 3rd column: absolute depth [m] % 1 txt-file with start and endpoint of horizons with depth, m.w.e. and age % % modified 02/10: no headers in output txt files! % modified 03/10: some interpolation-routines changed, rename: horzprocess2.m % modified 03/10: error estimation module, rename: horzprocess3.m % modified 06/10: added: output of horizon-depth in m.w.e., check for isochores, renam e: horzprocess4.m % modified 06/10: new density interpolation routine, rename: horzprocess5.m % modified 06/10: new density interpolation routine 2, rename: horzprocess6.m function horzprocess5(file, icecore1_density, icecore1_dating, icecore2_density, icecor e2_dating) % Set constants lspaced=299792458; z_rho_max=100; % Maximum depth of density interpolation icedens=0.9; % ice density threshold still somewhat arbitrary, could be set to 0.89 depthres=0.2; % Define depth resolution: depthsres % ----- INPUT from file ----- % ----- % Input from file 1: Read the data, divide into individual horizons after delimiter-cha </pre>	<pre> C:\WATLAB6p5\work\CollRad\Version5und6\horzprocess6.m ----- racter ">" fid = fopen(file, 'r'); i=1; k=1; trmax=1; filename=file, sprintf('horz_%d',i)); fout = fopen(filename, 'w'); while ~feof(fid) tline = fgetl(fid); % Skip the first 3 lines (header) if k<k4 tline=[]; % For end of horizon close active file and open next file elseif tline(1)='>' tline=[]; fclose(fout); i=i+1; % Number of horizon filename=[file, sprintf('_horz_%d',i)]; fout = fopen(filename, 'w'); % Write TWT and trace number to file, read TWT and trace separated by space else limit=regexptline, ' '; twt=tline(i:limit); trace=tline(limit:end); out= (strznum(twt) strznum(trace)); fprintf(fout, '%s\n', out); tracenum=strznum(trace); if tracenum>trmax trmax=tracenum; % Maximum trace number is needed later! end end k=k+1; end end fclose(fout); tracemax=trmax; maxhor=i; clear i; % Input from file 2: Plot the separate horizons into a single plot, Preference: Last % horizon = bedrock! figure; for j=1:maxhor filename=[file, sprintf('_horz_%d',j)]; % Create separate variables containing each horizon for further processing eval ([sprintf('Horizon_%d = load(filename);', j)]); eval ([sprintf('Horizon= Horizon_%d ', j)]); set(gca, 'YDir', 'reverse') if j==maxhor subplot(2,1,1), plot (Horizon(:,2),Horizon(:,1), 'k-', 'LineWidth',2); xlabel('trace'), ylabel('TWT'), title(file); hold on; else subplot(2,1,1), plot (Horizon(:,2),Horizon(:,1), 'r-', 'LineWidth',2); xlabel('trace'), ylabel('TWT'), title(file); end end </pre>

```

C:\WATLAB65\work\CollRadar\Version5und6\horzprocess6.m Page 4
den_newsres(i,j)= (IC2_den_newsres(i,2)-IC1_den_newsres(i,2))*(j-2)/(tracemax-2)+IC1_
den_newsres(i,2);
end
end
close(h);
% 5. Calculate velocity-depth profile based on Kovacs-relation and
% according TWT
h = waitbar(0,'Velocity-Interpolation in progress. Please wait...');
Velocity(:,1)=rho_resolution;
TravelT(:,1)=rho_resolution;
for j=2:(tracemax+1)
    waitbar(j/tracemax,h)
    for i=1:length(rho_resolution)
        Velocity(i,j)=TravelT(i,j)*lspeed*(1/(1+0.854*Density(i,r,j)));
        TravelT(i,j)=TravelT(i,1)./Velocity(i,j);
    end
end
close(h);
% For each horizon, add column with new depth coordinate
h = waitbar(0,'Calculating horizon data. Please wait...');
for i=1:maxhor
    waitbar(i/maxhor,h)
    eval(sprintf('Horizon_Horizon_%d;', i));
    time=0.5*Horizon(j,1);
    t=Horizon(j,2);
    % ATTENTION: Depth is represented by interpolating for TWT/2!
    me)', i)); % eval(sprintf('Horizon_%d(j,3)-interp1(TravelT(:,tr+1), TravelT(:,1),t*
ime, 'pchip', 'r', i));
% For each horizon, add column with depth coordinate in depth m.w.e.
eval(sprintf('zfe=Horizon_%d(j,3)', i));
rho=Density(:,tr);
zw=0;zi=0;k=1;
while zi<zfe
    zw=zw+rho(k)*depthres;
    zi=zi+depthres;
    k=k+1;
end
end
eval(sprintf('Horizon_%d(j,4)=zw;', i));
end
close(h);
% Plot the horizons
for i=1:maxhor
    set(gca,'YDir','reverse')
    if i==maxhor
        subplot(2,1,2);
        eval(sprintf('plot(Horizon_%d(:,2),Horizon_%d(:,3), 'k-', 'LineWidth', 2)', i, i)
));
        xlabel('trace'),ylabel('depth [m]',title(file));
        hold on
    else
        subplot(2,1,2);
        eval(sprintf('plot(Horizon_%d(:,2),Horizon_%d(:,3), 'LineWidth', 2)', i, i));
    end
end

```

```

C:\WATLAB65\work\CollRadar\Version5und6\horzprocess6.m Page 3
hold on;
end
end
% Input from file 3: Read all icecore ascii data
IC1_den=load(icecore1_density);
IC1_dat=load(icecore1_dating);
IC2_den=load(icecore2_density);
IC2_dat=load(icecore2_dating);
%----- START PROCESSING -----
%----- 11.06.10 Improved Interpolation-Module -----
% Idea: Linear interpolation between density-profiles from start- to endpoint.
% Extend density profiles downwards with constant ice density.
% 1. Bring both density profiles to common resolution and extend density
% profiles to z_rho_max with icedens
% @Startpoint
if IC1_den(end,1)<z_rho_max
    start=IC1_den(end,1)+0.1;
    rho_extend_start=0.1:z_rho_max;
    rho_extend(2,:)=0.9;
    rho_extend=rho_extend';
    Density1=[IC1_den; rho_extend];
end
% @Endpoint
if IC2_den(end,1)<z_rho_max
    start=IC2_den(end,1)+0.1;
    rho_extend_start=0.1:z_rho_max;
    rho_extend(2,:)=0.9;
    rho_extend=rho_extend';
    Density2=[IC2_den; rho_extend];
end
% 3. Define depth resolution for mixed density profiles and interpolate
% density input data accordingly
rho_resolution=0.1:z_rho_max;
IC1_den_newsres=interp1(Density1(:,1),Density1(:,2),rho_resolution,'linear'); % Problems
might occur because z_rho_max >> local depth_max
IC2_den_newsres=interp1(Density2(:,1),Density2(:,2),rho_resolution,'linear');
IC1_den_newsres=[rho_resolution' IC1_den_newsres'];
IC2_den_newsres=[rho_resolution' IC2_den_newsres'];
% 4. Distance-weighted density mixing down to z_fe
h = waitbar(0,'Density-Interpolation in progress. Please wait...');
Density(:,1)=rho_resolution;
for j=2:(tracemax+1)
    waitbar(j/tracemax,h)
    for i=1:length(Density(:,1))

```

```

C:\WATLAB6p5\work\CollRadRad\Version5und6\horzprocess6.m
Error1=[IC1_dat(i:end-1,3) Err1]; % vector with age and according error
% Same procedure at Endpoint
Depth_diff=diff(IC2_dat(:,2)); % m.w.e.
Dat_diff=diff(IC2_dat(:,3)); % age a BP
Diff2=Dat_diff./Depth_diff2;
% Include dating error of +/- 3 a
Err2= sqrt(Diff2.^2.+Delta_Dat^2);
Error2=[IC2_dat(i:end-1,3) Err2]; % vector with age and according error
% Step 2: Calculate dating error according to age of each horizon via interpolation.
for i=1:maxhor
    Starthor(i,5)=interpl(Error1(:,1),Error1(:,2),Starthor(i,4),'linear'); % Age error
    Endhor(i,5)=interpl(Error2(:,1),Error2(:,2),Endhor(i,4),'linear');
    Starthor(i,5)=round(Starthor(i,5)); % Round age to nearest integer
    Endhor(i,5)=round(Endhor(i,5));
end
% New: Check for isochrone
for i=1:maxhor
    Age_Start=Starthor(i,4);
    Age_End=Endhor(i,4);
    Error_Start=Starthor(i,5);
    Error_End=Endhor(i,5);
    Iso_Start(i)=Age_Start-Error_Start;
    Iso_Start(i)=Age_Start+Error_End;
    Iso_End(i)=Age_End-Error_End;
    Iso_End(i)=Age_End+Error_End;
    if Age_Start==Age_End
        Iso(i)=1;
    elseif Age_Start < Age_End
        if Iso_Start(2) >= Iso_End(1)
            Iso(i)=1;
        else
            Iso(i)=0;
        end
    else
        if Iso_Start(1) <= Iso_End(2)
            Iso(i)=1;
        else
            Iso(i)=0;
        end
    end
end
Iso=Iso';
% ----- OUTPUT -----
% 1. Horizons
for i=1:maxhor
    eval(sprintf('Horizon= Horizon_%d', i));
inputfilename = [file, sprintf('_horz_%d',i)];

```

```

C:\WATLAB6p5\work\CollRadRad\Version5und6\horzprocess6.m
xlabel('trace'),ylabel('depth (m)'),title(file);
hold on
end
end
% ----- Calculate age of horizons at start and endpoint / ice core -----
% Define start and endhorizon
for i=1:maxhor
    eval(sprintf('Horizon=Horizon_%d', i));
    Starthor(i,:)=[Horizon(i,:);
    Endhor(i,:)=[Horizon(end,:);
    Starthor(i,2)=[]; % no trace nr.
    Endhor(i,2)=[]];
% Convert column 2 (m abs) in m.w.e. (column 3) based on the dating-files.
% And column 3 into age in year BP
for i=1:maxhor
    Starthor(i,3)=interpl(IC1_dat(:,1),IC1_dat(:,2),Starthor(i,2),'linear');
    Endhor(i,3)=interpl(IC2_dat(:,1),IC2_dat(:,2),Endhor(i,2),'linear');
    Starthor(i,4)=interpl(IC1_dat(:,2),IC1_dat(:,3),Starthor(i,3),'linear');
    Endhor(i,4)=interpl(IC2_dat(:,2),IC2_dat(:,3),Endhor(i,3),'linear');
    Starthor(i,4)=round(Starthor(i,4)); % Round age to nearest integer
    Endhor(i,4)=round(Endhor(i,4));
end
% ----- ERROR ESTIMATION module -----
% For the last 100 years BP, dating uncertainties for all cores are +/- 3
% years (see Schäfer, 1995, and Jung, 1993, for CC, Ambruster, 2000, for
% KCS and KCH and Bohléber, 2008, for KCI)
% Delta_Dat=3.0;
% Preliminary implementation: Use constant depth uncertainty \Delta z_w
% \approx = 0,42 m.w.e. valid only for 250 MHz Data!
Delta_zw=0.42;
% which mainly stems from:
% 1. Uncertainty in Picking of horizon and uncertainty in density data
% 2. Depth-uncertainty from envelope of wave-packet
% For more details see pdf: "GPR-Horizonte_Fehlerrechnung.pdf"
% Step 1: Calculate vector with approximate dating derivatives.
% At Starting Point
Depth_diff=diff(IC1_dat(:,2)); % m.w.e.
Dat_diff=diff(IC1_dat(:,3)); % age a BP
Diff1=(Dat_diff./Depth_diff1).*Delta_zw;
% Include dating error of +/- 3 a
Err1= sqrt(Diff1.^2.+Delta_Dat^2);

```

```

C:\MATLAB6p5\work\ColleRadar\Version5und6\horzprocess6.m Page 7
outputfilename = [file, sprintf('%e', i)];
fid1 = fopen(inputfilename, 'rt');
fid2 = fopen(outputfilename, 'wt');
j=1;
% nline = ['TWT [ns] ', ' ', 'trace # ', ' ', 'depth [m abs]', '\n'];
% fprintf(fid2, nline);
while feof(fid1) == 0;
    tline = fgetl(fid1);
    temp1 = num2str(horizon(j,3));
    temp2 = num2str(horizon(j,4));
    nline = [tline, ' ', temp1, ' ', temp2, '\n'];
    fprintf(fid2, nline);
    j=j+1;
end
fclose(fid1);
fclose(fid2);
end

% 2. Age comparison
Output = [Starthor Endhor Iso];
[M,N]=size(Output);
header = ['START: TWT [ns] ', '\t', 'depth [m abs]', '\t', 'depth [m we]', '\t', 'age [yr',
' ear BP]', '\t', 'Error [a]', '\t', 'END: TWT [ns]', '\t', 'depth [m abs]', '\t', 'depth',
h [m we]', '\t', 'age [year BP]', '\t', 'Error [a]', '\t', 'isochrone? I=yes, 0=no', '\n']\r
;
outputfilename = [file, '_proc6']; % include version number
fid = fopen(outputfilename, 'wt');
fprintf(fid, header);
for i=1:N
    for j=1:N
        temp1=num2str(Output(i,3), 4);
        temp2=[temp1, '\t'];
        fprintf(fid, temp2);
    end
    fprintf(fid, '\n');
end
fclose(fid);

% ----- Delete temp horizon files -----
for i=1:maxhor
    filename = [file, sprintf('horz_%d', i)];
    eval(sprintf('delete %s', filename));
end
return

```

C:\WATLAB65\work\Koaax\Sim_Zelle\Sim... \Tsimsetupforprint.m	Page 2
<pre> function out=Tsimsetup(parameters) % Forward-model of scattering parameters for HD coaxial cell, following Oswald et al., ✓ % but now including a first order estimate of impedance mismatch at calibration plane pK lus % coax cable and port connection not accounted for in 1-port calibration. % Input parameters as vector: parameters=[f delta(Teflon) lstecker lcable permittivity] % Pascal Bohleber, 31.01.11 % % 08.02.11: Adaption for optimization at a specific frequency. Input % parameters = [freq param1 param2 param3] % Deploy T-matrix approach. % % ----- Set constants ----- mu=1+4*pi*1e-7; % hier mu_0 benutzen! eps0=8.854e-12; c=299792458; Zref=50; % cell parameters rin=0.013; rou=0.003; l=0.2; % ----- Old Oswald-based Calculations ----- % Set input parameters for Debye model f= [3e5; (1.5e9-3e5)/1600; 1.5e9]; % from 300kHz to 1.5GHz, 1601 points w=2*pi.*f; sigma=1e-9; e_static=3.19; % Debye-parameters for permittivity e_inf=3.19; f_relax=1e3; tau=1/(2*pi*f_relax); % 3. Debye model for frequency dependent epsilon e=e_inf+(e_static-inf)/(1+i.*w.*tau); R=(1/(2*pi)).*sqrt(pi.*f.*mu*sigma).*(1/(rou+1/rin)); L=(mu/(2*pi)).*log(rou/rin); C=(2*pi*eps0.*real(ert)).*log(rou/rin); G=(2*pi/(log(rou/rin))).*(eps0.*imag(ert).*w*sigma); gamma=sqrt((R+i.*w.*L).*(G-i.*w.*C)); Zw=sqrt((R+i.*w.*L)./(G-i.*w.*C)); % Oswald scattering parameters calculated analytically s11=(Zw.^2-Zref^2).*tanh(gamma.*l)./(2*Zw+Zref+tanh(gamma.*l).*(Zw.^2+Zref^2)); s12=2./(2.*cosh(gamma.*l)+sinh(gamma.*l)).*(Zw./Zref).*(Zw./Zref).*(Zref./Zw)); s21=s12; s22=s11; </pre>	<pre> C:\WATLAB65\work\Koaax\Sim_Zelle\Sim... \Tsimsetupforprint.m % ----- New Transmission-Matrix Approach ----- % Calculate "disturbed" scattering parameters assuming a small impedance % mismatch (delta) delta = parameters(1,1); % % ----- Define transmission parameters for each component ----- % 0) Teflon discs - Now with loss term! etefl=2.05+1i*0; ltefl=0.01; loss=parameters(1,2); % betatefl=2*pi.*f.*sqrt(etefl)/c; % Old: No loss betatefl=2*pi.*f.*sqrt(etefl+loss)/c; % Gorziti & Slob % % Ztefl=Zref+delta; Ztefl2=Zref+delta.*ones(l,length(f)); % 1) Cell between cone-shaped coax connectors Zkegel1=Zref+0.*ones(l,length(f)); betazelle=-imag(gamma); Zkegel2=Zref+0.*ones(l,length(f)); lkegel1=0.06; % l minus lstecker betakegel1=2*pi.*f.*(1+loss)/c; % 2) Connector after second cone Zstecker=Zref+0.*ones(l,length(f)); lstecker=0.06; betastecker=0; % set later equal to betacable % 3) Coaxial cable Zcable=53.*ones(l,length(f)); Ccable=83e-12; lcable=parameters(1,3); betacable=2*pi.*f.*Zcable.*Ccable; betastecker=betacable; % 4) Port Zport=Zref.*ones(l,length(f)); % ----- Transmission-Matrices! ----- % Use separate functions for Transmission Matrix (TM) components: TLT.m for % TM, verbt for connectors (empty TL) for k=1:length(f) % Transmission matrix components Verb0=verbt(Zkegel(k),Zw(k)); Zelle=TLT(betazelle(k),l); Verb1a=verbt(Zw(k),Ztefl2(k)); Verb1b=TLT(betatefl(k),ltefl); Verb1c=verbt(Ztefl2(k),Zkegel2(k)); Regel=TLT(betakegel(k),lkegel); </pre>

Acknowledgements

Every time you go out on the ice, there are slight flaws. You can always think of something you should have done better. These are the things you must work on.

– Dorothy Hamill

Working on this thesis comprised the opportunity to meet and work with many people; in offices, (cold) labs, “on the ice”, at conferences, and of course, coffee breaks. These personal contacts were an important part of the past years, valuable scientifically, but also on a personal level. I want to express my gratitude to the following people for their individual contribution, and the exhausted reader is thus asked to read a little further through the following (inevitably incomplete) acknowledgements.

I would like to thank my advisor PD Dr. Olaf Eisen, for giving me the opportunity to work on this thesis within his LIMPICS project, for his scientific guidance, detailed proofreading and all the mobile support on his journey from Reutheidelhaven to Bremerlingenberg. I especially thank him for introducing me to GPR and for subletting his office to me for the past months.

I also would like to thank Prof. Dr. Kurt Roth for being my co-advisor and referee of this thesis, for kindly providing the coaxial cell and borehole radar setups, and also for his encouraging support throughout the thesis.

The final stage of this work was supported by the completion grant of the graduate academy of the University of Heidelberg.

Special thanks go to Dietmar Wagenbach, who first introduced me to glaciology, and inspired me to become a scientist. I cordially thank him for his continuous support, and especially for his experienced and patient proofreading.

I further thank Hannes Konrad, with whom it has been a pleasure to work with and to share the project of mapping the age-distribution at CG. The common interest in some of the more theoretical aspects of environmental physics was not the only basis of

our good cooperation, but might also make our scientific paths cross again in the future. To Norman Wagner I am greatly thankful for his extensive support with the coaxial cell. Unquestionably, the coaxial cell project would not have finally succeeded to this extent without his contribution. The respective chapter of this thesis additionally profited from his comments and suggestions.

I also thank Carsten Schindler for his technical recommendations, Benedikt Oswald for the optimisation algorithm and Shuji Fujita for his comments and general interest in the coaxial cell. Mathias Hoppe is acknowledged for his struggle with the initial technical challenges, and for his help preparing ice samples. I am grateful for the skillful construction of the refined cell made by the IUP workshop. Sepp Kipfstuhl kindly provided his expertise measuring the crystal orientation of the artificial ice samples. I would also like to thank him for hosting me at AWI numerous times, likewise Frank Wilhelms, readily sharing his experience in measuring dielectric ice properties. I also would like to include a general thank you to the people at AWI.

Far more down south I would like to thank Ingeborg Auer, Reinhard Böhm and Wolfgang Schöner of the ZAMG in Vienna for their support with the instrumental temperature data. I would also like to thank Manfred Mudelsee for his advice regarding the isotope time series analysis.

I thank Susanne Preunkert, particularly for hosting me at LGGE in Grenoble. I would also like to thank Christian Vincent at LGGE for introducing me to his flow model and sharing it for further use within this study. The borehole radar study within this work was made possible by the practical support of Thomas Richter and Michael Eidner of boratec, Weimar, which is greatly appreciated.

I would like to thank the entire IUP-Eisgruppe for their everyday support over the years, Barbara May for her help in the lab and Christoph Elsässer for sharing insights and the common interest in time series analysis. I would also like to thank my IUP-colleagues, especially Anne, Felix, Gabi, Martin and Sam—with all of which it has been a pleasure to work and not-work with. The LIMPICS-group appears to spatially group in case of field expeditions only, those were however pretty bonding experiences, not least for once descending from CG on a rope. So thanks to my Colle-agues Achim, Anja, Coen, Reinhard and also Olaf for the fieldwork together, especially for the help with the GPR-measurements.

Finally, I would like to express my gratitude to all the people who have supported me in life outside science. Especially to my parents and my sister Laura. Also to all my friends, in particular Bert, Mike and Phil. I am deeply thankful to Maren for her caring support throughout the years.